Institut für Theoretische Physik
Fakultät Mathematik und Naturwissenschaften
Technische Universität Dresden

# Complex Patterns in Extended Oscillatory Systems

## Komplexe Muster in Ausgedehnten Oszillatorischen Systemen

Dissertation
zur Erlangung des
Doktorgrades der Naturwissenschaften
(Doctor rerum naturalium)

vorgelegt von
Lutz Brusch
geboren am 1. Juni 1972 in Dresden

Dresden 2001

*Chaos often wins when confronted with order*
*because chaos is better organized. [R. Bendlin]*

Eingereicht am 15. Juni 2001

1. Gutachter: Prof. Dr. P. Fulde
2. Gutachter: Prof. Dr. G. Diener
3. Gutachter: Prof. Dr. L. Kramer

Verteidigt am 14. August 2001

# Abstract

Many universal features of extended oscillatory systems, *i.e.* dissipative systems that show oscillations or traveling waves at the onset of pattern formation, are qualitatively described in the framework of an amplitude equation, namely the complex Ginzburg-Landau equation (CGLE). In some recent experiments in hydrodynamical systems even a quantitative description has been achieved with the CGLE.

Previous studies of the CGLE by numerical simulations revealed transitions from stable wave solutions to different realizations of spatio-temporal chaos as parameters are varied. The present bifurcation and stability analysis of some complex patterns facilitates a deeper understanding of spatio-temporal chaos. A mechanism for the formation of space-time defects is provided.

Depending on parameters in the CGLE the wave solutions may become unstable via the Eckhaus instability. In its supercritical case stable modulated amplitude waves (MAWs) coexist with the unstable waves above their instability.
Using continuation software (AUTO97), the MAWs are calculated and their existence and stability properties analysed. They form a continuous two-parameter family of coherent structures. Their shape does not change when described in a comoving reference frame. The average phase gradient $\nu$ and the spatial period $P$ of the modulation parametrize the family of MAWs. MAWs bifurcate supercritically (subcritically) for small (large) wavenumber and disappear in saddle-node bifurcations at larger values of the control parameters. The saddle-node bifurcations occur first at infinite spatial period of the modulation and shift to larger values of the control parameters as the period is decreased. MAW-like structures with parameters $\nu, P$ beyond a saddle-node bifurcation may evolve to a defect,*i.e.* the local phase gradient diverges and the resulting state has a different total $\nu$. Secondary instabilities of the MAWs enhance or reduce the probability of defect formation.

Numerical simulations are used to illustrate the discovered mechanisms. Combining these ingredients the transition from phase to defect chaos in the one-dimensional CGLE is studied and explained in detail. We conjecture the saddle-node bifurcation for $\nu = 0, P \to \infty$ to be a lower bound for this transition and phase chaos to persist in the thermodynamic limit for parameter values below this line.

The obtained results for $\nu > 0$ can be applied most directly to hydrodynamical experiments. They also offer a new and consistent interpretation of the existence of super-spirals as well as their breakup. Super-spirals have recently been observed by other authors as the superimposed spiral modulation of a chemical concentration pattern.

In addition the bifurcation analysis is applied to a biological problem, an aspect of the local calcium dynamics in the cell. The results on the existence and type of temporal bursts of calcium concentration verify and support findings, recently obtained by other authors via numerical simulations.

# Zusammenfassung

Zahlreiche universelle Eigenschaften von beliebigen räumlich ausgedehnten dissipativen Systemen, die (fern des Gleichgewichts) Oszillationen oder laufende Wellen zeigen, lassen sich qualitativ durch eine Amplitudengleichung, die komplexe Ginzburg-Landau Gleichung (CGLE), beschreiben. Für einige Experimente der Hydrodynamik ist auch die quantitative Modellierung durch die CGLE erfolgreich.

Im Rahmen der CGLE werden die Instabilitäten einfacher Muster und das Auftreten von raum-zeitlichem Chaos untersucht, letzteres vorwiegend mittels numerischer Simulationen der Gleichung. Die Bifurkations- und Stabilitätsanalyse einiger komplexer Muster in dieser Arbeit ermöglicht ein tieferes Verständnis des raum-zeitlichen Chaos. Ein Mechanismus für die Bildung von raum-zeitlichen Defekten wird vorgeschlagen.

In der CGLE können Wellen für bestimmte Parameterwerte instabil werden (Eckhaus Instabilität). Falls diese Instabilität superkritisch ist, so koexistieren oberhalb der Instabilität stabile modulierte Amplitudenwellen (MAWs) und die instabil gewordene Welle. Wir benutzen die Software AUTO97, um diese modulierten Amplitudenwellen und deren Instabilitäten zu berechnen. MAWs bilden eine kontinuierliche zweiparametrische Familie von kohärenten Strukturen, das sind Lösungen, deren Form sich in einem mitbewegten Bezugssystem nicht verändert. Der mittlere Phasengradient $\nu$ und die räumliche Periodizität $P$ der Modulation parametrisieren die Familie der MAWs. Diese entstehen superkritisch (subkritisch) bei kleinen (großen) Wellenzahlen nahe der Eckhaus Instabilität und enden in Sattel-Knoten Bifurkationen bei größeren Werten der Kontrollparameter. Die Sattel-Knoten Bifurkationen der MAWs mit $P \to \infty$ liegen bei kleineren Parameterwerten als die Bifurkationen der MAWs mit kürzerer Periode. MAW-ähnliche Strukturen mit Parametern $\nu, P$, die größer sind als die kritischen Parameterwerte an der Sattel-Knoten Bifurkation, können sich zu Defekten entwickeln. Defekte sind lokalisierte Ereignisse, bei denen der Phasengradient divergiert und in deren Ergebnis ein Zustand mit verändertem $\nu$ entsteht. Sekundäre Instabilitäten der MAWs können die Defektentstehung begünstigen oder verzögern.

Die entdeckten Mechanismen der Defektentstehung werden durch numerische Simulationen illustriert. Eine Kombination dieser Argumente wird zur Erklärung des Überganges von Phasen- zu Defektchaos in der eindimensionalen CGLE benutzt. Wir vermuten, dass keine Defekte entstehen können, wenn für die jeweiligen Parameterwerte keine Sattel-Knoten Bifurkation existiert. Hier kann der Zustand des Phasenchaos im Grenzfall unendlich ausgedehnter Systeme für unendliche Zeiträume bestehen. Dann bilden jene Parameterwerte bei denen die Bifurkation mit $P \to \infty$ auftritt, die untere Schranke für Defektentstehung.

Die gewonnenen Ergebnisse für $\nu > 0$ lassen sich auf hydrodynamische Experimente anwenden und erlauben eine Interpretation der Existenz und des Aufbrechens von Super-Spiralen. Letztere wurden von anderen Autoren als überlagerte Modulation von spiralförmigen chemischen Konzentrationsmustern beobachtet.

Die Bifurkationsanalyse wird darüber hinaus auf eine biologische Fragestellung der lokalen Kalziumdynamik in Zellen angewendet. Dabei können die Erkenntnisse über “Kalzium-Bursts” unterstützt werden, die andere Autoren durch numerische Simulation gewonnen hatten.

# Contents

Abstract . . . 3

Zusammenfassung . . . 4

List of Figures . . . 7

**1 Introduction . . . 13**

1.1 The Topic . . . 13

1.2 Organization . . . 14

1.3 Principles of Pattern Formation . . . 15

1.3.1 Dissipative systems . . . 15

1.3.2 Experimental observations . . . 16

1.3.3 Modelling . . . 22

1.4 The Complex Ginzburg-Landau Equation . . . 26

1.4.1 Derivation . . . 26

1.4.2 Analytical results: solutions . . . 28

1.4.3 Analytical results: stability . . . 28

1.4.4 Numerical results: phase diagram . . . 30

1.4.5 Analytical results: phase equation . . . 33

1.5 Technical Tools . . . 34

**2 Transition from Phase to Defect Chaos . . . 37**

2.1 Introduction . . . 37

2.2 Modulated Amplitude Waves . . . 39

2.2.1 Coherent structures approach . . . 39

2.2.2 Bifurcation scenario for MAWs . . . 41

2.2.3 Evolution of perturbed MAWs . . . 47

2.2.4 Breakdown of phase description . . . 50

2.3 Large scale chaos . . . 52

2.3.1 Identification of MAWs in the phase-chaotic regime . . . 53

2.3.2 $L_1$ transition . . . 55

2.3.3 $L_3$ transition . . . 57

2.3.4 Mechanism for the selection of $p$ . . . 57

2.4 Further refinements . . . 61

2.5 Discussion . . . 62

**3 Fully Nonlinear Analysis of the Eckhaus Instability** 65
3.1 Introduction 65
3.2 Stable modulated amplitude waves 68
3.2.1 Coherent structures approach 68
3.2.2 Existence limits of MAWs 69
3.2.3 Tertiary instabilities 74
3.3 Defect formation in wound-up phase chaos 80
3.3.1 Beyond the saddle-node bifurcation 80
3.3.2 Limit of wound-up phase chaos 82
3.4 Discussion 84

**4 Experimental Observations of MAWs** 85
4.1 Hydro-thermal convection 85
4.2 Other hydrodynamic and chemical systems 89

**5 Super-Spiral-Breakup** 93
5.1 Introduction 93
5.2 Experimental observations 95
5.3 Eckhaus Instability of the Wave Field 97
5.4 Meandering Instability of the Source 101
5.5 MAWs and Meandering in 1D Simulations 107
5.6 Conclusion 114

**6 Bifurcation Analysis of Calcium Bursts** 117
6.1 Introduction 117
6.2 The model 118
6.3 Bifurcation analysis 120
6.4 Classification of bursting 122
6.5 Conclusion 124

**7 Summary and Outlook** 127

**Appendix A Continuation software : AUTO97** 129
A.1 Continuation procedure 129
A.2 Codes for complex Ginzburg-Landau equation 130

**Appendix B Scaling of bifurcation thresholds** 137

**Appendix C Linear stability analysis** 139
C.1 Bloch method 139
C.2 Goldstone modes and SN eigenmode 140
C.3 Splitting instability 141
C.4 Interaction instability 141
C.5 Parameter dependence of instabilities 142

**Appendix D MAWs in finite systems** . . . . . . . . . . 147

**Appendix E Meandering Instability** . . . . . . . . . . 149

**Bibliography** . . . . . . . . . . 151

**Acknowledgement** . . . . . . . . . . 165

**Versicherung** . . . . . . . . . . 167

# List of Figures

1.1 Example of pattern formation in physics . . . . . . . . . . . . . . . . . . . . 17
1.2 Defect formation in the experiment . . . . . . . . . . . . . . . . . . . . . . 18
1.3 Experimental setup for chemical pattern formation . . . . . . . . . . . . . 19
1.4 Spiral waves in a chemical experiment . . . . . . . . . . . . . . . . . . . . . 20
1.5 Examples of pattern formation in biology . . . . . . . . . . . . . . . . . . . 21
1.6 Classification of primary instabilities . . . . . . . . . . . . . . . . . . . . . 24
1.7 Eckhaus instability . . . . . . . . . . . . . . . . . . . . . . . . . . . . . . . 30
1.8 Examples of STC states in the CGLE . . . . . . . . . . . . . . . . . . . . . 31
1.9 Phase diagram of CGLE . . . . . . . . . . . . . . . . . . . . . . . . . . . . 32

2.1 Phase diagram including new results . . . . . . . . . . . . . . . . . . . . . 38
2.2 Examples of ODE solutions . . . . . . . . . . . . . . . . . . . . . . . . . . 40
2.3 Bifurcation diagrams for $\nu = 0, P = 30, c_3 = 2$ . . . . . . . . . . . . . . . 42
2.4 Spatial profiles of MAWs with $\nu = 0$ . . . . . . . . . . . . . . . . . . . . . 44
2.5 Features of the drift pitchfork bifurcation . . . . . . . . . . . . . . . . . . . 45
2.6 Locations of the saddle-node bifurcations . . . . . . . . . . . . . . . . . . . 46
2.7 Period doubling bifurcations . . . . . . . . . . . . . . . . . . . . . . . . . . 47
2.8 Relation of MAW and STC . . . . . . . . . . . . . . . . . . . . . . . . . . . 48
2.9 Dynamics near lower branch MAWs . . . . . . . . . . . . . . . . . . . . . . 49
2.10 Dynamics near upper branch MAWs . . . . . . . . . . . . . . . . . . . . . 50
2.11 Phase equations . . . . . . . . . . . . . . . . . . . . . . . . . . . . . . . . 52
2.12 Dynamics beyond the SN . . . . . . . . . . . . . . . . . . . . . . . . . . . 53
2.13 Snapshots of defect formation . . . . . . . . . . . . . . . . . . . . . . . . 54
2.14 Probability densities for $c_1 = 3$ . . . . . . . . . . . . . . . . . . . . . . . 56
2.15 Probability densities for $c_3 = 2$ . . . . . . . . . . . . . . . . . . . . . . . 57
2.16 Linear stability : splitting . . . . . . . . . . . . . . . . . . . . . . . . . . . 58
2.17 Linear stability : interaction . . . . . . . . . . . . . . . . . . . . . . . . . . 60
2.18 Theoretical bounds on the transition . . . . . . . . . . . . . . . . . . . . . 62
2.19 Summary of phenomena near the transition . . . . . . . . . . . . . . . . . 63

3.1 Simulation of supercritical Eckhaus instability . . . . . . . . . . . . . . . . 66
3.2 Spatial profiles of $A$ in simulations . . . . . . . . . . . . . . . . . . . . . . 66
3.3 Maximum conserved phase gradient $\nu_M(c_3)$ . . . . . . . . . . . . . . . . . 67
3.4 Transient decrease $\tilde{\nu}(t)$ of average phase gradient . . . . . . . . . . . . . . 68

3.5 Maximum Lyapunov exponent in wound-up phase chaos . . . . . . . . . . . 69
3.6 Bifurcation diagram for $\nu = 0.25, P = 25, c_1 = 3.5$ . . . . . . . . . . . . . . . . 70
3.7 Spatial profiles of MAWs . . . . . . . . . . . . . . . . . . . . . . . . . . . . . 71
3.8 Bifurcation diagram for subcritical Eckhaus instability . . . . . . . . . . . . 72
3.9 Unfolding of drift pitchfork bifurcation . . . . . . . . . . . . . . . . . . . . . . 72
3.10 Existence domains of MAWs in $L \to \infty$ . . . . . . . . . . . . . . . . . . . . . 73
3.11 Existence domains of MAWs in $L = 2\pi/\nu$ . . . . . . . . . . . . . . . . . . . 75
3.12 Tertiary instability : aperiodic MAWs . . . . . . . . . . . . . . . . . . . . . . 76
3.13 Stable MAW in $L \to \infty$ . . . . . . . . . . . . . . . . . . . . . . . . . . . . 77
3.14 Stability domains of MAWs for $\nu = 0.25$ . . . . . . . . . . . . . . . . . . . . 78
3.15 Stability domains of MAWs for $c_3 = 0.5$ . . . . . . . . . . . . . . . . . . . . 79
3.16 Defect formation : dynamics along SN manifold . . . . . . . . . . . . . . . . 81
3.17 Theoretical bounds for $\nu_M(c_3)$ . . . . . . . . . . . . . . . . . . . . . . . . . 83

4.1 Experimental observations on Rayleigh-Bénard convection . . . . . . . . . . 86
4.2 Experimental observations of hydrothermal waves . . . . . . . . . . . . . . . 87
4.3 Experimental observations in rotating Rayleigh-Bénard convection . . . . . . 88
4.4 Experimental observations in the Taylor-Dean system . . . . . . . . . . . . . 90

5.1 Experimental observations of super-spirals . . . . . . . . . . . . . . . . . . . 94
5.2 Simulation of a spiral wave . . . . . . . . . . . . . . . . . . . . . . . . . . . . 96
5.3 Simulation of stationary wave source . . . . . . . . . . . . . . . . . . . . . . 97
5.4 Spatial profile of stationary wave source . . . . . . . . . . . . . . . . . . . . 98
5.5 Bifurcation diagrams of MAWs from wave source . . . . . . . . . . . . . . . 99
5.6 “Phase diagram” of super-spirals . . . . . . . . . . . . . . . . . . . . . . . . 102
5.7 Experimental observations of a meandering wave source . . . . . . . . . . . . 103
5.8 Meandering instability in normal form analysis . . . . . . . . . . . . . . . . . 104
5.9 Frequency of the meandering motion . . . . . . . . . . . . . . . . . . . . . . 105
5.10 Period of the meandering motion . . . . . . . . . . . . . . . . . . . . . . . . 106
5.11 Length scale ratio of MAWs . . . . . . . . . . . . . . . . . . . . . . . . . . . 107
5.12 Simulations of oscillating wave source . . . . . . . . . . . . . . . . . . . . . . 109
5.13 Spatial profiles of oscillating wave source . . . . . . . . . . . . . . . . . . . . 110
5.14 Period of oscillation in simulations . . . . . . . . . . . . . . . . . . . . . . . 111
5.15 Comparison of MAWs with simulations : bifurcation diagram . . . . . . . . . 112
5.16 Comparison of MAWs with simulations : length scale ratio . . . . . . . . . . 113
5.17 Breakup radius . . . . . . . . . . . . . . . . . . . . . . . . . . . . . . . . . . 114

6.1 Experimental observation of bursting . . . . . . . . . . . . . . . . . . . . . . 118
6.2 Schematic drawing of the cell . . . . . . . . . . . . . . . . . . . . . . . . . . 119
6.3 Bifurcation diagram at weak stimulation . . . . . . . . . . . . . . . . . . . . 120
6.4 Bifurcation diagram at large stimulation . . . . . . . . . . . . . . . . . . . . 121
6.5 Frequency encoding . . . . . . . . . . . . . . . . . . . . . . . . . . . . . . . . 122
6.6 Portraits of simple spiking and complex bursting . . . . . . . . . . . . . . . . 123

6.7 Phase space representation of bursts . . . . . . . . . . . . . . . . . . . . . . 125

B.1 Scaling of bifurcation points . . . . . . . . . . . . . . . . . . . . . . . . . . . . 138

C.1 Stability spectrum near $L_3$ . . . . . . . . . . . . . . . . . . . . . . . . . . . . 140
C.2 Stability spectrum near $L_1$ . . . . . . . . . . . . . . . . . . . . . . . . . . . . 142
C.3 Instability domains in cut near $L_1$ . . . . . . . . . . . . . . . . . . . . . . . . 143
C.4 Instability domains in cut near $L_3$ . . . . . . . . . . . . . . . . . . . . . . . . 144

D.1 Existence domains of MAWs ($n$=20,4,2) . . . . . . . . . . . . . . . . . . . . . 147
D.2 Existence domains of MAWs ($n$=1,1/2,1/4) . . . . . . . . . . . . . . . . . . . 148

# 1 Introduction

## 1.1 The Topic

In order to convey some of the fascination of the topic “Complex Patterns in Extended Oscillatory Systems” let us begin by defining the title more explicitly. A thorough introduction of the involved concepts and terms together with a selection of important References will follow in Section 1.3.

*Patterns* denote *non*uniform and often *non*stationary states of a system driven away from equilibrium and represent the spatial and temporal evolution of observable quantities, *e.g.* the velocity field of a fluid, the concentration field of chemical reactands or biological species. Simple patterns, *e.g.* nonlinear waves or pulse trains, often arise just above onset of pattern formation (the primary instability) and may appear periodic in space and/or time.

*Complex patterns* in contrast may replace (via a secondary instability) simple patterns as the system is driven further away from equilibrium. They show quasiperiodic or more complicated even chaotic behavior. The focus will be set on existence and stability properties of some particular complex patterns in model systems, *i.e.* modulated amplitude waves. Their relations to chaos and to experiments will be discussed.

*Oscillatory systems* are a subclass of dissipative systems for which the primary instability of the uniform state gives rise to traveling waves or homogeneous oscillations above onset. This should be further restricted to the supercritical case without hysteresis of the primary pattern, *i.e.* the amplitude of waves or oscillations continuously increases starting from zero at the instability threshold. The above formulation excludes systems with an instability towards a stationary pattern (Turing pattern) and excitable systems where a stable uniform state coexists with patterns.

The study of the complex Ginzburg-Landau equation, *i.e.* a universal description of oscillatory systems close to the onset, will reveal complex patterns and underlying principles relevant for all oscillatory systems. In particular a fully nonlinear analysis of the secondary Eckhaus instability will be presented.

*Extended* denotes systems of large spatial extension compared to the typical length scale of the pattern. This offers the possibility of spatio-temporal chaos with the number of excited degrees of freedom being proportional to the system size (extensive). The phase space necessary to describe the state of the system becomes infinite-dimensional for an extended system even in one spatial dimension. This is called the thermodynamic limit. The properties of spatio-temporal chaos are very different from those of deterministic chaos in low-dimensional systems, *e.g.* the famous Lorenz system. In order to get a better understanding of spatio-temporal chaos the underlying mechanisms will be studied in some selected systems.

## 1.2 Organization

The results of this Thesis are presented in the following way. The introduction will continue with an overview of principles of pattern formation and related experiments in the next Section. In Section 1.4 some analytical results on the model (CGLE) are summarized and Section 1.5 introduces the technical tools used in this field. However, as a phenomenological model system the CGLE is even sometimes studied just because of the diversity of states and behavior it exhibits.

Chapter 2 will treat the transition between two spatio-temporal chaotic states (named "phase" and "defect" chaos) in the one-dimensional *complex Ginzburg-Landau equation* (CGLE). Previously the transition has been studied by numerical simulations but questions remained, *e.g.* at which parameter values the transition occurs as well as if phase chaos even exists in the thermodynamic limit. We present the first systematic analysis of *modulated amplitude waves* (MAWs), *i.e.* complex patterns that are exact solutions of the CGLE. Their limit of existence will be shown to cause the above mentioned transition and the open questions are answered.

Chapter 3 extends the analysis of MAWs and provides new insight into "wound-up" phase chaos. Applying bifurcation and stability analysis the existence limits of wound-up phase chaos are obtained which previously have been approximated by statistics on numerical simulations in the groups of P. Grassberger and M. San Miguel. The results are compared to stable MAWs experimentally observed in fluid dynamics.

Chapter 4 lists and shortly discusses promising experimental efforts that may be used to observe the proposed scenarios including MAWs.

Chapter 5 concerns the breakup of spiral waves in two-dimensional systems which gives rise to *spatio-temporal chaos* (STC). Recent observations of super-spirals in experiments with an autocatalytic chemical reaction will be consistently interpreted. The coincidence of two independent secondary instabilities causes stable super-spiral structures.

Chapter 6 is devoted to a biological system, a suggested model of signal encoding in cells by variation of the calcium concentration. A bifurcation analysis will supplement results of previous numerical simulations.

Each Chapter will introduce the examined phenomenon together with a discussion of relevant experimental observations followed by semi-analytical investigations (bifurcation and stability analysis) and closing with numerical simulations verifying the suggested mechanisms. It will become clear that the same mechanisms, *i.e.* bifurcations and instabilities of complex patterns in oscillatory systems, can be found in many different fields of physics, chemistry and biology.

A summary and an outlook are given in Chapter 7. Finally Appendices A-E provide special details and data as well as explicit algebraic calculations that have been used.

Many uncommon terms used in the paragraphs above will be explained below. The first appearance of an important term is emphasized by *italic* font. Several abbreviations (see table 1.1) will be used throughout the Thesis.

| abbreviation | expanded phrase |
|---|---|
| *i.e.* | that is, that means |
| *e.g.* | for instance, for example |
| MAW | modulated amplitude wave |
| CGLE | (cubic) complex Ginzburg-Landau equation |
| QCGLE | quintic complex Ginzburg-Landau equation |
| STC | spatio-temporal chaos |
| PDE | partial differential equation (here always nonlinear) |
| ODE | ordinary differential equation (here always nonlinear) |
| BFN | Benjamin-Feir-Newell criterion |
| c.c. | complex conjugate |
| h.o.t. | higher order terms |
| HB | Hopf bifurcation |
| DP | drift pitchfork bifurcation |
| SN | saddle-node bifurcation |
| PD | period doubling bifurcation |

Table 1.1: List of abbreviations.

## 1.3 Principles of Pattern Formation

### 1.3.1 Dissipative systems

Pattern formation is possible far away from equilibrium in *open* systems under continuous through flow of energy and/or matter. One may consider the diversity of life [1] on earth to be the most overwhelming example of pattern formation. It relies upon the flux of energy originating in the radiation of the sun. Within a *closed* system on the other hand patterns may only survive as a transient in accordance with the second law of thermodynamics.

The necessary extension of thermodynamics to open systems far from equilibrium was initiated by I. Prigogine and coworkers [2, 3, 4]. He characterized pattern forming systems as *dissipative systems* : they take up energy with low entropy and export energy with high entropy. Instead of the total amount of energy the *rates* at which energy or matter are consumed by the system become important quantities characterizing the “distance” from equilibrium. Away from equilibrium there is no free energy functional defined and no minimization principle holds. As a result the well developed tools of classical statistical mechanics are often not applicable for studying systems far from equilibrium.

Important tools have been provided by applied mathematicians in the fields of *dynamical systems* and *bifurcation and stability* theory [5, 6, 7, 8, 9, 10]. The idea of pattern formation via the instability of a uniform state goes back to hydrodynamics in the second half of the 19th century and scientists as H. Helmholtz [11], Lord Kelvin [12], Lord Rayleigh [13], W. Orr [14] and A. Sommerfeld [15]. The concept has been extended to reaction-diffusion systems in a seminal article by A. M. Turing [16]. He proposed a mechanism of local nonlinear (autocatalytic, self-amplifying) kinetics and spatial diffusive coupling which was later observed in a chemical reaction [17]. Another widely used tool, the iterative numerical solution (simulation) of nonlinear model systems, became available due to the rapid development of computer resources. This enabled the study of complex patterns [18], especially of *spatio-temporal chaos* (STC) [19, 20, 21]. Thus over the past two decades many text books and review articles [22, 23, 24, 25, 26, 27, 28, 29, 30, 31, 32] have been accumulated and give a comprehensive overview of pattern formation in physical, chemical and biological systems.

### 1.3.2 Experimental observations

The first experimental studies of pattern formation were carried out by H. Bénard [33] in a fluid placed between two horizontal plates and heated from below. The vertical temperature difference $\Delta T = T_{\text{bottom}} - T_{\text{top}}$ across the fluid is an external driving that can be adjusted by the experimentalist. A control parameter, the Rayleigh number $R$ (dimensionless ratio of destabilizing and stabilizing forces and proportional to $\Delta T$), serves as a measure for the "distance" from equilibrium which corresponds to $\Delta T = 0$. A non-equilibrium state is enforced as $\Delta T$ increases. Below a threshold $R_c$ heat is transported solely by conduction through the resting fluid. Above $R_c$ convection sets in, *i.e.* the fluid moves as parallel rolls. Heat is now transported by both conduction and convection. At higher $R_c$ turbulent behavior is observed.

Lord Rayleigh suggested a mechanism for the instability of the stationary conducting state of the fluid [34]. The linear temperature field of the conducting state corresponds to fluid layers of larger density above such of lower density; a situation that is intrinsically unstable in the gravitation field. However, the viscosity of the fluid needs to be overcome which stabilizes the resting fluid below $\Delta T_c$. Above $\Delta T_c$ the stationary fluid is unstable but the lower layers cannot raise as a whole. Amplifying small inhomogeneities fluid raises and falls in alternating domains forming the convection pattern of parallel rolls. Further analysis revealed the parameter-region of stable roll patterns above threshold, the so-called *Busse balloon* [35].

This system is known as Rayleigh-Bénard convection. It was used for some of the most accurate measurements on pattern formation and has become a paradigm. For a recent review see [36]. The primary instability in Rayleigh-Bénard convection leads to a stationary pattern of the velocity field,*i.e.* rolls at fixed position and orientation. Other examples of this type are Bénard-Marangoni convection [37, 38], where the upper surface of a shallow fluid is open to the air and temperature dependent surface tension destabilizes instead of buoyancy, and Taylor-Couette flow [39, 40], where the fluid is placed in the gap between two vertical concentrical rotating cylinders. There the centrifugal force replaces the buoyancy force and circular rotating rolls (called Taylor vortices) are established in planes perpendicular to the axis of the cylinder.

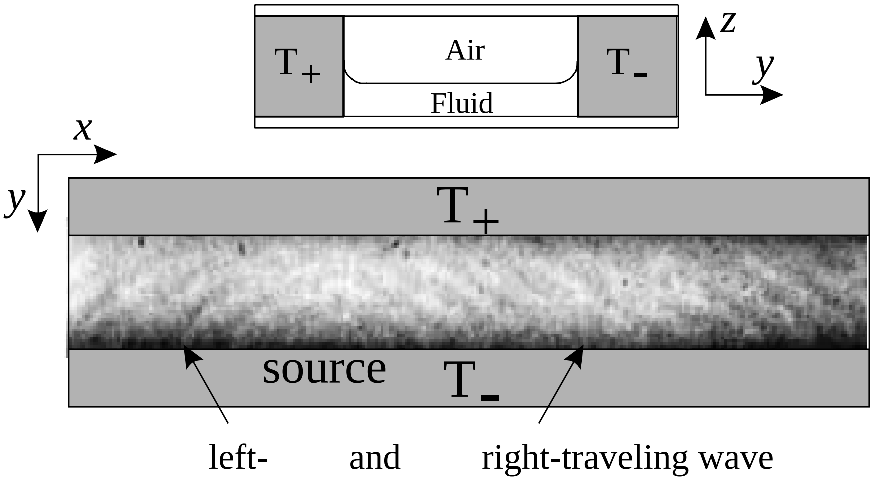

Fig. 1.1: Experimental setup (cross section and top view) and hydrothermal waves obtained by shadowgraphy in [44]. The fluid layer (silicon oil) is 1.7mm deap, 250mm long and 20mm across. A self-organizing source emits a left- and a right-traveling wave.

In contrast the *oscillatory systems* by definition show homogeneous oscillations or traveling wave patterns. Relevant physical systems again come from the field of fluid dynamics where it is easier to visualize the patterns and to control geometrical constraints as well as the distance from threshold. Visualization of the patterns in shallow fluid layers is achieved via *shadowgraphy*, the optical observation of induced modulations of the refraction index [41].

*Hydrothermal waves* are the most prominent example of oscillatory systems. They represent traveling modulations of the temperature field in the bulk of a fluid placed in a channel [42, 43, 44, 45]. The velocity field and the local orientation of the free surface change accordingly. Fig.1.1 shows the side view (top) and a snapshot of the top view (bottom) of the experiment by J. Burguete *et al.* [44]. A horizontal temperature gradient is applied at the walls of the channel. The dependency of surface tension on temperature leads to a primary convection roll (Marangoni effect) with fluid raising near the hot wall and falling near the cold wall. Above a threshold $\Delta T_c \approx 4.5K$ hydrothermal waves propagate on the surface in a direction oblique to the temperature gradient [45]. The instability of the primary convection roll to hydrothermal waves has been described analytically on the basis of Navier-Stokes and heat transport equations by M. K. Smith and S. H. Davis [46]. The experimentally observed onset of hydrothermal waves is in satisfactory agreement with the theoretical predictions [47].

The experimental setup can be designed quasi one-dimensional in the direction perpendicular to the temperature gradient [43, 44]. The properties of the hydrothermal waves may be changed by varying the geometrical and physical parameters. Regimes with irregular dynamics were observed. The wavelength of the hydrothermal wave may no longer remain constant but is modulated along the wave [43]. The subsequent maxima and minima in the spatial profile of the wave will be called “humps” and “dips”. As time progresses subsequent humps of the wave may come closer and merge when the dip between them disappears [44].

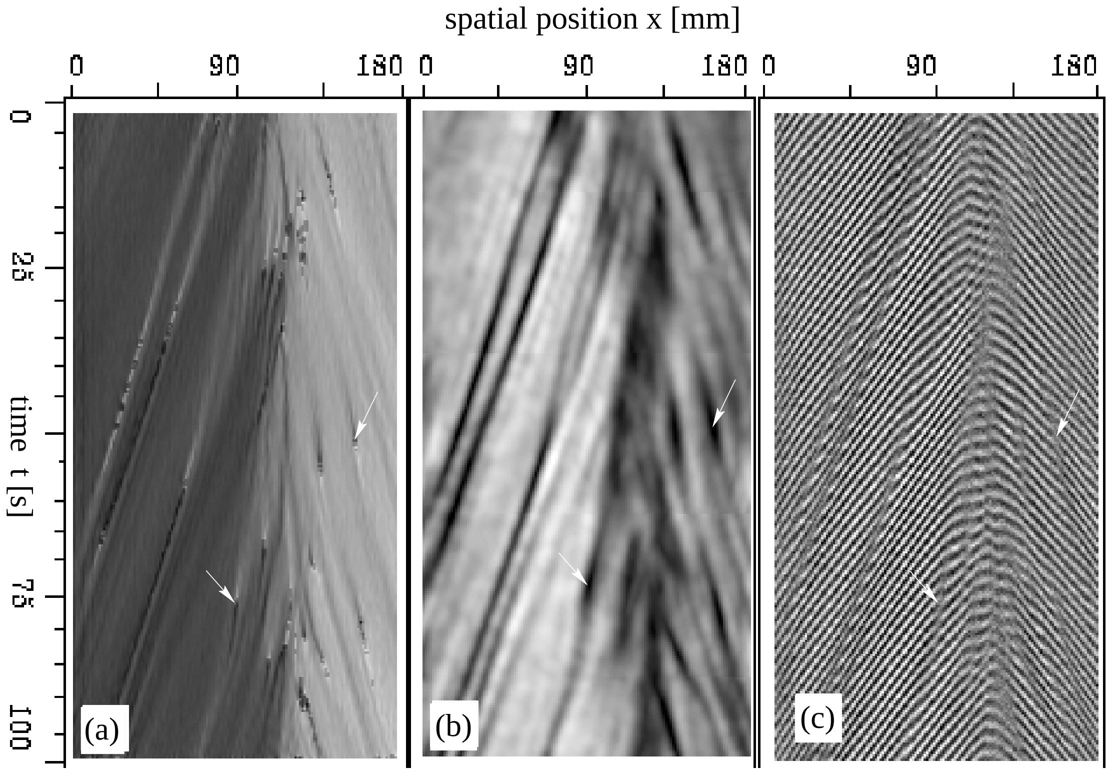

Fig. 1.2: Space-Time plots of (a) local wavenumber $q$ (bright: $q > 0$, dark: $q < 0$) and (b) local amplitude $|A|$ (white: $|A| = 1$, black: $|A| = 0$) derived from (c) the original data of hydrothermal waves emitted by a source at $x \approx 120$. The waves travel along a narrow channel in the experimental setup as shown in Fig.1.1 and data was collected along a horizontal ($x$) cut by [44]. Localized compressions of the wave sequence in (c) result in pulses of local wavenumber (a) and depressions of the pattern amplitude (b). Events in space-time where the original wave annihilates one wavelength appear as changes (bright to dark or vice versa) in the local wavenumber (a) of black points ($|A| = 0$) in (b). These localized events are called defects and two examples are marked by arrows in the different representations (a-c).

Then the phase of the wave is ill-defined for one moment in time at the position in space where the humps merge and one wavelength of the wave is annihilated. This event is called a space-time *defect*, a localized disturbance of the surrounding pattern. See Fig.1.2 for an experimental observation.

Defects may also persist in time and act as organizing centers (*e.g.* as core of spiral waves in two dimensions) and select certain properties (*e.g.* wave length) of the surrounding pattern. Therefore the temporal process of creating or annihilating such defects is a major influence on the state of the system. These processes determine many properties of STC. For Rayleigh-Bénard convection this has recently been demonstrated [20]. In Chapter 2 we will investigate the process of defect formation in detail.

Other examples of extended systems displaying such chaotic dynamics in one spatial dimension include: heated wire convection [48, 49], printers instability and film drag experiments [50], eutectic growth [51], binary convection [52], sidewall convection [53], the Taylor-Dean system [54] and internal waves excited by the Marangoni effect [55].

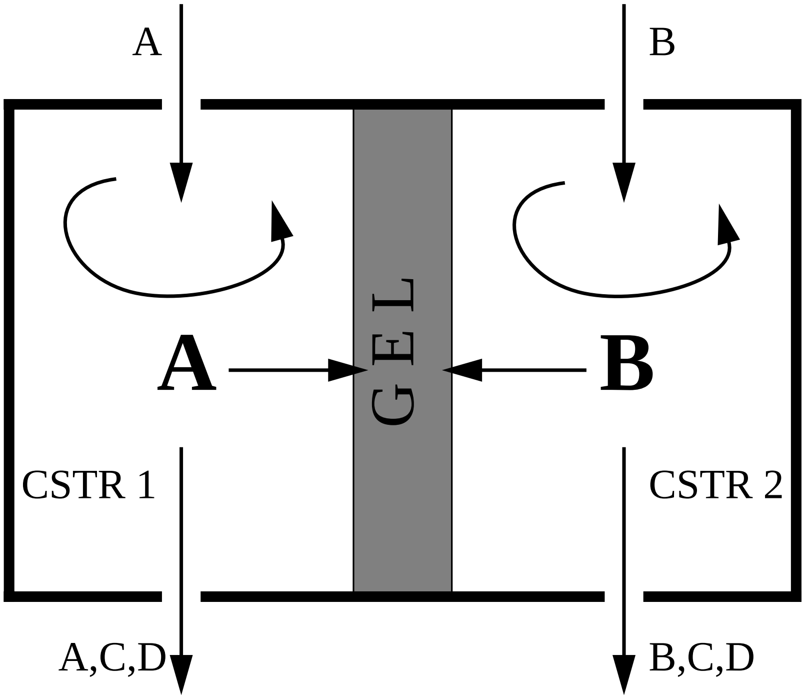

Fig. 1.3: Continuously stirred tank reactors (CSTR1 and 2) used to study two-dimensional pattern formation of a chemical reaction A+B→C+D in the separating gel matrix.

Studying a secondary (oscillatory) instability of Rayleigh-Bénard convection in a cylindrical geometry B. Janiaud *et al.* [56] compared modulated waves from theory (CGLE) and experiment. The separating plane between two adjacent fluid rolls in a Rayleigh-Bénard convection pattern becomes unstable to a traveling wave locally modulating the size of the rolls.

Such modulated waves will be studied in detail in Chapter 3 which supplements the observation of these waves in experiments (Chapter 4) and simulations [57, 58, 59]. M. C. Cross and P. C. Hohenberg have provided an extensive collection of experimental studies with emphasis on fluid dynamics [30].

Early observations of propagating concentration waves in chemical systems go back to R. Luther (in Leipzig) and were discussed in connection with signal transport along nerve fibres [60]. First experimental studies were conducted with a chemical system which is now known as the *Belousov-Zhabotinsky reaction* [61, 62, 63],*i.e.* the catalyzed oxidation of citric acid by bromate. B. P. Belousov and A. M. Zhabotinsky observed oscillating concentrations [64] of the reactands and propagating concentration waves [65]. Spiral wave patterns were discovered by A. T. Winfree [66] in the same reaction. In much the same way as Rayleigh-Bénard convection for physical systems the Belousov-Zhabotinsky reaction became a paradigmatic model system for pattern formation in chemical systems. Here the oscillatory variant of the reaction is of special importance but it also shows different (excitable) behavior under specific conditions.

In recent experiments [67, 68, 69, 70, 71] the reaction zone is restricted to a planar

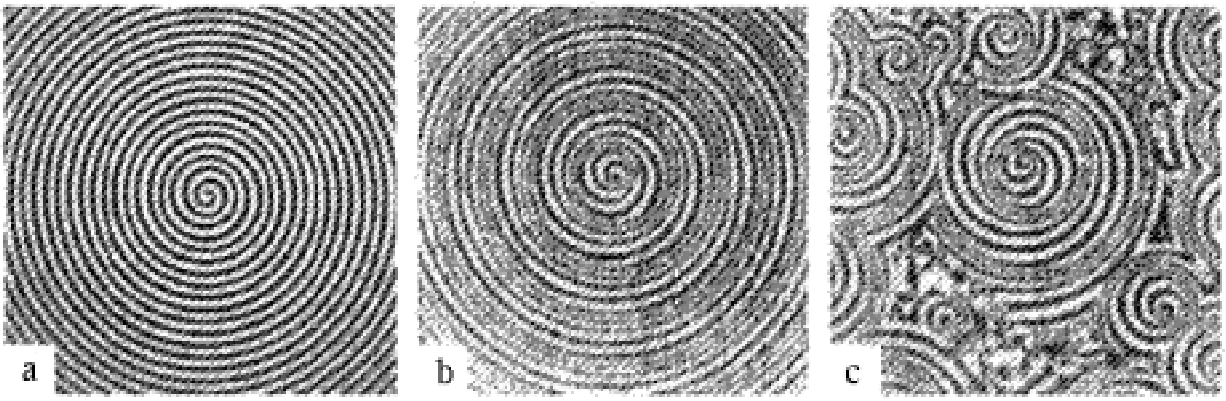

Fig. 1.4: Transition from stable spiral wave to spiral defect chaos as the concentration of one chemical increases in the Belousov-Zhabotinsky reaction [70]. (a) Stable spiral wave, (b) super-spiral and (c) super-spiral breakup.

two-dimensional matrix (gel or porous glass disc). This simplifies optical measurements of the patterns which appear as different colors depending on the binding structure of some agents (*e.g.* ferroin) within chemical complexes. Possible convection due to reaction heat is suppressed by the matrix but the chemicals may diffuse from and to adjacent compartments. As reservoirs one uses continuously stirred tank reactors with continuous through flow of the reactands. The adjusted ratio of supplied reactands provides control of the distance from equilibrium. See Fig.1.3 for a schematic diagram.

In a wide range of concentrations the pattern consists of spiral waves rotating around a core and continuously emitting waves in radial direction (see Fig.1.4a). For certain concentrations the spiral core (wave source) starts to move which imposes modulations on the emitted wave field similar to the Doppler effect. The modulations of the wave length form an overlaid structure, the *super-spiral* shown in Fig.1.4b . Further change of parameters may lead to the breakup of the spiral structure into fragments of spirals. This state of *spiral defect chaos* or *defect mediated turbulence* is a particular realization of STC (see Fig.1.4c). In Chapter 5 we will analyse this phenomenon in detail and suggest a new mechanism for the breakup of super-spiral waves.

An intensively studied field concerns catalytic reactions of gases on surfaces where the local coverage with reactands exhibits traveling, spiral and target waves as well as spatio-temporal chaos [72, 73, 74]. Another recent review of pattern formation in chemical systems was published by A. DeWit [32].

Finally in biological systems similar dynamical phenomena appear. The most prominent example of such systems is the aggregation of the slime mould *Dictyostelium discoideum* under starvation conditions [75, 76, 77]. The individual cells communicate by releasing the chemoattractant cAMP and move (chemotaxis) toward a common center where they form a multicellular organism and differentiate to create surviving spores. The events of cAMP release and of cell motion arrange on rotating spirals (see Fig.1.5).

Another system studied for a long time is the signal propagation in nerve cells [78, 79].

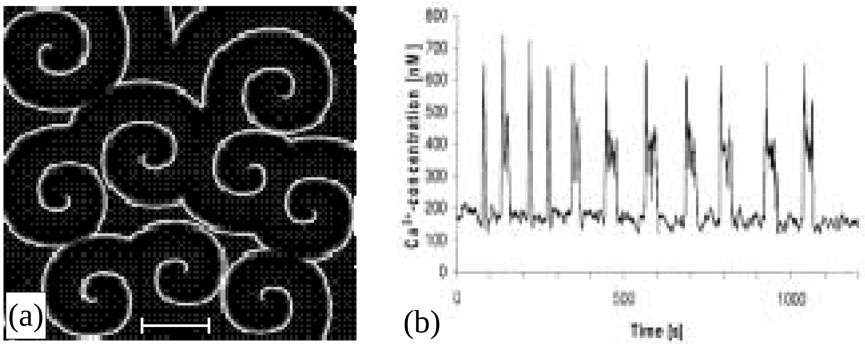

Fig. 1.5: (a) Dark field waves in *Dictyostelium discoideum* aggregation that represent the alternating cell motion [77]. The bar at the bottom represents $100\mu$m. (b) Bursting $[\mathrm{Ca}^{2+}](t)$ derived from the intensity signal of a bioluminescent $\mathrm{Ca}^{2+}$ indicator in incubated hepatocytes of rat [88]. This typical response to agonist stimulation will be studied by means of bifurcation analysis in Chapter 6.

The cell membrane of nerve cells separates different concentrations of ions ($\mathrm{Na}^+$, $\mathrm{K}^+$, $\mathrm{Cl}^-$) inside and outside. Voltage gated channels allow specific ions to penetrate the membrane reducing concentration gradients and increasing the electrical potential difference. Pumps slowly restore the initial condition. Given an excitation at the axon hump an action potential with fixed shape and velocity will propagate along the axon.

*Ventricular fibrillation* in (excitable) cardiac tissue of the heart muscle is another strongly debated phenomenon [80, 81, 82, 83, 84, 85]. Ventricular fibrillation may cause sudden cardiac death and was suggested to be triggered by the breakup of spiral waves of electrophysiological activity. If ventricular fibrillation is detected the common treatment is defibrillation; high voltage pulses applied to the chest of the patient. Analysing the instability of the electrophysiological pattern in suitable models could improve the therapy.

As a last example we want to mention the process of *signal transduction* which denotes the response of a cell to very low concentrations of hormones delivered by the blood stream. There are more than a thousand different hormones and specific receptors the organism uses to control its actions. Inside a cell a particular process has to be activated by the hormone which shortly binds to the specific receptor on the membrane and then detaches to activate other cells as well. Hence there needs to be a *second messenger* that carries the information inside the cell. There are only a limited number of such species, namely cAMP, NO· radicals and $\mathrm{Ca}^{2+}$ ions. The information contained in the diversity of the hormones and receptors must not be lost by encoding it in the intracellular concentration of just a few second messengers. $\mathrm{Ca}^{2+}$ alone is activated by half of the hormones. This has long been a puzzle. Nature solves the problem by facilitating the *dynamics* of the concentration signal $[\mathrm{Ca}^{2+}](t)$ [86, 87]. $[\mathrm{Ca}^{2+}](t)$ was experimentally observed to oscillate with the frequency and pulse shape encoding the specific hormone. In most cases $[\mathrm{Ca}^{2+}](t)$ can be treated homogenous within the cell. Hence this phenomenon, called *bursting*, is a temporal rather than spatio-temporal pattern. In Chapter 6 we will study the bifurcation structure of $[\mathrm{Ca}^{2+}](t)$ oscillations in a model recently suggested and studied by U. Kummer *et al.* [88].

### 1.3.3 Modelling

Far from equilibrium all of the above mentioned (physical, chemical and biological) systems share common features despite the different microscopic mechanisms. Similar patterns,*e.g.* traveling waves and spiral waves, are observed in velocity, temperature, concentration, electrophysiological potential and cell density fields. These *self-organizing* patterns represent the stable asymptotic behavior for long times even when the system is maintained under homogeneous and stationary external conditions. The underlying mechanisms are very robust and the patterns are only weakly influenced by noise.

The form of the final pattern,*e.g.* orientation of rolls or regular pattern versus STC, often depends on initial conditions. There exist different *attractors* that represent coexisting stable states of the system. Any initial condition lies in the *basin* of attraction of a specific attractor and thereby determines the final state. This feature is called *multistability.*

It was mentioned for individual examples above : these coexisting asymptotic states of the system may include chaotic dynamics,*e.g.* STC. This causes an additional dependence on initial conditions within one basin of attraction. If two identical replica of such a system evolve from similar initial conditions then their properties will be increasingly different, *i.e.* the distance of their states in phase space increases exponentially. This feature prevents detailed predictions of the future state of the system and was named deterministic *chaos.*

Although the underlying individual mechanisms involve interacting microscopic species such as atoms and molecules or cells the patterns evolve on macroscopic scales. Thereby large numbers of individual events or elements are contained within characteristic scales of the pattern. Hence, noise becomes negligible on macroscopic scales. This enables the modelling by deterministic evolution equations.

Most convenient is the formulation of the model in terms of *nonlinear partial differential equations* (PDEs). [1] Note that nonlinearities in the equations prevent superposition of solutions. We choose the vector $\boldsymbol{u}(\boldsymbol{x}, t)$ to describe the evolving fields,*e.g.*, temperature, concentration or components of the velocity. $\boldsymbol{x}$ denotes coordinates in space and $t$ denotes time. A control parameter $\mu$ is selected out of a set of parameters $\boldsymbol{\mu}$. Then the evolution of the system shall be given by a set of PDEs [30]. These may be the Navier-Stokes and heat equations for Rayleigh-Bénard convection or rate equations determined by stoichiometry for a chemical reactions mechanism.

$$\partial_t \boldsymbol{u}(\boldsymbol{x}, t) = \boldsymbol{F}(\boldsymbol{u}, \partial_x \boldsymbol{u}, \ldots; \boldsymbol{\mu}) \tag{1.1}$$

Partial derivatives with respect to time or spatial coordinates are denoted by $\partial_t$ and $\partial_x$.

*Reaction-diffusion systems* (1.2) constitute a prominent sub-class with purely diffusive spatial coupling (tensor $\mathcal{D}$ of diffusion coefficients) that is appropriate for most chemical systems. [2]

---

[1] The alternatives,*e.g.* cellular automata or coupled map lattices which may be easier to study, will be discussed later.

[2] The intensively studied *FitzHugh-Nagumo* equations [89, 90] and its variants [73, 104] belong to this class. As further simplification one can in some cases identify fast amplifying (activator) and slow stabilizing (inhibitor) processes.

$$\partial_t \boldsymbol{u}(\boldsymbol{x},t) = \boldsymbol{f}(\boldsymbol{u};\boldsymbol{\mu}) + \mathcal{D}\nabla^2 \boldsymbol{u} \tag{1.2}$$

Within a parameter range $\mu < \mu_c$ [3] ,*e.g.* near equilibrium, there shall exist a stable homogeneous stationary solution $\boldsymbol{u}_0$ of the PDEs (1.1). This corresponds to the relaxed state of the system without any pattern.

The linear stability of $\boldsymbol{u}_0$ can be characterized by the growth or decay of small perturbations expressed in Fourier *modes*. This concept goes back to Lord Rayleigh [13] and A. M. Turing [16]. The ansatz for small $\epsilon$ and chosen wave vector $\boldsymbol{k}$

$$\boldsymbol{u}(\boldsymbol{x},t) = \boldsymbol{u}_0 + \epsilon \boldsymbol{u}_1 \mathrm{e}^{i\boldsymbol{k}\cdot\boldsymbol{x}+\sigma t} + \text{c.c.}\ , \tag{1.3}$$

contains a growth rate $\sigma$ with complex values and the eigenvector $\boldsymbol{u}_1$ which also describes the dependence in transverse (to $\boldsymbol{k}, \boldsymbol{x}$) directions while c.c. stands for complex conjugate.

Inserting the ansatz (1.3) into the PDE (1.1) and expanding in powers (linear to lowest order) of the small quantity $\epsilon$ yields an expression for the growth rate $\sigma(\boldsymbol{k},\boldsymbol{\mu})$. If $\mathrm{Re}[\sigma(\boldsymbol{k})] < 0$ for all $\boldsymbol{k}$ then the solution $\boldsymbol{u}_0$ is linearly stable at the particular $\boldsymbol{\mu}$. If a control parameter is increased to a *critical* value $\mu = \mu_c$ then $\mathrm{Re}[\sigma(\boldsymbol{k})]$ shall be zero for a critical mode $\boldsymbol{k} = \boldsymbol{k}_c$. Above $\mu_c$ a whole band of modes around $\boldsymbol{k}_c$ will have positive $\mathrm{Re}[\sigma(\boldsymbol{k})]$ and such modes will grow in time and change the state. Hence $\boldsymbol{u}_0$ has become unstable. The point $\mu = \mu_c$ in parameter space is called the primary instability *threshold*.

The imaginary part $\Omega_c = \mathrm{Im}[\sigma(\boldsymbol{k}_c, \mu_c)]$ at the instability is used to classify the type of instability [30]. For zero frequency $\Omega_c = 0$ the instability is called *stationary* (type $\mathrm{I_S}$) and a stationary pattern grows as in the case of Rayleigh-Bénard convection, whereas for $\Omega_c \neq 0$ the instability is *oscillatory*. In the latter case and $\boldsymbol{k}_c \neq 0$ in addition (type $\mathrm{I_O}$) traveling waves appear,*e.g.* hydrothermal waves. For $\boldsymbol{k}_c = 0$ the homogeneous mode becomes unstable (type $\mathrm{III_O}$) and the system will show homogeneous oscillations as in the Belousov-Zhabotinsky reaction. See Fig. 1.6 for a schematic representation of the classification scheme.

Above threshold $\epsilon = (\mu - \mu_c)/\mu_c > 0$ the perturbations grow and nonlinearities become important since they couple different modes. There is no general method to predict the eventual pattern. However, above but close to threshold the band of unstable modes ($\boldsymbol{k}$) has wavenumbers close to the critical one ($\boldsymbol{k}_c$). Compare the case $\epsilon > 0$ in Fig. 1.6. Nonlinear combinations of these modes will typically have modulations on longer scales $\sim |\boldsymbol{k} - \boldsymbol{k}_c|^{-1}$ rather than on short scales $\sim |\boldsymbol{k}_c|^{-1}$. The same distinction between modulation (envelope or amplitude) and primary pattern holds for the time scales. This universal feature allows the separation of length and time scales to achieve an approximation close to threshold which is a considerable simplification of the PDEs (1.1).

The concept called *amplitude equations* or *envelope equations* goes back to A. C. Newell, J. A. Whitehead [91] and L. A. Segel [92]. It bears a strong resemblance to the perturbative approach near second-order phase transitions by L. D. Landau [93, 94, 95, 96] and the

---

[3] In general a manifold $\boldsymbol{\mu}_c$ separates the parameter space but to emphasize ordering with respect to $\boldsymbol{\mu}_c$ we choose an appropriate cut $\mu$ in that space.

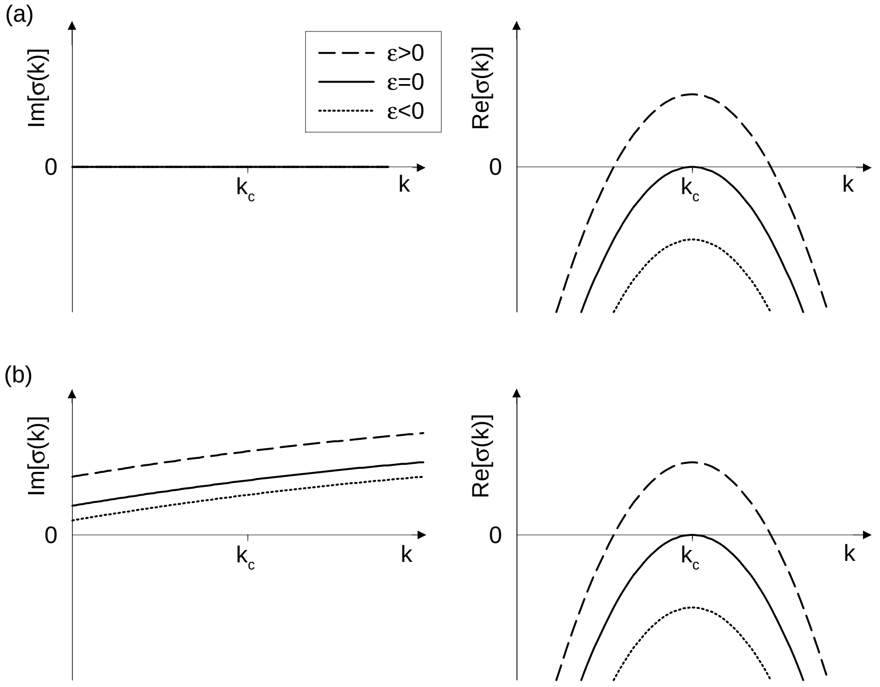

Fig. 1.6: Classification of primary instabilities [30] via $\sigma(\boldsymbol{k})$. Left panels show $\mathrm{Im}[\sigma(\boldsymbol{k})]$ and right panels $\mathrm{Re}[\sigma(\boldsymbol{k})]$. (a) Stationary periodic instability ($\Omega_c = 0, \boldsymbol{k}_c \neq 0$), type $\mathrm{I_S}$, (b) oscillatory instability ($\Omega_c \neq 0$) which has a periodic or wave type $\mathrm{I_O}$ ($\boldsymbol{k}_c \neq 0$). For the uniform or homogeneous type $\mathrm{III_O}$ shift the axis to get $\boldsymbol{k}_c = 0$.

procedure of eliminating fast modes that adiabatically follow the slow modes that has been referred to as “slaving” by H. Haken [97]. Detailed descriptions are contained in [22, 98, 99]. The form of the amplitude equation only relies on the type of instability and the symmetry properties of the system. Far above threshold *quantitative* results of the amplitude formalism differ from the full system but *qualitative* aspects are still captured ,*e.g.* the types of patterns that coexist, regular or chaotic behavior or the mechanisms of instabilities and transitions between different states [30]. This emphasizes the common principles of pattern formation that underly both the real systems and their different levels of modelling. This might be a reason for the observed *universality* [100] of features in nonequilibrium systems, although they belong to different fields such as physics, chemistry or biology.

The lowest order approximations are only adequate for *supercritical* instabilities for which the amplitude of the pattern continuously increases with $\mu$. This case is also called *forward* in contrast to *subcritical* or *backward* instabilities where the pattern sets in with a finite amplitude and may show a hysteresis below $\mu_c$. In the latter case higher order terms (h.o.t.) have to be taken into account.

In order to separate the different length and time scales in the amplitude equation an appropriate ansatz is used with the slow variables $\tilde{\boldsymbol{x}}, \tilde{t}$ being the only arguments of the complex valued amplitude $A$.

$$\boldsymbol{u}(\boldsymbol{x}, t) = \boldsymbol{u}_0 + A(\tilde{\boldsymbol{x}}, \tilde{t})\boldsymbol{u}_1 \mathrm{e}^{i(\boldsymbol{k}_c \cdot \boldsymbol{x} + \Omega_c t)} + \mathrm{c.c.} \tag{1.4}$$

The ansatz (1.4) is inserted into the full model (1.1) which then is expanded systematically in the small quantity

$$\epsilon = \frac{\mu - \mu_c}{\mu_c} \quad . \tag{1.5}$$

The technically involved calculations use multiple scales expansions [101]. For the *stationary* instability ($\Omega_c = 0$) in one spatial dimension this leads to

$$\tau_c \partial_t A = \epsilon A + \xi_c^2 \partial_x^2 A - g_c |A|^2 A \tag{1.6}$$

with scales $\tau_c, \xi_c, g_c$ of the modulation and $x$ chosen in the direction $\boldsymbol{k}_c$ The single PDE (1.6) is called *real Ginzburg-Landau equation* because of real coefficients (apart from the $y$-direction) whereas $A$ has complex values. The coefficients can be scaled to unity by using $\tilde{\boldsymbol{x}}, \tilde{t}$ and $\tilde{A} \propto A/\sqrt{\epsilon}$.

The *complex Ginzburg-Landau equation*, the amplitude equation for the oscillatory case will be discussed in the next Section. As for the real Ginzburg-Landau equation all microscopic details of the full system are condensed in the values of a few coefficients. The results derived for the amplitude equation can in principle be applied to a huge variety of systems that share the same instability. This corresponds to the universality of features in the different systems.

The coefficients have been calculated for a wide range of systems [30, 102, 103, 104]. On the other hand, in many examples from chemistry and biology it is not possible to derive the complete set of PDEs (1.1) because the systems involve too many different species with unknown influence upon each other, *e.g.* metabolic pathways. However, these systems may show a simple instability as discussed above, *e.g.* oscillations in glycolysis [76], which is described by a simple amplitude equation. In these cases the coefficients can be inferred from properties of measured complex patterns [44],*e.g.* velocities, or determined from quenching experiments [105, 106]. In the latter case one artificially changes the concentration of single species and observes the recovery of the pattern.

The name "Ginzburg-Landau equation" is reminiscent of the formal similarity with the Ginzburg-Landau theory of superconductivity. There a similar equation holds for the order parameter near a second-order phase transition. See [107] for the original static formulation while the dynamical extension (coupling to an electric field) was derived in [108, 109]. For an extensive history of the CGLE see [122]. Besides the most frequent stationary and oscillatory instabilities there are other instabilities that involve additional slow modes [110, 111]. Neither these nor excitable [73] or bistable [112] systems will be discussed in this Thesis.

Within the amplitude equation the simple patterns may undergo *secondary* instabilities. Typical examples are the *Eckhaus* instability [113], a longitudinal long wavelength instability of stationary and traveling waves. If the wavenumber of the simple wave pattern becomes too large then the Eckhaus instability relaxes the compression; either by close packing and modulation of waves within a localised region in the supercritical case or by annihilation of a finite number of waves to recover a stable wavenumber in the subcritical case. In the limit of homogeneous oscillations the instability is called *Benjamin-Feir* instability [114]. A last example is the *zig-zag* instability, a transverse long wavelength type.

Similar to the amplitude equation near the primary instability one can derive *phase equations* that are valid near the secondary instability in the amplitude equation [22, 115, 116, 117]. The simplest and best studied phase equation is known as the *Kuramoto-Sivashinsky equation* [22]. In Section 2.2.4 solutions of phase equations of different order are compared with a fully nonlinear treatment of the Eckhaus instability in the CGLE. Above the secondary instability there may exist stable complex patterns (see Chapter 3) but even if these complex patterns are unstable they determine the dynamics to a large degree (see Chapter 2). We name these complex patterns of the CGLE *modulated amplitude waves* (MAWs) since the plane waves in the amplitude description acquire saturated modulations. The MAWs will be shown to form a two-parameter family of solutions.

For many phenomena,*e.g.* breakup of spiral waves (see Chapter 5), it is helpful to start the investigation in a one-dimensional system since there a wide range of tools is available. In higher spatial dimensions the mechanisms identified in the one-dimensional system may already explain much of the phenomenology but additional effects remain to be explored. Following this approach we will study MAWs in the one-dimensional CGLE and later interprete some results in a two-dimensional system.

Since hydrothermal waves were observed in quasi one-dimensional geometry these are promising candidates for comparison with our theoretical predictions. In the CGLE the primary patterns are analytically known plane waves and hence the characterization of the complex patterns is easier than in other systems.

## 1.4 The Complex Ginzburg-Landau Equation

### 1.4.1 Derivation

The complex Ginzburg-Landau equation (CGLE) describes the long wavelength modulations (envelopes or amplitudes) of both traveling waves ($\boldsymbol{k}_c \neq 0$, type $\mathrm{I_O}$) and homogeneous oscillations ($\boldsymbol{k}_c = 0$, type $\mathrm{III_O}$). Here we shortly summarize the derivation in both cases which is similar to the procedure (1.4-1.6) and discuss some general properties of the equation. Since many phenomena already occur in the one-dimensional system (see above) we will restrict the analysis to one dimension.

For a single right-traveling wave the ansatz

$$\boldsymbol{u}(x,t) = \boldsymbol{u}_0 + A\,\mathrm{e}^{i(k_c x - \Omega_c t)}\boldsymbol{u}_1 + \text{c.c.}\ . \tag{1.7}$$

with slow variables $\tilde{x}, \tilde{t}$ of the complex valued amplitude $A$ is inserted into the full model (1.1). The resulting equations are expanded systematically in the small quantities (1.5) and yield

$$\tau_c \partial_t A + v_c \partial_x A = \epsilon(1 + ic_0)A + \xi_c^2(1 + ic_1)\partial_x^2 A - g_c(1 - ic_3)|A|^2 A\ . \tag{1.8}$$

The linear frequency shift $c_0$ can be eliminated by $A \to A\mathrm{e}^{i\epsilon c_0 t/\tau_c}$. The advective term proportional to the group velocity $v_c$ of the primary wave can be absorbed in the ansatz by introducing a moving coordinate frame $x + v_c t/\tau_c \to x$. We assume $\epsilon > 0$ (above threshold) and $g_c > 0$ (supercritical instability) whereas $\tau_c > 0, \xi_c > 0$ are fulfilled a priori. With the scaling

$$\tilde{x} = \sqrt{\epsilon}\frac{x}{\xi_c} \tag{1.9}$$

$$\tilde{t} = \epsilon\frac{t}{\tau_c} \tag{1.10}$$

and transformation

$$\tilde{A} = \sqrt{\frac{g_c}{\epsilon}}A \tag{1.11}$$

one derives the dimensionless form of the CGLE which reads after dropping the tildes

$$\boxed{\partial_t A = A + (1 + ic_1)\partial_x^2 A - (1 - ic_3)|A|^2 A} \tag{1.12}$$

after dropping the tildes.

Now $A$ is of order unity whereas the original amplitude scales like $\sqrt{\epsilon}$. Also the long length and time intervals in Eq. (1.8) rescale to order unity by multiplication with $\sqrt{\epsilon}$ and $\epsilon$ to yield the slow variables $\tilde{x}, \tilde{t}$, respectively. All microscopic details of the studied system (1.1) are now contained in the scales $\tau_c, \xi_c, g_c$ and the two imaginary parts $c_1, c_3$ of the coefficients, hence the name *complex* Ginzburg-Landau equation. Solutions of the CGLE will be studied under variation of $c_1, c_3$. This corresponds to comparing realizations of the studied system with different choices of the parameters in $\boldsymbol{\mu}$. The actual calculation of $c_1, c_3$ from $\boldsymbol{\mu}$ is rather involved [30, 102, 103, 104]. The coefficients $c_1, c_3$ can alternatively be obtained from quenching experiments [105, 106] (see above).

The CGLE (1.12) is invariant under translation in $x$ and a constant phase shift $A \to Ae^{i\theta}$. The former shifts the long wave length modulation along the primary pattern and the latter corresponds to a spatial shift of the primary pattern itself. The first term on the right hand side of the CGLE (1.12) represents the growth of the unstable modes which is saturated and stabilized by the last nonlinear term. Note the negative sign of the last term that corresponds to the supercritical instability. In the subcritical case $g_c < 0$ in Eq.(1.8) and higher order terms have to be incorporated to balance the growth. The quintic complex Ginzburg-Landau equation is such an extension [119].

The same strategy applied to the uniform instability of type $\mathrm{III_O}$ with the ansatz

$$\boldsymbol{u}(x,t) = \boldsymbol{u}_0 + A(\tilde{x},\tilde{t})\mathrm{e}^{-i\Omega_c t}\boldsymbol{u}_1 + \text{c.c.} \tag{1.13}$$

also leads to the CGLE (1.12).

For an isotropic system with type $\mathrm{I_O}$ instability one in general expects traveling waves in both directions, left (L) and right (R), respectively. The appropriate ansatz reads

$$\boldsymbol{u}(x,t) = \boldsymbol{u}_0 + \left[A_L(\tilde{x},\tilde{t})\mathrm{e}^{i(-k_c x - \Omega_c t)} + A_R(\tilde{x},\tilde{t})\mathrm{e}^{i(k_c x - \Omega_c t)}\right]\boldsymbol{u}_1 + \text{c.c.}\ . \tag{1.14}$$

and yields two coupled CGLEs

$$\begin{aligned}\partial_{\tilde t}A_L - c_0\partial_{\tilde x}A_L &= \epsilon A_L + (1+ic_1)\partial_{\tilde x}^2 A_L - (1-ic3)|A_L|^2 A_L \\ &\quad -g_1(1-ic_2)|A_R|^2 A_L \qquad (1.15)\\ \partial_{\tilde t}A_R + c_0\partial_{\tilde x}A_R &= \epsilon A_R + (1+ic_1)\partial_{\tilde x}^2 A_R - (1-ic3)|A_R|^2 A_R \\ &\quad -g_1(1-ic_2)|A_L|^2 A_R \qquad (1.16)\end{aligned}$$

The interaction of $A_L$ and $A_R$ via the last terms was studied theoretically [119] and experimentally [120].

The CGLE (1.12) has two intensively studied limits : for $c_1, c_3 \to 0$ it reduces to the relaxational real Ginzburg-Landau equation (1.6) and for $c_1^{-1}, c_3^{-1} \to 0$ it reduces to the nonlinear Schrödinger equation which is used to describe electro-magnetic pulses in optical fibres [121] and possesses soliton-like solutions.

### 1.4.2 Analytical results: solutions

A recent and detailed review of the CGLE has been presented by I.S. Aranson and L. Kramer [122]. In the following we summarize previous results for simple patterns and their instabilities. These will serve as starting point for the investigations in later Chapters.

The CGLE admits plane wave solutions

$$A_0(x,t) = \sqrt{1-q^2}\, \mathrm{e}^{i(qx-\omega t)} \ , \qquad (1.17)$$

with wavenumber $q \in [-1,1]$ and frequency $\omega = -c_3 + q^2(c_1+c_3)$. The spatially uniform oscillating solution $A_0(x,t) = \mathrm{e}^{ic_3 t}$ is the limit case for vanishing $q$. In the full model (1.1) the corresponding solution reads

$$\begin{aligned}\boldsymbol{u}(x,t) &= \boldsymbol{u}_0 + \sqrt{\epsilon}\sqrt{\frac{1-\xi_c^2 q'^2/\epsilon}{g_c}}\mathrm{e}^{i[(k_c+q')x-\tilde\omega t]}\boldsymbol{u}_1 + \text{c.c.} + \text{h.o.t.} \qquad (1.18)\\ \tilde\omega &= (\Omega_c - q' v_c \tau_c + q'^2(c_1+c_3)\frac{\xi_c^2}{\tau_c} - \epsilon\frac{c_0+c_3}{\tau_c}) \ .\end{aligned}$$

The solution departs from $\boldsymbol{u}_0$ as $\sqrt{\epsilon}$ which is typical for the *supercritical* oscillatory instability and can easily be found in experimental data. The possible mode shift $q' \in [-\sqrt{\epsilon}/\xi_c, \sqrt{\epsilon}/\xi_c]$ is also of order $\sqrt{\epsilon}$ and measured in the original “fast” variables. Solutions with $q' \neq 0$ have a reduced amplitude.

Other known solutions are fronts, pulses, sources and sinks that are combinations of different plane waves [119]. Well known examples are the Nozaki-Bekki hole solutions, localized depressions of the modulus $|A|$ emitting plane waves [125, 126]. Their stability properties have been analysed in [127, 128, 129, 130].

### 1.4.3 Analytical results: stability

The linear stability analysis of the plane wave solution $A_0$ (1.17) can be performed by considering the perturbed solution

$$A(x,t) = (1 + a(x,t))A_0(x,t) \qquad (1.19)$$

$$a(x,t) \;=\; (\delta a_+ \mathrm{e}^{ikx} + \delta a_- \mathrm{e}^{-ikx})\, \mathrm{e}^{\lambda_k t} \; . \tag{1.20}$$

A straightforward but involved linearization in $\delta a_\pm$ gives the growth-rate $\lambda_k$ [123]

$$\lambda_k = -k^2 - 2iqc_1k - (1-q^2) \pm \sqrt{(1+c_3^2)(1-q^2)^2 - [c_1k^2 - 2iqk - c_3(1-q^2)]^2} \; . \tag{1.21}$$

The first term ($-k^2$) represents a typical feature of diffusive processes, perturbations of short wavelength modes are quickly damped,*i.e.* their growth-rate $\lambda_k$ has large negative real part. Hence for most choices of $c_1, c_3, q$ the secondary instability is of long wavelength type. A Taylor-expansion of the growth-rate $\lambda_k$ (1.21) up to fourth order in $k$ leads to

$$\lambda_k \;=\; -iv_gk - D_2k^2 + i\Omega_gk^3 - D_4k^4 \tag{1.22}$$

$$v_g \;=\; 2q(c_1+c_3) \tag{1.23}$$

$$D_2 \;=\; 1 - c_1c_3 - \frac{2q^2(1+c_3^2)}{1-q^2} \tag{1.24}$$

$$\Omega_g \;=\; 2[c_1(1-q^2) + 2c_3q^2](1+c_3^2)\frac{q}{(1-q^2)^2} \tag{1.25}$$

$$D_4 \;=\; [c_1^2(1-q^2)^2 + 12c_1c_3(1-q^2)q^2 + 4(1+5c_3^2)q^4]\frac{1+c_3^2}{2(1-q^2)^3} \; . \tag{1.26}$$

The real part Re$[\lambda_k]$ becomes positive (Re$[\lambda_{k_{HB}}]$=0) and the plane wave linearly unstable for $k < k_{HB} = \sqrt{-D_2/D4}$ which is possible only for $D_2 < 0$. This renders stable a band of wavenumbers $q \in [-q_E, q_E]$ with

$$q_E^2 = \frac{1-c_1c_3}{2(1+c_3^2) + 1 - c_1c_3} \tag{1.27}$$

We will call this limit $q = q_E, k = 0$ the *Eckhaus* instability [113] and reserve the term *Benjamin-Feir* instability [114] for the uniform case $q_E = 0$. See Fig.1.7 for an illustration. There appear other combinations of these terms in the literature. The homogeneous oscillation is the most stable among these solutions and it becomes linearly unstable at

$$0 = 1 - c_1c_3 \tag{1.28}$$

which is called the *Benjamin-Feir-Newell* criterion (BFN) [98]. In a two-dimensional CGLE the transverse perturbations always satisfy Eq.(1.28) and are therefore never more unstable than the longitudinal perturbations.

From Eq.(1.22) one easily obtains the wave length $P_{HB}$ of the mode with Re$[\lambda_k]$=0 beyond the Eckhaus instability

$$P_{HB} = 2\pi\sqrt{\frac{-D_2}{D_4}} \tag{1.29}$$

and its velocity

$$v_{HB} = -\mathrm{Im}[\lambda_{k_{HB}}]/k_{HB} \; . \tag{1.30}$$

B. Janiaud *et al.* showed that the Eckhaus instability is supercritical only for small enough wave number $q$ and large $P_{HB}$ [56]. They experimentally observed stable modulations of the underlying plane wave. For bigger $q$ the instability is subcritical. See Chapter 3 for details.

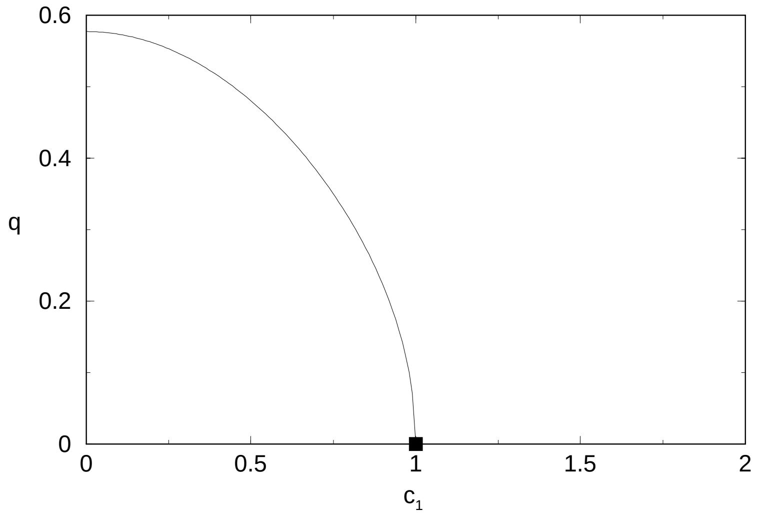

Fig. 1.7: Linear instability thresholds for plane wave solutions of the CGLE for $c_1 = c_3$. The curve denotes the Eckhaus (1.27) and the square the Benjamin-Feir instability where the Benjamin-Feir-Newell criterion (1.28) holds. Plane waves parametrized by their wavenumber $q$ are stable to the left of the curve.

In general the Eckhaus instability is of convective nature [166, 124]. To lowest order the perturbations travel with the group velocity $v_g$ of the plane wave. At larger values of $c_1, c_3$ the instability becomes absolute [166, 124]. This distinction is less relevant for the phenomena studied here since the latter involve perturbations of finite size and saturated modulations very different from the plane waves. [4]

### 1.4.4 Numerical results: phase diagram

As a function of $c_1$ and $c_3$, the CGLE exhibits two qualitatively different spatio-temporal chaotic states known as phase chaos (when $A$ is bounded away from zero) and defect chaos (when the phase of $A$ displays singularities where $A = 0$). See Fig.1.8 for examples of these states.

The transition from phase to defect chaos can either be hysteretic or continuous; in the former case, it is referred to as $L_3$, in the latter as $L_1$ (Fig. 1.9). In order to characterize defect chaos the concepts from low-dimensional deterministic chaos [131] had to be extended. For STC the attractor dimension grows proportional to the system size [30, 20, 21] hence one uses dimension densities,*i.e.* attractor dimension per volume. One may compute the dimension density from the Lyapunov spectrum [132] using the Kaplan-York conjecture [133]. The dimension density of defect chaos was shown to increase with the coefficients $c_1, c_3$ [134, 135] and is larger than that of phase chaos [136]. Another concept is determining the density of defects,*i.e.* total number of defects divided by system size and duration of the

---

[4] If a localized perturbation grows but travels away such that the perturbation decays at any fixed positions for long times then the state is called *convective* unstable [165]. If the perturbation grows faster and destabilizes the state at any fixed position then it is called *absolute* instability [29]. Transitions from convective to absolute instability have been observed analytically [166, 167] as well as numerically [168, 169] and experimentally [170, 120].

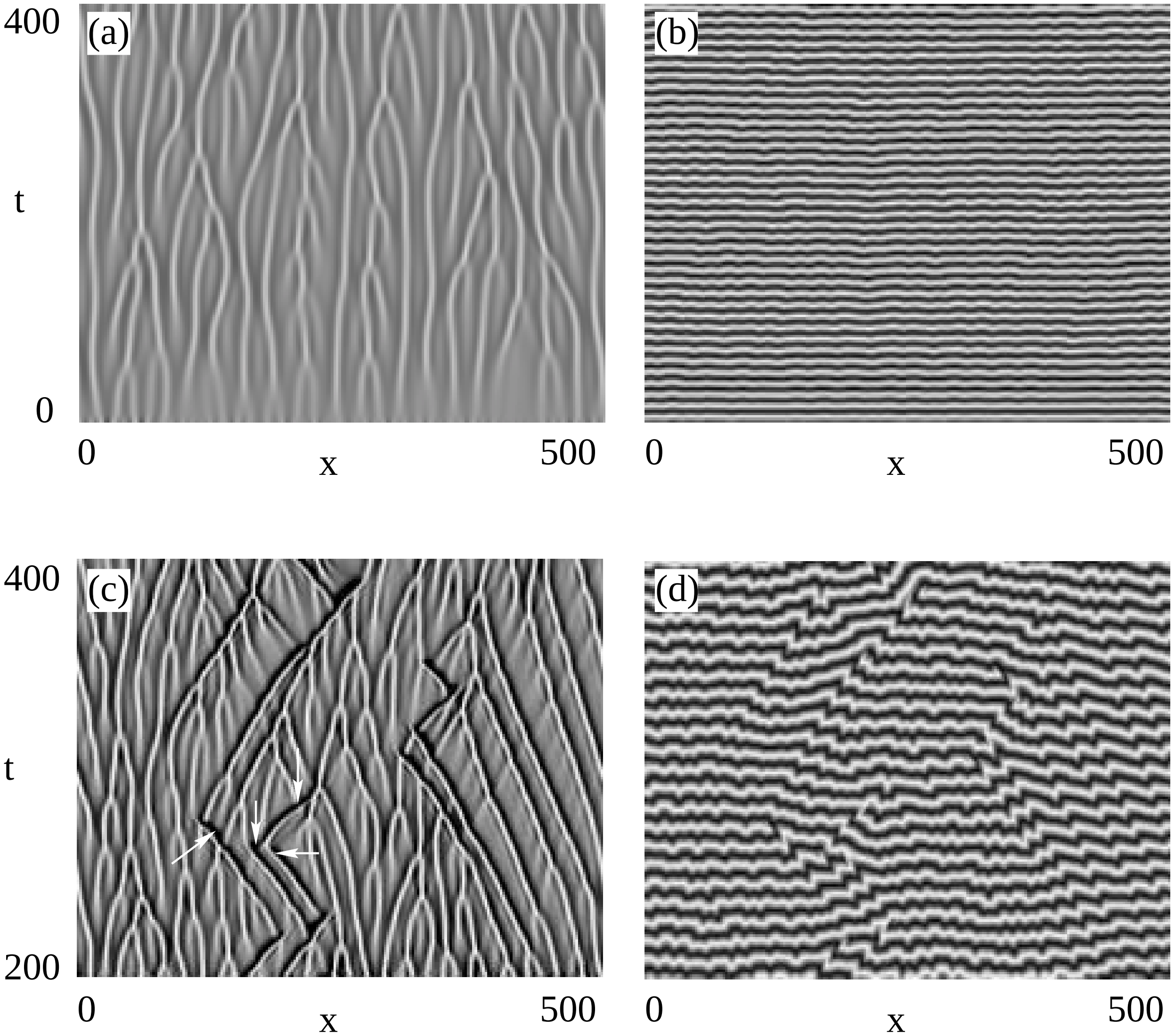

Fig. 1.8: Gray-scaled representation of phase chaos: (a) the modulus $|A(x,t)|$ (low values=dark, high=bright), (b) the phase $\arg(A(x,t))$ (0 and $2\pi$=dark, $\pi$=bright) and defect chaos: (c) the modulus $|A(x,t)|$ with some defects labelled by white arrows and (d) the phase $\arg(A(x,t))$ which jumps by $2\pi$ at the same position in $(x,t)$. Both states of STC are distinguished by the absence (phase chaos in a,b) or presence (defect chaos in c,d) of space-time defects. Parameters are $c_1 = 3.5, c_3 = 0.6$ (a,b) and $c_3 = 0.8$ (c,d), respectively.

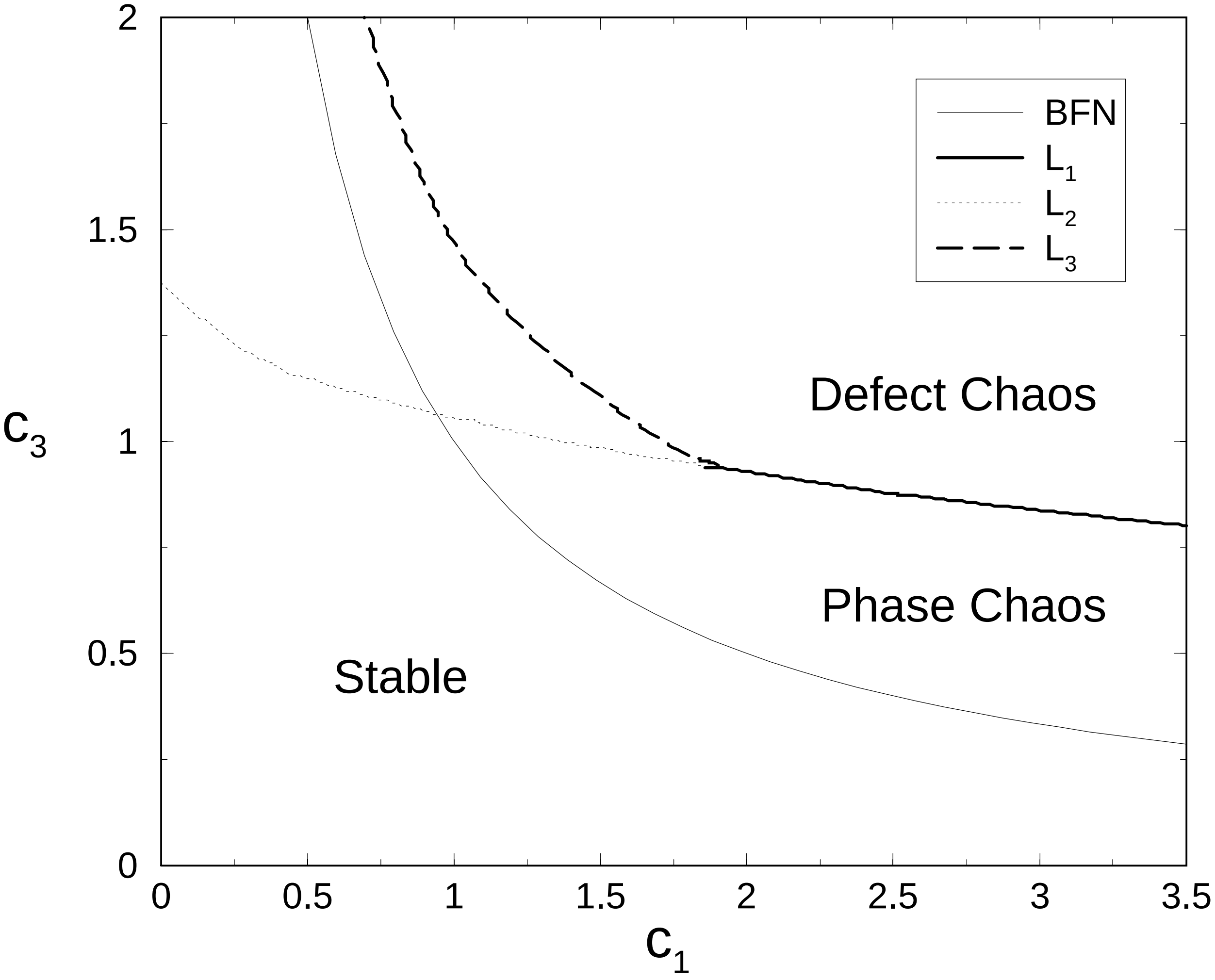

Fig. 1.9: Phase diagram of the one-dimensional CGLE [137, 138] showing the BFN, $L_1$, $L_2$ and $L_3$ transitions. The same transitions are observed in higher dimensions [146, 147] with $L_1$, $L_3$ closer to BFN. Between the $L_2$ and $L_3$ curves, there is the hysteretic regime where either phase or defect chaos can occur; in the latter case, defects persist up to the $L_2$ transition.

simulation. The defect density increases above the transition to defect chaos [137, 138],*i.e.* for increasing $c_1, c_3$. T. Bohr *et al.* compared typical length scales of structures finding much smaller scales in defect chaos than in phase chaos [21]. Localized structures have also been characterized in terms of their convective Lyapunov spectrum [140]. A. Torcini and P. Grassberger [58, 141] as well as R. Montagne *et al.* [59, 142] characterized the transition from phase to defect chaos by the vanishing of wound-up phase chaos,*i.e.* above the transition the chaotic asymptotic state always has zero average phase gradient. The transition was suggested [141] to resemble a crisis [143] that has been studied by C. Grebogi *et al.* [144]. All these investigations showed that phase chaos can be considered a rather "mild" realization of STC whereas defect chaos is a very "strong" one.

Despite these intensive studies [21, 58, 59, 119, 134, 135, 136, 137, 138, 139, 140, 141, 142, 145, 146, 147] , the phenomenology of the CGLE and in particular its "phase" diagram

[137, 138] are far from being understood. Moreover, it is under dispute whether the $L_1$ transition (see Fig. 1.9) is sharp, and whether a pure phase-chaotic (*i.e.* defect-free) state can exist in the thermodynamic limit [135, 147]. Note that, since the CGLE is a universal model system, the precise location of the transition curves is important. If future work provides values of the coefficients for new experimental systems then the typical behavior can be estimated from the location within the phase diagram. We focus on the main quadrant of the phase diagram where the Benjamin-Feir instability occurs and the phenomena of interest are observed. However, there exists a symmetry that maps two half planes of the phase diagram onto each other $c_1 \to -c_1, c_3 \to -c_3$.

### 1.4.5 Analytical results: phase equation

Phase equations are based on the observation that close to the onset of phase chaos (near the Benjamin-Feir-Newell curve) the amplitude is "slaved" to the phase dynamics, $\phi(x,t) = \arg(A)$. In this situation a phase equation can be obtained by a gradient expansion [22, 25]. To lowest order the expansion reads

$$\frac{\partial \phi(x,t)}{\partial t} = \Omega_2^{(1)} \frac{\partial^2 \phi}{\partial x^2} + \Omega_2^{(2)} \left( \frac{\partial \phi}{\partial x} \right)^2 + \Omega_4^{(1)} \frac{\partial^4 \phi}{\partial x^4} \tag{1.31}$$

and is known as the *Kuramoto-Sivashinski* equation [148, 149]. The coefficients are $\Omega_2^{(1)} = 1 - c_1 c_3, \Omega_2^{(2)} = -(c_1 + c_3)$ and $\Omega_4^{(1)} = -c_1^2(1 + c_3^2)/2$.

Recently, Abel *et al.* [150] numerically quantified the increasing discrepancies between the phase equation and the full dynamics in the CGLE with increasing distance from the Benjamin-Feir-Newell curve.

There is no transition to defect chaos in the Kuramoto-Sivashinski equation [22] and the phase in phase chaos is always well defined. On large scales the phase field has been suggested [151] to follow the *Kardar-Parisi-Zhang* equation (KPZ) [152]

$$\frac{\partial_t h(x,t)}{\partial t} = \tilde{\nu} \frac{\partial^2 h}{\partial x^2} + \frac{\tilde{\lambda}}{2} \left( \frac{\partial h}{\partial x} \right)^2 + \eta(x,t) \tag{1.32}$$

which also models the kinetic roughening of stochastic interfaces $h(x,t)$. For literature on the Kardar-Parisi-Zhang equation see [153] or the comprehensive reviews [154, 155]. The leading order terms of Eq.(1.31) are indeed equal to those of Eq.(1.32). The forth order term in Eq.(1.31) and higher order terms in other phase equations give contributions that fluctuate on short scales which may be accounted for by the noise term in Eq.(1.32). However, it is not clear and has been tested only numerically [147] if the underlying deterministic processes of phase chaos lead to a $\delta$-correlated Gaussian noise $\eta(x,t)$. Again the numerical approach limits the study to large but finite systems which may still be smaller than crossover scales of Eq.(1.32). Note the parameters $\tilde{\nu}, \tilde{\lambda}$ need to be extracted from the same numerical study.

## 1.5 Technical Tools

A standard tool in nonlinear science is the numerical simulation of the dynamics. That involves a time stepping and a spatial discretization of the model (1.1). The steps need to be chosen small enough to ensure a correct representation of the dynamics. This is often the first and straightforward approach applied to a model. It reproduces phenomena and allows one to test suggested mechanisms. The phenomena studied in the following Chapters (except Chapter 5) have been observed in simulations before,*e.g.* the phase diagram (Fig.1.9) of the one-dimensional CGLE was derived from simulations [137, 138].

However, for systems of large spatial size this approach is particularly demanding in computation time. Especially if one studies STC that may involve large distances and long transients. Therefore simulations provide (a large number of) examples at chosen values of the parameters and specific to the size and duration of the simulation. This also is the reason for ongoing discussions about the location and properties of the transition from phase to defect chaos in the one-dimensional CGLE [21, 137, 138, 134, 135].

One possibility to circumvent this is the change to a coarse grained toy model with rough discretization in space (coupled ordinary differential equations), or space and time (coupled map lattice [156, 157]) or space, time and the field (cellular automaton [158, 159]). Such models may be used to study universal mechanisms but require some experience in order to incorporate the essential features and interactions. Throughout this Thesis such techniques are not employed.

In order to get an understanding of the behaviour one has to facilitate additional more efficient methods such as bifurcation and stability analysis [6, 7, 8, 9]. Applying this analysis to complex patterns one often depends on numerical tools.

We will use the well established software package AUTO97 [160, 161] to perform bifurcation analysis and continuation of solutions under parameter variation. AUTO97 is free-ware and can be downloaded from the URL `http://indy.cs.concordia.ca/auto/`. It treats a set of nonlinear ordinary differential equations (ODEs) which restricts the class of solutions to *coherent structures* that retain their shape while traveling. [5] Also the complex pattern MAW will be expressed as coherent structure. Hence the calculation of coherent structures to partial differential equations amounts to continuation of stationary (within a comoving reference frame) solutions to a boundary value problem. Periodic boundary conditions are applied and two constraints are needed to select a unique solution out of the two-parameter family of MAWs.

We fix the spatial size of the system $L = P$ and the average phase gradient $\nu$ by an integral constraint for the solution. Thereby two equations are added to the system of ODEs. On the other hand constraints require additional variables (free parameters) to be adjusted. This is a special capability of AUTO97. Often the primary continuation parameter is $c_1$ or $c_3$ while parameters of the MAW ansatz ($v$ and $\omega$) are calculated. An additional pinning condition (one derivative of the solution set to zero at the boundary) is used to suppress trivial spatial translation. See Appendix A for a detailed discussion. This approach can be considered "quasi-analytical" and it provides numerical representations of the exact solutions. Results,*i.e.* quantities of the solutions versus varied parameter, are presented in bifurcation diagrams.

---

[5] Especially in the literature on hydrodynamics definitions of "coherent structure" are used that allow an evolution in any comoving reference frame. In the field of pattern formation the term is defined more restrictiv, as quoted here.

Many other continuation programs,*e.g.* CANDYS/QA [162] and RWPKV [163], only allow one to set the system size but no additional constraints and therefore only compute one free parameter (velocity $v$). This is sufficient for simple coherent structures and was extensively used in the field of pattern formation. The present systematic bifurcation analysis of complex patterns (the two-parameter family of MAWs) is the first to our knowledge and makes use of the additional capabilities of AUTO97.

A subsequent investigation of the role of these solutions for the state of the system is necessary. At this stage stability analysis of the computed solutions provides some answers. The *linear* stability,*i.e.* against infinitesimal perturbations, is computed via a Fourier decomposition of the eigenmodes which are functions of the spatial variables. This leads to an eigenvalue problem. The eigenmodes partly determine in what manner a possible instability changes the solution. We will compute the eigenmodes with largest real parts of their eigenvalues $\lambda$. For details see Appendix C.

In an infinitely extended system there are infinitely many eigenvalues and corresponding eigenmodes. The set of eigenvalues forms the continuous *spectrum* which lies on continuous curves in the plane (Re[$\lambda$],Im[$\lambda$]). We approximate this spectrum by analysing a finite system with periodic boundary conditions. This procedure was shown to be exact [164].

Numerical simulations of a finite system with periodic boundary conditions always detect the convective instability while boundary conditions that absorb perturbations will stabilize the state until the absolute instability threshold. Simulations are needed to represent the dynamics of a state that is not an infinitesimal perturbation of a known solution. We will also use simulations to *illustrate* the mechanisms that are infered from the bifurcation and stability analysis. The innovative time-splitting code of A. Torcini [141] was employed.

The dynamics of $A(x,t)$ in a one-dimensional system may be presented as a movie [171] showing the temporal evolution of a function,*e.g.* $|A(x)|$, or by a space time plot, a two-dimensional graph with space $x$ as the abscissa and time $t$ as the ordinate. The values of $|A|(x,t)$ are encoded in gray-scale (black corresponds to small and white to large values) at each pixel. This is the preferred representation throughout the Thesis.

# 2 Transition from Phase to Defect Chaos

## 2.1 Introduction

In this Chapter the relationship between *modulated amplitude waves* MAWs and large scale chaos is studied in detail, providing a comprehensive description of various aspects of the CGLE chaotic dynamics. The focus is set on the transition from *phase* to *defect chaos* for the one-dimensional complex Ginzburg-Landau equation (CGLE)

$$\partial_t A = A + (1 + ic_1)\partial_x^2 A - (1 - ic_3)|A|^2 A \ , \tag{2.1}$$

where $c_1$ and $c_3$ are real coefficients and the field $A = A(x, t)$ has complex values (same as Eq.(1.12)).

In many cases the evolving patterns show an erratic behavior in space and time: such behavior is commonly referred to as *spatio-temporal chaos* (STC) [22, 30, 25, 29, 122] and was observed experimentally in a variety of systems [43, 44, 45, 48, 50, 51, 52, 53, 54, 55, 56, 67, 69, 70]. Compare also Section 1.3.2.

For different choices of the coefficients numerical investigations of the CGLE have revealed the existence of various steady and spatiotemporally chaotic states [22, 30, 25, 29, 122, 56, 57, 58, 59, 119, 134, 135, 136, 137, 138, 139, 140, 141, 142, 145]. Many of these states appear to consist of individual structures with well defined propagation and interaction properties. It is thus tempting to use these structures as building blocks for a better understanding of spatiotemporal chaos. Here we will essentially follow such an approach.

As a function of the coefficients $c_1$ and $c_3$, the CGLE (2.1) can exhibit two qualitatively different spatiotemporal chaotic states known as phase chaos (when the modulus $|A|$ is at any time bounded away from zero) and defect chaos (when $|A|$ can vanish leading to phase singularities). Compare Fig. 1.8 in Section 1.4.4 and see the “phase diagram” Fig. 2.1. It is under dispute whether the transition from phase to defect chaos is sharp or not, and if a pure phase-chaotic, (*i.e.,* defect-free) state can persist in the thermodynamic limit [135, 147]. We will address these issues by suggesting a *mechanism* for the formation of defects related to the range of existence of MAWs.

The outline of this Chapter is as follows: Section 2.2 is devoted to the study of the coherent MAW structures. In Section 2.2.2 we study the bifurcation diagram of the MAWs, starting from the homogeneous oscillation. In Section 2.2.3 the incoherent dynamics of

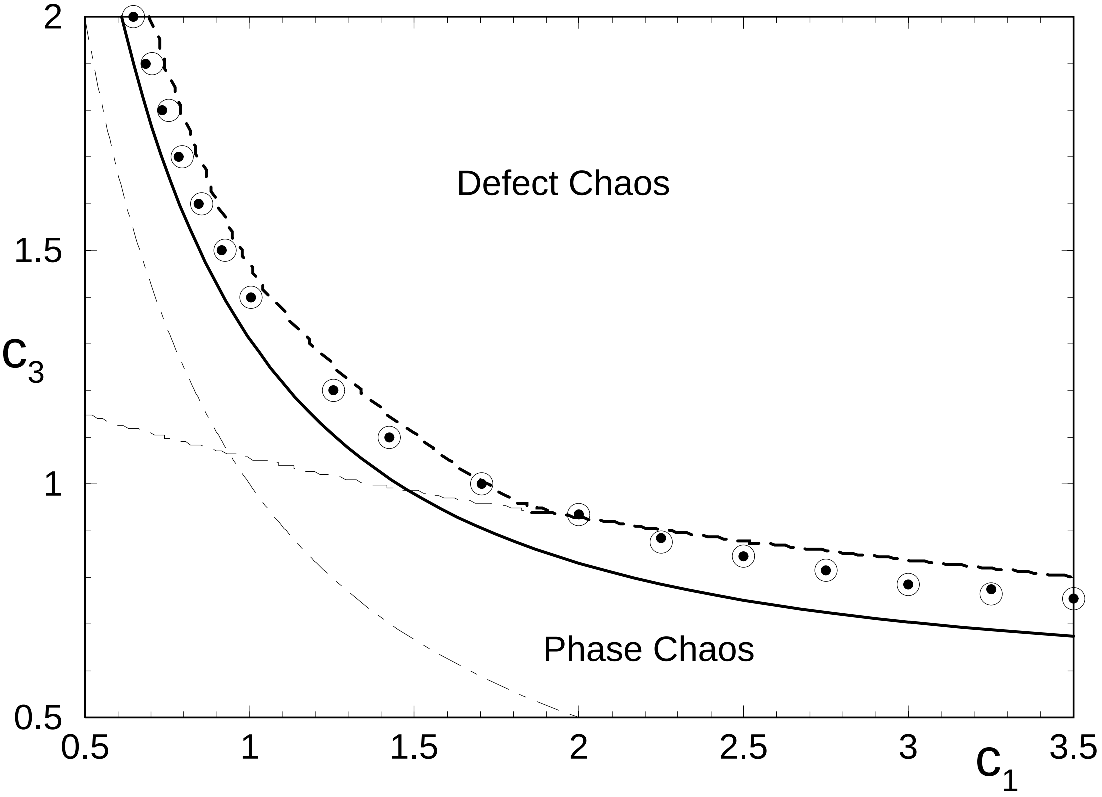

Fig. 2.1: Phase diagram of the CGLE, showing the Benjamin-Feir-Newell curve (thin dot-dashed) where the transition from stable homogeneous oscillations to phase chaos takes place. The curves $L_1$ (long dashed), $L_2$ (thin dashed) and $L_3$ (dashed) as obtained in [137, 138] separate the various chaotic states. Also the results obtained in this Chapter 2 are included, for details see the text. The filled circles correspond to our estimates of the $L_1$ and $L_3$ transitions based on direct simulations of the CGLE along the 17 cuts in coefficient space that we studied. The open circles correspond to the location in coefficient space where the maximal inter-peak spacing $p_{max}$ is equal to the maximal MAW period $P_{SN}$. Only small discrepancies between these two can be observed. Finally the full curve shows the $P_{SN} \rightarrow \infty$ limit which we conjecture to be a lower boundary for the transition from phase to defect chaos.

near-MAW structures is presented. We show that for $p > P_{SN}$, *i.e.,* beyond the saddle-node bifurcation, near-MAWs evolve to defects. To illustrate the origin of the saddle-node bifurcations in Section 2.2.4 we compare bifurcation diagrams of coherent structures for different phase gradient expansions of the CGLE. For the lowest order expansion (known as the Kuramoto-Sivashinsky equation [22]) the saddle-node bifurcation is absent while it is captured by expansions of higher order. This explains why the divergence of the phase gradient was exclusively observed in simulations [139] of higher order expansions. In Section 2.3 we study various aspects of spatiotemporal chaos in the CGLE, and relate the observed continuous ($L_1$) and discontinuous ($L_3$) transitions (see Figs. 1.9,2.1) to properties of the MAWs. *The transition to defect chaos takes place when near-MAWs with periods larger than $P_{SN}$ occur in a phase chaotic state.* In Section 2.3.4 the typical values of $p$ in the phase chaotic regime are related to the competition of two instabilities of the MAWs, and it is possible to give a good estimate for the numerically measured transition from phase to defect chaos from these considerations. A discussion of the presented results and some final remarks are reported in Section 2.4.

## 2.2 Modulated Amplitude Waves

In this Section we study the main properties of modulated amplitude waves (MAWs) with $\nu = 0$. First, in Section 2.2.1 the coherent structure framework that we use to describe the MAWs is introduced. The bifurcation diagram of MAWs is explored in Section 2.2.2, with a particular focus on the saddle-node bifurcations that limit the range of existence of MAWs. In Section 2.2.3 we study the nonlinear evolution of near-MAWs that are “pushed” beyond their saddle-node bifurcation and show that this leads to the formation of defects. Finally, in Section 2.2.4 a bifurcation analysis of MAW-like coherent structures is performed in various *phase equations* that have been proposed as approximated models for the phase chaotic dynamics of the CGLE, and we show that only higher order phase equations reproduce the saddle-node bifurcation.

### 2.2.1 Coherent structures approach

*Coherent* structures in the CGLE are uniformly propagating structures of the form

$$A(x,t) = a(x-vt)e^{i\phi(x-vt)}e^{i\omega t} \ , \tag{2.2}$$

where $a$ and $\phi$ are real-valued functions of $z := x - vt$. Coherent structures have been studied extensively [141, 119, 145] and play an important role in various regimes of the CGLE [57, 58, 59, 141, 142, 119, 145].

The restriction to uniformly propagating structures reduces the CGLE to a set of three coupled nonlinear ordinary differential equations (ODEs) [1]. These ODEs are readily found

---

[1] By substituting $\kappa := a_z/a$ one reproduces the form of the ODEs used in [119] which is more appropriate for studies of fronts.

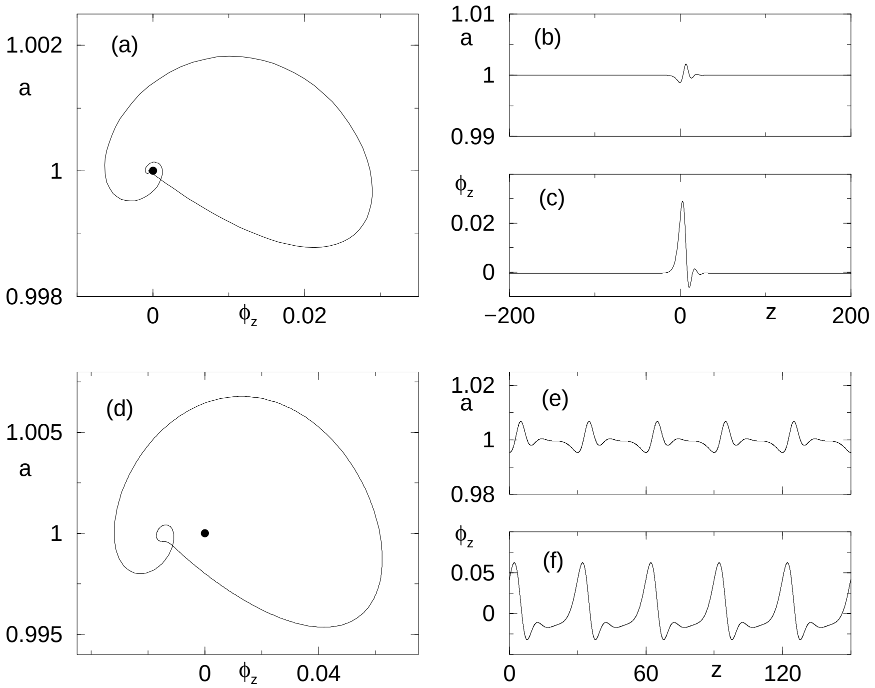

Fig. 2.2: Examples of ODE solutions and corresponding amplitude and phase gradient profiles of MAWs. (a) Homoclinic orbit for $c_1 = 0.55$ and $c_3 = 2$; (b,c) corresponding profiles. (d) Limit cycle for $c_1 = 0.60, c_3 = 2$ and $P = 30$; (e,f) corresponding profiles. Dots in (a,d) denote the unstable fixed point $(1, 0, 0)$ from which these orbits emerged.

by substitution of Ansatz (2.2) into the CGLE (2.1) and read as:

$$\begin{aligned} a_z &= b \\ b_z &= \psi^2 a - \gamma^{-1}[(1 - c_1\omega)a + v(b + c_1\psi a) - (1 - c_1 c_3)a^3] \\ \psi_z &= -2b\psi/a + \gamma^{-1}[c_1 + \omega + v(c_1 b/a - \psi) - (c_1 + c_3)a^2] \ , \end{aligned} \tag{2.3}$$

where $b := a_z$, $\psi := \phi_z$, and $\gamma := 1 + c_1^2$. Solutions of the ODEs (2.3) correspond to coherent structures of the CGLE.

The simplest relevant solutions of these ODEs are the fixed points given by $(a, b, \psi) = (\sqrt{1 - q^2}, 0, q)$; these correspond to plane wave solutions of the CGLE where $A(x, t) = \sqrt{1 - q^2} \exp i(qx + \omega t)$ and $\omega = c_3 - q^2(c_1 + c_3)$. An example of more complex solutions of the ODEs (2.3) are heteroclinic orbits which correspond to coherent structures that asymptotically connect different states. Examples of such structures are fronts that connect nonlinear plane waves to the homogeneous state $A = 0$ [119] and Nozaki-Bekki holes that connect plane waves of different wavenumber $q$ [119, 125].

Here we present an extensive study of the structures that are associated with the *limit cycles* of the ODEs (2.3) [2]. These limit cycles correspond to spatially periodic solutions of the CGLE that we have already referred to as MAWs (Fig. 2.2). For appropriate choices of

---

[2] For completeness we point out that the ODEs (2.3) also contain complicated multi-loop orbits that correspond to more complex coherent structures which have a small basin of attraction and little relevance for the dynamics of the CGLE.

$c_1$ and $c_3$, the period $P$ of these MAWs can be made arbitrarily large, and in this limit the limit cycles approach a homoclinic orbit connecting the stable and unstable manifold of one of the plane wave fixed points (Fig. 2.2a). Some of these infinite period MAWs have also been referred to as "homoclinic" holes, and have been studied extensively recently [145, 172]; they are qualitatively different from the well-known Nozaki-Bekki holes [125].

Even if the coefficients $c_1$ and $c_3$ are fixed, MAWs are not uniquely determined. Counting arguments, similar to those developed in [119], yield that in general we may expect a two-parameter family of solutions. Let us first perform the counting for the homoclinic orbits. As shown in [145], these orbits connect the one-dimensional unstable manifold of a fixed point with its two-dimensional stable manifold. In general, one needs to satisfy one condition to make such a connection, in other words, such a homoclinic orbit is of codimension one. Since the coherent structure Ansatz (2.2) has two freely adjustable parameters ($\omega$ and $v$), we therefore expect a one parameter family of homoclinic orbits.

The situation for the limit cycles of the ODEs is even simpler. Limit cycles are of codimension zero in parameter space, and so we expect a two parameter family of limit cycles. In other words, if we have found a limit cycle for certain values of $v$ and $\omega$, then we expect this limit cycle to persist for nearby values of the parameters $v$ and $\omega$.

Obviously, we can parameterize this family of limit cycle coherent structures by $v$ and $\omega$, but this is not very insightful. Instead we will use the following two quantities that are more directly accessible in studies of the CGLE: the spatial period $P$ of the MAWs, and their average phase gradient $\nu := (\int_0^P dx\phi_x)/P$. Note that for homoclinic holes, $P$ simply goes to infinity; thus homoclinic orbits and limit cycles are members of a single family.

The multiplicity of the MAWs can also be obtained by considering the instability of the plane wave solutions from which the MAWs emerge [173] (see Section 2.2.2 below). The plane waves form a one-parameter ($q$) family and undergo the well-known Eckhaus instability when the coefficients $c_1, c_3$ are increased beyond certain critical values which depend on $q$. In the unstable regime, a plane wave with wavenumber $q$ is unstable to a whole band of perturbations with wavenumbers $k \in [0, k_{max}(q)]$ [25, 29]. For finite systems of size $L$, this instability thus only appears when $L > L_{min} = 2\pi/k_{max}$. Therefore for each $q$ there is a unique one-parameter ($L$) family of perturbations that can render the plane wave unstable and at each of the corresponding bifurcations a new MAW solution emerges. Hence also by this line of reasoning MAWs form a two-parameter family. Note that the wavenumber $q$ of the plane wave determines the average phase gradient $\nu$ and the length $L$ has to be compatible with the spatial period $P$. For $L = L_{min}$, typically a MAW branch with period $P = L$ is born.

### 2.2.2 Bifurcation scenario for MAWs

The general counting arguments given in the previous Section do not provide information on the range of existence of MAWs as a function of the coefficients $c_1$ and $c_3$ and the parameters $\nu$ and $P$. Here we will focus our analysis on the $\nu = 0$ case since this is most relevant for

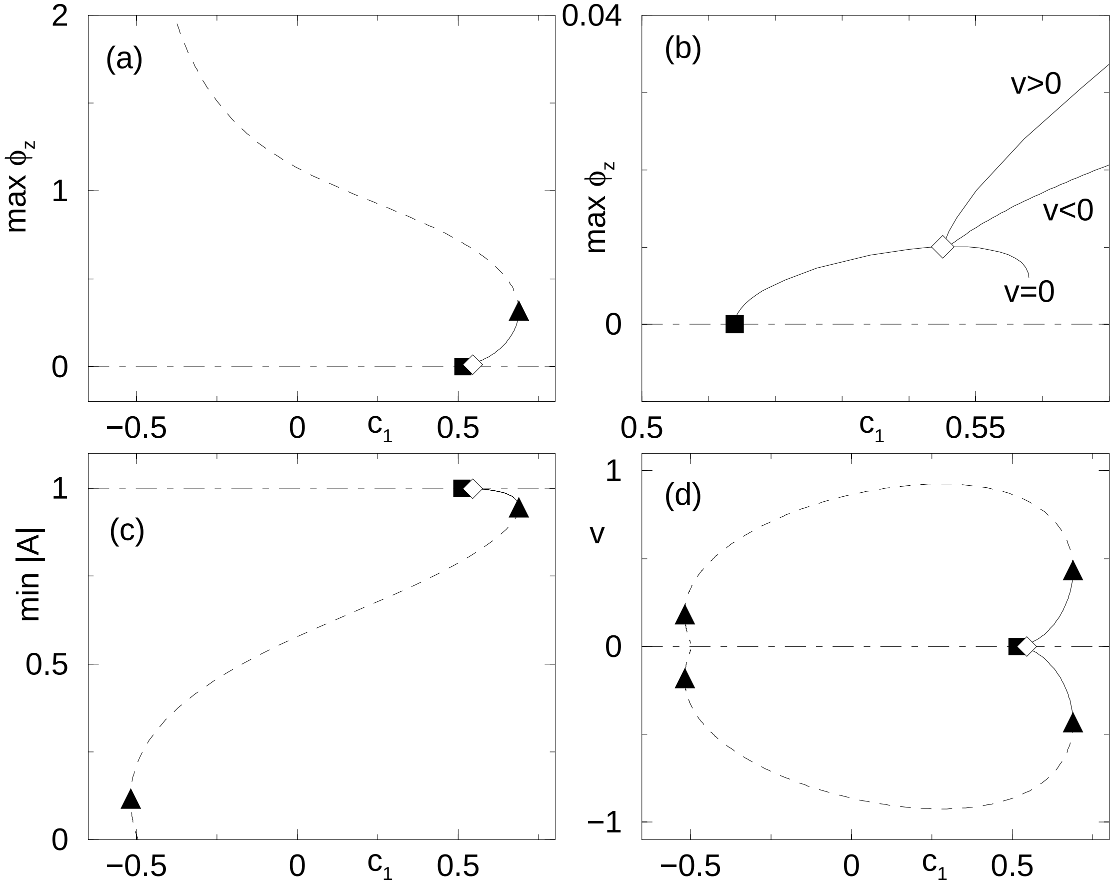

Fig. 2.3: Bifurcation diagrams for fixed $c_3 = 2$ and $P = 30$, showing Hopf (filled square), drift pitchfork (open diamond) and saddle-node (triangle) bifurcations. The dot-dashed line represents the homogeneously oscillating solution of the CGLE, while lower and upper branch MAWs are represented by full and dashed curves respectively. (a) Overview of the maximum phase gradient of the MAWs as function of $c_1$, (b) close-up, (c) the minimum of $|A|$, and (d) the velocity $v$. For details see text.

the transition to defect chaos [3]; the $\nu \neq 0$ case will be treated in Chapter 3.

All bifurcation computations have been performed with the aid of the software package AUTO97 [161]. AUTO97 can trace MAW solutions through parameter space, and when it detects bifurcations it can follow the newly emerging branches. See Appendix A for a detailed discussion of the method. AUTO97 discretizes the ODEs (2.3) on a periodic domain of length $L$, and $L$ will play the role of the period $P$ of the MAWs. Control of the average phase gradient $\nu = \nu_0$ is implemented via the integral constraint $\int_0^L \psi dz = L\nu_0$. Since periodic boundary conditions result in translational invariance, we introduce an additional "pinning" condition $a_z(0) = 0$ in order to obtain unique solutions.

Under these conditions, the continuation procedure works as follows. First of all, $\nu$ and $P$ are set to fixed values, and throughout this paper we will set $\nu = 0$. Starting from a known solution such as a plane wave or a coherent structure obtained by other means, AUTO97 is set up to trace the MAWs along trajectories in $c_1$, $c_3$ space, while calculating the parameters $\omega$ and $v$ of these MAWs.

The results of our bifurcation analysis are summarized in Fig. 2.3. When $c_1$ or $c_3$ is increased, the uniformly oscillating state of the CGLE ($A(x,t) = e^{ic_3 t}$) becomes unstable via a Hopf bifurcation, from which stationary MAWs emerge (Section 2.2.2). These stationary, left-right symmetric solutions undergo a drift pitchfork bifurcation, which leads to left and right traveling MAWs (Section 2.2.2, see also Fig. 2.3b); as discussed later, these are the solutions relevant for the dynamics in the phase chaotic regime. Following these branches of traveling MAWs, we encounter a saddle-node bifurcation where an "upper" and "lower" branch of MAWs merge (Section 2.2.2, see also Fig. 2.4); this bifurcation limits the range of existence of MAWs and is closely related to the formation of defects. The upper branch MAWs can be continued back to negative values of $c_1$, where they terminate in a solution consisting of a periodic array of shocks and stationary Nozaki-Bekki holes [125]. Upper branch MAWs with $P \to \infty$ have been studied under the name homoclinic holes [145, 172].

It should be noted that, without loss of generality, we focus here on solutions with $v > 0$, for which the main peak of the phase gradient profile is positive (see Fig.2.4). Solutions with $v < 0$ can be obtained from right moving MAWs by applying the mapping $x \to -x, z \to -z, v \to -v, a_z \to -a_z, \phi_z \to -\phi_z$.

### Benjamin-Feir instability - Hopf bifurcation

Since the average phase gradient $\nu$ is conserved across bifurcations, we start the continuation procedure from the uniformly oscillating solution $A(x,t) = e^{ic_3 t}$ that has $\nu = 0$. On an infinite domain this uniformly oscillating solution becomes unstable via the so-called Benjamin-Feir instability when $c_1 c_3 \geq 1$ [30]. In a finite domain of size $L$, the onset of this instability is

---

[3] The maximal "conserved" (during time evolution) average phase gradient vanishes approaching the transition to defect chaos [58, 59]. This result is rigorous only on scales of the system size but for smaller portions $\nu$ can fluctuate around 0. Typically we observe quasi-coherent structures (near-MAWs) in the phase chaotic regime with associate $\nu$-values in the interval $[-0.01, +0.01]$. MAWs with such small $\nu$ do not deviate much from the $\nu = 0$ MAWs, therefore the comparison of the observed structures with the $\nu = 0$ MAWs is satisfactory.

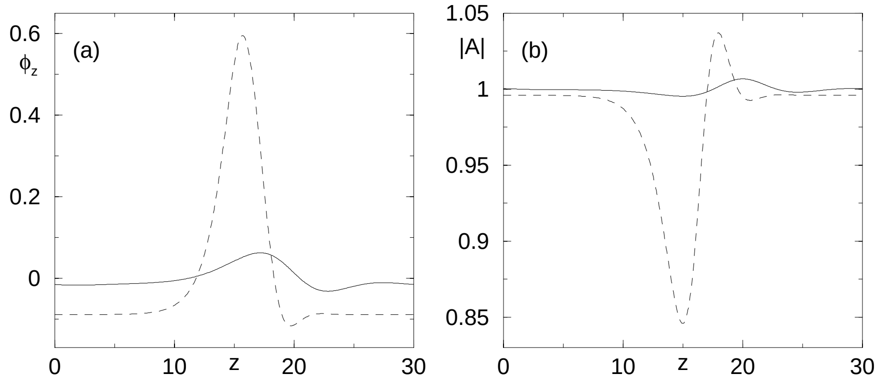

Fig. 2.4: (a) Phase gradient and (b) amplitude profiles of a lower branch (full curve) and upper branch (dashed curve) MAW, obtained for $c_1 = 0.6, c_3 = 2, P = 30$.

shifted to higher values of the product $c_1 c_3$ [4]; this finite size effect is relevant for our studies since the spatial period $L = P$ is fixed in the continuation procedure.

In the ODEs (2.3), the fixed point $(a, b, \psi) = (1, 0, 0)$ corresponds to the homogeneously oscillating solution. For given values of the period $P$, this fixed point undergoes a Hopf bifurcation (HB) at values of $c_1$ and $c_3$ where in the CGLE (2.1) the mode with wavenumber $2\pi/P$ becomes unstable ($P = P_{HB}$). This Hopf bifurcation was analytically shown to be supercritical for sufficiently small $\nu$ and large $P$ in earlier studies [56, 173]; our numerical results are consistent with this. For finite $P$, the solution bifurcating from the fixed point is a limit cycle which approaches a homoclinic orbit in the limit $P \to \infty$. The solutions of the CGLE that correspond to these orbits are stationary, reflection symmetric MAWs; an example of these is shown in Fig. 2.9a.

### Drift pitchfork bifurcation

When the CGLE coefficients $c_1$ and/or $c_3$ are increased further, the stationary MAW undergoes a drift pitchfork bifurcation [174] from which two new branches of asymmetric ($v \neq 0$) MAWs emerge (see Fig. 2.3b); one of these moves to the left, one to the right. The locations of both the Hopf and the drift pitchfork bifurcation approach the Benjamin-Feir-Newell curve for large $P$ (Fig. 2.5a), while for smaller $P$ the drift pitchfork occurs for increasingly larger coefficients $c_1$ and $c_3$. However, only when these coefficient lie in the range shown as the shaded area in Fig. 2.5b, the pitchfork bifurcation can occur. Otherwise, only stationary MAWs are found. For increasing $c_1$ and $c_3$ these MAWs become pulse-like and finally approach the solitonic solutions of the nonlinear Schrödinger equation [119] (Fig. 2.5c,d).

After the branch of stationary MAWs has become unstable via the drift pitchfork bifurcation, it terminates in a period doubling bifurcation of a MAW branch with half the period. In Appendix B an analytical approximation for the location of the drift pitchfork bifurcation is derived. For the case $\nu \neq 0$, the initial plane wave already breaks the reflection symmetry,

---

[4] For finite size systems the smallest allowed wavevector is $k_{min} = 2\pi/L$, therefore the uniform oscillation becomes unstable for $k_{min} = k_{HB}$ and this condition allows to derive the corresponding critical values of the parameters $c_1$ and $c_3$. Compare Section 1.4.3 and Eq.1.29 for an approximation.

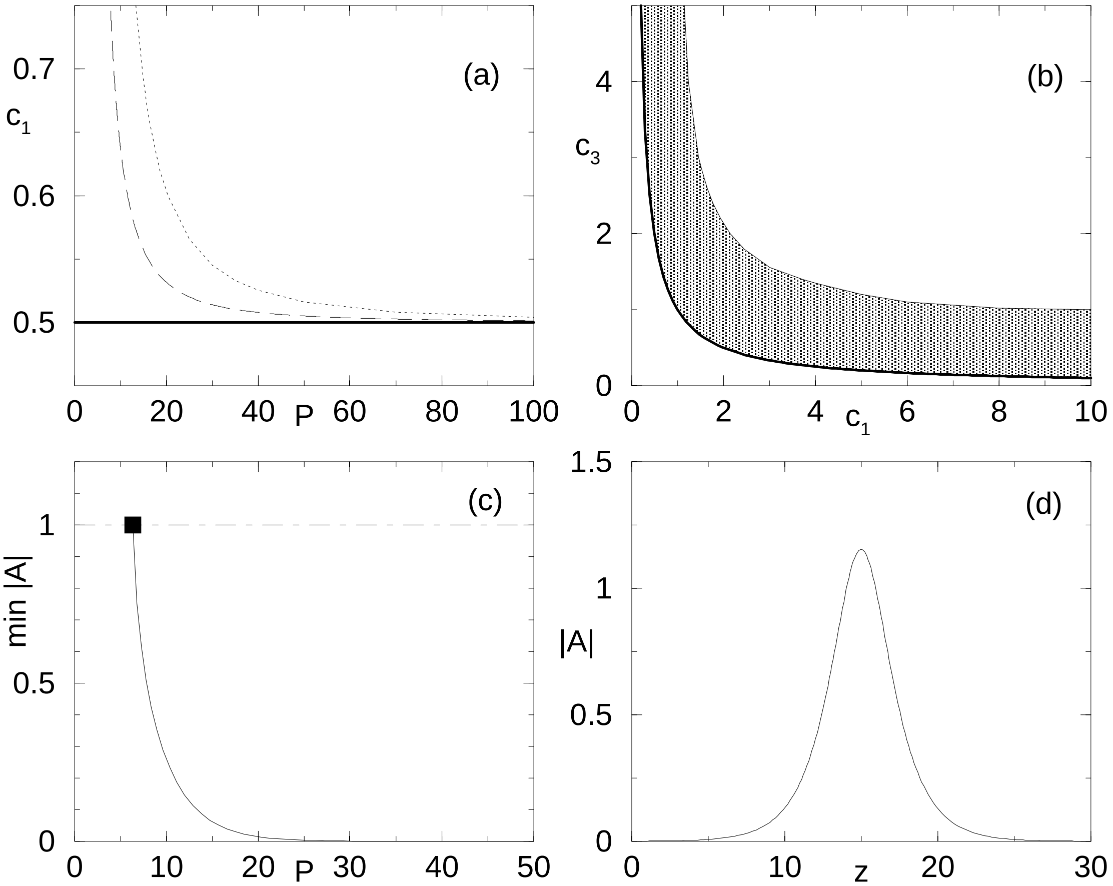

Fig. 2.5: (a) Location of Hopf (dashed curve) and drift pitchfork bifurcation (dotted curve) in $c_1, P$ space for $c_3 = 2.0$. (b) The shaded area reported in the $c_1, c_3$ coefficient space indicates where the drift pitchfork bifurcation does occur. The thick full curve in (a,b) indicates the Benjamin-Feir-Newell instability for infinite domains. (c) Example of a bifurcation diagram for large values of the coefficients $c_1 = 10, c_3 = 5$ where the drift pitchfork bifurcation does not occur. For increasing $P$ the MAW solutions approach regular arrays of stationary pulses; an example of such a pulse is shown in (d) for $P = 30$.

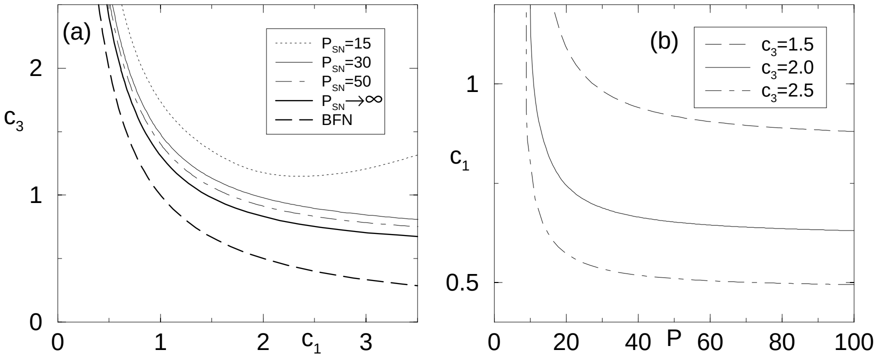

Fig. 2.6: Locations of the saddle-node bifurcations in the $c_1, c_3$ plane (a) and the $P, c_1$ plane (b). BFN denotes the Benjamin-Feir-Newell curve.

the initial MAW has nonzero velocity and the drift pitchfork bifurcation is replaced by its typical unfolding [6].

## Saddle-node bifurcation

Along the branch of right traveling MAWs that we described above, the maximum of the phase gradient grows with increasing $c_1$ and $c_3$ until a saddle-node (SN) bifurcation is reached, where these MAWs merge with another branch of MAW-like solutions. To distinguish these branches we refer to them as the "lower" and the "upper" branch; for examples see Figs. 2.3,2.8. The lower branch MAWs are the key to understand more of the phenomenology of phase chaos. The upper branch MAWs can, similarly to the lower branch MAWs, be parameterized by $\nu$ and $P$, but for the same parameters, they present more pronounced modulations (see Fig. 2.4).

The most important aspect of the saddle-node bifurcation is that it limits the range of existence of MAWs, since we will show that this limit is responsible for the transition from phase to defect chaos. Fixing $\nu = 0$, the locations of these bifurcations form a two-dimensional manifold in the three dimensional space spanned by $c_1$, $c_3$ and $P$. In Fig. 2.6a the saddle-node curves are shown in the $c_1, c_3$ coefficient plane for a number of fixed periods $P$; for larger $P$, the values of $c_1, c_3$ where the bifurcation takes place decrease. In Fig. 2.6b the saddle-node curves for a number of fixed values of $c_3$ are shown in the $P, c_1$ plane; for larger $c_3$ ($c_1$), the saddle-node occurs for smaller values of $P$ and $c_1$ ($c_3$) [5]. Once the coefficients $c_1$ and $c_3$ are fixed, we define $P_{SN}$ as the period for which the saddle-node bifurcation occurs. Note that there is also a range of coefficients $c_1$ and $c_3$ (between the $P \to \infty$ and $c_1 c_3 = 1$ curve where the saddle-node bifurcation does *not* occur.

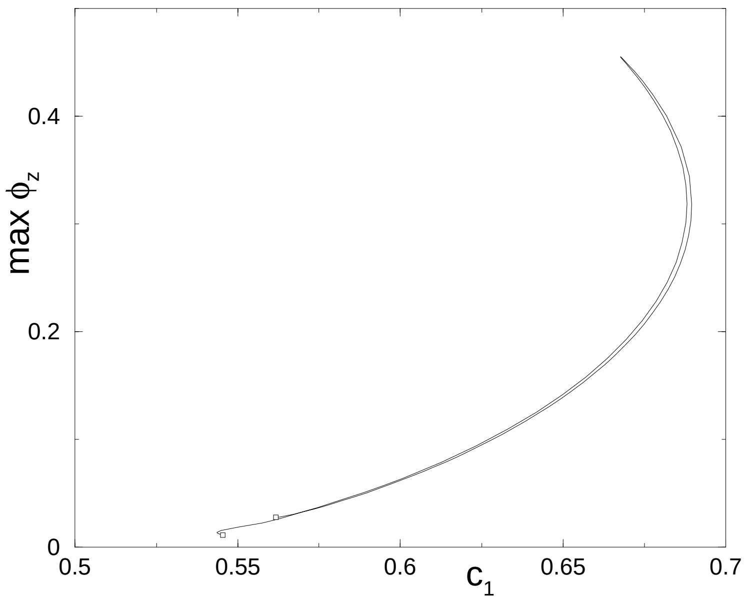

Fig. 2.7: Bifurcation diagram for aperiodic solutions at $c_3 = 2.0, L = 2 * 30$. The branch connects 2 PD bifurcations of periodic MAWs with period $P = 30$.

**Period doubling bifurcation**

As a short side-remark some information shall be given on more complex combined MAWs which are only important in short systems of a few periods $P$. [6] In systems of size $L$ multiple of $P$ the branch of periodic MAWs undergoes a sequence of period doubling bifurcations (PD). Branches of aperiodic solutions emerge which locally have a similar shape as the periodic MAW but differ in the extent of the plateau region in the spatial profile. The PD bifurcations may be sub- or supercritical depending on parameters. Fig. 2.7 shows an example for $L = 2*30$. The branch connects 2 PD bifurcations of MAWs with $c_3 = 2.0, P = 30$ (Fig. 2.3). Their lower branch encounters 3 such pairs of PD bifurcations. In Sec. 2.3 the system size is chosen sufficiently large and the combined coherent structures have a vanishing probability of surviving. We observe the single MAW description to be restored for big system size.

### 2.2.3 Evolution of perturbed MAWs

In this Section we will show that many basic aspects of the phenomenology of the CGLE can be understood from a typical bifurcation diagram of MAWs such as shown in Fig. 2.8. We have chosen fixed coefficients $c_1 = 0.65$ and $c_3 = 2$ and varied the spatial period $P$ of MAWs that exist at these coefficients. Three families of solutions are represented: the

---

[5] An exception on this rule occurs for large $c_1$, where the dependence of $c_3$ on $P$ at the saddle-node becomes non-monotonic.

[6] If one studies phase chaos in short systems extending over a few periods $P$ these combined coherent structures play a role. Their existence can prevent defects up to their SN although the distance between neighbouring humps exceeds the period of all existing single MAWs.

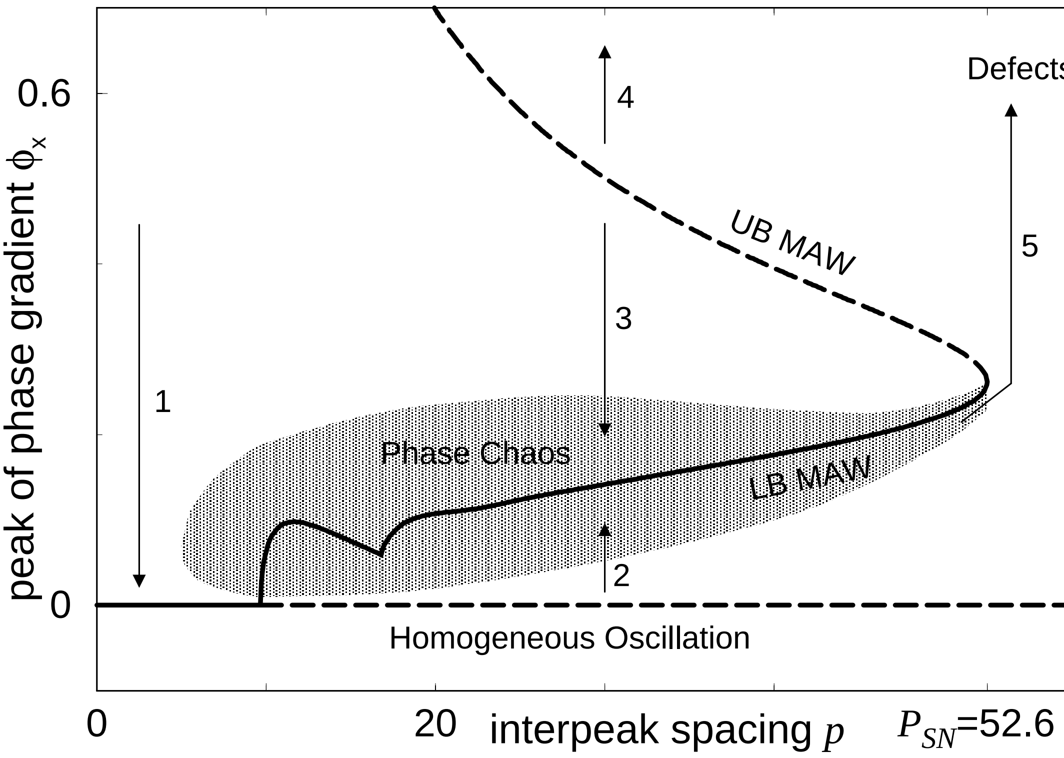

Fig. 2.8: Illustration of the relation between MAW structures and phase chaos for $c_1 = 0.65, c_3 = 2$. Both for MAWs and for an extended profile obtained from a phase chaotic state one can extract the values of subsequent phase gradient peaks (vertical axis) and their inter-peak spacing (horizontal axis). The curves show the bifurcation diagram for the lower branch (LB) MAWs and upper branch (UB) MAWs while the shaded area indicates the typical values for near-MAW structures that occur in phase chaos. Full (dashed) curves denote stable (unstable) solutions for system size $L = p$. Arrows show the typical evolutions of near-MAWs. The coefficients here are equal to those in Fig. 2.19 (f,i,j) and for this case we have found that phase chaos is only a long lived transient: the shaded area reaches $P_{SN}$ just before defects appear.

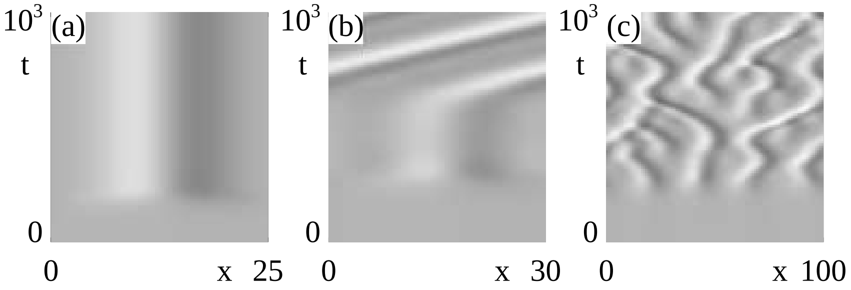

Fig. 2.9: The evolution of an unstable homogeneous state towards lower branch MAW dynamics, for $c_1 = 3$ and $c_3 = 0.6$. The coefficients $c_1$ and $c_3$ are chosen such that no saddle-node bifurcation occurs for any $P$. (a) Evolution towards a stable stationary lower branch MAW for system size $L = 25$ and (b) towards a stable drifting lower branch MAW for system size $L = 30$. Note that for the coefficients chosen, the drift pitchfork bifurcation occurs at $P = 27.7$. (c) Evolution towards phase chaos for system size $L = 100$. Incoherent evolution of structures characterized by local concentrations of phase gradients can be clearly observed. We think of these structures as "near" MAWs.

homogeneous oscillation, the lower branch (LB) and the upper branch (UB) MAWs. The shaded area schematically indicates the near-MAW structures observed in phase chaotic states such as shown in Fig. 2.19 (f,i,j). The arrows in Fig. 2.8 represent the dynamical evolution of perturbed MAWs, and their direction can be obtained by performing a linear stability analysis.

*Linear stability* - As discussed in Section 2.2.2, the homogeneous solution is stable against short wavelength perturbations (arrow 1), and turns unstable via the Hopf bifurcation that also generates the lower branch MAWs (arrows 2). As discussed in [145, 172], upper branch MAWs have at least one unstable eigenvalue, and the dynamical evolution of perturbations is directed away from upper branch MAWs (arrows 3,4).

The linear stability of lower branch MAWs will be discussed in more detail in Section 2.3.4. It turns out that perturbations of lower branch MAWs can evolve in many ways, but in almost all cases the ensuing dynamics remains close to the lower MAW branch (shaded area in Fig. 2.8). The only exception we have found to this rule is when a MAW is pushed beyond the saddle-node bifurcation (arrow 5).

*Nonlinear evolution* - Here we want to go beyond the linear analysis and study the nonlinear evolution of MAWs along the arrows of Fig. 2.8. The examples (at different choices of the coefficients) of the dynamics shown below are not exhaustive, but should serve to illustrate typical behavior which appears to be very robust.

*arrow 2* - When the uniform oscillation becomes linearly unstable perturbations grow. To the left of the saddle-node, perturbations evolve to dynamics dominated by lower branch MAWs (Fig. 2.9). For small system sizes, stable MAWs may occur (Fig. 2.9a,b), while for larger systems periodic sequences of MAWs are unstable with respect to the so-called *interaction* or *splitting* instabilities [176] that will be discussed in Section 2.3.4. Hence a perturbed unstable homogeneous state typically does not converge to a train of coherent MAWs, but instead evolves to phase chaos (Fig. 2.9c). In the context of the bifurcation diagram, note that the disordered structures observed in the phase chaotic evolution are

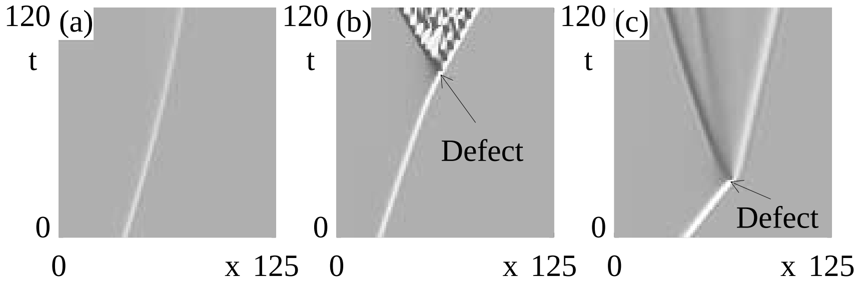

Fig. 2.10: Evolution of perturbations of the upper branch MAWs. The coefficients $c_1$ and $c_3$ are chosen such that no saddle-node bifurcation occurs for any value of $P$. (a) A slowing down and spreading of the phase gradient characterizes the decay to a lower branch MAW for $c_1 = 0.55$ and $c_3 = 2$. (b) For the same coefficients, another perturbation leads to an increase in velocity and divergence of the phase gradient. A defect occurs, from which hole-defect dynamics spreads for these coefficients. (c) For $c_1 = 3$ and $c_3 = 0.6$ a perturbed upper branch MAW leads to a defect, but defects do not percolate through the system.

quite similar to lower branch MAWs. The shaded area in Fig. 2.8 represents this "near-MAW" behavior.

*arrows 3,4* - Upper branch MAWs are always unstable due to the positive eigenvalue associated with the saddle-node bifurcation. The resulting incoherent dynamics has been studied quite extensively in the context of hole-defect dynamics [145, 172]. *(i)* When a perturbation has pushed an upper branch MAW towards the "lower" part of the bifurcation diagram, the structure decays towards lower branch MAWs (arrow 3). An example of a space time plot for the decay towards a lower branch MAW is shown in Fig. 2.10a. *(ii)* When the perturbation pushes the MAW towards the "upper" side of the diagram, the phase gradient peak that characterizes MAWs grows without bound, and at the same time the minimum of $|A|$ approaches zero: a defect is formed (arrow 4). The dynamics *after* such a defect has formed depends on the values of the coefficients $c_1$ and $c_3$. Two different examples are shown in Fig. 2.10b,c. For more details see Section 2.3.

*arrow 5* - So far we have encountered two scenarios: if the phase gradient peak of a structure is "larger" than that of an upper branch MAW, then it will grow out to form defects. If it is "smaller", it will decay back in the direction of the lower branch MAWs. The latter process frequently occurs in phase chaos, preventing the formation of defects, while the former process needs to be initiated by appropriate initial conditions. However, when the upper and lower branches approach each other and disappear in a saddle-node bifurcation, there are no structures left to prevent arbitrary small perturbations to grow out to defects. This dynamical process, which is represented by arrow 5 in Fig. 2.8, is the core of our argument: defect formation takes place beyond the saddle-node bifurcation.

### 2.2.4 Breakdown of phase description

An alternative approach to describe the creation of defects from phase chaotic states is via blow-ups in so-called phase-equations [139]. Phase equations are based on the observation that close to the onset of phase chaos (near the Benjamin-Feir-Newell curve) the amplitude is "slaved" to the phase dynamics. In this situation a phase equation can be obtained by a gradient expansion [25, 29]. The expansion including all parity-symmetric terms up to fourth order [139] reads

$$\begin{aligned}\frac{\partial \phi}{\partial t} &= \Omega_2^{(1)} \frac{\partial^2 \phi}{\partial x^2} + \Omega_2^{(2)} \left(\frac{\partial \phi}{\partial x}\right)^2 + \Omega_4^{(1)} \frac{\partial^4 \phi}{\partial x^4} \\ &\quad + \Omega_4^{(2)} \frac{\partial \phi}{\partial x}\frac{\partial^3 \phi}{\partial x^3} + \Omega_4^{(3)} \left(\frac{\partial^2 \phi}{\partial x^2}\right)^2 + \Omega_4^{(4)} \left(\frac{\partial \phi}{\partial x}\right)^2 \frac{\partial^2 \phi}{\partial x^2}\end{aligned} \tag{2.4}$$

where $\Omega_2^{(1)}=1-c_1c_3, \Omega_2^{(2)}=-(c_1+c_3), \Omega_4^{(1)}=-c_1^2(1+c_3^2)/2, \Omega_4^{(2)}=-2c_1(1+c_3^2), \Omega_4^{(3)}=-c_1(1+c_3^2), \Omega_4^{(4)}=-2(1+c_3^2)$. The lowest order description of phase chaos is obtained when the parameters $\Omega_4^{(2)}, \Omega_4^{(3)}$ and $\Omega_4^{(4)}$ are set equal to zero; the resulting equation is known as the Kuramoto-Sivashinsky equation [22]. In this limit one can derive an analytic scaling relation for the coefficients at bifurcation points, see Appendix B.

The phase equations with higher order terms included have been studied via direct integration by Sakaguchi [139]. For the full Eq. (2.4), Sakaguchi observed finite time divergences of the phase gradient for coefficients close to the transition from phase to defect chaos in the CGLE. He attributed such divergences to the occurrence of defects in the CGLE. No blow-up of the phase gradient is observed for Eq. (2.4) without the last term, or for the simple Kuramoto-Sivashinsky equation. Recently, Abel *et al.* [150] quantified the increasing discrepancies between the phase equations of different orders and the full dynamics in the CGLE with increasing distance from the Benjamin-Feir-Newell curve and identified the relative importance of the various terms in Eq. (2.4).

Since the essential ingredient of our theory is the occurrence of a saddle-node bifurcation, we have investigated the bifurcation scenario for various truncations of the phase equations (2.4). In the context of phase dynamics, our Ansatz (2.2) becomes of the form

$$\phi(x,t) = \tilde{\phi}(x-vt) + (\omega - c_3)t \ . \tag{2.5}$$

We have studied MAW-like structures occurring in the phase equations by employing the same methodology as for the CGLE; the average phase gradient value $\nu$ is fixed to 0 and $P$ parameterizes the spatial period of the MAW. In Fig. 2.11 we compare bifurcation diagrams and MAW profiles for different expansions at the parameters $c_1 = 3.5, P = 50$.

For all phase equations considered here the coherent structures are again born in a Hopf and undergo a drift pitchfork bifurcation, beyond which the maximal phase gradients increase. This leads to increasing discrepancies between different approximations. In particular, the coherent structures for Eq. (2.4) exhibit saddle-node bifurcations at parameter values not far from those for corresponding MAWs in the CGLE; nevertheless the MAWs of Eq. (2.4) deviate substantially from the CGLE MAWs for the upper branch of MAWs. The Kuramoto-Sivashinsky equation, and Eq. (2.4) without the last term, do not exhibit a saddle-node bifurcation. Since these latter two models do not experience blow-up, we can safely conclude that these observations confirm our picture, and that the saddle-node bifurcations of coherent structures play the same crucial role in both the full CGLE and its phase equations.

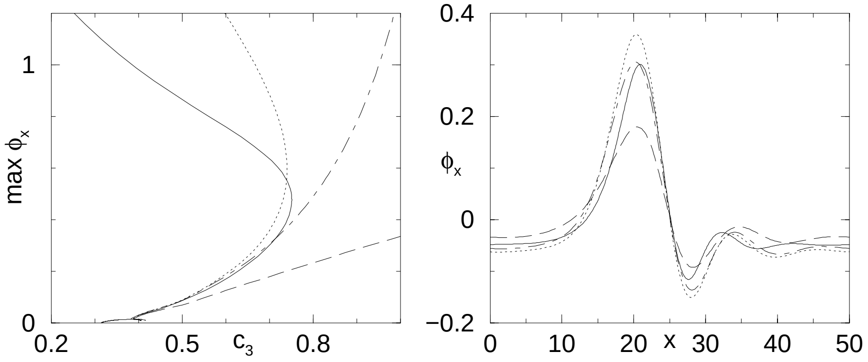

Fig. 2.11: Comparison of different phase expansions : Eq.(2.4) (dotted), Eq.(2.4) without the last term (dot-dashed), Kuramoto-Sivashinsky Eq. (dashed) and CGLE (full curve). Parameters are $c_1 = 3.5, \nu = 0, P = 50$. (a) Bifurcation diagrams and (b) spatial profiles of lower branch coherent structures at $c_3 = 0.7$.

## 2.3 Large scale chaos

In this Section we will study the dynamical evolution of the CGLE near the transitions from phase to defect chaos. The transition between these two states can either be hysteretic or continuous: in the former case, the transition is referred to as $L_3$, in the latter as $L_1$.

How are defects generated from phase chaos? Let us start to consider a *small* system in which a stable lower branch MAWs has been created. When we fix the coefficients $c_1$ and $c_3$ and steadily increase the size of the system, and hence the period $P$ of the MAW, we find that as soon as we push $P$ beyond $P_{SN}$, the MAW structure blows up to form defects. An example of this is shown in Fig. 2.12a. In a similar fashion, defects are created when the system size $L$ is fixed, and either $c_1$ or $c_3$ are increased until $P_{SN} < L$ (Fig. 2.19c,d).

How is this related to phase chaos? As shown in Fig. 2.12b, typical phase chaotic states show much more incoherent dynamics, containing many MAW like structures but of much smaller period. Our central conjecture is therefore that the transitions from phase to defect chaos are triggered by the occurrence of near-MAW structures in a phase chaotic state with $\nu = 0$ and periods larger than $P_{SN}$, the spatial period of the critical nucleus for defect creation.

To test this conjecture, we have numerically investigated the distribution of inter-peak spacings $p$ of the phase gradient profile (see Fig. 2.19e,f). In Section 2.3.1 we discuss the definition of $p$ and the details of our numerical analysis. In particular, we have examined in the $c_1, c_3$ plane 17 different "cuts" across the $L_1$ and $L_3$ transition lines. In Section 2.3.2 the results of our numerics along a cut through the $L_1$ transition line are presented, while Section 2.3.3 is devoted to the $L_3$ transition. We will show that the presence of inter-peak spacings $p$ larger than $P_{SN}$ accurately predicts the transition from phase to defect chaos (Fig. 2.1). In the last Section 2.3.4 we will show that a reasonable, parameter-free estimate of the numerically observed transitions can be obtained via a linear stability analysis of the MAWs.

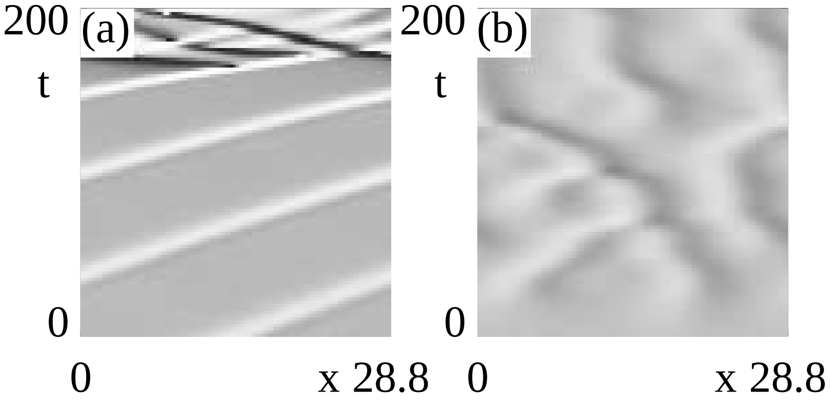

Fig. 2.12: Defect formation at $c_3 = 2, c_1 = 0.7$. (a) Defect formation. As initial condition we took a lower branch MAW with $P < P_{SN} = 26.8$ which we embedded in a background of zero wavenumber. The system size $L$ here is equal to 28.8, which is larger than $P_{SN}$ and a defect is formed; for $L < P_{SN}$ this defect formation does not take place. (b) Random initial conditions in general evolve to MAW like structures with $P < P_{SN}$ which do not lead to defects; the "critical" nucleus that leads to defect formation has a rather small basin of attraction here.

### 2.3.1 Identification of MAWs in the phase-chaotic regime

To verify our main conjecture, we have to characterize the MAW structures occurring in the phase-chaotic regime. In general this is a complicated task, since the phase gradient profile of a typical phase chaotic state (see Fig. 2.19e,f and 2.13) consists of many peaks of different size, spacing and shape; a priori it is unclear how to compare these to MAW profiles. However, a close inspection of the defect forming process reveals that while closely spaced phase gradient peaks evolve in a quite erratic way, well spaced peaks appear to have a more regular dynamics and frequently their overall shape resembles that of MAWs (see Fig. 2.13). These large period near-MAWs modify their shape quite slowly with respect to the other structures present in the chaotic field, and propagate over a disordered background. Therefore we study the distribution of inter-peak distances $p$, keeping in mind that the tail of this distribution is relevant for defect generation.

The phase gradient profile of a coherent MAW (see Figs. 2.19a and Fig. 2.4a) shows a secondary maximum. To obtain the correct period $P$ of a near-MAW, such small extrema should be neglected when the inter-peak spacing $p$ is measured. We introduce a cutoff for the size of the phase gradient peak equal to the size of the secondary extremum of the MAW with the largest $P$. As an additional result of this cutoff, small fluctuations are not considered as MAW peaks. It should be noted that the tail of the distribution of $p$ is rather insensitive to the precise value of this cutoff.

In order to estimate the probability density $D(p)$, for every time interval $\tau = 0.5$, the inter-peak periods $p$ of the spatial profile of the phase gradient are determined. In addition, for every snapshot the largest value $p_{max}$ of the inter-peak spacing $p$ is stored separately, and this leads to the distribution $D(p_{max})$. From the spatial profile of $|A|$ the distribution $D(|A|)$ and the minimal amplitude value $|A|_{min}$ can be derived. This latter quantity is used to detect defects: when $|A|_{min}$ falls below a value of 0.1, we take this as an indication of a defect.

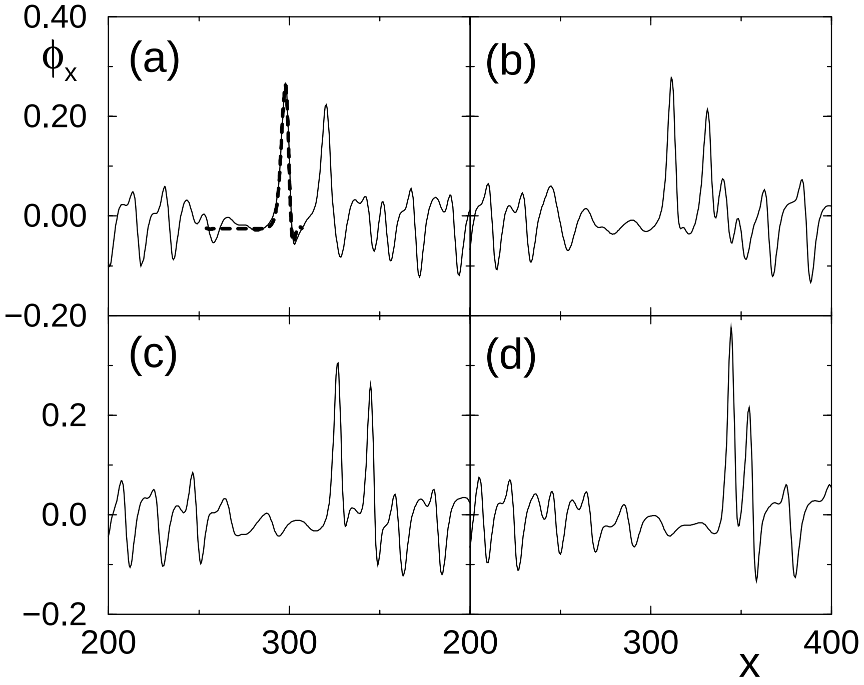

Fig. 2.13: Local phase gradient of the chaotic field just before defect formation for $c_1 = 0.65$ and $c_3 = 2$. Panel (a) is a snapshot of the field at a time $t = 120$ before the occurrence of the defect, (b) , (c) and (d) are successive snapshots taken at time intervals $\delta t = 30$. In (a) also the shape of the MAW at the saddle-node is superimposed (thick dashed line) on the profile.

A. Torcini has conducted extensive simulations which have been possible thanks to excellent computer resources at the *Max Planck institute for the physics of complex systems* in Dresden and an innovative time-splitting code which ensures precision and stability comparable with pseudo-spectral codes, but is noticeably faster [141]. The spatial resolution $\Delta x$ has been set to 0.5 and the integration time step to 0.05. Simulations have been carried out for integration times ranging from $t = 5 \times 10^5$ to $t = 3 \times 10^7$ and for a typical system size $L = 512$; occasionally, runs have been performed with $L = 100, 200$ and 5000. Typically, our runs start from random initial conditions of the type $A_k(t = 0) = |A|_k(t = 0) \cdot \mathrm{e}^{i\phi_k(t=0)}$ (where $A_k(t) = A(k\Delta x, t)$ and $\phi_k(t) = \phi(k\Delta x, t)$) with

$$|A|_k(0) = 1 + r_k \tag{2.6}$$

$$\phi_k(0) = \phi_{k-1}(0) * 0.8 + q_k \tag{2.7}$$

where $r_k$ and $q_k$ are random numbers uniformly distributed in $[-0.05, +0.05]$ and $\phi_1(0) = 0.0005$. This initial condition (2.7) leads to a smooth phase and the formation of defects due to initial discontinuities is avoided.

In Sections 2.3.2 and 2.3.3 we will consider in detail two particular cuts in the $(c_1, c_3)$ coefficient space, one across the $L_1$ and one across the $L_3$ curve. In particular, we will analyze the behavior of the probability densities $D(|A|)$, $D(p)$ and $D(p_{max})$ for both transitions.

### 2.3.2 $L_1$ transition

In this Section we concentrate on the $L_1$ transition that is observed when the value of $c_1$ is fixed at 3.0 and $c_3$ is varied.

*Transition to defect chaos* - Starting from random initial conditions we have integrated the dynamics of the CGLE for long durations. For a fixed system size $L$ we observe that, as a function of the total integration time, the value of $c_3^*$ for which defects are formed appears to decrease. Similar behavior occurs when the system size $L$ is increased for fixed integration times. For example, for an integration time of $3 \times 10^7$ and $c_1 = 3$ we find for system size 100, 200 and 512 critical values $0.82, 0.81$ and $0.79$, respectively. For a size $L = 5000$ and integration times $3 \times 10^6$ a critical value of 0.79 is also found.

Note that even the lowest value of $c_3^*$ for the numerically measured transition obtained here is far above the lower bound $c_3^\infty = 0.704$ which is the value of $c_3$ where the size of the critical nucleus for defect formation diverges ($P_{SN} \to \infty$). Below, we will give an estimate of the critical value $\hat{c}_3$ for which the defect density should vanish in the thermodynamic limit by extrapolating finite time and finite size data.

*Distribution of p* - Let us now consider the distribution of $p$'s for various coefficients $c_3$ near the $L_1$ transition. It is clear from the data reported in Fig. 2.14 that the shape of these distributions is quite insensitive to the presence or absence of defects. This can be partly explained by the fact that just above the $L_1$ transition defects arise in the system as rare isolated events occurring during the spatio-temporal evolution, as shown in Fig. 2.10c. This is fully consistent with earlier observations that the $L_1$ transition is continuous [137, 138, 135]. We focus on the tail of the probability density $D(p)$, since this gives information on the probability to observe defects. Our numerical results suggest an exponential decay, *i.e.,* $D(p) \propto \exp(-\alpha \cdot p)$ with $\alpha = 0.6$ for sufficiently large $p$.

Similarly to the apparent transition value $c_3^*$, the values associated to extremal events $|A|_{min}$ and $p_{max}$ depend on integration times and system sizes. By assuming that $D(p)$ remains finite (but likely exponentially small) for large $p$, we can expect that for long enough times, rare events associated with large values $p$ will occur, and hence, defects can form after possibly very long transients.

*Crossover behavior* - A good order parameter to identify the occurrence of the transition starting from the defect chaos phase near the $L_1$ transition is the *defect density* $\delta_D$ which measures the number of defects occurring per space and time unity. In the defect chaos regime $\delta_D > 0$, while it vanishes at the $L_1$-transition. Now we can relate this order parameter to the tail of the distribution of $p$. Our conjecture states that defects should arise when $p > P_{SN}$, therefore the defect density $\delta_D$ should be related to the probability to have structures of period $p > P_{SN}$, *i.e.*,

$$\delta_d \propto \int_{P_{SN}}^{\infty} dp D(p) \propto \mathrm{e}^{-\alpha P_{SN}} \ ; \tag{2.8}$$

where $D(p) \propto \exp(-\alpha \cdot p)$ has been used. If we now assume that the distribution $D(p)$ does not vary significantly across the transition (as is evident from Fig. 2.14), then the change in the probability to have $p > P_{SN}$ is dominated by the changes in $P_{SN}$ with $c_3$. A reasonable

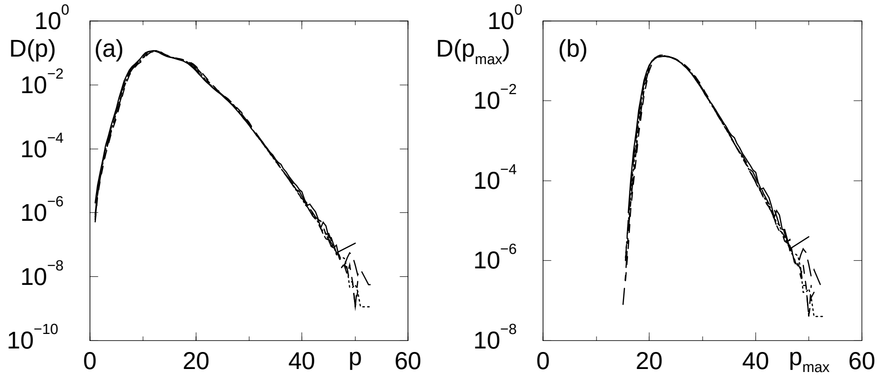

Fig. 2.14: Probability densities (a) $D(p)$ and (b) $D(p_{max})$ for $c_1 = 3$ and various values of $c_3$ on a lin-log scale. The curves refer to $c_3$ below $c_3^* = 0.79$ (namely to $c_3 = 0.77$ and $0.78$), as well as to values corresponding to the defect chaotic regime: $c_3 = 0.79$, $0.80$ and $0.81$. The system size was $L = 512$ and the integration times where $t = 5 \times 10^5$ for $c_3 = 0.81$, $t = 5 \times 10^6$ for $c_3 = 0.80$ and $t = 25 \times 10^6$ for all other values.

fit of our bifurcation data for $P_{SN}$ (see Fig. 2.6) in the interval $30 \leq P_{SN} < 300$ is

$$P_{SN} \approx \frac{\beta}{c_3 - c_3^\infty} \ , \tag{2.9}$$

where $\beta \approx 4.38$. Combining this result with the Ansatz (2.8), we immediately obtain the following expression for the defect density:

$$\delta_d \propto \mathrm{e}^{-\alpha\beta/(c_3 - c_3^\infty)} \ . \tag{2.10}$$

A similar expression was proposed in [137, 135] for the defect density near the $L_1$ transition.

In order to verify if the expression (2.10) is reasonable also for our choice of the parameters, we have estimated the probability [141]

$$w(|\hat{A}|) = \int_0^{|\hat{A}|} d|A| D(|A|) \ , \tag{2.11}$$

to observe an amplitude less than $|\hat{A}|$. This quantity gives a more precise characterization of the $L_1$-transition than $\delta_D$, because it measures not only the extreme events corresponding to true defects, but also the tendency of the system to generate structures characterized by small $|A|_{min}$. We estimated the quantity (2.11) for several $|\hat{A}|$ values and for various $c_3$ parameter values in the defect chaos regime. Reporting $\ln[w(|\hat{A}|)]$ as a function of $1/(c_3 - \hat{c}_3)$ a reasonable linear scaling is observed in the range $0.795 \leq c_3 \leq 0.85$, for $0.1 \leq |\hat{A}| \leq 0.5$, with the choice $\hat{c}_3 = 0.72$. The value $\hat{c}_3$ where the defect density should asymptotically vanish is much smaller than $c_3^*$ obtained via direct numerical simulations but still bigger than $c_3^\infty = 0.704$ where $P_{SN} \to \infty$.

We can now easily estimate the integration time needed to observe a tiny shift of the apparent value $c_3^*$ towards the corresponding asymptotic value $c_3^\infty \approx 0.704$. Limiting our analysis to system size $L = 512$, a typical time-scale to observe a defect at $c_3 = 0.79$ is $t \sim 3 \times 10^7$. At this value of $c_3$, $P_{SN} = 46.5$, while for $c_3 = 0.739$, $P_{SN} = 105$ . Invoking the exponential decay of $D(p)$, one immediately finds that the time scale to observe a defect at $c_3 = 0.739$ is of order $10^{17}$, which is completely outside the reach of present day computers.

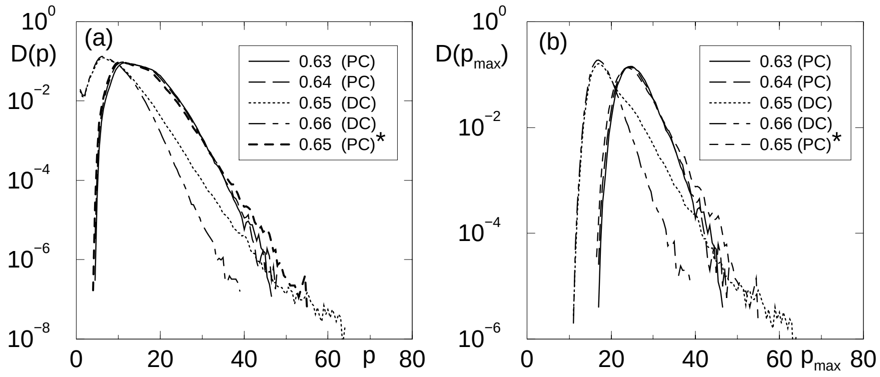

Fig. 2.15: Probability densities (a) $D(p)$ and (b) $D(p_{max})$ for $c_3 = 2$ and various values of $c_1$ reported in a lin-log scale. The data are for a system size $L = 512$ and for integration times ranging from $t = 5 \times 10^5$ for $c_1 = 0.63$,0.64,0.66 and 0.65 (PC)$^\star$ to $t = 2.5 \times 10^6$ for $c_1 = 0.65$ (DC). The labels DC and PC indicate that we are in presence or absence of defects, respectively. The label (PC)$^\star$ refers to the regime before defect formation at $c_1 = 0.65$.

### 2.3.3 $L_3$ transition

In order to characterize the $L_3$ transition from phase to defect chaos in more detail $c_3 = 2$ has been fixed, while the coefficient $c_1$ is varied. The $L_3$ transition is hysteretic [137, 138]: to the left of $L_3$ one may have phase or defect chaos depending on the initial conditions. Beyond the $L_3$ phase chaos breaks down and defects occur spontaneously for any initial condition. In order to study the dynamics across this transition we therefore initialized the simulations with initial conditions (2.6),(2.7) or used relaxed phase chaos configurations corresponding to values of $c_1$ far below the $L_3$ line.

The probability densities $D(p)$ and $D(p_{max})$ are shown in Fig. 2.15. For $c_1 < c_1^* = 0.65$ all distributions collapse on a unique curve, but as soon as defects arise the distributions change substantially. Whenever a defect is generated, hole-defect dynamics takes place (see Fig. 2.10b). As a result phase chaos is replaced by defect chaos. The noticeable modification of the distributions thus reflects the fact that the $L_3$ transition is discontinuous. Also the probability density for $|A|$ changes abruptly across the $L_3$ transition.

### 2.3.4 Mechanism for the selection of $p$

When approaching the transition to defect chaos from the Benjamin-Feir-Newell curve, three parameter regions, corresponding to different dynamical regimes, can be distinguished (Fig. 2.18). The first encountered region corresponds to infinite values of $P_{SN}$ : here we expect no defects to occur, irrespectively of system size and integration time. The phase chaos is the asymptotic regime in this first region. Then, when $c_1$ and/or $c_3$ are increased, a crossover regime is reached where extreme events (large inter-peak spacings) may lead to defect formation. Here phase chaos can persist as a long lived transient, but eventually we expect it to break down. Then, when $c_1$ and/or $c_3$ are even further increased, we experience a dramatic drop in transient times, and defect chaos sets in quite rapidly. We understand this drop to occur when typical values of $p$ (and not rare extreme events) become larger

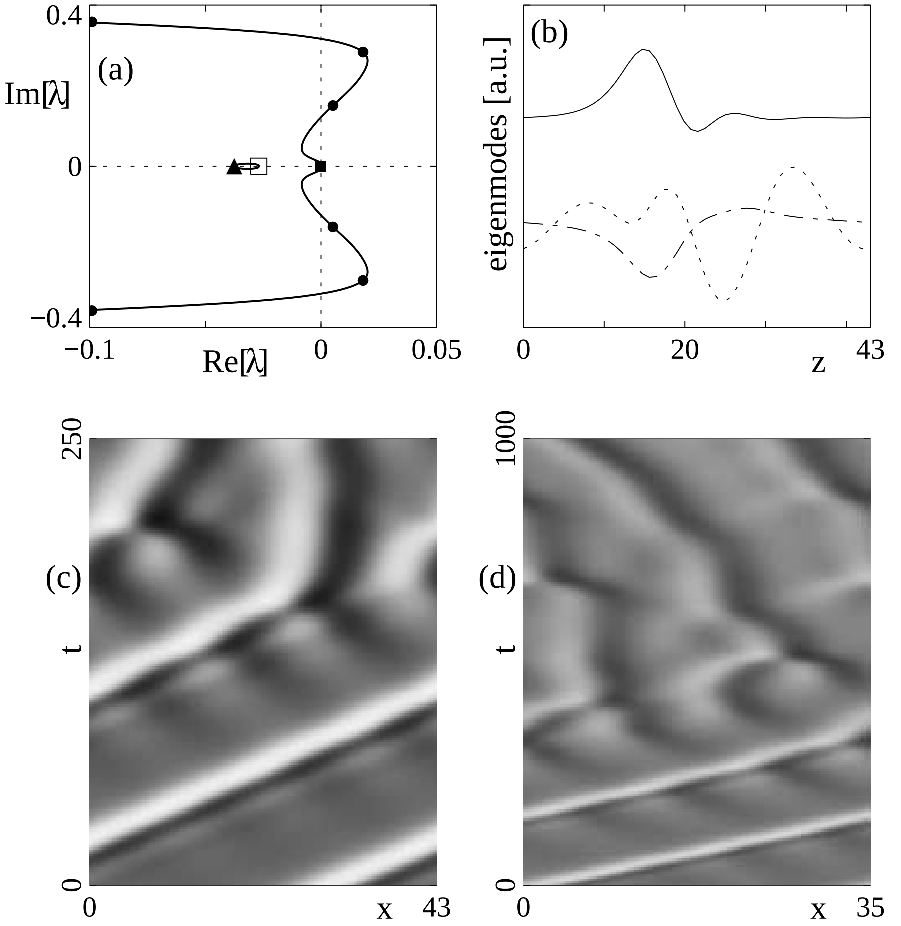

Fig. 2.16: Results of the linear stability analysis : (a) leading part of the eigenvalue spectrum (continuous spectrum denoted by the full curve, Goldstone modes by a filled square, saddle-node by filled triangle, interaction by open square and splitting modes in $L = P$ by dots, respectively), (b) splitting eigenmodes (dot-dashed and dotted, $\lambda_{split} = 0.018 \pm 0.28i$) of the phase in $L = P$ compared with spatial MAW profile of the phase gradient (full curve). (c,d) Space time plots showing the splitting of a MAW initially perturbed by small noise. Parameters are $c_1 = 3, c_3 = 0.72, P = 43$ near $L_1$ for (a-c) and $c_1 = 0.65, c_3 = 2, P = 35$ near $L_3$ for (d).

than the corresponding $P_{SN}$ values.

An approximate prediction for the location of the apparent phase to defect chaos transition (numerically obtained from the defect density) can be achieved in terms of a simple linear stability analysis of the MAWs (Figs. 2.16 and 2.17). See Appendix C for the method and more detailed results. A key element in our framework is the "typical large value" of $p$ as a function of coefficients $c_1$ and $c_3$; below we will identify two linear instabilities that act to either increase or decrease $p$, and their balance sets a scale for typical $p$ that will predict the location of the transition from phase to defect chaos rather well.

Due to translational and phase symmetries both MAW branches have neutral modes, *i.e.,* Goldstone modes. The eigenvalue associated with the saddle-node bifurcation is positive for MAWs of the upper branch and negative for the lower branch. In what follows the lower branch MAWs are considered exclusively.

*Splitting* - The spatial structure of a MAW of large period consists, roughly, of a homogeneous plane wave part and a local peak part. For the parameter regime we consider here, fully extended plane waves are linearly unstable, and so we may expect that the MAW spectrum will be dominated by this instability for sufficiently large values of $P$. Our linear stability analysis indeed shows that for appropriate parameters ($L = P$) and small enough $P$, all eigenvalues $\lambda_i < 0$, but when we increase $P$, MAWs become linearly unstable ($\lambda_{split} > 0$, Fig. 2.16). The shape of the unstable eigenmodes (Fig. 2.16b) suggests that this instability leads to the growth of a new peak in the homogeneous part of the MAW, and this is indeed the behavior observed in numerical simulations of the perturbed MAW (Fig. 2.16c,d). As a result two (or more) short MAWs with smaller $P$ will appear. We interpret this process as the *splitting* of a MAW in two or more smaller MAWs and we call the eigenmodes associated to such instability "splitting modes".

Clearly, this instability tends to reduce the peak-to-peak distances $p$ and prevents MAWs to cross the SN boundary; in the phase chaotic regime this instability *tends to inhibit defect generation.*

*Interaction* - By using a Bloch Ansatz [177, 178], we extended the stability analysis to systems with $n$ identical pulses ($L = nP$). For $n > 1$, an additional instability may appear [179] (see Fig. 2.17). Eigenvalues $\lambda_{int} > 0$ are found mainly for small $P$ (typically $P < 30$). The shape of the eigenmodes, *i.e.,* an alternating sequence of positive and negative translational Goldstone modes (Fig. 2.17b), suggests that the instability is due to the *interaction* between adjacent MAWs. This interaction shifts adjacent peaks into opposite directions, thereby creating occasional larger values of $p$ (Fig. 2.17c,d). In phase chaos this process leads to an increase of the spacing $p$ between some peaks, thus *enhancing the generation of defects.*

*Competition of Instabilities* - Both the splitting and interaction mechanisms are similar to instabilities observed in the Kuramoto-Sivashinsky equation [25, 29, 176]. We believe that phase chaos is governed by the competition of these two mechanisms that tend to increase or decrease the inter-peak spacings $p$. Almost independent of the coefficients the splitting instability dominates for MAWs with $P > 30$. This can explain why large inter-peak spacings $p > 30$ become rare as reported in Figs. 2.14,2.15.

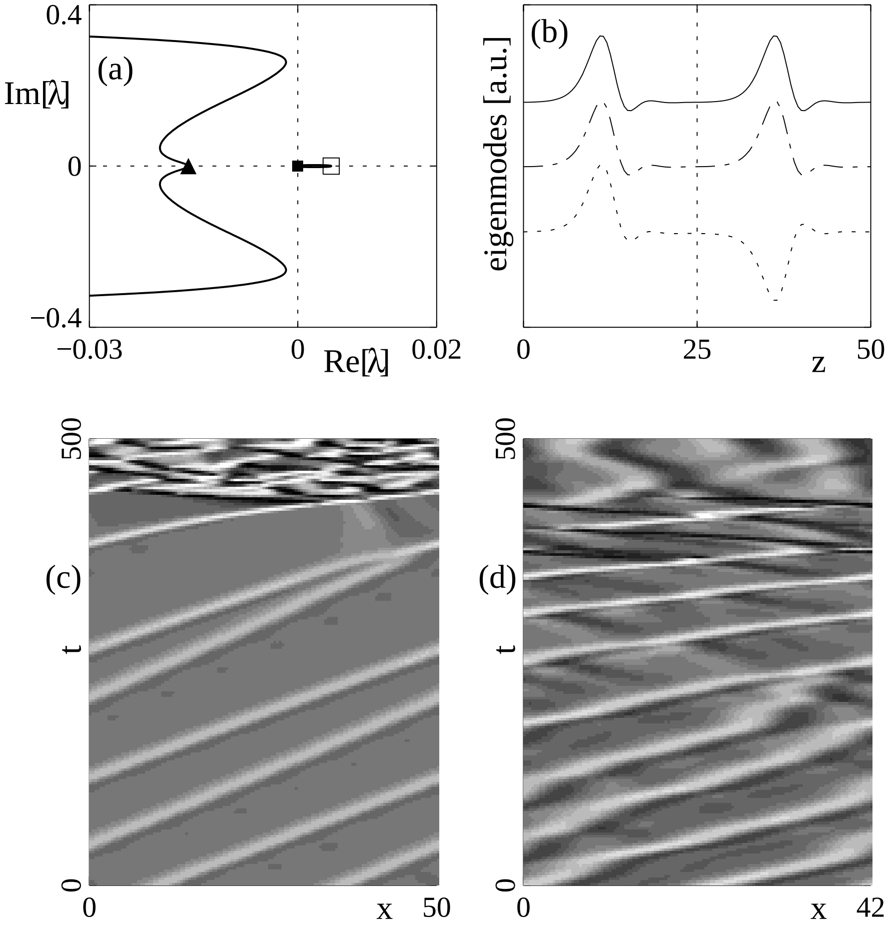

Fig. 2.17: Results of the linear stability analysis : (a) leading part of the eigenvalue spectrum (continuous spectrum denoted by the full curve, Goldstone modes by a filled square, saddle-node by filled triangle and interaction by open square at $\lambda_{int} = +0.0048$, respectively), (b) Goldstone mode (dot-dashed) and interaction eigenmode (dotted curve) for the phase compared with spatial MAW profile of the phase gradient (full curve) in $L = 2P$. (c,d) Space time plots showing the attraction of two periods of the same MAW initially perturbed by the interaction eigenmode. Parameters are $c_1 = 0.7, c_3 = 2, P = 25$ near $L_3$ for (a-c) and $c_1 = 3, c_3 = 0.85, P = 21$ near $L_1$ for (d).

We suggest a connection between the interchanging dominance of these two different instabilities and the sudden change of $\delta_D$ (near $L_1$) or the transient times before defect occurrence (near $L_3$). We calculated the linear stability spectra for a variety of coefficients and periods $P$ close to $P_{SN}$. From these we obtain a curve in coefficient space (Fig. 2.18) where the real parts of interaction and splitting eigenvalues are *equal*. For larger $c_1$ or $c_3$, $P_{SN}$ occurs in the range where interaction and defect formation dominate, while for smaller $c_1$ and $c_3$, splitting dominates and defect formation becomes rare.

As shown in Fig. 2.18, the curve where the two instabilities are equally strong near the saddle-node bifurcation gives a rather good estimate of where the apparent transition from phase to defect chaos occurs. Notice that in this "balance of instabilities" picture, there is no tunable parameter: once we have calculated $P_{SN}$ and the instabilities of the MAWs for a range of coefficients, a precise prediction for the "transition" from phase to defect chaos can be given.

## 2.4 Further refinements

In order to accurately test our results, we have measured for each of the 17 cuts and for several values of the coefficients across the $L_1$- or $L_3$-lines the amplitude distribution $D(|A|)$ and the phase gradient peak-to-peak spacing distribution $D(p)$. We conjectured that defects occur if and only if $p > P_{SN}$. Indeed, we observe that in 11 out of 17 points such conjecture is fulfilled. On the remaining 6 points the theoretical conjecture leads to an estimation of the transition lines within a maximal error bar of 3%. The points determined following the conjecture are indicated as empty circles in Fig. 2.1. The small deviations may have different reasons, that we summarize below:

*(i)* If fluctuations occurring during the phase chaotic dynamics are only moderate, such as happens near the $L_3$ transition line or for small system sizes, more complex coherent structures can survive for a short time. Here we analyzed only the shortest coherent structures characterized by a single hump. We believe that this is sufficient to understand the main aspects of the dynamics of large systems. However, longer combined MAWs with more than one hump emerge from periodic MAWs via period doubling bifurcations. The existence of the long combined MAWs is limited by saddle-node bifurcations analogously to single MAWs, but these bifurcations occur at slightly bigger values of the parameters $c_1$ and $c_3$. Therefore the appearance of these more complicated structures can delay defect formation even if one inter-peak spacing within the structure is bigger than $P_{SN}$ of the single MAW.

*(ii)* Near the $L_1$ line the dynamical fluctuations in the phase chaotic regime are stronger than in the proximity of the $L_3$ line. In this case and for sufficiently high values of the parameter $c_1$ we observed situations where not only the structure with the longest inter-peak spacing but also the neighboring structures were involved in the defect formation.

*(iii)* The assumption to consider MAWs with $\nu = 0$ is only an approximation. If the average phase gradient locally (on scales $P$) deviates from 0 then the saddle-node bifurcation slightly shifts towards smaller coefficients (see Chapter 3).

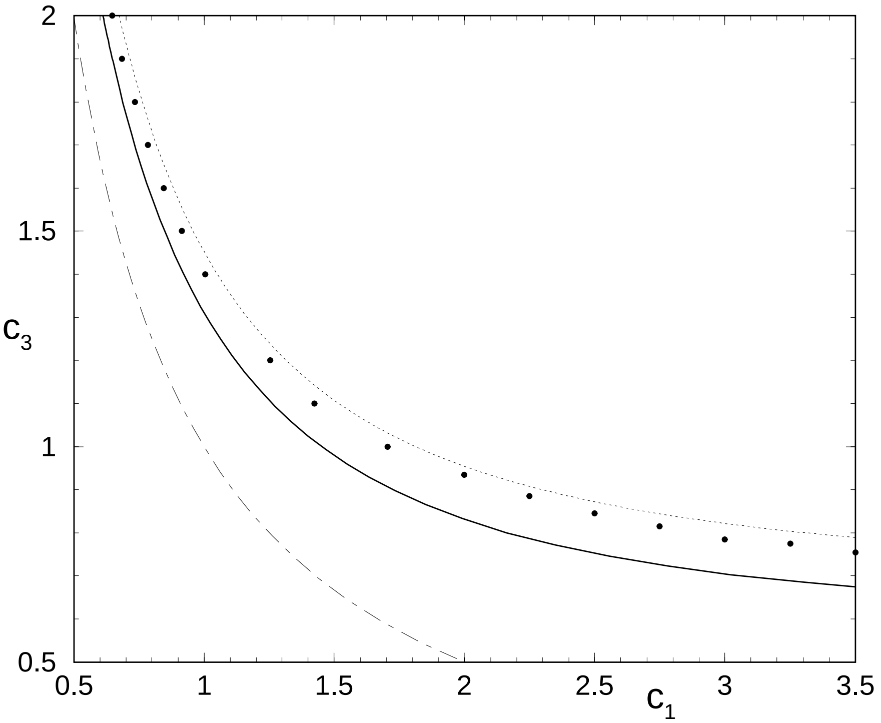

Fig. 2.18: Space of $(c_1, c_3)$-coefficients for the CGLE with the Benjamin-Feir-Newell curve (dot-dashed), the lower bound $P_{SN} \rightarrow \infty$ (full) and the stability-based estimate (dotted) for the transition from phase to defect chaos. The symbols refer to our numerical data for the appearance of defects.

As far as the (numerically) improved $L_3$ and $L_1$ lines are concerned, we observe that both these lines lie to the left of the ones determined in earlier numerical studies [138]. This is due to the fact that our simulations are of longer duration then those performed previously. This confirms the expectation that such transition lines will shift towards the Benjamin-Feir-Newell curve for increasing systemsize and integration times [135]. Moreover, some authors claim that indeed in the thermodynamic limit $L_1$ and $L_3$ will coincide with the Benjamin-Feir-Newell curve and the phase chaos regime will disappear [147]. On the basis of our simulations we cannot exclude such a possibility for higher space dimensions, but based on the results presented in this paper we conjecture that the saddle-node line for $P \rightarrow \infty$ provides a lower boundary for the transition from phase to defect chaos in the one-dimensional CGLE.

## 2.5 Discussion

The main points of this Chapter are summarized in the following and illustrated in Fig. 2.19. *(i)* Our investigation starts with the study of MAWs, which are uniformly propagating, spatially periodic solutions of the CGLE. These MAWs are parameterized by the average phase gradient $\nu$ and their spatial period $P$. Our study is confined to the case $\nu = 0$ for reasons specified below. Spatial profiles and the stable propagation of a particular MAW are presented in Fig. 2.19a-c. Isolated MAW structures consisting of just one spatial period

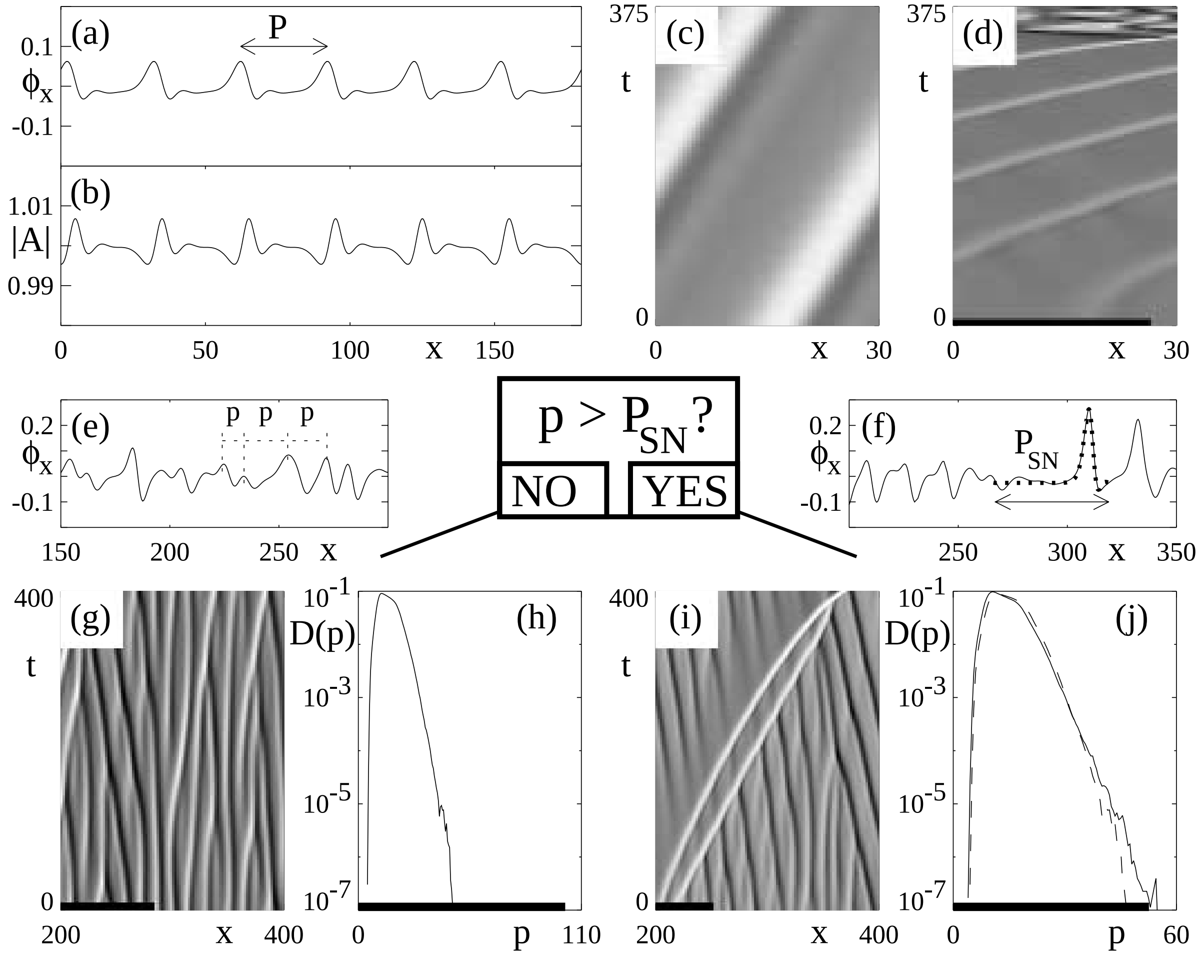

Fig. 2.19: Summary of our main results which constitute a picture for the formation of defects from phase chaotic states. (a,b) Example of a coherent structure: phase gradient and modulus of a period $P = 30$ MAW at $c_1 = 0.6, c_3 = 2$. (c) Space time plot showing the stable propagation of the MAW from (a,b) in a small system of size $P$ with periodic boundary conditions. Subsequent space time plots also show the phase gradient encoded in gray-scale (minima appear dark, maxima bright). (d) The same MAW as initial condition creates defects at $c_1 = 0.7, c_3 = 2$ where $P > P_{SN} = 26.8$. Black bars above the x-axis denote the size of $P_{SN}$ specific to the parameters of the panel. (e,g,h) Large scale chaos at $c_1 = 0.63, c_3 = 2, L = 512$. (e) Snapshot of the phase gradient profile with individual inter-peak spacings $p$. (g) Space time evolution of phase chaos and (h) distribution $D(p)$ showing $p \ll P_{SN}$ and no defects. A transient of $t \approx 10^4$ is not shown. (f,i,j) Large scale chaos at $c_1 = 0.65, c_3 = 2, L = 512$. (f) Snapshot of the phase gradient profile $t = 120$ before the first defect forms and the MAW (dotted, $P = P_{SN}$) overlayed onto the long structure. (i) Transient phase chaos with a fast and long structure traveling through the system which eventually nucleates defect chaos at $t = 400, x = 360$ (a transient of $t \approx 10^4$ is not shown). A snapshot of this structure was shown in (f). (j) The tail of the distribution of $p$ reaches $p > P_{SN}$ due to the long structure; this leads to the break down of phase chaos. The distribution $D(p)$ shown in (h) is also reported (dashed line). From the comparison of the two it is evident that the distributions do not modify dramatically when $c_1$ is increased, while $P_{SN}$ decreases noticeably.

$P$ play an important role in defect formation. In particular, for fixed CGLE coefficients the range of existence of coherent MAWs is limited by a saddle-node ($SN$) bifurcation which occurs when $P$ reaches a maximal period $P_{SN}$. *(ii)* If the MAWs are driven into conditions with $P > P_{SN}$ a dynamical instability occurs leading to the formation of defects (Fig. 2.19d). *(iii)* Slowly evolving structures reminiscent of MAWs ("near-MAWs") are observed in the phase chaotic regime (Fig. 2.19e,f). In order to characterize such states, we have examined the distribution $D(p)$ of spacings $p$ between neighboring peaks of the phase-gradient profile. In particular for sufficiently long spacing $p$, the observed phase chaos structures are often very similar to a single period of a coherent MAW (Fig. 2.19f). *(iv)* When a phase chaotic state displays spacings $p$ larger than $P_{SN}$, phase chaos breaks down and defects are formed (*e.g.* at $t = 400, x = 360$ in Fig. 2.19i). Thus, the MAW with $P = P_{SN}$ may be viewed as a "critical nucleus" for the creation of defects. In phase chaos defect formation is similar to the dynamical process by which isolated MAW structures generate defects (Fig. 2.19d). Therefore purely phase chaotic states are those for which $p$ remains bounded below $P_{SN}$ (Fig. 2.19g), while defect chaos can occur when $p$ becomes larger than $P_{SN}$ (Fig. 2.19i). *(v)* A more detailed study of the probability distribution of the $p$'s shows that for large $p$ the probability decays exponentially (Fig. 2.19h,j). As long as $P_{SN}$ has a finite value, we expect that, possibly after a very long transient time, defects will be generated. *(vi)* However, in a finite domain of the phase chaotic region, MAWs of arbitrarily large $P$ exist: we expect that in this region, even in the thermodynamic limit, phase chaos will persist. The region of persistent phase chaos is bounded by the Benjamin-Feir-Newell curve (thin dot-dashed) and the curve along which $P_{SN} \to \infty$ (full curve in Fig. 2.18).

In the phase chaotic regime of the 2d CGLE the correspondence between long inter-peak spacings (here diameter of cells) and the strength of the local modulation has already been noticed numerically [147]. Additional mechanisms present in 2d remain to be explored. Thereby it might turn out that phase chaos exists in the thermodynamic limit in 1d only but not in 2d as previously conjectured [147].

Altogether, our study leaves little space for doubt that the transition from phase chaos to defect chaos in the CGLE is governed by coherent structures and their bifurcations. From a general viewpoint, our analysis shows that there is no collective behavior that drives the transition. Instead, strictly local fluctuations drive local structures beyond their saddle-node bifurcation and create defects.

# 3 Fully Nonlinear Analysis of the Eckhaus Instability

## 3.1 Introduction

The Eckhaus instability of plane wave solutions has been introduced in Section 1.4.3. So far the analysis has considered infinitesimal perturbations and is therefore a linear stability analysis. In this Chapter arbitrarily large perturbations are included as the entire flow in phase space is analysed, thus the title "fully nonlinear analysis". This introductory Section gives an outlook and summarizes previous numerical observations [56, 57, 58, 59, 141, 142, 173] on phase chaos with $\nu \neq 0$.

In Section 3.2 the analysis of MAWs is extended to arbitrary average phase gradients of $A(x,t) = |A(x,t)| \mathrm{e}^{i\varphi(x,t)} \sim \mathrm{e}^{i(qx-\omega t)}$. Again the two parameter family of MAW solutions is parametrized by the spatial period $P$ of the modulation and the average phase gradient

$$\nu := \frac{1}{P} \int_0^P dx \varphi_x \ . \tag{3.1}$$

For plane wave solutions clearly $\nu$ equals the wavenumber $q$. In analogy, the phase gradient $\varphi_x$ is often called "local wavenumber".

It will be shown that MAWs in infinitely large systems are stable within certain parameter regions [1]. This is of special interest for experimentalists because in some recent experiments in quasi-one-dimensional geometries, supercritical Eckhaus instabilities of plane wave trains and the corresponding emergence of stable saturated MAWs have been observed [43, 55, 70, 187]. For a discussion of the experimental implications of MAWs see Chapter 4.

Fig. 3.1 shows a typical transient from an Eckhaus unstable plane wave to saturated modulations in the simulation. The average phase gradient $\nu$ selected by the initial plane wave is maintained over the whole simulation. The dynamics approaches a state where modulus and phase of the underlying plane wave are modulated by a traveling pulse train. The pulse-like modulations of the modulus $|A|(x,t)$ are visible in Fig. 3.1(a) and as wiggles on $\mathrm{Re}[A(x,t)]$ in Fig. 3.1(b). The wiggles move to the right with the same velocity $v$ as the pulses while the underlying wave,*i.e.* locations of constant phase, move to the left with the phase velocity $\omega/q$. This illustrates that the traveling modulations can be described as

---

[1] Note, in the limit case $\nu = 0$ stable MAWs only exist in short systems with $L = P$ and periodic boundary conditions.

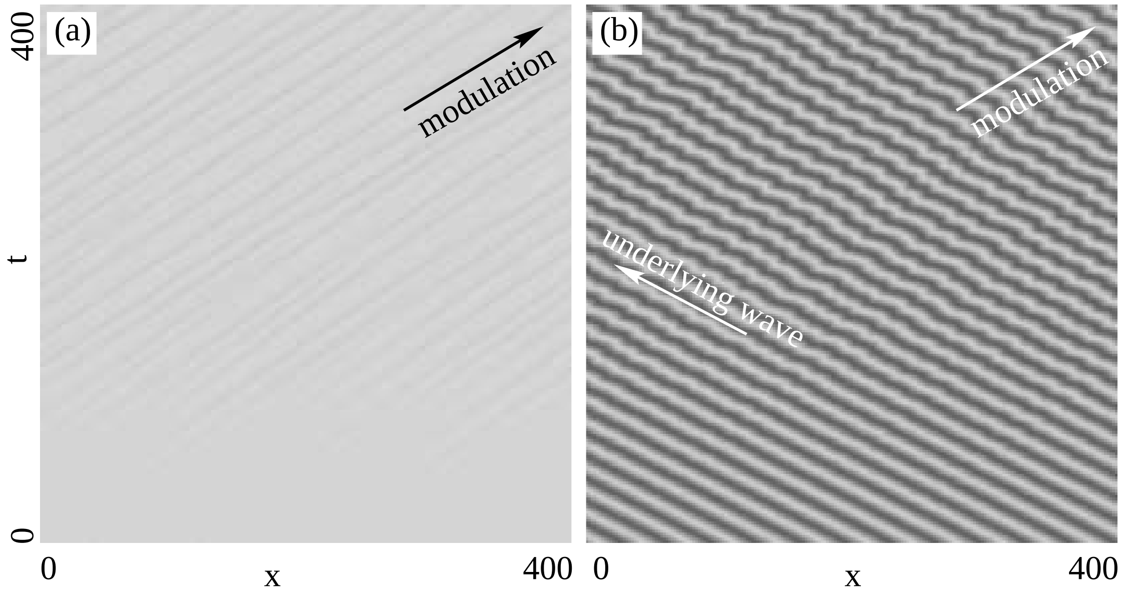

Fig. 3.1: Space-time plots of a numerical simulation were the Eckhaus instability saturates for $c_1 = 3.5, c_3 = 0.5$, initiated with noise added to a plane wave of $q = 0.184$. (a) The modulus $|A|$ (high=bright, low=dark) and (b) the real part $\mathrm{Re}[A]$ (positive=bright, negative=dark) are shown. Note the independent motion of the underlying wave (only in (b)) and the modulations.

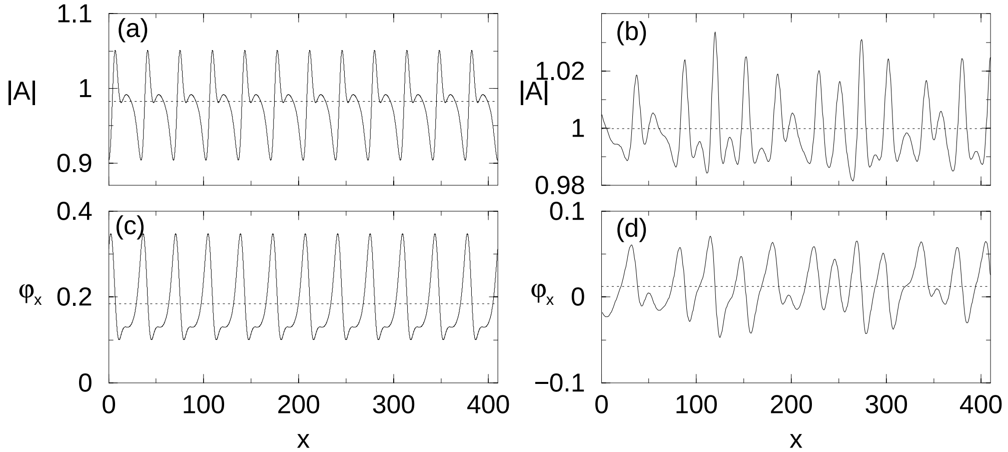

Fig. 3.2: Portraits of modulus $|A|$ and phase gradient $\varphi_x$ of solutions after long time integration. Dotted lines indicate the corresponding values for the initial plane wave. Solution (a),(c) has parameters as in Fig. 3.1 and is identified as periodic MAW. Solution (b),(d) is a snapshot and the state keeps changing as time goes on. It was initiated at $c_3 = 0.45$ with a perturbed plane wave of wavenumber $q = 0.0123$. Its trajectory has a positive Lyapunov exponent 0.00472 [180]. This is an example of wound-up phase chaos.

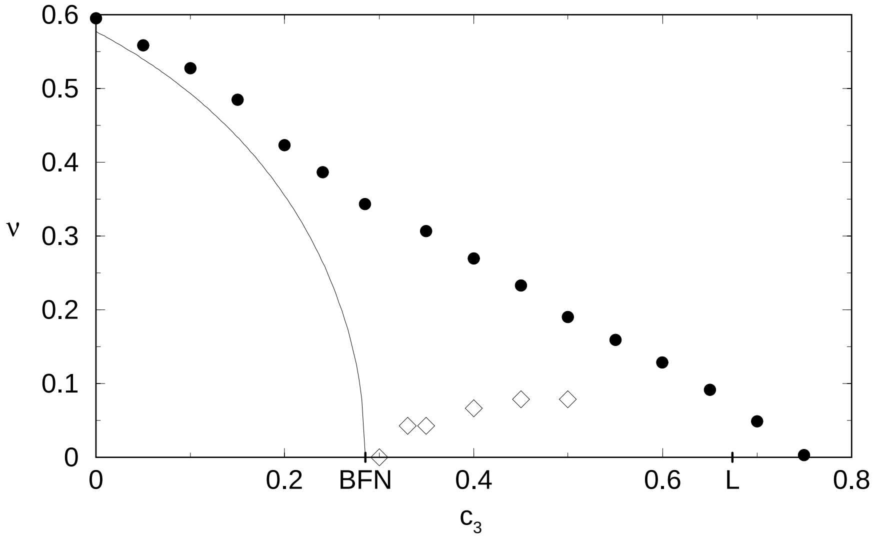

Fig. 3.3: Maximum (dots) conserved average phase gradient $\nu_M(c_3)$ for fixed $c_1 = 3.5$ obtained from numerical simulations ($L \sim 10^3, t \sim 10^5$) for 30 different initial conditions (noise added to plane wave with wavenumber $\nu$). Data is taken from Fig.1 in [58], Fig.3 in [141] and [180]. For $\nu \leq \nu_M$ no defects were present while above $\nu_M$ at least one initial condition caused defects. The full curve denotes the Eckhaus instability of plane waves with wavenumber $\nu$ and BFN at $c_3 = 1/c_1$ denotes the Benjamin-Feir instability for $\nu = 0$. For $\nu$ above the diamonds regular states were observed after transient phase chaos but below the diamonds most initial conditions led to persistent spatio-temporal chaos [58, 141]. L denotes the lower bound for defect chaos in the thermodynamic limit as obtained in Chapter 2.

coherent structures. In Fig. 3.2 the final state (a),(c) of the continued simulation is plotted in comparison to the snapshot of a chaotic state (b),(d) with $\nu = 0.0123$.

Some authors [59, 142] use the "winding number"

$$\tilde{\nu} := \frac{1}{2\pi} \int_0^L dx \varphi_x \tag{3.2}$$

instead of the average phase gradient $\nu$ to characterize phase chaos. The name "wound-up" phase chaos ($\tilde{\nu} \neq 0$) stems from the winding number $\tilde{\nu}$ which takes on integer values if periodic boundary conditions are applied to a system of size $L$.

For systems with periodic boundary conditions the average phase gradient of the whole system can only be changed, if a space-time defect occurs. In numerical simulations A. Torcini *et al.* [58, 141] and R. Montagne *et al.* [59, 142] observed persistent phase chaos with conserved $\nu \neq 0, \nu \leq \nu_M$ (no defects). The maximum conserved average phase gradient $\nu_M$ decreases as function of the coefficients $c_1, c_3$ (see Fig. 3.3) and vanishes above (and at) the transition from phase to defect chaos (compare Chapter 2). $\nu_M$ was therefore suggested [58] as an order parameter for this transition. In Section 3.3.2 lower and upper bounds for this limit $\nu_M(c_3)$ of wound-up phase chaos are derived from a stability analysis of the MAWs.

Above $\nu_M$ a transient with a finite number of defects reduces $\nu$ from the initial $\nu_i$ to a final $\nu_f < \nu_M$. The bigger $\nu_i$ the smaller $\nu_f$ will be (see Fig. 3.4). That a much smaller $\nu_f$

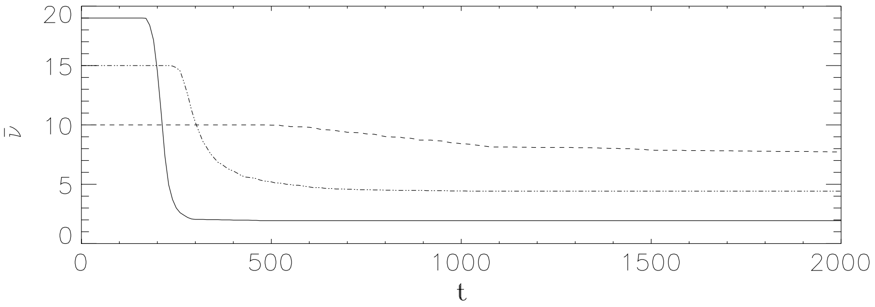

Fig. 3.4: Transient decrease $\tilde{\nu}(t) = 512 * \nu(t)/2\pi$ of the average phase gradient as observed by R. Montagne *et al.* [59] for $c_1 = 2.1, c_3 = 0.75, \tilde{\nu}_M = 9$. The larger $\tilde{\nu}_i = 10$ (dashed), 15 (dotted), 19 (solid) the smaller $\tilde{\nu}_f$.

results from the dynamics does not seem intuitive, since already $\nu \leq \nu_M$ is sufficient. In Section 3.3.1 this paradoxon will be solved.

For increasing $\nu$ at fixed coefficients the positive Lyapunov exponents of the wound-up phase chaos decrease (see Fig. 3.5). For $c_1 = 3.5, c_3 < 0.6$ and $\nu$ large enough the dynamics even become regular and a stable MAW extends over the whole system. The diamonds in Fig. 3.3 report this limit for fixed $c_1 = 3.5$. The stability analysis in Section 3.2.3 will clarify this observation.

The increased number of parameters $c_1, c_3, \nu, P$ calls for a restriction. Since a lot of numerical data are available for $c_1 = 3.5$ [135, 58, 141] we will restrict the detailed analysis to $c_1 = 3.5$ which shall be fixed throughout this Chapter. The results will be presented by projection of the $P$ direction onto the $c_3, \nu$ plane as well as in cuts through the space $c_3, \nu, P$ of free parameters. A rough investigation of the existence domains of MAWs revealed qualitatively the same results for fixed $c_1 = 0.4, c_1 = 1.2, c_1 = 2.1$ and $c_1 = 5$ as well as for fixed $c_3 = 0.83$ and varying $c_1$. Two of these choices were treated in [59, 142] and the limits of wound-up phase chaos agree well. One may also use a *similarity transformation* that maps coherent structures along curves $(c_1 + c_3)/(1 - c_1 c_3) = const$ in coefficient space [122]. By evaluating involved formulas (see [122]) for the transformed $\nu', P', \omega', v'$ the numerical data on the existence domains can be extended to other coefficients. The Section 3.4 will close the Chapter with a summary and discussion of the results on $\nu \neq 0$ phase chaos.

## 3.2 Stable modulated amplitude waves

### 3.2.1 Coherent structures approach

Following the analysis of the Eckhaus instability of plane waves in Section 1.4.3 we extend the ansatz (2.2) from Section 2.2.1 to

$$A(x,t) = a(z) \mathrm{e}^{i\tilde{\phi}(z)} \mathrm{e}^{i(qx - \tilde{\omega}t)} \tag{3.3}$$

and immediately rewrite it

$$A(x,t) = a(z) \mathrm{e}^{i\phi(z)} \mathrm{e}^{i\omega t} \ , \tag{3.4}$$

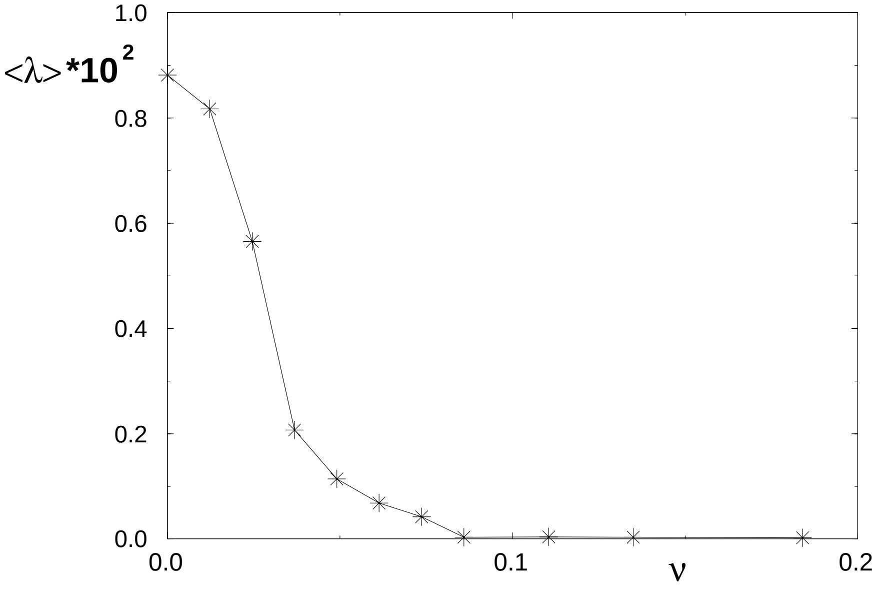

Fig. 3.5: Averaged maximum Lyapunov exponent $\langle\lambda\rangle$ in wound-up phase chaos as obtained by A. Torcini *et al.* [141]. Zero $\langle\lambda\rangle$ reveals nonchaotic solutions for $\nu$ large but below $\nu_M$. Parameters are $c_1 = 3.5, c_3 = 0.5$ and averages are performed over simulations with different realizations of noise added to a plane wave with wavenumber $q = \nu$ as initial condition.

where $a$ and $\phi$ are real-valued functions of $z := x - vt$ and $\phi(z) = \tilde{\phi}(z) + qz, \omega = qv - \tilde{\omega}$. Here $a$ and $\phi$ also represent coherent structures and the ansatz (3.4) is equal to the form (2.2).

Substitution of ansatz (3.4) into the CGLE (2.1) yields the same set of three coupled nonlinear ordinary differential equations (ODEs) as Eqs. (2.3). The continuation software AUTO97 [161] is used to compute the limit cycles of the ODEs (2.3) that correspond to spatially periodic functions $a(z), \phi(z)$. In order to choose a unique solution out of the continuous two-parameter family of limit cycles we fix the period of the limit cycle $L = P$ and its average phase gradient by $\int_0^L \psi dz = L * \nu$ with $\psi := \phi_z$.

The continuation procedure (see Appendix A) starts from an analytically known plane wave solution (1.17) and detects a Hopf (HB) bifurcation (filled square) where the mode with wave length $P$ destabilizes the plane wave. Continuing the emerging branch of MAWs the free parameters $\omega$ and $v$ are adjusted by the continuation algorithm. The continuation follows one unique branch by fixing $\nu = q$ and $L = P$. Fig. 3.6 shows examples of resulting bifurcation diagrams. $\omega(q)$ is an even and $v(q)$ an odd function of the wavenumber $q$ hence plane waves traveling to the left and right are both described by the same Eqs.(2.3) with $x \rightarrow -x$ and $q, v, z, b, \psi$ flip sign. Therefore it is sufficient to consider positive wavenumbers $q$.

### 3.2.2 Existence limits of MAWs

Upon increasing $c_3$ the modulations grow and develop a localized depression $|A|_{min}$ where $\phi_x$ has a maximum (see Fig. 3.7). As for $\nu = 0$ these MAWs are called the *lower* branch

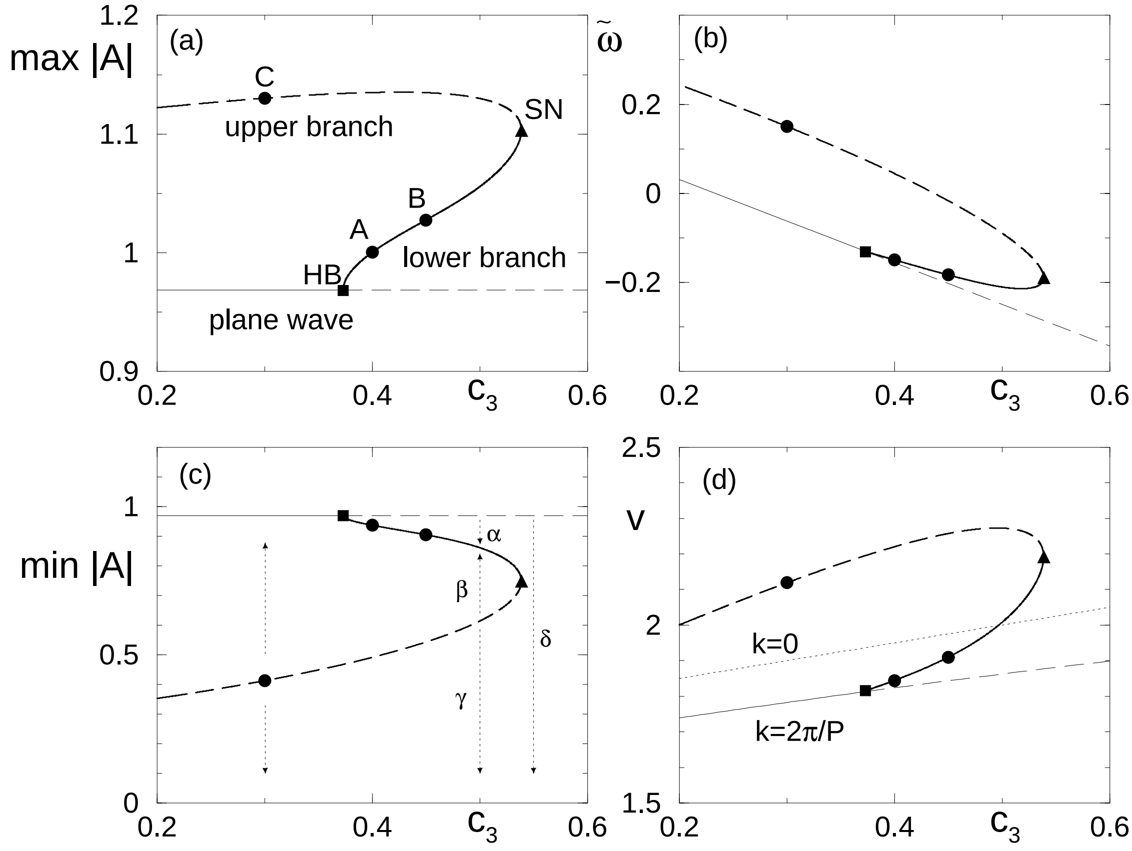

Fig. 3.6: Examples of bifurcation diagrams for MAWs with $\nu = 0.25, c_1 = 3.5, P = 25$. (a) Maximum of the modulus, (b) oscillation frequency $\tilde{\omega} = qv - \omega$, (c) minimum of $|A|$ and (d) velocity $v$ versus $c_3$. The plane wave that is stable (unstable) against models of wavelength $P$ is represented by the thin full (dashed) line. The stable lower branch (unstable upper branch) of MAWs is denoted by the thick full (dashed) curve. HB denotes the Hopf bifurcation (square) of the plane wave solution while SN stands for the saddle-node bifurcation (triangle) that limits the existence of MAWs. In (c) arrows represent the typical evolution of initial profiles with a respective minimum of $|A|$, greek letters refer to simulations in Fig. 3.16. In (d) the dotted line denotes the group velocity ($k = 0$) and the line below gives the velocity of the mode with wavelength $P$. A, B and C mark parameter values where solutions are plotted in Fig. 3.7.

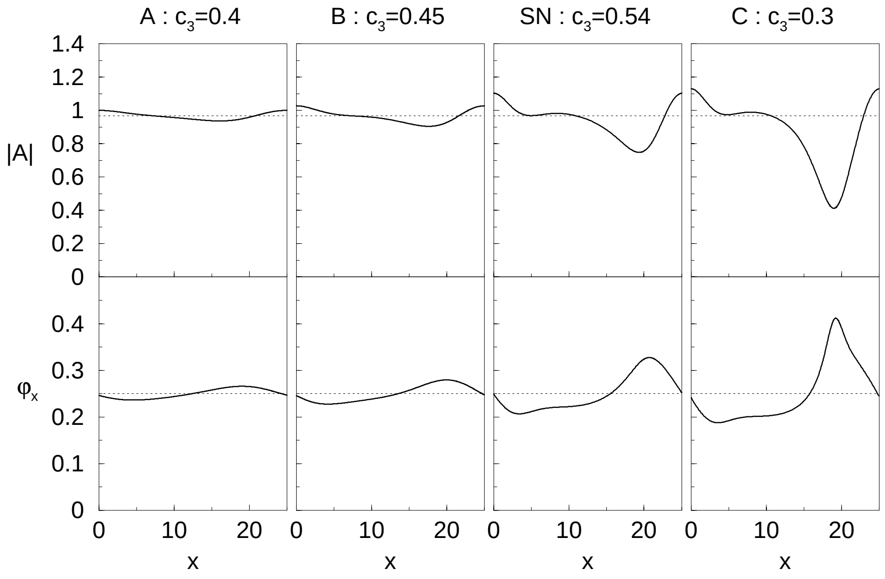

Fig. 3.7: Modulus and phase gradient for examples of MAW solutions. Parameters correspond to indicated points in Fig. 3.6. Dotted lines show the curves for the unstable plane wave with $A = \sqrt{1-q^2}$ and $\phi_x = q = 0.25$.

in contrast to the coexisting *upper* branch MAWs. Examples of these lower branch MAWs were obtained by numerical simulations earlier [56, 57, 58, 59, 141, 142] and were studied in detail by G. Hager [173]. Numerical simulations could neither uncover unstable upper branch MAWs nor elucidate the existence limit of MAWs. The bifurcation analysis presented here reveals : both branches (upper and lower) meet and terminate in a saddle-node (SN) bifurcation (filled triangle). Due to the SN bifurcation the upper branch MAWs always have at least one unstable eigenmode and we will not consider them in the following. The upper branch continues to negative $c_3$ and there connects to another instability of the plane wave with identical $\nu, P$ (see also Fig. 3.8).

For large $\nu$ and small $P$ the Hopf bifurcation is no longer supercritical and the unstable upper branch emerges directly from the plane wave. This is in agreement with analytical predictions [56]. Fig. 3.8 shows an example which also includes the second HB at negative $c_3$. For $\nu = 0$ the MAWs emerge stationary and acquire $v \neq 0$ above a subsequent drift pitchfork bifurcation (compare Chapter 2). In the present case $\nu \neq 0$ the plane wave already breaks the reflection symmetry, the initial MAW has a nonzero velocity and the drift pitchfork (DP) bifurcation (filled diamond) is unfolded. See Fig. 3.9 for an example at fixed $c_3 = 2$ . The branch emerging at the HB corresponds to the MAWs discussed above. The second branch emerges at the period doubling bifurcation of MAWs with half the period. It always has unstable manifolds that lead the dynamics away from it to the coexisting MAWs of shorter period. Therefore this branch plays no essential role and is not treated further.

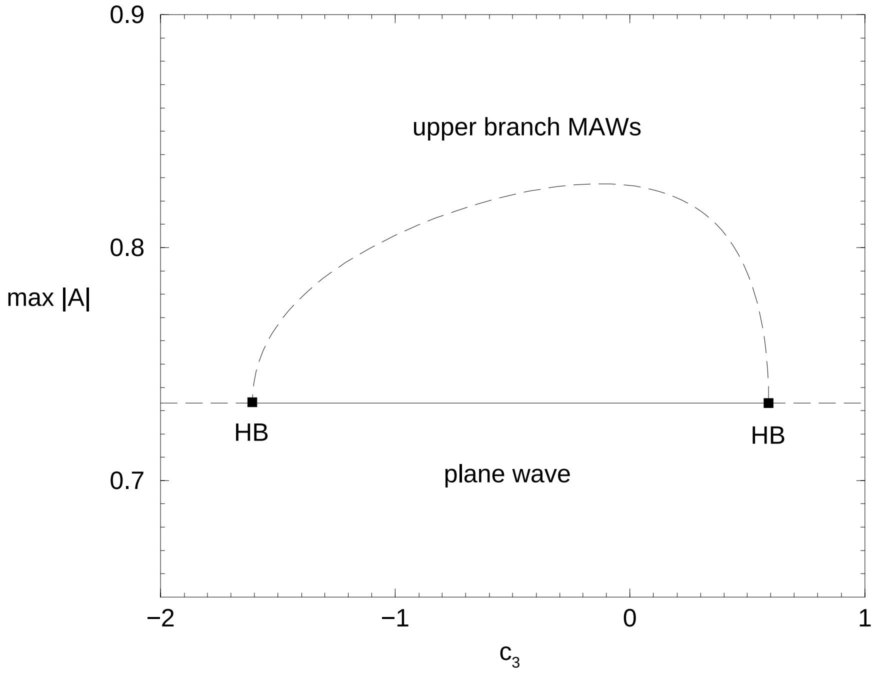

Fig. 3.8: Bifurcation diagram with exclusively upper branch MAWs for $\nu = 0.68, P = 2\pi/\nu \approx 9.24$. The solid line indicates stable and the dashed curves unstable solutions. The Hopf bifurcations are both subcritical.

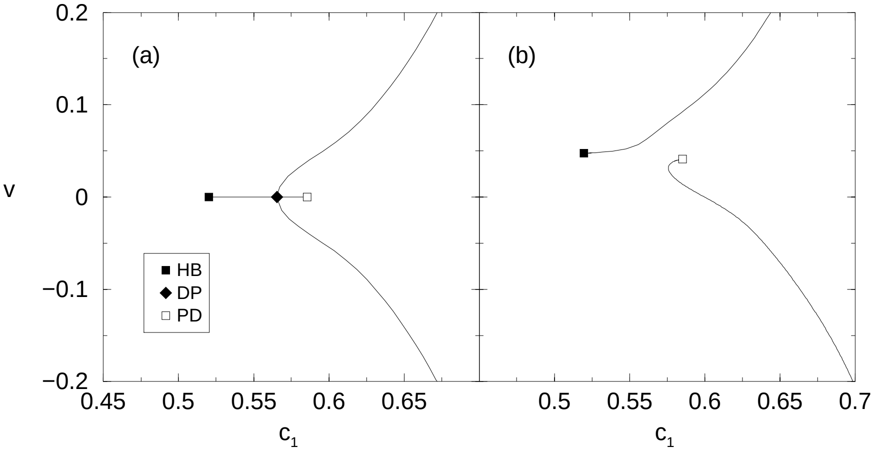

Fig. 3.9: Bifurcation diagrams showing the velocity $v$ versus $c_1$. (a) Branches with $v \neq 0$ emerge at the drift pitchfork bifurcation for $c_3 = 2, P = 25, \nu = 0$. (b) The bifurcation is unfolded for $\nu \neq 0$, here $c_3 = 2, P = 25, \nu = 0.01$. A symmetric pair of branches exists for $\nu \to -\nu$ and $v \to -v$.

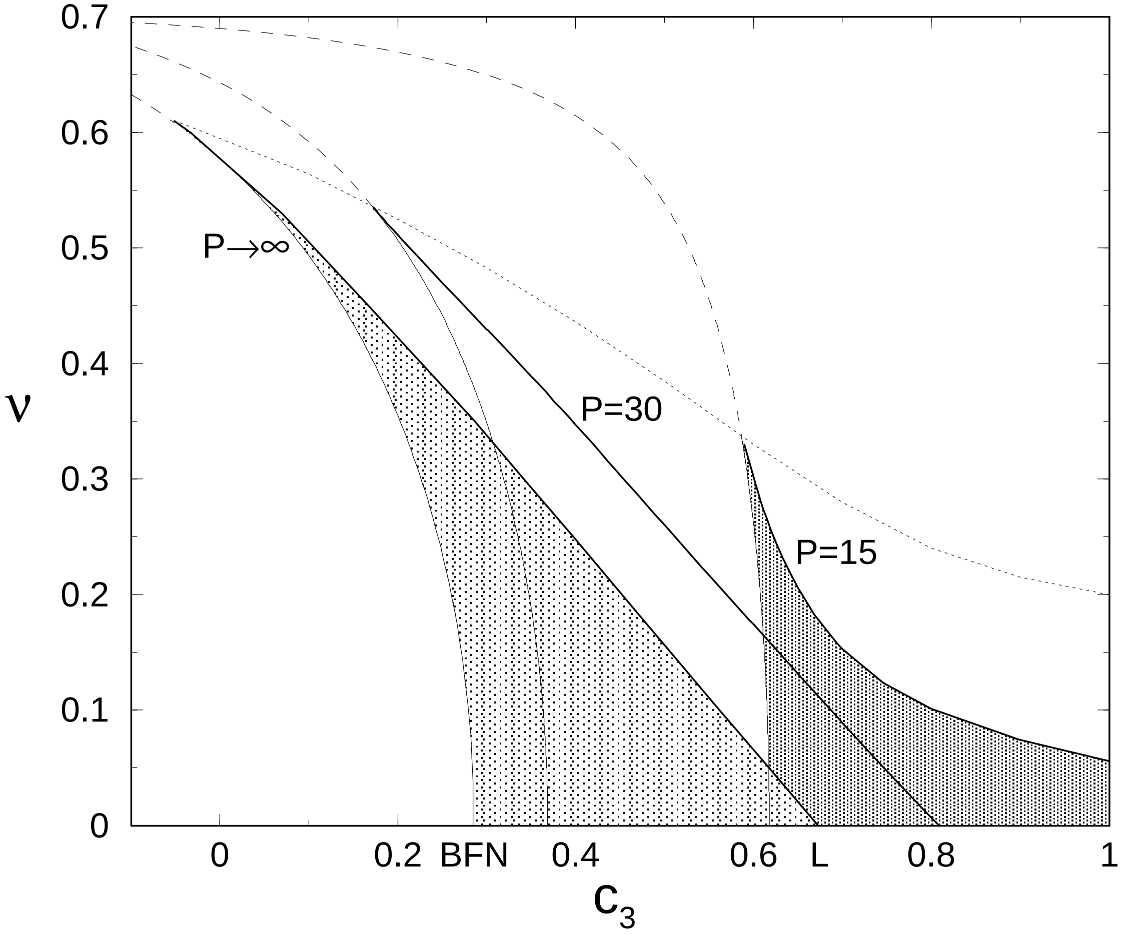

Fig. 3.10: Existence domains of MAWs with period $P$ projected onto the $(c_3, \nu)$ parameter plane. Thin curves denote the Eckhaus instability and HB which occur supercritical (full curve) or subcritical (dashed) depending on $\nu$ and $P$. The thick curves give the SN. Hence lower branch MAWs exist below the dotted curve. Three examples for $P = 15$ (right, dark shaded domain), $P = 30$ (middle, empty), $P \to \infty$ (left, light shaded) are shown.

### Infinite system size

We analysed the existence of lower branch MAWs in the entire parameter space $(c_3, \nu, P)$ with fixed $c_1 = 3.5$. The system size is assumed infinitely large in order to allow for arbitrary periods $P$ of MAWs. Fig. 3.10 shows examples of existence domains for $P = 15, P = 30$ and $P \to \infty$. We find that both HB and SN shift to larger $c_3$ as the period $P$ is decreased. The same was already observed in the limit case $\nu = 0$.

### Finite system size

Experimental setups and numerical simulations are restricted to finite system size $L$ but often use periodic boundary conditions (annulus) in order to study bulk effects of extended systems and to minimize boundary effects. The periodic boundary conditions also restrict possible modes of perturbations [2]. As described by Eq. (1.21) the instability threshold of plane wave solutions depends on the wavelength $2\pi/k$ of the perturbation. Since in the studied range of coefficients the Eckhaus instability is a long-wavelength instability the plane waves will be stabilized by the finite size of the system. The instability threshold is shifted to larger values of the coefficients $c_1, c_3$ and can be computed from Eqs. (1.21,1.22) with $k = 2\pi/L$.

Clearly the selection of perturbations by periodic boundary conditions also restricts the possible MAWs. Their average phase gradient $\nu$ and the period $P$ of periodic MAWs have to be consistent with the system size and this renders discrete the two-parameter family of MAWs. A subset of the solutions shown in Fig. 3.10 can be observed. For existence domains of MAWs in systems with intermediate size ($L = 1 \ldots 20 * 2\pi/\nu$) see Appendix D.

Here we focus on the extreme case. The shortest system with periodic boundary conditions only contains one wavelength of the plane wave hence $L = 2\pi/\nu$. A. Torcini studied this case by numerical simulations ($\nu_U$ in Fig.1 of [58]) and started from a set of initial conditions (different realizations of noise added to a plane wave). The quantity $\nu_U$ denotes the largest $\nu$ for which none of the initial conditions produced a defect in analogy to $\nu_M$ for large systems. In the following these data (symbols in Fig. 3.11) are compared to the existence domain of MAWs.

Whithin the light shaded area in Fig. 3.11 plane wave solutions with wavenumber $\nu$ are stable in the short system. The stability area extends over the phase chaos and into the defect chaos region. This effect is important for experiments where based upon the observation of stable plane waves one can not necessarily infer coefficients $c_1, c_3$ in the Benjamin-Feir stable regime. The dashed line denotes a subcritical instability and only unstable upper branch MAWs exist to the left of this curve. For smaller $\nu$ the instability again turns supercritical and stable lower branch MAWs exist above the instability inside the dark shaded region. The thick full curve gives the SN bifurcation for MAWs with $P = L$. The thin curves show the respective limits of periodic MAWs with shorter period. Defects are expected beyond the SN and the subcritical instability which exactly reproduces the data from earlier simulations (Fig.1 of [58]) except at small $\nu$. A. Torcini reported [180] that simulations with $\nu \leq \nu_U$ resulted in modulations with a single hump (squares) or with two (triangles) or three (stars) humps of different size. The latter two are observed above the SN of MAWs with $P = L$. Here the initial condition may fall into the basins of attraction of MAWs with shorter period which only exist at small $\nu$. In the next Section the appearence of MAWs with many humps of different size ("aperiodic MAWs") will be studied which accounts for the observed states denoted by triangles and stars in Fig. 3.11.

### 3.2.3 Tertiary instabilities

Next we consider larger systems of size $L = n * P$. MAWs with $n$ subsequent periods $P$ attached to each other are trivial extensions of the results before. We call these *periodic* MAWs. However, the effective interaction between adjacent periods is attractive in certain

---

[2] The wavelength of perturbations is an integer fraction of the system size.

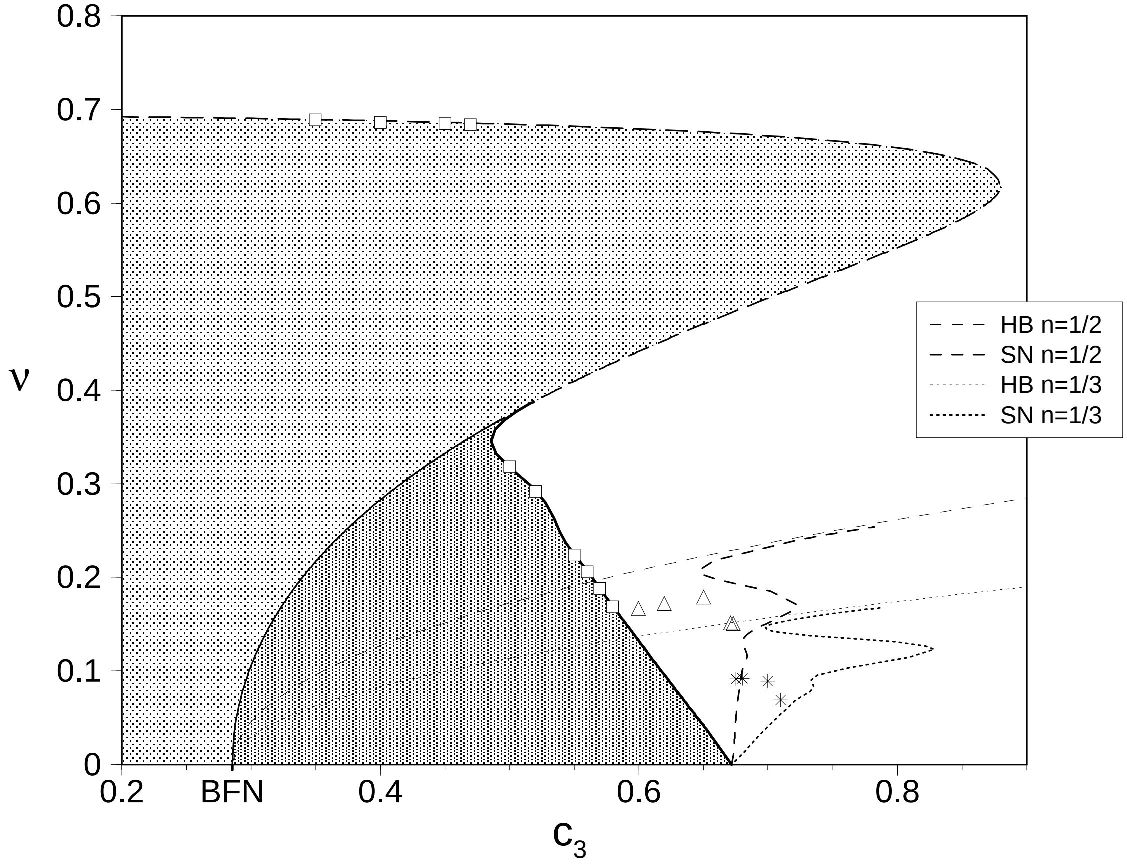

Fig. 3.11: For short system size $L = 2\pi/\nu$ plane waves are stable for parameter choices inside the light shaded area. MAWs with a single hump ($P = L$) exist inside the dark shaded area bounded by the supercritical HB to the left an the SN to the right. Thin curves give the limits of periodic MAWs with two humps $P = L/2$ (dashed) and three humps $P = L/3$ (dotted). See the legend for the different cases. Symbols denote maximal $\nu = \nu_U$ that did not create defects but resulted in stable asymptotic states in simulations of the short system. Plane waves and single MAWs (squares), aperiodic MAWs with 2 humps (triangles) and aperiodic MAWs with 3 humps (stars) have been observed. Data are taken from Fig.1 in [58] and [180].

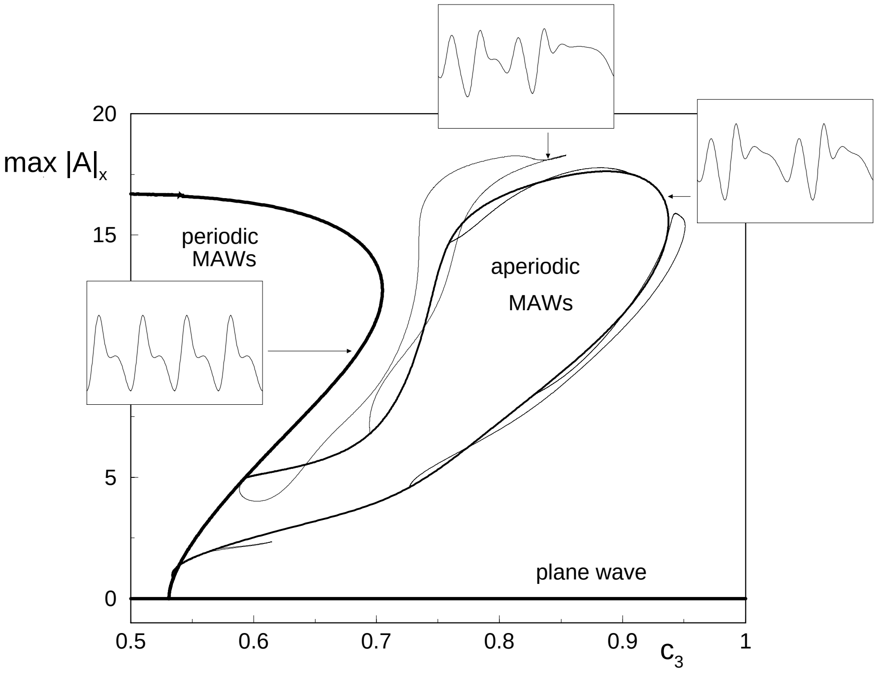

Fig. 3.12: Bifurcation diagram for $\nu = 0.184, P = 17$ and $L = 4 * P$ hence 4 pulse-like modulations interact. The maximum of the amplitude gradient is plotted since the interaction causes pulse shifts and the amplitude of single humps changes little. Thicker lines correspond to smaller overall period of the modulation. The insets show typical solutions.

parameter regions (see Figs. 3.14 and 3.15). This causes period doubling (PD) bifurcations (open squares) at the transitions from repulsive to attractive interaction. Note, this corresponds to a tertiary instability in the original system. There new branches of *aperiodic* MAWs emerge from the primary branch of periodic MAWs. M. Or-Guil *et al.* observed a similar scenario caused by the interaction of pulses in an excitable reaction-diffusion system [179]. The new solutions do not show equidistant modulations. Instead one puls gains more space and the other ones are compressed. The new branches extend to larger $c_3$ than the corresponding periodic MAWs. Fig. 3.12 shows how these branches arrange in a system with 4 interacting pulses ($L = 4 * P$). As long as the PD bifurcations are supercritical, then the aperiodic MAWs are stable again. They represent the saturated solution for attractive interaction between subsequent modulations. For large systems a whole sequence of period doublings will lead to aperiodic MAWs with an overall period of the system size. Hence they may represent an erratic spatial sequence of humps and depressions. This spatial sequence propagates coherently as a whole structure. We named these patterns aperiodic MAWs to emphasize the connection among both types of coherent structures. Examples were already observed in numerical simulations. R. Montagne *et al.* [59, 142] call them “frozen phase turbulence” while A. Torcini *et al.* [58, 141] use the term “type $\beta$”.

The observed coexistence of a large number of stable aperiodic MAWs results in a strong dependence of the final state in a numerical simulation on the initial conditions. Although each regular final configuration must be consistent with a particular periodic or aperiodic

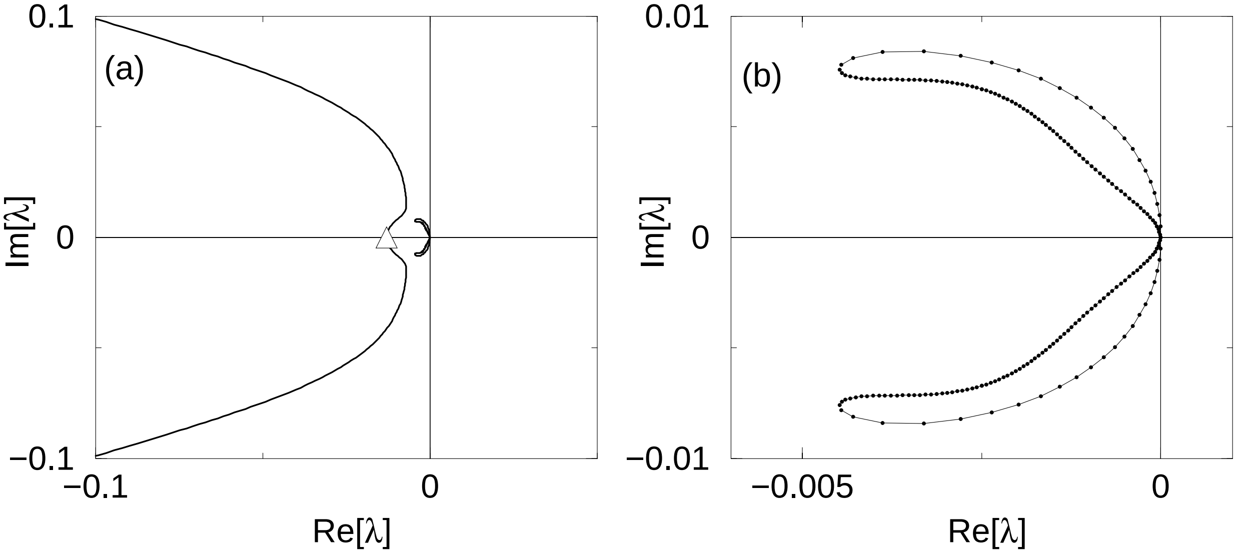

Fig. 3.13: (a) Leading part of the eigenvalue spectrum with the SN eigenvalue at $\lambda_{SN} = -0.013$ denoted by the triangle. (b) Blow-up of the spectrum close to the Goldstone modes. The corresponding eigenmodes represent different combinations of pulse shifts that all relax back to the periodic MAW. Parameters are $c_3 = 0.4, \nu = 0.184, P = 2\pi/\nu$. The dots in (b) correspond to system size $L = 100 * P = 3415$.

MAW it is difficult to reproduce averages over results obtained from different initial conditions. The averages are convenient for a rough study of typical behavior by numerical simulations and these numerical observations reported in Fig. 3.11 are only partially reproduced by the present analysis.

A linear stability analysis (see Appendix C) reveals that within certain parameter domains periodic MAWs are stable even in the infinite system. Fig. 3.13 shows the eigenvalue spectrum of an example. From Fig. 3.13b we conclude that for this example the entire spectrum in the infinite system will be confined to the negative half-plane. [3] As in the limit case $\nu = 0$ also for $\nu \neq 0$ MAWs of large $P$ are unstable to delocalized eigenmodes that create more humps on the plateau of the unstable MAW. This splitting reduces the periods of MAWs.

Figs. 3.14 and 3.15 represent cuts through the parameter space at fixed $\nu = 0.25$ and $c_3 = 0.5$, respectively. They show the typical arrangement of stable and unstable parameter regions of MAWs. Other examined cuts for $c_3 = 0.1, 0.2, 0.3, 0.4, 0.6, 0.7$ qualitatively show the same order.

The cut through parameter space $c_3, \nu, P$ at $\nu = 0.25$ is shown in Fig. 3.14. The HB (dashed) approaches the Eckhaus instability for $P \to \infty$ as the lower bound of the existence domain. From above the domain is limited by the SN (solid curve). For small $P$ (large $c_3$) the HB is subcritical and no MAWs exist. In the infinite system $L \to \infty$ MAWs are found to be linearly stable for a broad range of parameters (dark shaded area). At low $P$ the interaction instability occurs (white area) [4] whereas at large $P$ the long plateau

---

[3] Further increasing system size provides additional eigenvalues that fill the gaps of the existing set.

[4] Attraction is monotonic (white tongues) between pairs of PD bifurcations and oscillatory (temporary

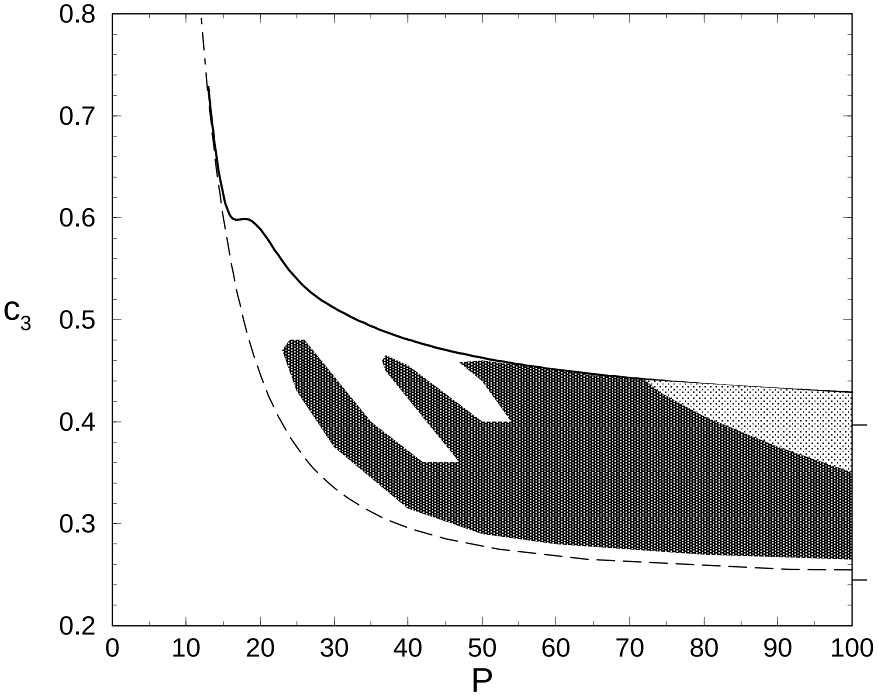

Fig. 3.14: Stability domain (dark area) of periodic MAWs for $\nu = 0.25, L \to \infty$. MAWs exist between supercritical HB (dashed) and SN (full curve). The tickmarks at the right frame give the asymptotic values for $P \to \infty$. The dot-dashed curve denotes the subcritical HB. MAWs are unstable to splitting within the light shaded domain at large $P$. Within the white domain at small $P$ periodic MAWs are unstable to interaction and aperiodic MAWs coexist.

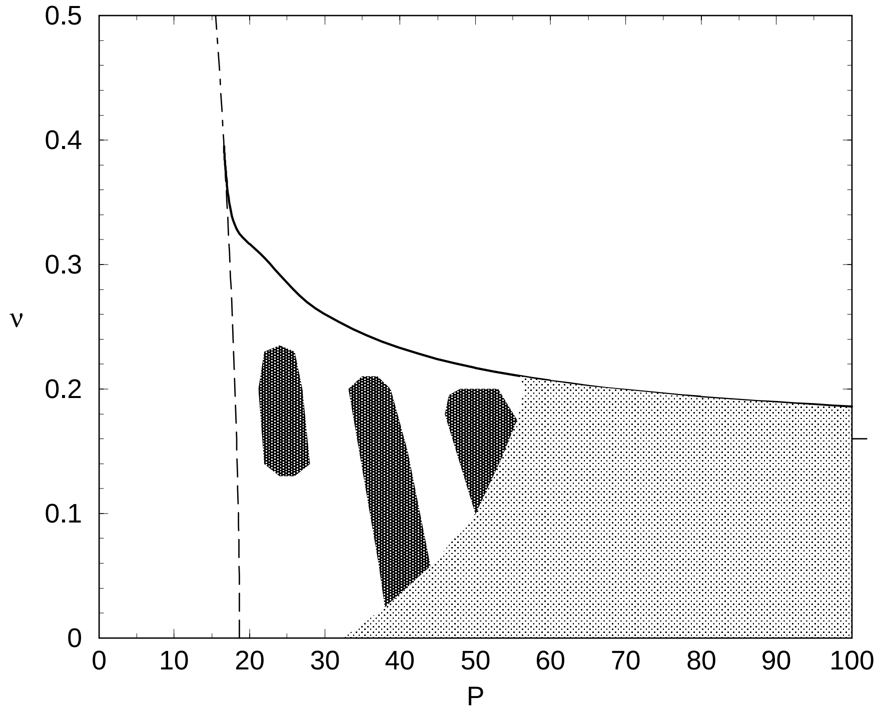

Fig. 3.15: Stability domains (dark areas) of periodic MAWs for $c_3 = 0.5, L \to \infty$. Curves and instability domains (splitting=light shaded, interaction=white) have the same meaning as in Fig. 3.14.

of the MAW is unstable to splitting (light shaded area). Typical initial conditions will evolve to stable MAWs since spatial intervals of $A(x, t_0)$ that initially contain many closely spaced perturbations will locally increase $P$ while long unperturbed intervals will gain new modulations. These instabilities are well separated and after a transient the numerical simulation will show nonchaotic behavior.

A cut perpendicular to the previous one is shown in Fig. 3.15. Curves and shadings have the same meaning as discussed above. Starting from random initial conditions at $\nu > 0.1$ the two instabilities may again (after a long chaotic transient) lead to a stable MAW with local periods $P$ inside the stable windows. At lower $\nu < 0.1$ the probability of approaching a stable configuration dramatically decreases since only a third of the previous stable $P$ intervals remains. Below $\nu = 0.02$ no stable state can be prepared at all. Instead one observes wound-up phase chaos with increasing maximum Lyapunov exponent (Fig. 3.5). As in the limit case $\nu = 0$ (phase chaos) the dynamics is driven by the subsequent increase of spatial periods (interaction) and annihilation of localized modulations together with the splitting of long periods that produces new closely spaced modulations. This dynamical process is the stronger the more dominant the instabilities are. For decreasing $\nu$ the splitting instability extends to shorter periods $P$ and significantly overlaps with the domain of the interaction instability. Based on this consideration the observed large maximum Lyapunov exponents below $\nu = 0.03$ correspond to the dominance of the instabilities at low $\nu$ and

---

subsequent attraction/repulsion) between tertiary HB in the remaining intervals.

the smaller maximum Lyapunov exponents for $0.03 < \nu < 0.09$ to the small probability of approaching the single stable domain. At $\nu > 0.09$ almost every simulation approaches a stable MAW. A more quantitative characterization of the simulations is needed to test the above conjecture.

## 3.3 Defect formation in wound-up phase chaos

In this Section the formation of defects and the resulting change of the average phase gradient are presented. For $\nu \neq 0$ Subsection 3.3.1 will confirm the scenario of defect formation past the saddle-node bifurcation of the relevant MAW as discovered in the case of $\nu = 0$ (compare Chapter 2). Also earlier observations from numerical simulations (compare Fig. 3.4),*e.g.* the dependence of $\nu_f$ on $\nu_i$, can be interpreted. The Subsection 3.3.2 is then devoted to the limit $\nu_M$ of wound-up phase chaos. For a certain range of parameters the limit $\nu_M$ is reproduced by means of the stability properties of MAWs at the saddle-node bifurcation. Beyond this parameter range,*i.e.* at low $\nu$ close to the transition to defect chaos, one is left with a similar situation as in the case $\nu = 0$ and again has to consider the competition between two tertiary instabilities.

### 3.3.1 Beyond the saddle-node bifurcation

The role of the SN bifurcation for the dynamics has been studied in Section 2.2.3 for the limit case $\nu = 0$. For $\nu \neq 0$ we find the same behavior. Fig. 3.16 gives examples for $\nu = 0.25, P = 2\pi/\nu$ that correspond to the arrows in the bifurcation diagram Fig. 3.6c. Arbitrary small perturbations to a plane wave lead to defects only beyond the SN whereas below the SN such perturbations have to be very large to overcome the saddle-type upper branch MAW. Since for parameters below the SN of $P \to \infty$ there are no SN we again conclude : from typical initial conditions (noise added to a plane wave) defects may only form above the SN of $P \to \infty$. The SN of $P \to \infty$ is again a lower bound for defect formation.

For large systems the formation of defects depends on the local period of initial perturbations in the same way as for $\nu = 0$ (compare Chapter 2). For larger values of $\nu$ or $c_3$ the SN occurs for smaller $P$ as shown in Figs. 3.14,3.15. Therefore local periods $p$ beyond the SN and subsequent defect formation are more probable at larger $\nu, c_3$.

In contrast to the case $\nu = 0$ there is only a short transient of phase chaos in the simulations with nonzero initial $\nu_i > \nu_M$ (see Fig. 3.4). The distribution of local periods $p$ of the perturbations is determined by the realization of the noise in the initial condition. For local periods above but close to the SN (as in Fig. 3.16$\delta$) the perturbation increases to a modulation similar to MAWs and remains almost saturated for some transient time. [5] This transient of defect formation is the shorter the further the SN is exceeded. If initial

---

[5] Clearly the existence of saturated solutions for nearby parameters leads to slow dynamics in these areas of the phase space.

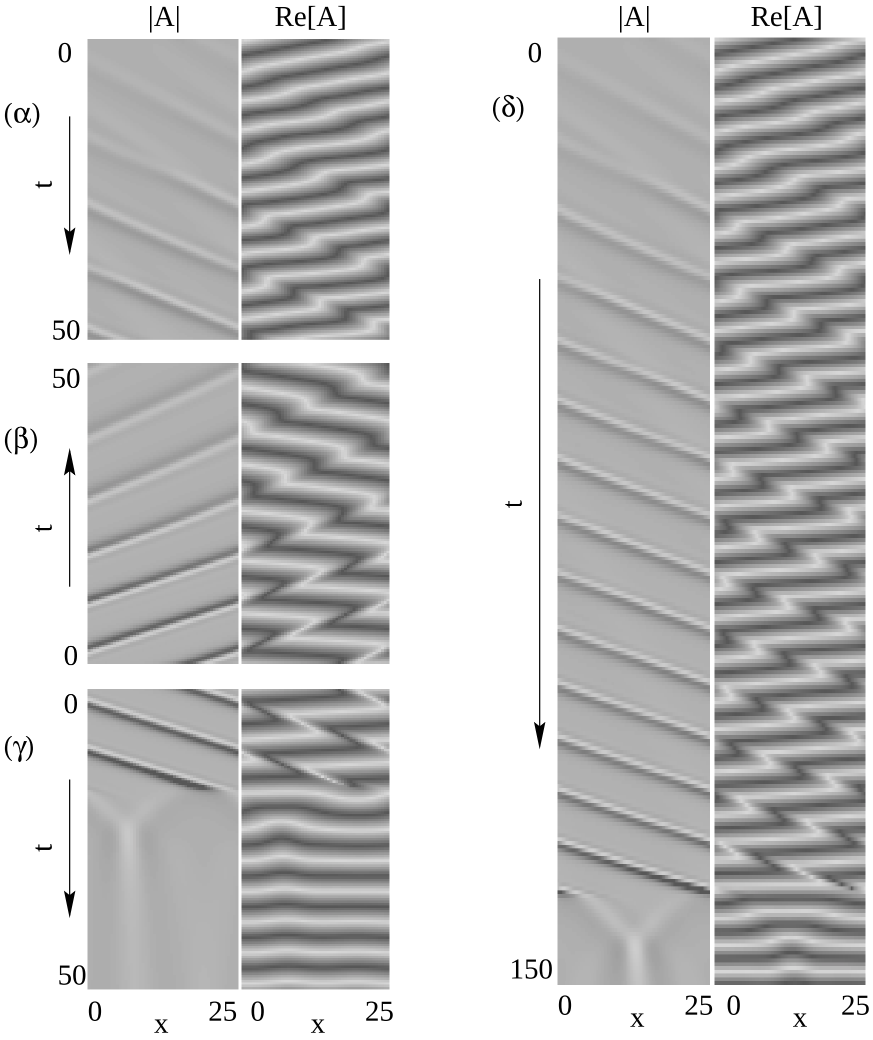

Fig. 3.16: Numerical simulations illustrate the dynamics near the SN corresponding to the arrows ($\alpha$ - $\delta$) in Fig. 3.6c. ($\alpha$) plane wave perturbed at one point and ($\beta$) unstable saddle-type MAW plus noise converge to the stable MAW. ($\gamma$) unstable saddle-type MAW plus a different realization of noise evolves to a defect that changes $\nu$ to 0. ($\delta$) as ($\alpha$) but beyond the SN which makes defect formation possible for arbitrary small perturbations of the plane wave. Note the long living transient of a noncoherent modulation. ($\alpha$ - $\gamma$) are at $c_3 = 0.5$ below the SN and ($\delta$) belongs to $c_3 = 0.55$ above the SN for $\nu = 0.25, P = L = 2\pi/\nu = 25.13$.

conditions are prepared with $\nu_i \gg \nu_M$ then the same local periods are far beyond the corresponding SNs. The transients of defect formation are short.

From these two observations it is clear why the curve $\nu(t)$ in Fig. 3.4 drops the earlier for larger $\nu_i$. On the other hand this is not sufficient to explain the observed final $\nu_f$. Another argument has to consider the time scales of competing processes. The result of the strictly local defect formation will not instantaneously effect distant spatial locations in the simulation. Instead the local change of the average phase gradient $\nu$ via a defect will take a transient time to relax over the entire system. For large $\nu_i$ defect formation happens on a short time scale and independently leads to defects at many different spatial locations before the relaxation of the decreased average phase gradient $\nu_f \ll \nu_M$ can stop defect formation. For small $\nu_i$ defects form slowly and the reduced $\nu_f$ can relax the phase gradient at distant locations before other defects occur.

This competition of two time scales, the transient of defect formation versus the spatial relaxation of the phase gradient can explain the dependence of the final $\nu_f$ on the initial average phase gradient $\nu_i$ (compare Fig. 3.4). This statement emphasizes the local character of defect formation but is still qualitative and shall inspire further quantitative analysis and simulations.

### 3.3.2 Limit of wound-up phase chaos

For random initial conditions with $\nu_i$ in the narrow range between the SN of $P \to \infty$ and the existence limit of MAWs (see Fig. 3.10) it depends on the specific realization of the noise whether a defect can form or a stable MAW results. In order to understand the observed limit $\nu_M(c_3)$ of wound-up phase chaos ,*i.e.* no defects form below $\nu_M(c_3)$, it is sufficient to consider the SNs of periodic MAWs since these SNs occur at the lowest values of $c_3, \nu$. Although initial conditions with large $P$ beyond a SN could lead to defects this is prevented if the splitting instability is present. Then the period is decreased before a defect can form. Following the SN curve in Figs. 3.14, 3.15 one encounters a transition between SNs with a splitting instability at large $P$ and SNs without this instability at short $P$. Defect formation in wound-up phase chaos mostly occurs for parameters where the splitting instability is *not* active near the SN.

Fig. 3.17 summarizes the different bounds that we derived for the limit of wound-up phase chaos. The domain of stable plane waves at low $c_3$ is limited by the Eckhaus instability (thin curve). Within the shaded area only HBs of different period $P$ occur but no SNs and this area is limited by the lowest SN curve of $P \to \infty$ (thick solid). No defects can form from random initial conditions within the shaded area. The dashed curve limits the existence of MAWs. Saddle-node bifurcations exist in the window between this curve and the thick solid curve for $P \to \infty$. For any choice of initial conditions defects will always form above the dashed curve. The dotted curve gives the transition from active (below) to inactive (above) splitting at the SN as derived from linear stability analysis along cuts like Figs. 3.14,3.15. Splitting can prevent defect formation below this curve. Filled circles correspond to $\nu_M$ obtained from numerical simulations [58, 141]. Diamonds refer to the transition from chaotic (below) to regular (above) asymptotic states.

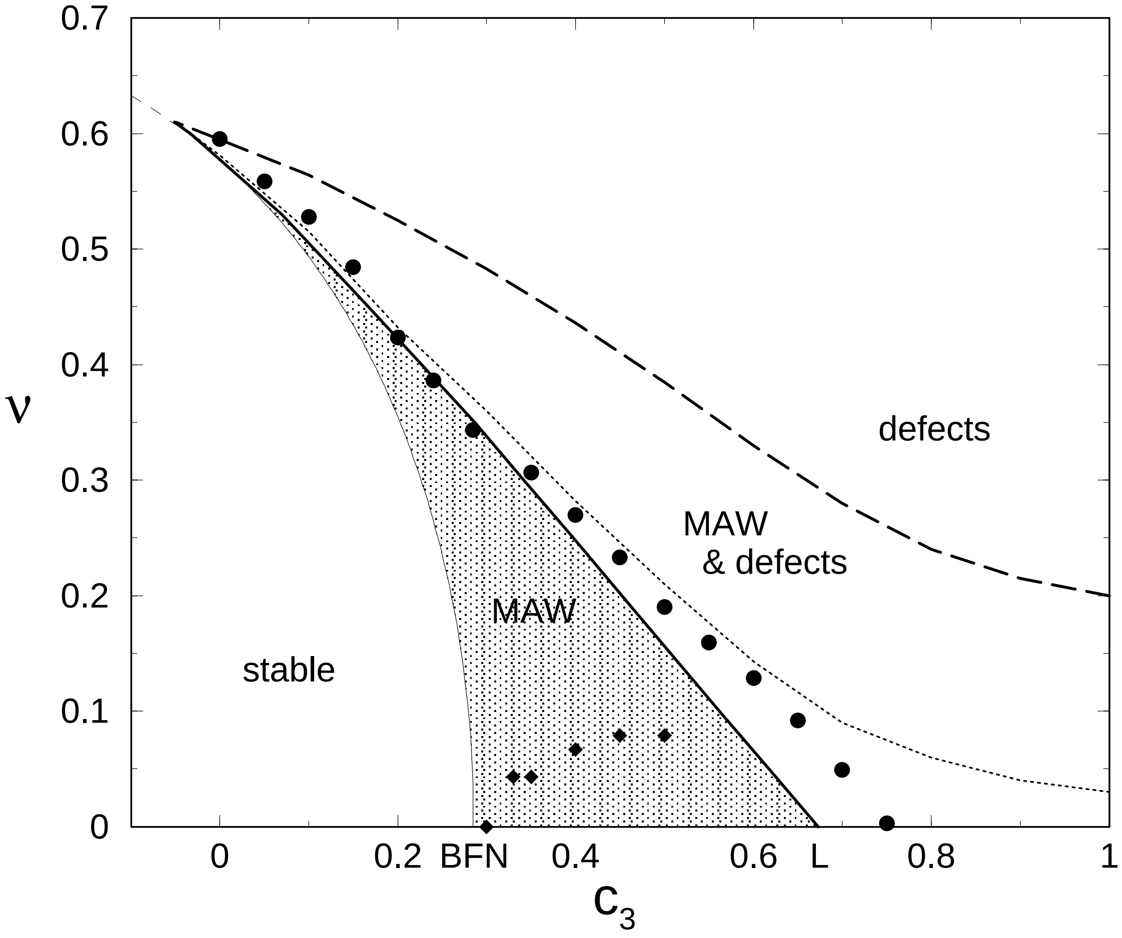

Fig. 3.17: Theoretical bounds for $\nu_M(c_3)$ (filled circles) : SN of $P \to \infty$ as lower bound (thick solid curve), existence limit of MAWs as weak upper bound (dashed) and the onset of splitting at SN as strong upper bound (dotted). Other curves as in Fig. 3.3. See text for details.

The SN for $P \to \infty$ (thick solid) is always a lower bound for defect formation which also holds in the limit $\nu = 0$ (L marks the transition from phase to defect chaos). As long as the dynamics is regular ($\nu > 0.1$) the upper bound for defect formation (no splitting at SN, dotted curve) reproduces well the numerical observations. This indicates that the splitting instability is an important mechanism. For chaotic states ($\nu < 0.1$) defect formation eventually becomes possible even despite the presence of the splitting instability. In this regime one has the same phenomena as in the limit case $\nu = 0$ and relies on the same statistical considerations. Here we observe a smooth crossover (as $\nu$ decreases) from a sharp to a statistical characteristic of the limit of wound-up phase chaos.

## 3.4 Discussion

The bifurcation analysis of modulated amplitude waves (MAWs) has been extended to nonzero average phase gradient ($\nu \neq 0$). Lower branch MAWs of specific spatial period $P$ exist between a supercritical Hopf bifurcation (HB) and a saddle-node (SN) bifurcation. We encounter the SN at decreasing values of $P$ as $c_1, c_3$ and $\nu$ are increased. As for $\nu = 0$ the SN that limits the existence of MAWs was shown to allow the formation of defects from random initial conditions and to rule many of the phenomena in wound-up phase chaos. The SNs restrict MAWs to a well defined area in parameter space. For parameter values of $c_1, c_3, \nu$ below this area plane wave solutions are stable,*i.e.* below the Eckhaus instability, whereas for parameters above this area defects will occur,*i.e.* above the SN. The strictly local character of defect formation can explain the dependence of $\nu_f$ on $\nu_i$.

The linear stability analysis revealed : MAWs are linearly stable for certain parameter domains even in systems of infinite size. These domains are limited by the interaction instability at low and the splitting instability at high values of the spatial period $P$ of the MAW. The competition of the two instabilities drives wound-up phase chaos and determines the Lyapunov exponents of the dynamics. Wound-up phase chaos may in phase space be characterized as evolution along the manifold of MAW solutions as for $\nu = 0$.

The splitting instability can prevent defect formation if the SN occurs at large $P$. This establishes a lower,*i.e.* the lowest SN for $P \to \infty$, and an upper bound,*i.e.* the onset of splitting at SN, for the maximum conserved $\nu$. Earlier numerical observations on $\nu_M(c_3)$ are well reproduced except at low $\nu < 0.1$, respectively large $c_3$. There the description of phase chaos relies on statistical considerations as in the limit case $\nu = 0$ in Chapter 2. Further work should characterize the crossover at $\nu = 0.1$ by statistical means.

# 4 Experimental Observations of MAWs

In general the experimental observation of MAWs is a difficult task [181]. The primary goal of experimentalists has so far been the characterization of the initial plane wave state. Triggered perturbations were used to determine adequat coefficients for the CGLE model. M. van Hecke *et al.* inspired many experimental efforts by a recent publication [184] on sources and sinks of plane waves. The observation of MAWs requires a precise measurement of the local phase gradient of a traveling wave which calls for high resolution experiments. The most promising candidates again are among hydrodynamic systems which shall be listed and shortly discussed in the following. Previously published data will be shown in space-time plots of the original unscaled coordinates.

## 4.1 Hydro-thermal convection

(*i*) An early experiment was performed by B. Janiaud *et al.* [56] studying the secondary (oscillatory) instability of a Rayleigh-Bénard convection pattern. The annular gap between two vertical concentrical cylinders was filled with argon under a pressure of 60 atm. The apparatus was heated from below which due to buoyancy forces excited a pair of counter-rotating convection rolls. Their axis lies in the horizontal plane and in order to force this axis to follow the curvature of the gap a small horizontal temperature gradient was applied across the gap. The horizontal cut through the gap can be described as a one-dimensional system with periodic boundary conditions. For low vertical temperature gradient the two convection rolls are stable tori with a circular separation zone. Upon increasing the vertical temperature gradient this separation zone shows a traveling wave modulation according to the oscillatory instability of Rayleigh-Bénard convection. This secondary instability is oscillatory for fluids with low Prandtl number Pr$<$ 1, therefore a gas was used. Fig. 4.1a shows an example of the stable traveling wave with a constant local wavenumber. For further increased vertical temperature gradient the plane wave undergoes the Eckhaus instability and a modulation of the local wavenumber appears that almost saturates while moving superimposed on the underlying traveling wave. In Fig. 4.1b a space-time plot of this modulation is presented. After a long transient the modulation increased and the resulting defect reduced the wavenumber of the underlying traveling wave. The Eckhaus instability was concluded to be subcritical. Above a subcritical instability the perturbation is expected

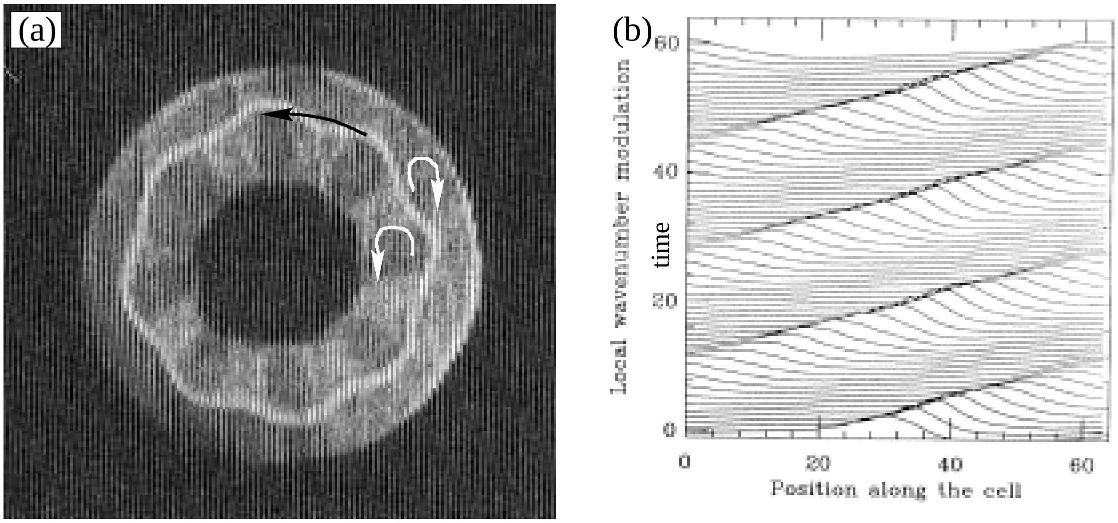

Fig. 4.1: (a) Top view of an annular channel with Rayleigh-Bénard convection inside. White arrows represent raising and falling fluid forming two rolls. The bright curve separates fluid of the inner from that of the outer roll. This separation zone has a stable sinusoidal modulation that travels along the annulus as indicated by the black arrow. (b) The local wavenumber of the traveling wave from (a) is shown in a space-time plot. A modulation travels on top of the underlying wave but does not saturate. After the displayed transient the modulation grows and leads to a defect with corresponding change of the average local wavenumber of the underlying wave. Both figures are taken from [56].

to exponentially grow which is not observed here. Instead the long living transient of a finite modulation is surprisingly similar to the dynamics past the SN of a MAW (compare Fig. 3.16$\delta$). Repeating the experiment with different geomentrical dimensions may render the Eckhaus instability supercritical and reveal the full scenario including stable MAWs.

(*ii*) Another well studied system are hydrothermal waves. For an overview see Section 1.3.2 and figures therein. N. Mukolobwiez *et al.* [43, 182] have used an annular convection cell with horizontal temperature gradient. They indeed observed a supercritical Eckhaus instability and a stable MAW (see Fig. 4.2a). Upon further increase of the temperature gradient modulations grow and lead to defects that decrease the wavenumber of the underlying wave (see Fig. 4.2b). After this transient a stable unmodulated plane wave is recovered. The scenario is consistent with the role of the saddle-node bifurcation of MAWs (see Section 3.3.1). Further experiments including laser-imprinting of initial conditions are discussed [183, 182]. By preparing the wavelength of initial perturbations one should recover the existence domains and instabilities of MAWs. Especially we conjecture short wavelength perturbations to saturate (MAW) while for the same experimental parameters a long wavelength perturbation leads to defects.

(*iii*) N. Garnier *et al.* [120, 182] observe hydrothermal waves emitted by a source at one end of the channel in a linear convection cell. The wave source selects a fixed wavenumber (see Chapter 5) and the wavelength of perturbations that grow while being advected away from the source. Depending on the temperature gradient defects may be created by the modulations. This scenario has a striking similarity with the simulations in Chapter 5. In

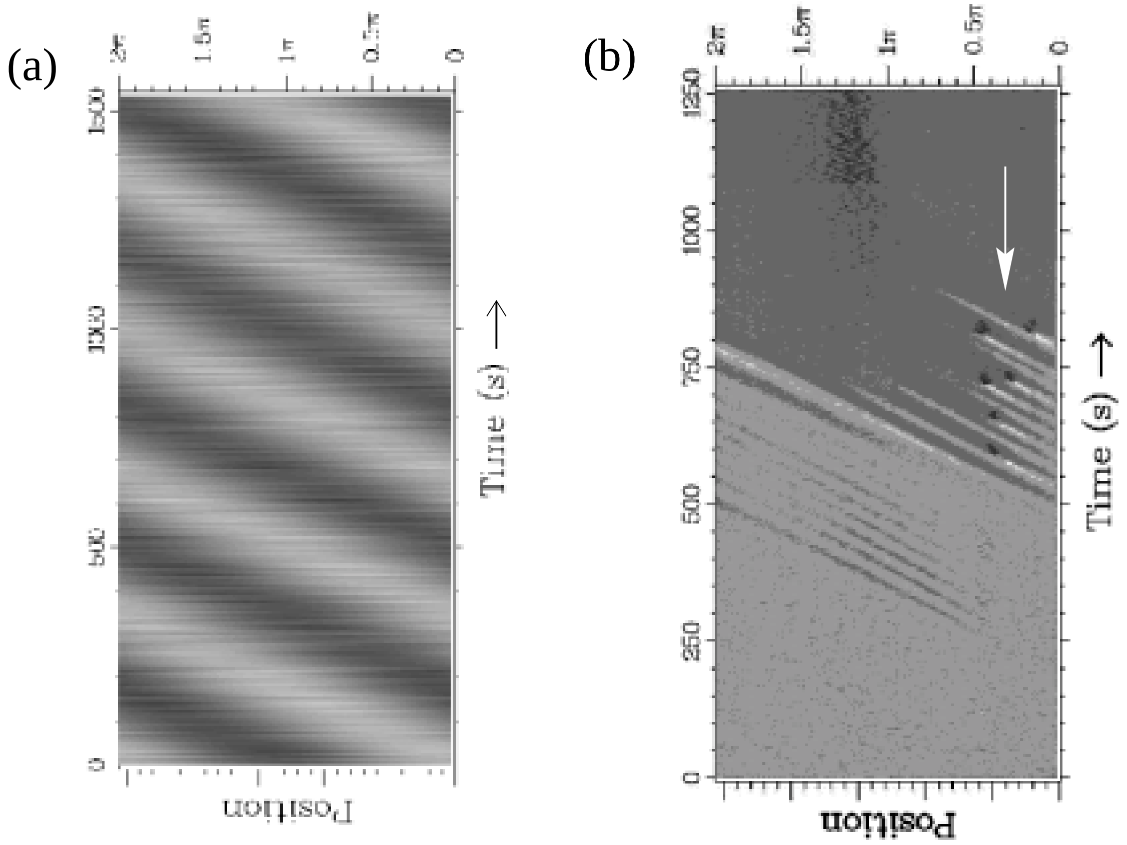

Fig. 4.2: (a) Space-time plot showing the local phase gradient of a hydrothermal wave [43]. The modulation (bright and dark bands) was stable for as long as the experiment was conducted. It moves on top of an underlying traveling wave. (b) Defects (arrow) form at higher temperature gradients where no stable modulation was found. Both figures are taken from [43].

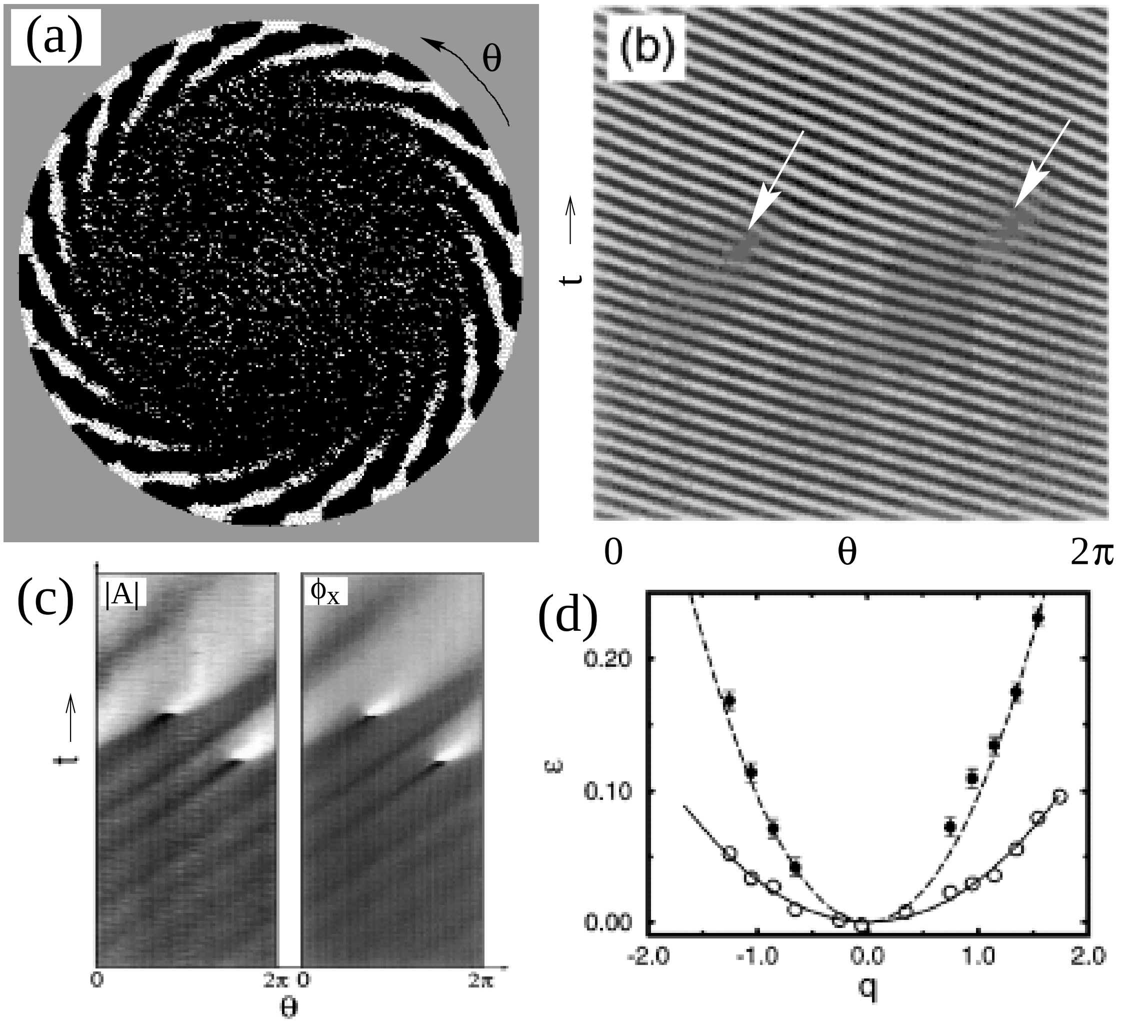

Fig. 4.3: (a) Top view of the rotating convection cell [53, 185] with 17 traveling convection rolls adjacent to the side wall. (b) Angle-time plot showing the traveling wave and two defects (arrows) that increase the number of rolls from 17 to 19. The Eckhaus instability of the initial wave is subcritical. (c) Another example of defect formation in the same system where the modulus of the wave and the phase gradient are displayed. (d) Stability diagram of traveling waves that exist above the open circles but are stable only above the full circles. The existence limit (lower parabola) has been fitted to the data and from that the Eckhaus instability limit (upper parabola) has been calculated in the CGLE model. The figures are taken from [53, 185].

the present setup both parameters $\nu$ and $P$ of the MAWs are selected by nonlinear effects at the source. Also here an additional mechanical of thermal forcing of the source could provide control over the perturbations and thereby reveal the full scenario including stable MAWs.

(*iv*) In order to study large systems W. van de Water [49] uses a narrow channel that is 2 meters long and heated by a wire (resistor) underneath the fluid surface. He was able to reproduce theoretical predictions by M. van Hecke *et al.* on wave sources [184]. Further progress could reveal MAWs on the emitted waves.

(*v*) Y. Liu *et al.* [53, 185] studied rotating Rayleigh-Bénard convection in a convection cell heated from below and mounted on a rotating plate. If the vertical temperature gradient is increased above a threshold a traveling-wave sidewall mode appears near the boundary. Fig. 4.3a shows the top view of the convection cell. The Eckhaus instability was found to be subcritical and no stable modulated waves were observed. See Fig. 4.3b,c for examples. The onset of the Eckhaus instability was in good agreement with predictions from the CGLE (Fig. 4.3d). The authors report [53] that the velocity of perturbations was significantly smaller than the expected group velocity. As a consequence they suggested higher order corrections to the CGLE in order to decrease the theoretical group velocity. We think the finite system size can account for this discrepancy since here the Eckhaus instability does not set in as the long wavelength instability ($k \to 0$). From Eq. (1.21) or (1.22) it is clear that shorter wavelength modes travel at a speed different from the group velocity term which the authors did not take into account. Hence the experiments on rotating Rayleigh-Bénard convection are good candidates for testing further predictions of the CGLE. In the same way as for the secondary instability of Rayleigh-Bénard convection one may observe stable MAWs for different geometrical and hydrodynamical parameters in this experiment.

## 4.2 Other hydrodynamic and chemical systems

(*vi*) The Taylor-Dean system (Fig. 4.4a) was studied by P. Bot *et al.* [54, 186, 187]. It consists of two concentrical horizontal cylinders where the gap is partly filled with a fluid (Kalliroscope tracer particles added for visualization). As the inner cylinder rotates the fluid is dragged upward on one side. The basic flow is a long roll parallel to the axis of the cylinders (arrow in Fig. 4.4a). Above a critical rotation frequency the roll is unstable and plane waves move along the roll axis. Above a second threshold the plane waves become unstable to traveling modulations which have the threefold period of the underlying plane wave. Therefore this state was named "triplet" [186]. The systematic study presented in this Chapter suggests that the triplet state is only one out of many coexisting stable solutions and it has been *selected* by the source and initial conditions,*i.e.*, the specific realization of the experimental setup. We conjecture that there are other modulated states than the triplet that can be observed. Altering the initial condition by mechanical means should excite a broader variety of states. Recently the generation of defects and spatio-temporal chaos have also been observed in this system [54].

(*vii*) Finally, the oscillatory variant of the Belousov-Zhabotinsky reaction offers the pos-

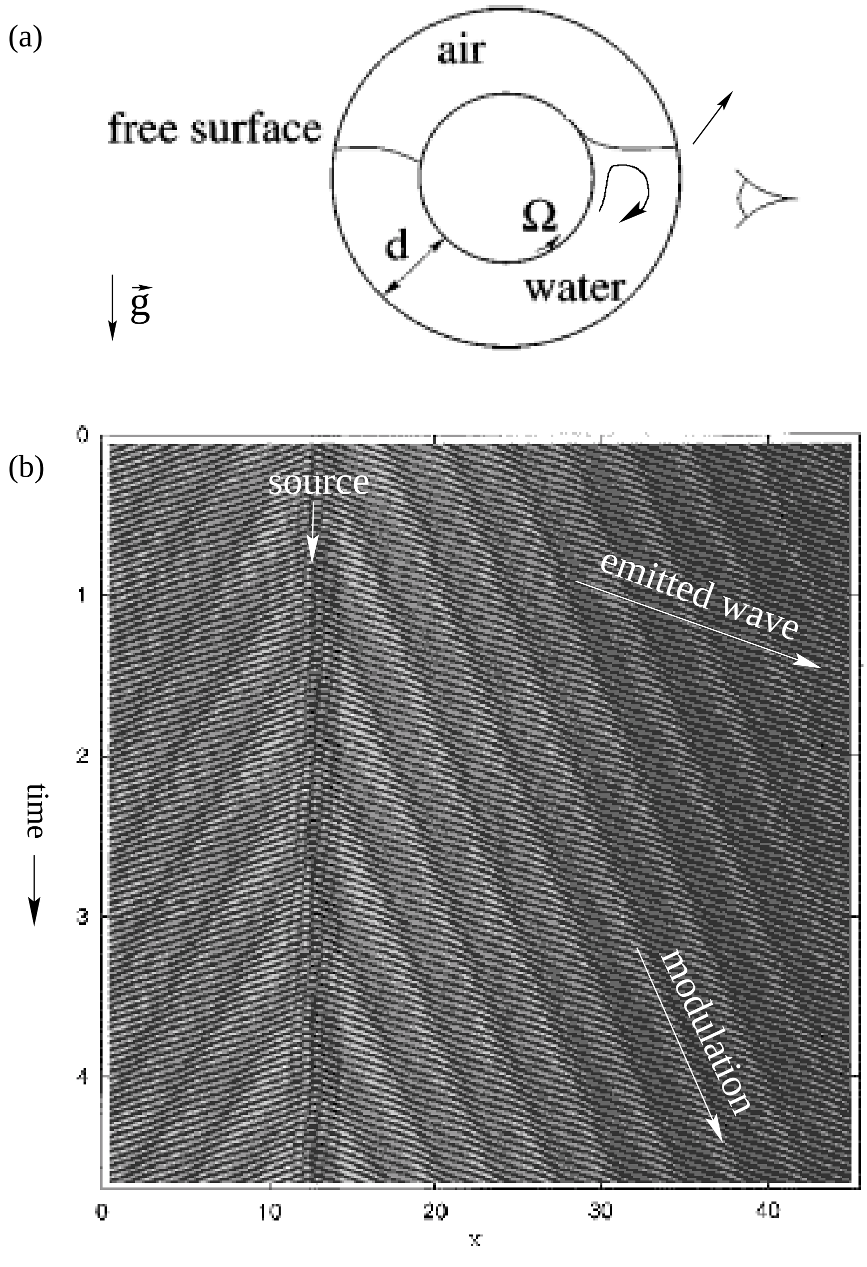

Fig. 4.4: (a) Vertical cut through the experimental setup of the Taylor-Dean system with the horizontal data acquisition line $x$ [54, 186, 187]. The gap between the two 55cm long concentrical cylinders has size $d$=62mm. (b) Space-time (increases downward) plot of the triplet state. Clearly a source emitts waves to both sides together with stable modulations. Both figures are taken from [187].

sibility to observe MAWs in a chemical system. So far the reaction has mostly been studied in planar two-dimensional geometry as in a petri dish or gel matrix. See Chapter 5 for a detailed investigation of "super-spirals" in that medium. Also one can imagine a one-dimensional setup with the reaction confined to a channel. Since the reaction-kinetics is sensitive to light one can use optical imprinting to study perturbations of traveling waves.

# 5 Super-Spiral-Breakup

## 5.1 Introduction

In this Chapter a consistent interpretation of modulated spiral waves with a meandering core and their breakup is presented. This work applies the results on modulated amplitude waves (MAWs) from Chapter 3 to the radial dynamics of two-dimensional spiral waves.

Qualitative agreement with recent experimental observations in an extended oscillatory chemical reaction is achieved. Stable "super-spirals" will be shown to be the cooperative effect of a supercritical Eckhaus instability of the wave field and the meandering instability of the tip trajectory. Often the meandering instability and the resulting dynamics occur on a slower time scale than the emission of waves by the source (see Appendix E). This separation of time scales allows their independent treatment. The emission of waves adiabatically follows the slowly moving source. Alternatively one can study extensions of the CGLE in order to get meandering by the saturation of the oscillatory core instability. I. Aranson *et al.* studied this instability which occurs at $c_1 > 6$ but is not saturated in the cubic CGLE [188].

The asymptotically planar wave field far away from the source is modeled by an amplitude equation : the one-dimensional complex Ginzburg-Landau equation (CGLE). In addition to plane wave solutions the CGLE possesses a two-parameter family of solutions called modulated amplitude waves (MAWs). To parameterize this family we choose their average phase gradient $\nu$ and the temporal period $T$ of the modulation. MAWs originate near the Eckhaus instability $T_{HB}(\nu)$ of the plane wave solutions and terminate in saddle-node bifurcations $T_{SN}(\nu)$. A stationary source $|A|(\boldsymbol{x} = \boldsymbol{x_0}, t) = 0$ emits spiral waves with an asymptotic wave number $q$. A subclass of MAWs with $\nu = q$ is selected.

In the core region an additional mechanism not present in the amplitude equation provides the instability of the wave source to meandering. Here the normal form approach by D. Barkley [194] is applied. Below we will refer to it as "Barkleys normal form". The periodic meandering of the source selects the temporal period $T = T_M$ of the modulation. For $T_M < T_{HB}(q)$ the modulations decay in radial direction and the common meandering spiral is recovered. For $T_{HB}(q) < T_M < T_{SN}(q)$ the modulations saturate in radial direction and form the "super-spiral". If $T_M > T_{SN}(q)$ then the modulations grow without bounds as they are convected away from the source and adjacent wave fronts annihilate in a finite distance $R_{BU}$ from the source ("super-spiral-breakup"). If the underlying plane wave solution is convectively unstable and not absolutely unstable [124, 166] then $R_{BU}$ is much larger than

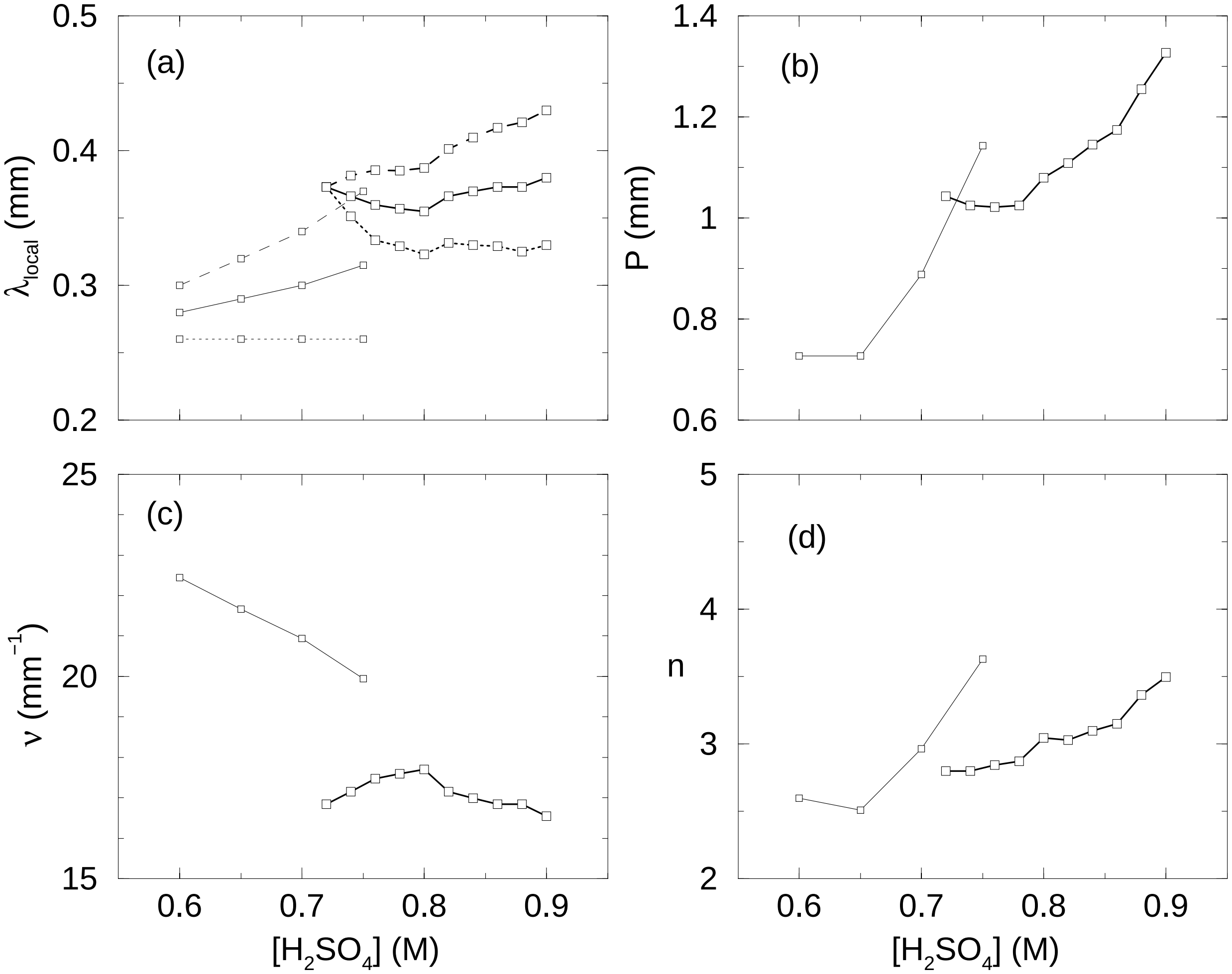

Fig. 5.1: Data digitized from published experimental observations in the wave field far away from the spiral core. Thick (thin) curves refer to Fig.3 in [70] (Fig.5 in [71]). (a) Maximum (dashed), minimum (dotted) and mean (full, $\lambda_C = \langle \lambda_{local} \rangle$) local wavelength. (b) Spatial period $P$ of the modulation of the local wavelength. (c) Mean wave number $\nu = 2\pi/\lambda_C$. (d) Ratio of length scales $n = P/\lambda_C = P * \nu/2\pi$.

the size of the meandering tip trajectory and for further increasing $T_M$ the radius $R_{BU}$ of regular spiral discs decreases. Within certain intervals the presented scenario is robust with respect to parameter variation. Depending on parameters (*e.g.*, with subcritical Eckhaus instability) other breakup scenarios skipping the super-spirals are possible.

In Section 5.2 we comment on recent experiments in an extended oscillatory system. The modelling of the observed wave field by an amplitude equation is performed in Section 5.3. There the relevant modulated amplitude waves (MAWs) are computed. Section 5.4 is devoted to the meandering tip motion modelled by Barkleys normal form approach. Finally in Section 5.5 the two ingrediences (MAW in the wave field and meandering tip) are combined. Simulations qualitatively reproduce the experimental observations on the breakup of super-spirals.

## 5.2 Experimental observations

Ouyang *et al.* experimentally studied the oscillatory variant of the Belousov-Zhabotinsky reaction [67, 68, 69, 70, 71]. The chemicals are supplied to two CSTRs (compartments $A$ and $B$) separated by a porous glass disc where the reaction pattern is observed (see Fig. 1.3). Increasing the concentration $[H_2SO_4]$ of sulfuric acid in compartment $B$ while fixing temperature (25±0.5°C) and the concentrations of all other reactands ($[\mathrm{MA}]_A$=0.4M, $[\mathrm{KBr}]_B$=30mM, $[\mathrm{NaBrO_3}]_{A(B)}$=0.6M, $[\mathrm{ferroin}]_B$=1.0mM [70]) a transition from simple rigidly rotating spiral waves to modulated spiral waves (above $[H_2SO_4]$=0.72M [70]) is observed (see Figs. 1.4 and 5.7). As $[H_2SO_4]$ is further increased the modulation of the emitted waves developes as shown in Fig. 5.1a. Positions (move outward with $v$) of equal degree of compression of the underlying wave (moves outward with $v_C$) arrange on rotating super-spirals. Above a threshold ($[H_2SO_4]$=0.94M [70]) the modulation near the periphery is strong enough to break wave fronts and chemical turbulence establishes outside a disc of radius $R_{BU}$. $R_{BU}$ decreases as $[H_2SO_4]$ is increased further.

Ouyang *et al.* distinguish *meandering* (with meandering sources but without super-spirals) and *modulated* (with meandering sources and super-spirals) spirals [71]. They argue the meandering tip motion in the case of modulated spirals is the *result* of perturbations moving from the periphery towards the source. Perturbations should travel with a “convective velocity” $V_g = v - v_C$ that points inward ($v < v_C$); the opposite direction of saturated travelling ($v$) modulations [70].

In this picture it is not clear (i) why the Eckhaus instability (long wavelength) does not appear with just one modulation $n \approx 20$ in the system and (ii) why small perturbations in the wave field should grow that fast and form saturated modulations within the system although they are advected to the periphery or the source, respectively.

In Section 5.3 we will show that saturated modulations have a velocity similar to that of infinitesimal perturbations to the underlying wave. In other words: saturated modulations approximately move with the group velocity. For a convective instability as observed in the experiment all perturbations travel in the same direction : outward. None of them travels inward with $V_g$.

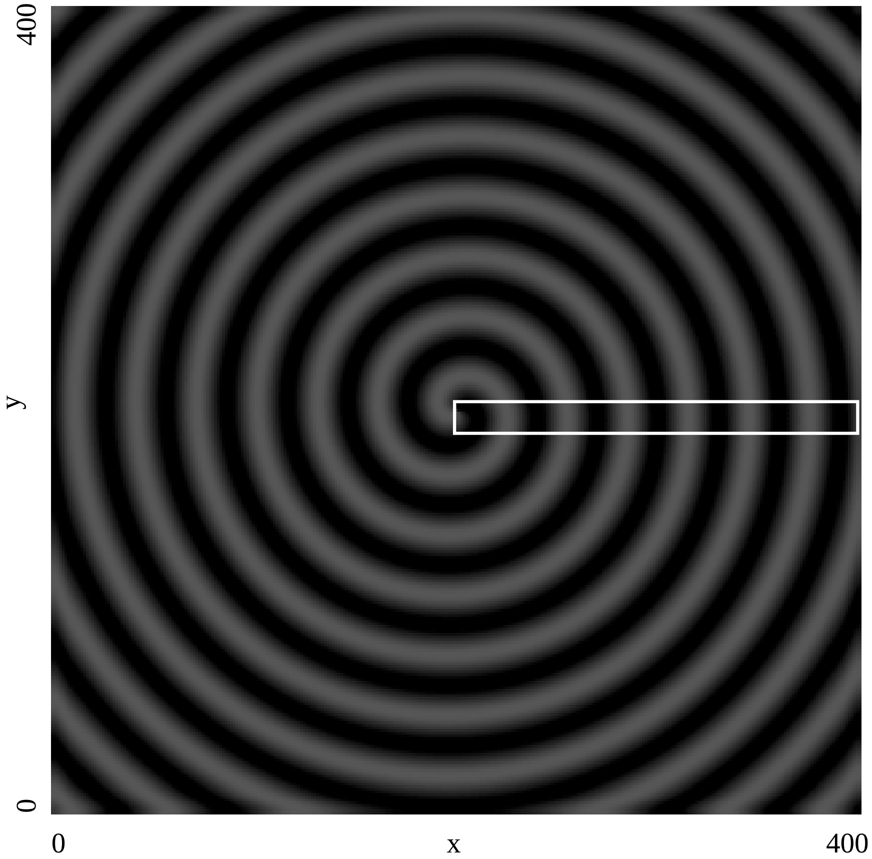

Fig. 5.2: Snapshot ($\mathrm{Re}[A(x, y, t = t_0)]$) of a rigidly rotating (counterclockwise) spiral wave. The white (black) arm of the spiral corresponds to $\mathrm{Re}[A] = |A|_{max}$ ($-|A|_{max}$). In the center $|A| = 0$. The white box denotes the one-dimensional cut that we use below in order to study the radial dynamics of the spiral wave. Parameters are $c_1 = 3.5, c_3 = 0.4$ and at the boundaries the normal derivative of $A$ is set to zero.

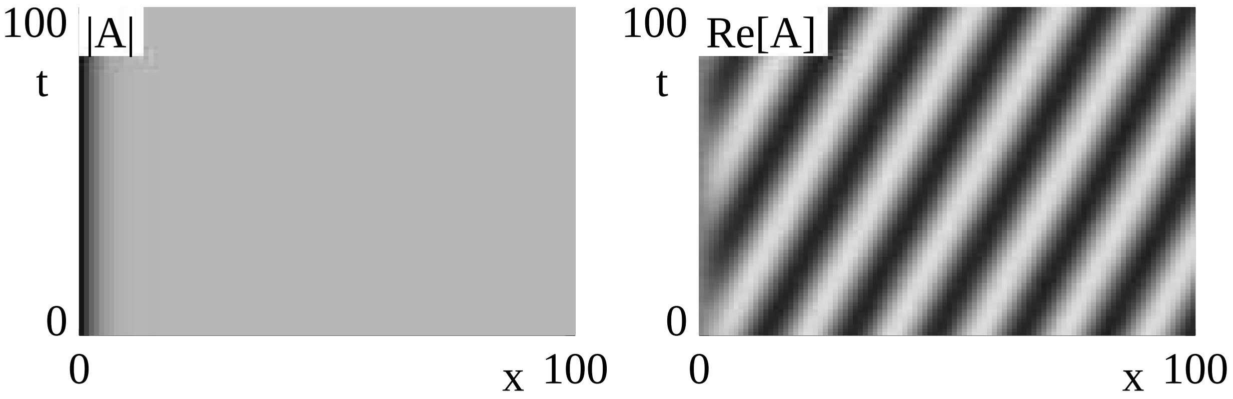

Fig. 5.3: Space time plots of $|A|$ (left) and $\mathrm{Re}[A]$ (right) with $A(x=0,t)=0$ and $\partial_x A(x=500,t)=0$ as boundary conditions. The left boundary constitutes the source, note the darker gray level (low values of $|A|$), and the waves travel to the periphery (open right boundary). Parameters are $c_1=3.5, c_3=0.4$.

We interpret the behaviour the other way around. The meandering tip motion has the same origin in both cases, the meandering and the modulated spiral, respectively. This implies that the tip motion is unstable in distinct domains of the parameter space but stable between them. Hence the saturated modulation of the modulated spirals is the *result* of the meandering tip motion in connection with the supercritical Eckhaus instability of the emitted waves. In the case of the meandering spirals the emitted (non-modulated) waves are stable, perturbations due to the meandering decay and super-spirals do not develop.

To provide a quantitative basis for the modelling, we collect the important experimental data in Figs. 5.1,5.9 and 5.10. From Fig. 5.1d we get the ratio of length scales $n = P\nu/2\pi \approx 3$ with the spatial period $P$ of the modulation and the average wavenumber $\nu = 2\pi/\lambda_C$. In our interpretation each measured $n$ was selected by the meandering tip motion. Likewise the time scale ratio $T/T_C$ of the temporal periods $T$ of the modulation and $T_C$ of the underlying wave (carrier) can be defined. The ratios $P\nu/2\pi$ and $T/T_C$ are independent of scaling when deriving an amplitude equation. Therefore the same ratios are desired for the MAWs in the CGLE below.

## 5.3 Eckhaus Instability of the Wave Field

Pattern formation in the oscillatory Belousov-Zhabotinsky reaction has been modelled by the CGLE [30, 67, 71]. In order to ease reading we repeat the CGLE (1.12) in one spatial dimension :

$$\partial_t A = A + (1+ic_1)\partial_x^2 A - (1-ic_3)|A|^2 A \ , \tag{5.1}$$

describing amplitude and phase of oscillating chemical concentrations.

The computations follow the same scheme as in Chapter 3. To parameterize the two parameter family of MAW solutions we choose the temporal period $T$ ($T = P/v$) of the

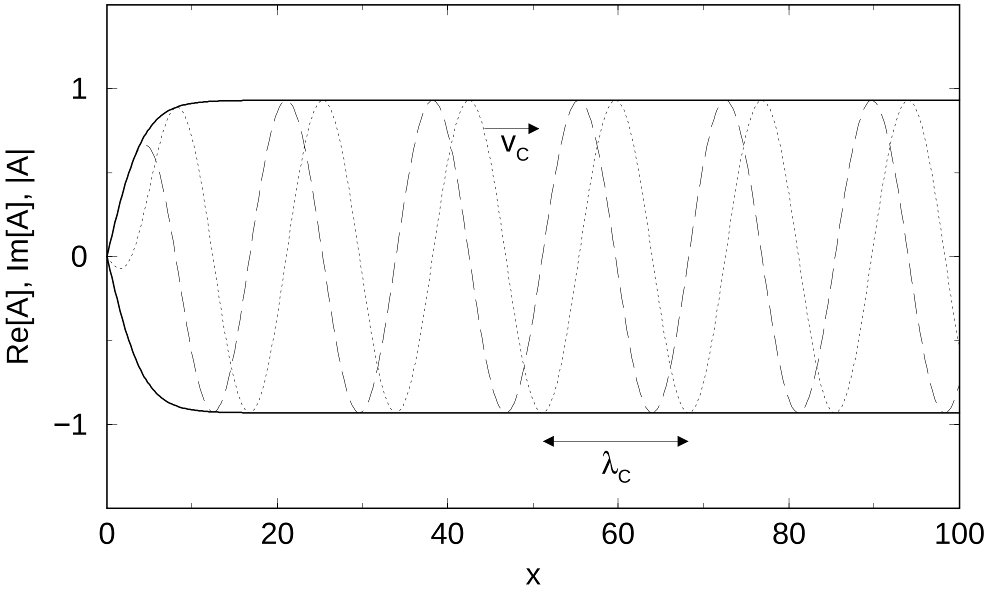

Fig. 5.4: Spatial profile of $\mathrm{Re}[A(x,t=t_0)]$ (dashed), $\mathrm{Im}[A(x,t=t_0)]$ (dotted) and $|A|(x,t=t_0)$ (full curve) with the source at $x=0$. Away from the wave source a plane wave with wave number $\nu = 2\pi/\lambda_C$ and phase velocity $v_C$ establishes. Parameters and boundary conditions as in Fig. 5.3.

modulation and the average wave number $\nu := 1/T \int_0^T dt\ \partial_x \arg A(x,t)$. This choice of parametrization is more appropriate in the case of meandering spirals studied in this chapter.

In the particular experiments [67, 69, 70, 71] a self-organising source periodically emits waves that travel to the periphery. Contours of the two-dimensional wave field form one-armed spiral wave patterns (see Fig. 5.7). The self-organising source selects a unique asymptotic wave number $q(c_1, c_3)$ of the emitted waves [189]. [1] This mechanism is qualitatively the same in the modelled chemical system as well as in the two-dimensional CGLE. Along any closed path around the source the phase of the wave field possesses a total jump of $2\pi$ . [2] The source is a topological defect associated to $|A| = 0$.

Simulations of the CGLE in two spatial dimensions also yield rigidly rotating spiral waves as illustrated in Fig. 5.2. For a detailed discussion see [122]. An one-armed spiral wave in polar coordinates $(r, \theta)$ is of the form

$$A(r,\theta,t) = F(r)\mathrm{e}^{i(-\omega t + \theta + f(r))} \tag{5.2}$$

with the asymptotic behavior $df(r)/dr \to q, F(r) \to \sqrt{1-q^2}$ for $r \to \infty$ (wave field) and $df(r)/dr \sim r, F(r) \sim r$ for $r \to 0$ ($|A| = 0$ in the spiral core).

The parameters in Fig. 5.2 are chosen beyond the Eckhaus instability of the emitted wave field but the spiral remains stable. This stability holds as long as the Eckhaus instability is of “convective nature” and no perturbations are applied in the center. This scenario has been described by I. S. Aranson *et al.* [124, 166]. In this section we will focus on

---

[1] It may be computed numerically in the two-dimensional case whereas it is known analytically for the one-dimensional source, see below.

[2] In general a $m$-armed spiral posseses a phase jump of $m * 2\pi$.

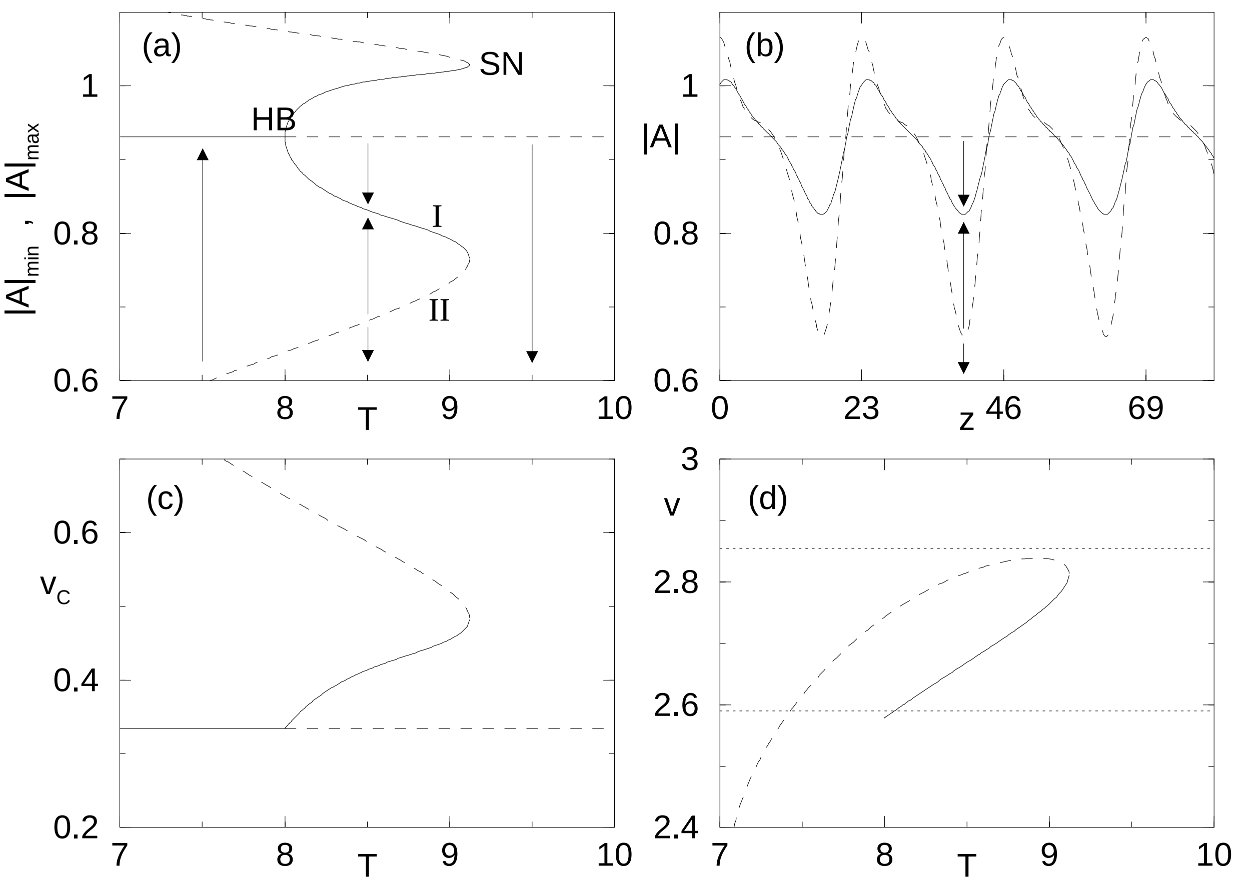

Fig. 5.5: Bifurcation diagrams of MAWs in the CGLE. (a) Maximum and minimum modulus of the modulation for varying temporal period $T$. Full (dashed) curves denote stable (unstable) solutions and the horizontal line is the plane wave solution. Arrows indicate transient dynamics of modulations that are not uniformly propagating. (b) Spatial profiles for $P = 23$ which corresponds to $T \approx 8.5$. (c) Velocity of the underlying wave (carrier) increases as the modulation developes. (d) Velocity of the modulations. Dotted lines give the analytical result for infinitesimal perturbations of long (upper) and short wavelength type ($P = 23$, lower). All these structures (underlying wave, modulations and infinitesimal perturbations) travel in the same direction. Parameters are $c_1 = 3.5, c_3 = 0.4$ and $\nu = q = 0.366$ from Eq. (5.4).

the radial dynamics away from the wave source neglecting concentration gradients in the perpendicular direction, *i.e.*, the small curvature of concentration contours is approximated by planar wave trains. The white box in Fig. 5.2 marks the one-dimensional system that we use below in order to study the radial dynamics of the spiral wave. Figs. 5.3 and 5.4 show results of simulations of the CGLE along the one-dimensional cut with an artificial wave source at the left boundary.

From now on we use the wave number selection by a Dirichlet boundary condition $A(x = 0, t) = 0$ in a one-dimensional system representing a radial cut through the wave source. Figs. 5.3 and 5.4 show a gray scaled space time plot and the spatial profiles of the field $A$ in the one-dimensional system. The wave number selection in both one and two dimensions yields close results [166, 189]. If $q$ becomes small ($q < 0.3$), the one-dimensional approximation overestimates the selected wave number in two dimensions.

Matching asymptotic expansions, Hagan [189] analytically obtained an expression for the selected wave number in the case $c_1 = 0$. Using scaling relations this result was expanded to arbitrary parameters [190]

$$\alpha(c_1, c_3) = \sqrt{\frac{3c_1(8(c_1 - c_3)^2 + 9(1 + c_1c_3)^2 - 4c_1c_3)^{1/2} + c_1(5 - 9c_1c_3) - 4c_3}{4(-2c_3 + 9c_1^3 + 7c_1)}} \tag{5.3}$$

$$0 = (c_1 + c_3)q^2 + 3\alpha(c_1, c_3)q - c_3 - 2c_1\alpha(c_1, c_3)^2 \tag{5.4}$$

where the positive $q(c_1, c_3)$ has to be chosen. Simulations as in Figs.5.3,5.4 are in good agreement with the analytical result.

Due to reflection symmetry of the CGLE solutions exist for $\nu = \pm q$ which only differ in propagation direction. The presence of a wave source breaks this symmetry and one unique solution remains. Without loss of generality we fix $\nu = q(c_1, c_3)$ at the value selected by the source in the one-dimensional system.

For properly chosen fixed parameters $c_1, c_3$ and increasing $T$ the branch of MAWs emerges from the plane wave fixed point at a Hopf bifurcation in the ODEs which results from the Eckhaus instability as discussed in Section 1.4.3. The modulation develops for $T$ above the period at the Hopf (HB) bifurcation $T_{HB}$. At a larger period $T_{SN}$ the stable branch (I) meets with a second but unstable branch (II) in a saddle-node (SN) bifurcation. No MAWs exist beyond $T_{SN}$.

Figs. 5.5a,c,d show typical bifurcation diagrams for MAWs with parameters as in Fig. 5.3. Full (dashed) curves denote stable (unstable) solutions. For these parameters the bifurcations occur at $T_{HB} = 8.0$ and $T_{SN} = 9.12$. Arrows in Fig. 5.5a,b denote the transient dynamics of perturbations. Small perturbations of the plane wave (*e.g.* due to weak meandering) can grow unbounded if $T > T_{SN}$. Large perturbations (*e.g.* due to strong meandering) can grow unbounded if their $|A|_{min}$ exceeds the corresponding value of the unstable (saddle) MAW solution, which changes with $T$. Fig. 5.5b shows typical spatial profiles. Fig. 5.5c,d give the velocities of the underlying wave ($v_C$), of the modulation ($v$) and of infinitesimal perturbations to the plane wave. They are all oriented in the same direction : outward.

Saturated modulations and infinitesimal modulations always travel in the same direction for all $c_1, c_3$ where the underlying wave is convectively unstable.

Repeating this bifurcation analysis for the whole parameter plane $(c_1, c_3)$ we identify a domain around $0.3 < c_3 < 0.5$ where MAWs exist with $\nu = q(c_1, c_3)$. To allow efficient computations in this region we used a fit $q(c_1, c_3) = 0.352 - 0.021c_1 + 0.0006c_1^2 + 0.22c_3 - 0.008c_1c_3$ to the wave number derived from Eq. (5.4).

Fig. 5.6 summarizes the results in the $(c_1, c_3)$ parameter space. The emitted plane waves of a spiral are convectively unstable above the thick full curve [166]. Stable super-spirals can only exist (inside the shaded area) where this instability is supercritical hence only above both (thick and thin) full curves. Increasing $c_3$ inside the shaded area the instability threshold $T_{HB}$ monotonously decreases starting from $\infty$ at the lower boundary of the area. Above the thick dot-dashed curve ($T_{HB} = T_{SN}$) the Hopf bifurcation is subcritical and super-spirals are unstable, this marks the upper boundary of the shaded area. The thick dashed curve inside the shaded area denotes the saddle-node bifurcation for $T_{SN} \to \infty$. Below this curve all modulations with $T > T_{HB}$ saturate but above this curve only modulations with $T_{HB} < T < T_{SN}$ saturate. For higher $T > T_{SN}$ no MAWs exist and modulations will grow unbounded causing super-spiral-breakup. Since the region of super-spirals entirely lies inside the domain of convective instability (see Fig. 5.6) a finite perturbation is needed to excite them. The meandering source will be sufficient. If the region of super-spirals and absolute instability overlapped then super-spirals could exist in the absence of meandering and the absolute instability would not immediately lead to spiral breakup. If such an overlap occurs in other models has to be investigated by a fully nonlinear analysis as presented here. The linear analysis for perturbations around the plane wave solutions [124, 166, 197] is not sufficient to answer this question.

## 5.4 Meandering Instability of the Source

An additional mechanism not present in the amplitude equation provides the instability of the wave source to “meandering”. The term meandering was introduced by A. T. Winfree [191]. The phenomenon of meandering spiral waves has been studied intensively [192, 193, 194, 195, 196] but mostly focused on the core region. Far away from the core the disturbance was previously assumed to exponentially decay or amplify depending on the stability of the asymptotic wave field neglecting nonlinear effects.

The *tip* of the spiral wave is conveniently defined as the point of strongest curvature on a contour $\mathrm{Re}[A] = a_0$ (often the wave front) [68]. This definition can easily be adapted in the image processing of experiments. However, the wave source $A = 0$ has a position different from but close to the tip. For the rigidly rotating spiral wave the tip trajectory is a circle with the stationary wave source in the center.

D. Barkley introduced [194] the normal form approach Eq. (5.5) unfolding the meandering instability around a codimension-two point. If we write the position of the tip

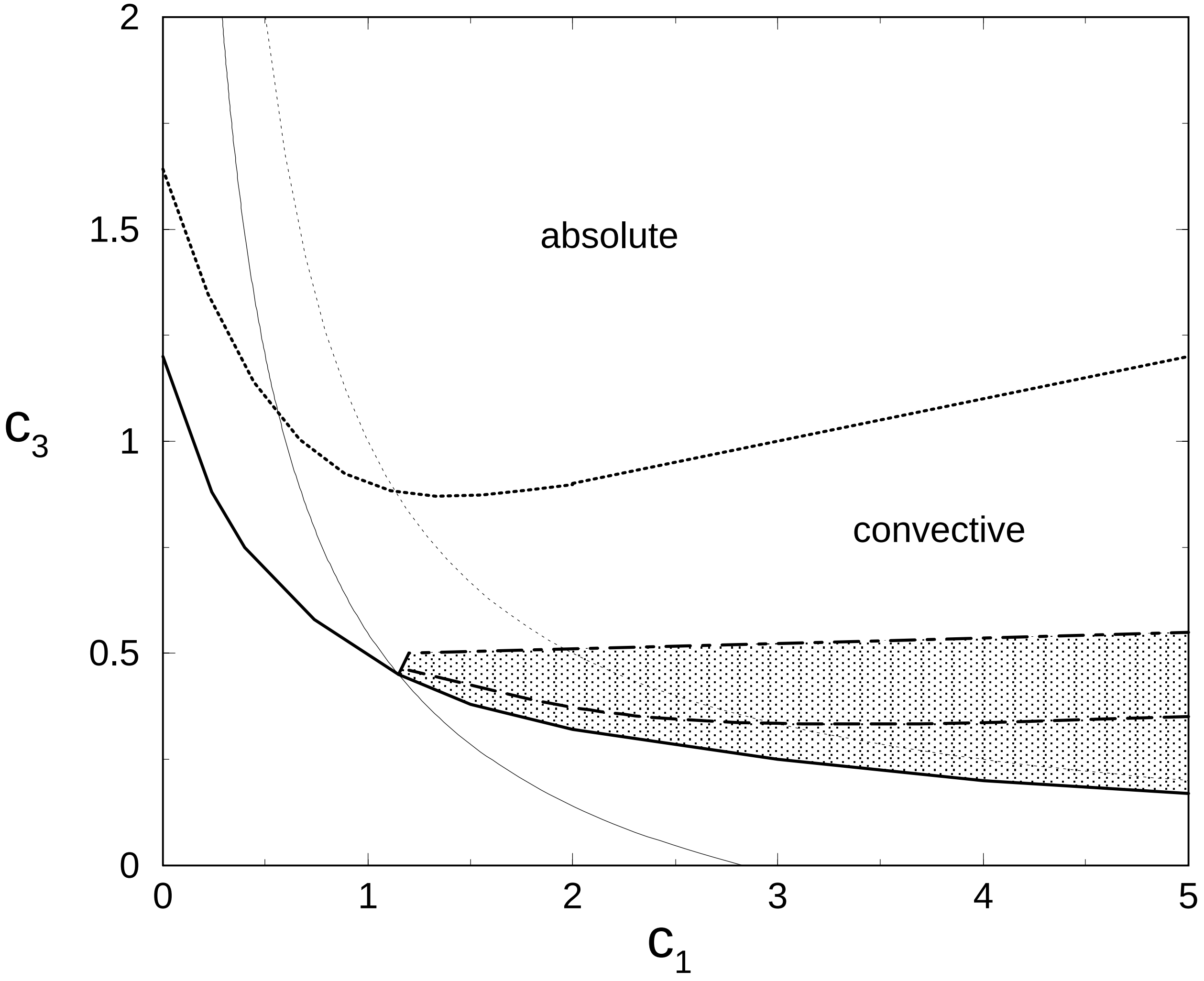

Fig. 5.6: Parameter space $(c_1, c_3)$ of the CGLE with BFN curve (thin dotted), lower boundary of supercritical Eckhaus instabilities for arbitrary $\nu$ (thin full) [56, 173], lower boundary of Eckhaus instabilities with $\nu = q(c_1, c_3)$ (thick full) and lower boundary of absolute instability with $\nu = q(c_1, c_3)$ (thick dotted). Above the thick dot-dashed curve ($T_{HB} = T_{SN}$) the Hopf bifurcation is subcritical and no stable MAWs exist. The thick dashed curve inside the shaded area denotes the saddle-node bifurcation for $T_{SN} \to \infty$.

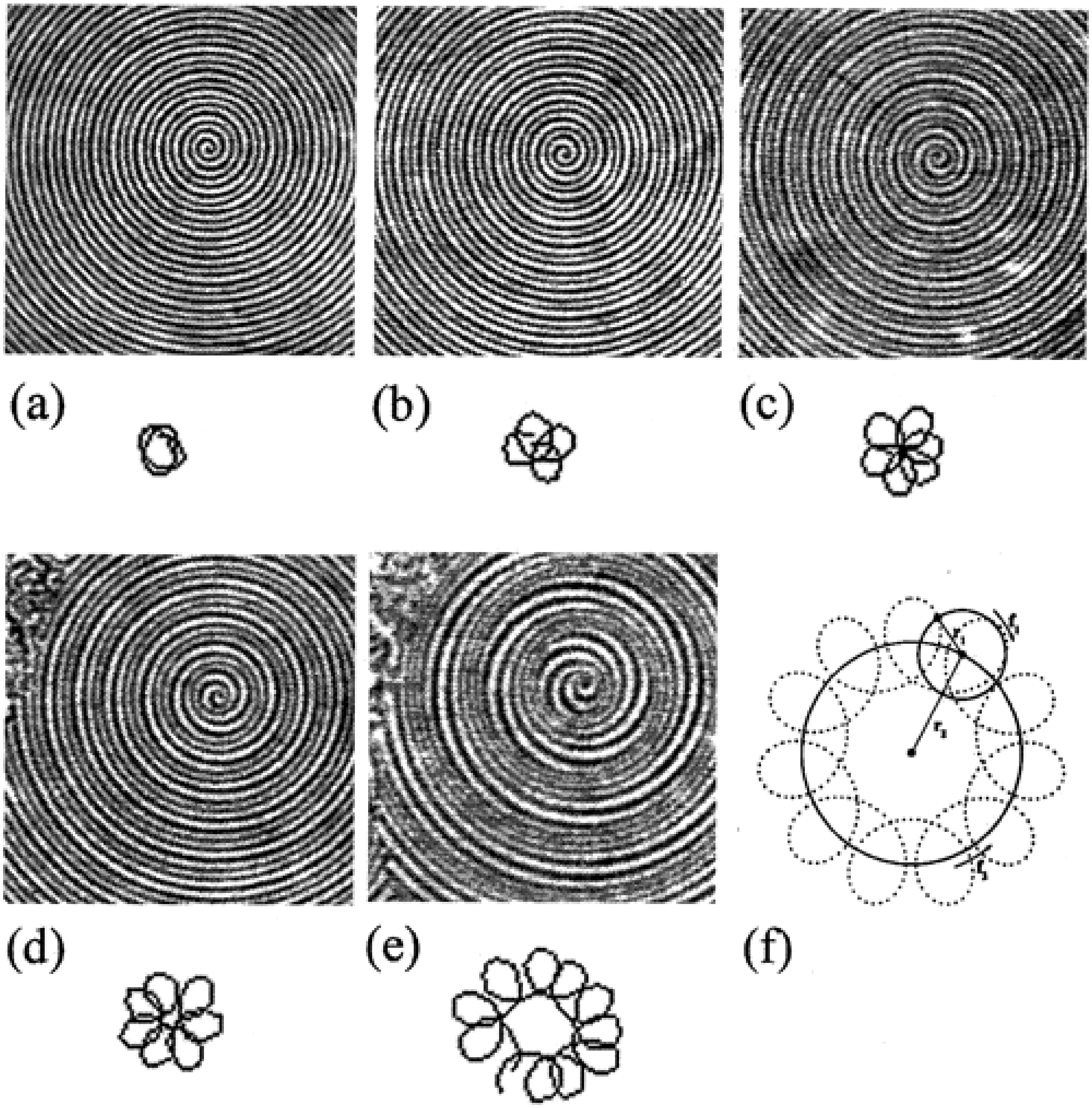

Fig. 5.7: Experimental observations of spiral waves emitted by a meandering wave source. The upper panels show snapshots of the chemical concentration pattern for increasing [$H_2SO_4$] from (a) to (e). The trajectory of the spiral tip is plotted below each snapshot. (f) schematically shows a tip trajectory (dotted) as produced by a tip moving around a rotating source (solid circle). The figure was taken from [71].

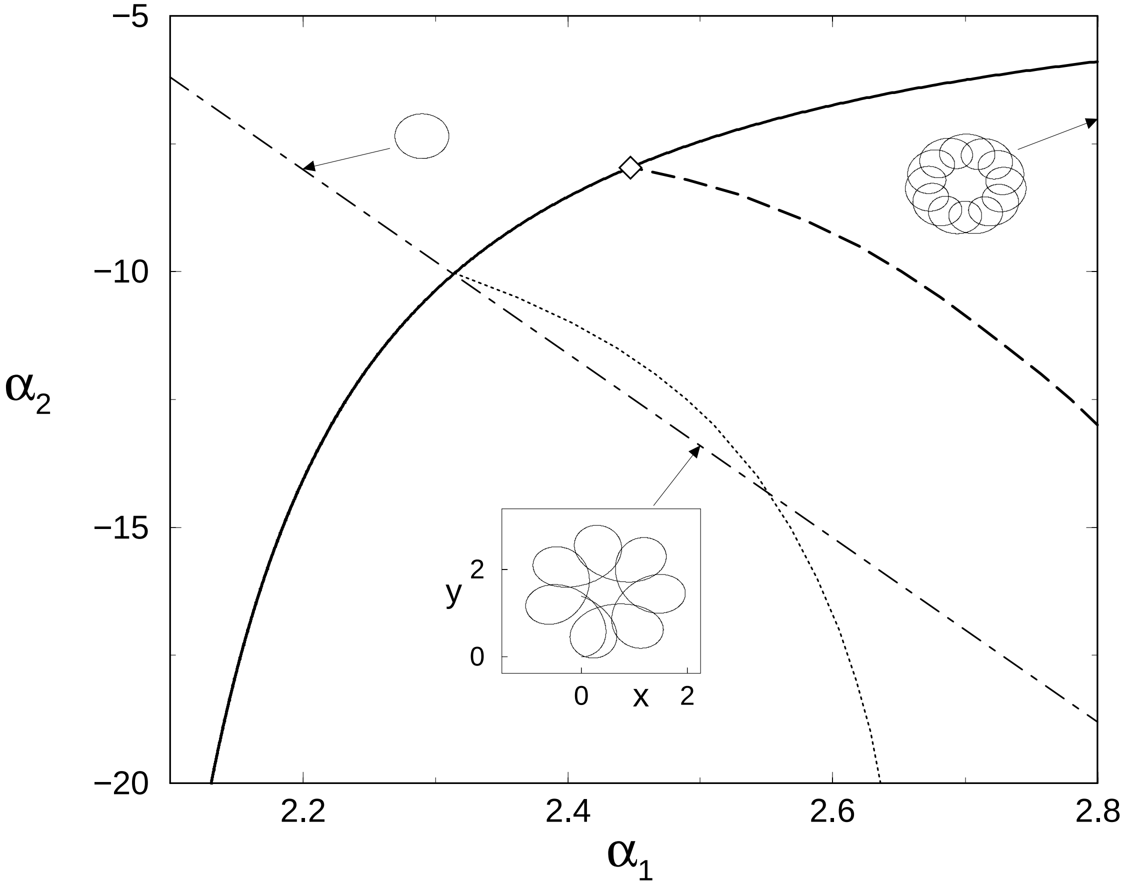

Fig. 5.8: Parameter space $(\alpha_1, \alpha_2)$ of Barkleys normal form for the meandering instability at fixed $\gamma_0 = 6$. The full curve denotes the locus of Hopf bifurcations, the thick dashed curve separates outward (below) from inward (above) meandering trajectories and the codimension-two point is given by the diamond. Along the dotted curve the tip meanders outward with a period $T_M = 30$ while $T_M$ diverges along the thick dashed curve. The dot-dashed curve illustrates a possible parameter variation Eq. (5.6) from top-left to bottom-right corresponding to experimental observations [70]. Insets show examples of tip trajectories all with the same scale. The lowest inset also illustrates the quasi-periodicity of the trajectory.

$p(t) = x(t) + iy(t)$ and its velocity $v(t) = \sqrt{\xi(t)} \exp i\phi(t)$ then the normal form reads :

$$\begin{aligned} \dot{x} &= \sqrt{\xi}\cos\phi\ , \qquad \dot{y} = \sqrt{\xi}\sin\phi\ , \qquad \dot{\phi} = \gamma_0\sqrt{\zeta}\ , \\ \dot{\xi} &= 2\xi[-1/4 + \alpha_1\xi + \alpha_2\zeta - \xi^2]\ , \\ \dot{\zeta} &= 2\zeta[\xi - \zeta - 1]\ . \end{aligned} \tag{5.5}$$

$\alpha_1, \alpha_2$ are parameters, $\gamma_0$ is a fixed constant and the subsystem $(\xi, \zeta)$ is decoupled from the subsystem $(x, y, \phi)$.

Fig. 5.8 shows the $(\alpha_1, \alpha_2)$ parameter plane for arbitrarily chosen $\gamma_0 = 6$. The data was obtained by means of AUTO97. The insets are examples of tip trajectories. The codimension-two point is denoted by the diamond. Along the full curve a Hopf bifurcation renders the circular tip trajectory unstable and the meandering motion appears. This bifurcation is always supercritical [194]. The thick dashed curve separates outward (below) from inward

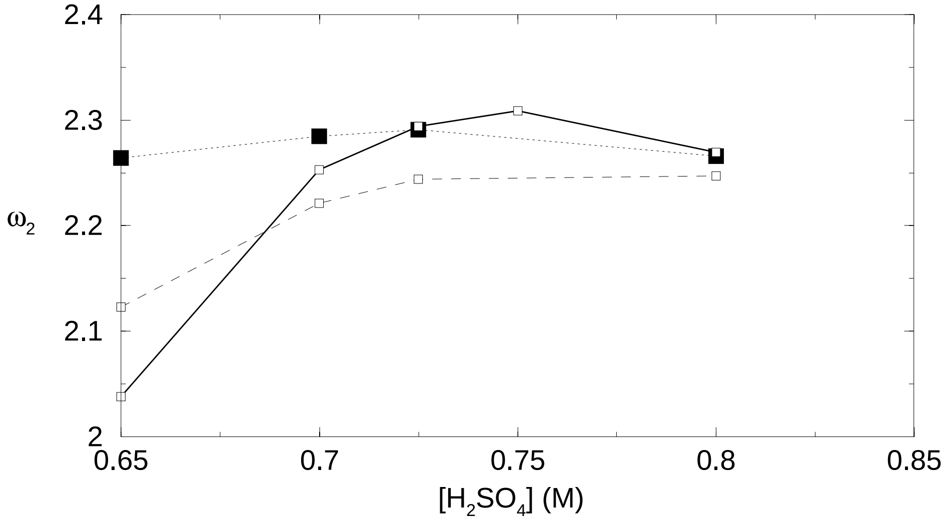

Fig. 5.9: The meandering frequency $\omega_2$ in a corotating frame as used in the normal form analysis by D. Barkley. The full curve gives the most accurate result based on measured $T_M, T_C$ with $\omega_2 = 2\pi(1/T_M + 1/T_C)$. The two other curves are estimates based on the approximate number $m$ of petals and $T_C$. The lower curve (dashed) used the wrong relation $2\pi/T_C * (m+1)/m$ (see Fig.7 in [71]). The filled squares give the corrected result $\omega_2 = 2\pi/T_C * m/(m-1)$. The latter matches the full curve at high [$H_2SO_4$] where $m$ becomes increasingly accurate.

(above) meandering trajectories. Variation of $\gamma_0$ does not alter the former but the latter curve and shifts the codimension-two point along the locus of Hopf bifurcations. The primary frequency of the spiral rotation $\omega_1 = \langle\dot{\phi}\rangle$ is proportional to $\gamma_0$. The second frequency $\omega_2$ is selected by a possible limit cycle in the $(\xi, \zeta)$ subsystem and can be observed in a corotating (with $\omega_1$) coordinate system. For $\omega_1 - \omega_2 > 0$ (or $< 0$) the tip rotates in the same (opposite) direction as the source and the trajectory possesses inward (outward) petals. Ouyang observed outward petals and $\omega_2 > \omega_1$. This epicycloidal trajectory has a period $T_M = 2\pi/(\omega_2 - \omega_1)$ [68], see Appendix E. Since $\gamma_0$ solely affects $\omega_1$ one has small (large) $\omega_1$ and larger domains with outward (inward) petals for small (large) $\gamma_0$.

Ouyang *et al.* report $T_M, T_C$ and the corresponding tip trajectories [71], see Fig. 5.7. They count the number $m$ of petals of the meandering tip trajectory. This is not reliable near the onset of meandering where the tip trajectory is almost circular but $m$ becomes increasingly accurate at higher [$H_2SO_4$]. From these data the meandering frequency $\omega_2$ can be calculated (Fig. 5.9). Relations depending on $m$ will give only rough approximations at low values of [$H_2SO_4$].

Per main loop $m-1$ ($m+1$) periods of the wave are emitted in the case of outward (inward) meandering where the tip rotates in the opposite (same) direction as the main loop. The reason is the one rotation on the main loop that annihilates (adds) one period if the tip moves in the opposite (same) direction. Ouyang *et al.* assume $T_M = mT_C$ which looks intuitive but needs to be replaced by $T_M = (m-1)T_C$ or $T_M = (m+1)T_C$ for outward, respectively inward, meandering.

Fig. 5.9 compares the different results. For [$H_2SO_4$] $> 0.7$ where $m$ is rather accurate

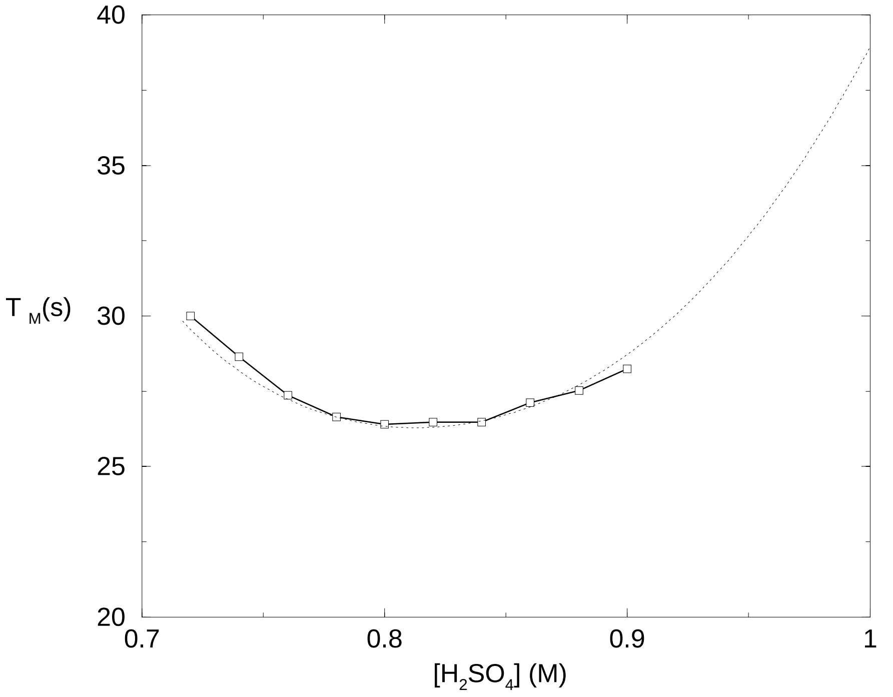

Fig. 5.10: The dependency $T_M([\mathrm{H_2SO_4}])$ is reproduced by the meandering instability. Comparison of experimental data (squares) from Fig.3 in [70] and theoretical data (dashed curve) obtained from numerical integration of Eqs. (5.5) along the dot-dashed curve (5.6) in Fig. 5.8.

we observe satisfactory agreement between $\omega_2$ computed from $T_M, T_C$ measured far away from the source (full curve) and $\omega_2$ computed from $m, T_C$ (filled squares). Hence the tip trajectory is in phase with the modulation in the far field. This supports the idea that the meandering source triggers the modulations in the wave field of the spiral.

Fig. 5.10 shows the variation of $T_M$ along the dot-dashed curve in the parameter plane Fig. 5.8. A parameter mapping

$$\begin{aligned} \gamma_o &= 6 \\ \alpha_2 &= -18\alpha_1 + 31.6 \\ [\mathrm{H_2SO_4}]/\mathrm{M} &= 0.85\alpha_1 - 1.25 \end{aligned} \tag{5.6}$$

was chosen to reproduce the experimental data. The modulation period $T_M$ decreases (increases) at lower (higher) $[\mathrm{H_2SO_4}]$. If increasing concentration $[\mathrm{H_2SO_4}]$ changes the parameters $\alpha_1$ and $\alpha_2$ in a similar way as suggested by Eq. (5.6) then the observed dependency of $T_M$ is caused by a single mechanism : the meandering instability; the minimum of $T_M$ appears naturally. Ouyang *et al.* mention the possibility of different mechanisms interchanging at $[\mathrm{H_2SO_4}]$=0.8M [70] to explain the minimum of $T_M$. This is not necessary.

The tip of the rigidly rotating spiral moves along a circle around the stationary source $(x_S, y_S)$. For the meandering spiral past the Hopf bifurcation (full curve in Fig. 5.8) the source is no longer stationary. To lowest order the source moves along a circle. This led to the caricature [68] “Moon-Earth (-Sun)” for the relation of tip and source : the tip (moon)

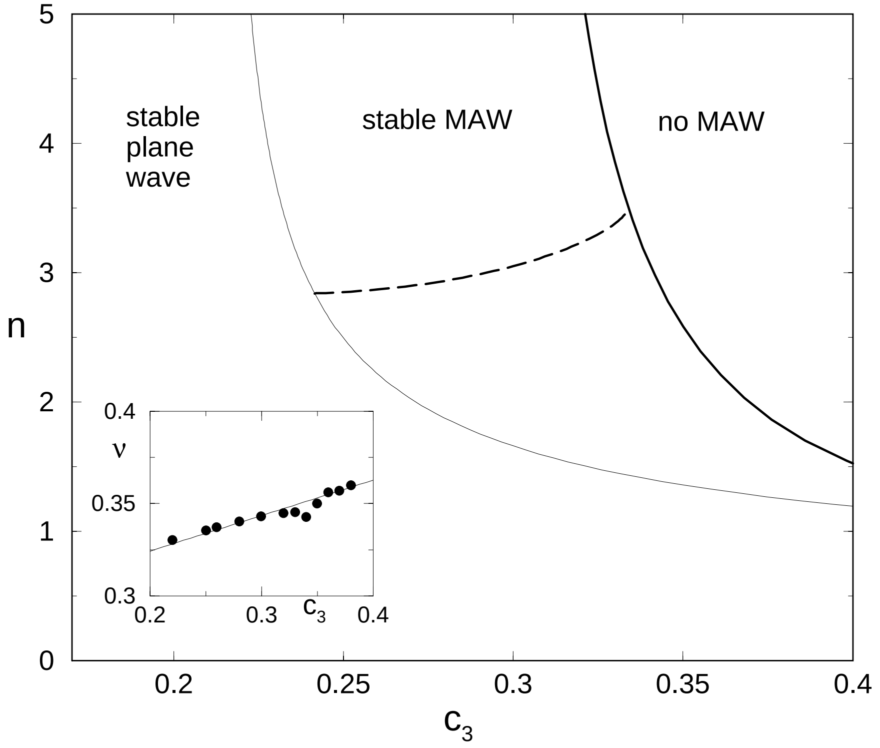

Fig. 5.11: Length scale ratio $n = P * \nu / 2\pi$ versus $c_3$ for fixed $c_1 = 3.5$. Stable MAWs exist between Hopf (thin full) and saddle-node (thick full curve). Fixing $T = T_M$ selects MAWs along the dashed curve. The inset shows the wavenumber $\nu$ as measured in one-dimensional simulations and calculated from Eq. (5.4).

orbits the source (earth) which moves around a center (sun). In Appendix E the trajectory of the source

$$x_S(t) = R_S \cos 2\pi t / T_M \tag{5.7}$$

is derived. In the one-dimensional simulations below we will force the wave source to oscillate as Eq. (5.7). The movement in the perpendicular direction $y_S(t)$ has little influence on the wave field far away from the source and we neglect this.

## 5.5 MAWs and Meandering in 1D Simulations

In this Section we will illustrate stable super-spirals and their breakup in one-dimensional simulations with an appropriate choice of boundary conditions. As mentioned before dimensionless quantities such as length or time scale ratios are not altered by scaling of space and time when deriving the amplitude equation. For the ratio of phase and group velocity on can get a rough estimate.

$$v_{ph} = \omega / q \tag{5.8}$$

$$v_{gr} = \partial\omega / \partial q \tag{5.9}$$

$$\frac{v_{ph}}{v_{gr}} = \frac{1}{2} - \frac{c_3}{2q^2(c_1 + c_3)} \tag{5.10}$$

Velocities of MAWs in the CGLE continuously deviate from the above result as their periods become shorter and as the modulations develop past the Hopf bifurcations (see Fig. 5.5c,d). Still $v_C/v$ stays close to or below 1/2. In the experiment $v_C/v \approx 2$ was observed [70]. Therefore it is only possible to either fit the ratio of spatial periods $n = P * \nu/2\pi$ or the ratio of temporal periods $T/T_C$. Clearly this is a drawback of the amplitude equation.

The reasons for slower modulations or faster carrier waves in the experiments can be curvature effects on the velocities, discrepancies in the wave number selection between the one- and two-dimensional systems or a feedback of the meandering tip motion on the wave number selection mechanism. Furthermore the amplitude description is rigorous only near the onset of oscillations but may quantitatively deviate from the finite amplitude situation in the studied experiment. These quantitative discrepancies may effect both the wave number selection mechanism of the wave source as well as the properties of modulated amplitude waves, *e.g.*, their velocities.

However, we believe the mechanisms and solutions as well as their bifurcation structure qualitatively are the same in the experimental oscillatory system and the amplitude description (CGLE). We consider these mechanisms as very robust with respect to parameter variations since MAWs with $\nu = q(c_1, c_3)$ exist for a broad range of parameters (shaded area in Fig. 5.6).

In order to illustrate the scenario we choose to fit the experimentally observed ratio of length scales $n$ (see thick curve in Fig. 5.1d) and will underestimate the time scale ratio. In the following we arbitrarily fix the parameter $c_1$ and vary $c_3$ to include stable super-spirals. In particular we choose the parameter mapping :

$$\begin{aligned} c_1 &= 3.5 \\ c_3 &= \frac{1}{2}\left[\mathrm{H_2SO_4}\right]/\mathrm{M} - 0.1 \\ T_M &= 42 - 135c_3 + 215c_3^2 \end{aligned} \tag{5.11}$$

where $T_M$ also possesses a minimum close to $c_3 = 0.3 \hat{=} [\mathrm{H_2SO_4}] = 0.8\mathrm{M}$ (see Fig. 5.14).

The results of the bifurcation analysis of the MAWs with $T = T_M$ are summarized in Fig. 5.11. Stable MAWs (dashed) only exist within an interval of $c_3$ limited by Hopf (thin full) and saddle-node (thick full curve) bifurcations. The inset compares the wavenumber $\nu$ (dots) measured in the simulations below and the analytical result Eq. (5.4) used for the bifurcation analysis. Both are in good agreement.

We performed simulations of the one-dimensional CGLE. Instead of fixing the left boundary $A(x = 0, t) = 0$ as in Fig. 5.3 the boundary condition now mimics the moving source. Since there exist no meandering spiral waves in the two-dimensional CGLE we can not use a time series of a point close to the source of a two-dimensional simulation as the boundary condition of the one-dimensional equivalent. We apply a temporal oscillation with period $T_M$ following Eqs. (5.11). Eq. (5.7) $x_S = R_S \cos 2\pi t/T_M$ is used to set $A(x \leq x_S, t) = 0$. $R_S$ is chosen between 0 and 5 as indicated below. For large $R_S$ one can get additional phenomena, *e.g.*, breakup near the source. Fig. 5.12 shows the resulting space time plots and Fig. 5.13 the corresponding profiles.

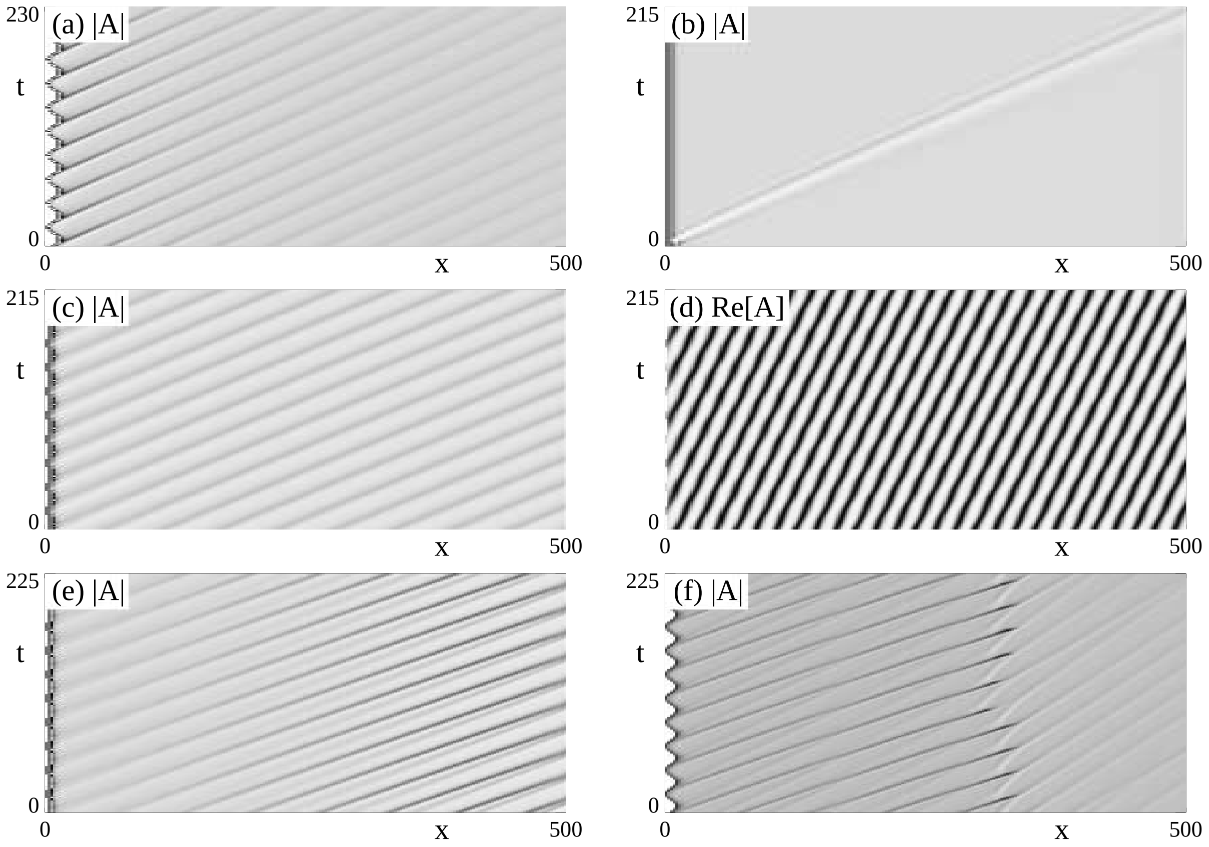

Fig. 5.12: Space time plots of simulations with oscillating left boundary ($A(x \leq x_S, t) = 0$). (a) $c_3 = 0.22, R_S = 5, T_M < T_{HB}$ lies before the Hopf bifurcation and even strong disturbances decay. (b) $c_3 = 0.26, R_S = 0, T_M > T_{HB}$ and the unmodulated plane wave is recovered due to the convective instability. Note, an initial disturbance grows and leaves the system. (c,d) $c_3 = 0.26, R_S = 0.5$, modulations grow and saturate as soon as meandering sets in. (e) $c_3 = 0.4, R_S = 0.5, T_M > T_{SN}$ lies beyond the saddle-node bifurcation but breakup is not visible in the short system. (f) $c_3 = 0.4, R_S = 5$ gives breakup at $x \approx 300$. Note the strongly oscillating boundary (white).

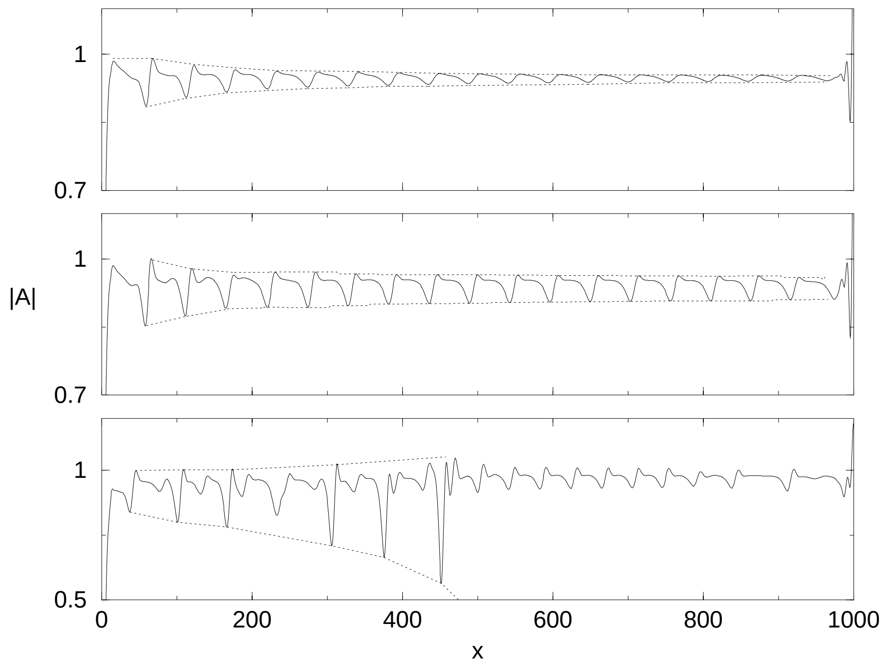

Fig. 5.13: Spatial profiles of the final state of the simulations with $R_S = 3$. Full curves denote $|A|(x, t = 500)$ and dotted curves are guides to the eye. (a-c) correspond to $c_3 = 0.22, 0.3, 0.4$, respectively.

If the period of the modulation would be selected solely by the stability properties of the wave field then one would expect a period similar to the fastest growing mode independent of the applied period $T_M$. The short calculations uses Eqs.(1.22),(1.29),(1.30) and we get $T_{HB} = P_{HB}/(v_g - \Omega_g k_{HB}^2)$ and for the fastest growing mode (maximum of Re$[\lambda_k]$) $T_{fastest} = \sqrt{2}P_{HB}/(v_g - \Omega_g k_{HB}^2/2)$. This mode is denoted by the dot-dashed curve in Fig. 5.14. The symbols representing the results of the simulations do not follow this prediction. Instead from Fig. 5.14 it is evident that the periodic meandering of the source selects the temporal period $T = T_M$.

For small $T_M$ (Figs. 5.12a and 5.13a) the small disturbances caused by the oscillating source decay and a nonmodulated wave field is emitted. The two-dimensional analogon is the common meandering spiral. Note, the wave field may be convectively unstable against long periods but these are not excited. For intermediate $T_M$ (Figs. 5.12c,d and 5.13b) the disturbances grow and saturate. The wave field exactly represents a MAW (see also Fig. 5.15). In two dimensions this corresponds to the modulated spiral wave with a super-spiral structure of the modulation. For large $T_M$ (Figs. 5.12f and 5.13c) the disturbances grow unbounded and lead to defects in a finite distance $R_{BU}$ where $|A|$ occasionally reaches zero. In the two-dimensional system this corresponds to the super-spiral-breakup.

Symbols in Figs. 5.14,5.16 correspond to individual simulations as in Figs. 5.12 and 5.13. The leftmost circle corresponds to $T_M < T_{HB}$ and a stable unmodulated wave was observed independent if $R_S = 0$ or $R_S > 0$. Measurements refer to the transient decay. The second circle also corresponds to an unmodulated wave if $R_S = 0$ as in the experiment at $[H_2SO_4]$=0.70. However for $R_S > 0$ we observe a saturated MAW in agreement with

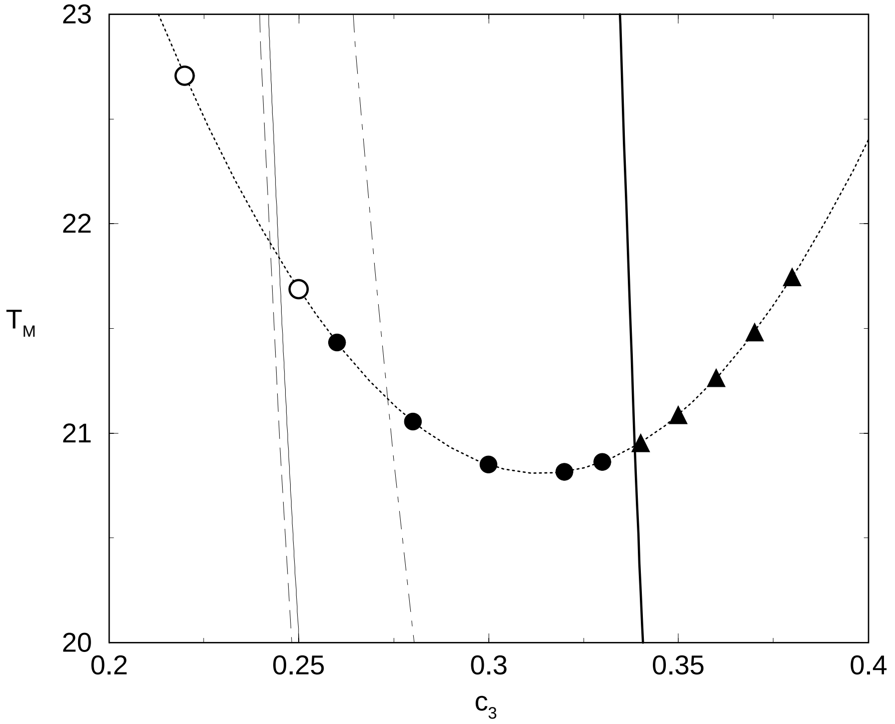

Fig. 5.14: Temporal period $T$ of the modulation far away from the source. Hopf bifurcation (thin full curve) and its analytical approximation (thin dashed), saddle-node bifurcation (thick full), fastest growing mode (dot dashed) and the period of meandering (dotted) are shown. Symbols correspond to simulations and are explained in the text.

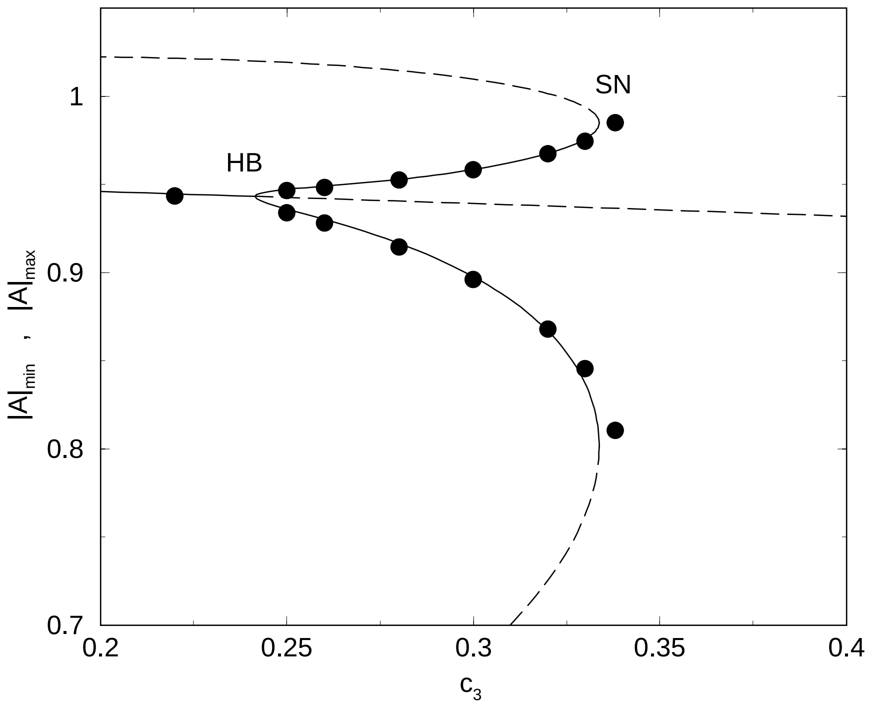

Fig. 5.15: Bifurcation diagram (curves) of MAWs with $T = T_M(c_3)$. Full (dashed) curves denote stable (unstable) solutions. Symbols denote measurements from the simuations with $R_S = 0.5$. The Hopf bifurcations occurs at $c_3 = 0.24$ and the saddle-node bifurcation at $c_3 = 0.334$. The rightmost dot corresponds to a simulation with $c_3 = 0.338$ where no breakup was observed in the finite system $L = 10.000$.

$T_M > T_{HB}$. The dots also refer to saturated MAWs for $R_S > 0$. For $c_3 \geq 0.34$ we observe breakup of the modulated wave in a system of size $L = 10.000$. Here $T_M > T_{SN}$ and measurements in the transient are denoted by triangles. The agreement of transitions between different states of the spiral and the bifurcation analysis of the MAWs is satisfactory. For $R_S > 0$ and $T_M < T_{HB}$ the modulations decay, for $T_{HB} < T_M < T_{SN}$ super-spirals are formed and for $T_M > T_{SN}$ the super-spirals break up.

In the bifurcation diagram Fig. 5.15 the maximum and minimum modulus of MAW profiles are plotted. The dots are measured values from simulations with $R_S = 0.5$ and are valid for any $0 < R_S < 5$. For $c_3 \geq 0.34$ the modulus does not saturate and defects are formed that break up the wave. Also these quantities show satisfactory agreement. For $R_S = 0$ ,*i.e., without* meandering we always obtain the *un*modulated plane wave.

The direct comparison with the experimental data is presented in Fig. 5.16. Increasing [$H_2SO_4$] the supercritical Eckhaus instability appears first (at [$H_2SO_4$]=0.69M) while the meandering instability occurs later (at [$H_2SO_4$]=0.72) where the wave train is convectively unstable. In the experiment the convectively unstable spiral appears stable since the source is stationary and relevant perturbations are missing. This is in agreement with early work in the group of Kramer [166]. Above [$H_2SO_4$]=0.72M the modulation rapidly increases with [$H_2SO_4$] since past the Hopf bifurcation MAWs already aquired a finite amplitude. Compare Fig.4 in [70].

Fig. 5.17 shows the breakup radius $R_{BU}$ for fixed $R_S = 0.5$. It decreases with the distance

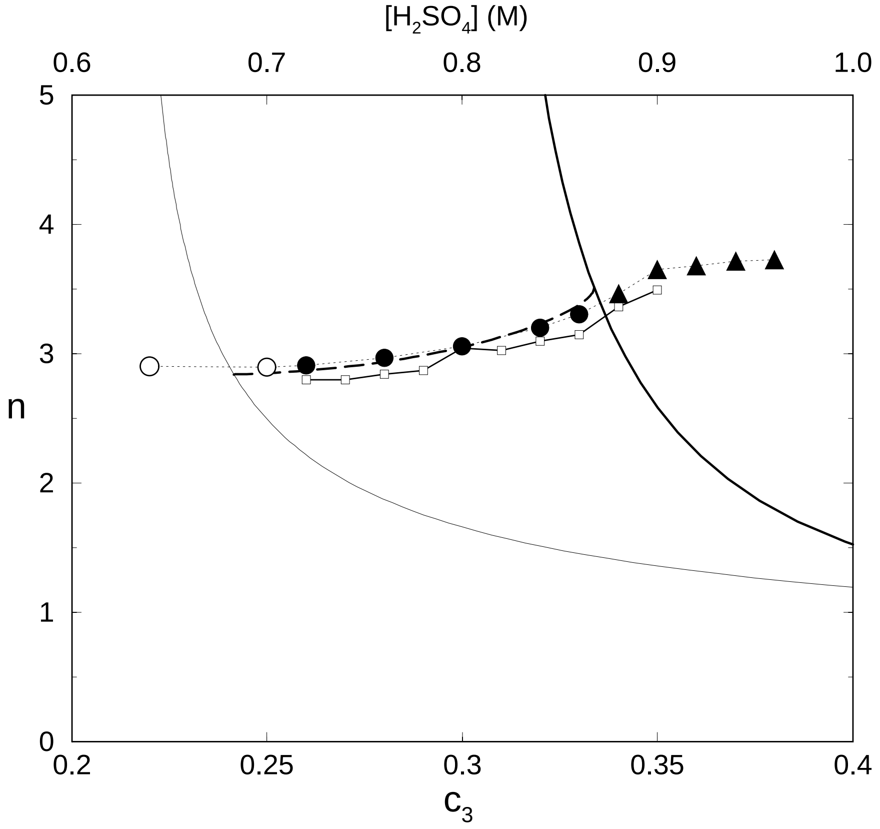

Fig. 5.16: Comparison of results from bifurcation analysis and simulations in terms of the length scale ratio $n$. Curves are as in Fig. 5.11. Symbols refer to the simulations as in Fig. 5.14. Open squares denote the experimental observations as in Fig. 5.1d which may be fitted by the numerics. However, the comparison is not quantitative since the time scale ratio of the super-spirals is underestimated as discussed in Sec. 5.5.

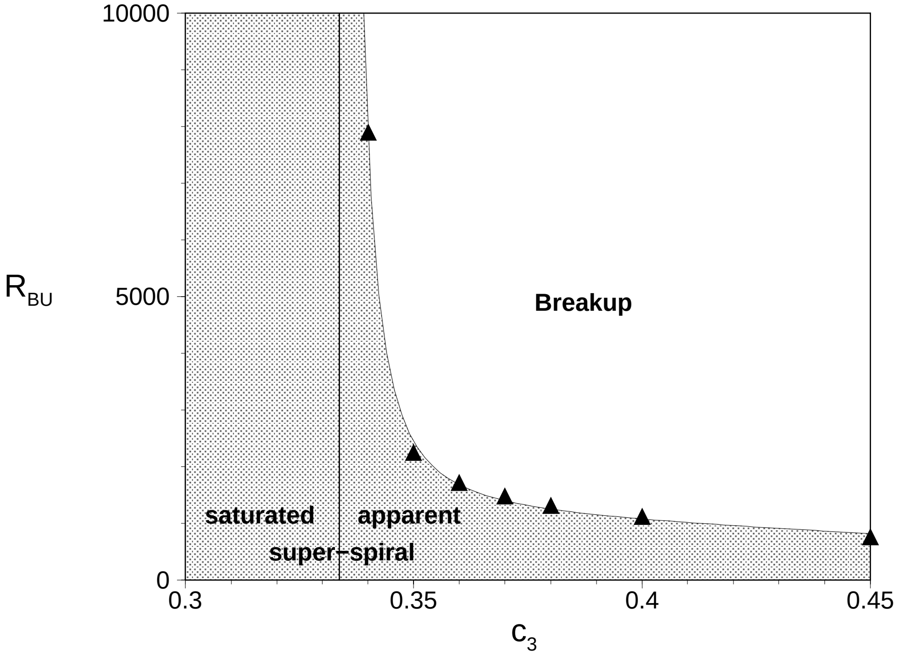

Fig. 5.17: The breakup radius $R_{BU}$ decreases with distance above threshold, the saddle-node bifurcation (vertical line at $c_3 = 0.334$). In systems of size within the shaded area one still observes (apparent) super-spirals with a long plateau of MAWs similar to that at the saddle-node bifurcation. $R_S = 0.5$ is fixed in these simulations (triangles). The curve is a guide to the eye.

from the saddle-node bifurcation and with increasing $R_S$. For $x < R_{BU}$ a long plateau of an almost saturated modulation remains until it eventually developes defects. This is due to the slow dynamics near the saddle-node bifurcation (see Fig. 5.15). In short systems of size smaller than $R_{BU}$ one does not notice the breakup threshold (Fig. 5.12e). It apparently shifts to higher values of the parameter. This is the reason why the experimental data of saturated super-spirals extend beyond the saddle-node curve in Fig. 5.16. If $R_S$ is increased then the breakup radius decreases at fixed $c_3$. This is illustrated in Fig. 5.12f for $R_S = 5$ and $c_3 = 0.4$.

## 5.6 Conclusion

We have investigated super-spiral breakup in oscillatory media by means of normal forms. Stable super-spirals are the cooperative effect of both the meandering instability (Barkleys normal form) and the supercritical Eckhaus instability (complex Ginzburg-Landau equation). The period of meandering $T_M$ excites the mode with $T = T_M$ in the wave field. The transition from rigidly rotating spirals to super-spirals and their breakup are determined by the coalescence of $T_M$ with $T_{HB}, T_{SN}$ which all vary with the parameters. The scenario is rather robust since it does not depend on details of the intersecting curves ($T_M, T_{HB}, T_{SN}$ as function of parameters).

Depending on parameters (*e.g.*, with subcritical Eckhaus instability) other breakup scenarios skipping the super-spirals are possible. Then no stable MAW solutions exist that could bound the growth of perturbations. The properties of the plane wave although convectively unstable then lead to breakup in a finite distance for $T_M > T_{HB}$.

Only in rare cases the two required instabilities may occur at the same values of the parameters. Interpreting the experiments [70, 71] we conjecture the Eckhaus instability to occur before the onset of super-spirals (Fig. 5.16). The latter happens at the meandering instability. Also we see no reason to distinguish areas $C_1$ and $C_2$ in the phase diagram Fig.1 in [71]. The period $T = T_M$ in the wave field is solely determined by a single mechanism, the meandering.

In order to test our conjecture further experiments should study different geometries for the same values of chemical concentrations. Since meandering is a purely two-dimensional effect one can discriminate its onset from that of the Eckhaus instability which is present in the one-dimensional system already. Stable MAWs should also persist in an annular or linear reactive channel (see also Section 4).

# 6 Bifurcation Analysis of Calcium Bursts

## 6.1 Introduction

Information encoding in the cell is one aspect of present day research on biological systems that can benefit from a dynamical systems approach. There are more than a thousand different hormones and specific receptors an organism uses to control its actions. Inside a cell a particular process has to be activated by a hormone which shortly binds to the specific receptor on the membrane and then detaches to activate other cells as well. Information within the cell is encoded in the dynamics of the concentrations of a few messenger species,*e.g.* cAMP, NO· radicals and $Ca^{2+}$ ions, rather than in the presence or absence of individuals out of a vast number of messengers [86, 87]. $Ca^{2+}$ alone is the second messenger for half of the hormones and the concentration $[Ca^{2+}](t)$ was experimentally observed to oscillate with the frequency and pulse shape encoding the specific hormone [88]. At low levels of stimulation $[Ca^{2+}](t)$ shows periodic spikes with increasing frequency as the stimulation raises. This feature is called frequency encoding. At higher stimulation level $[Ca^{2+}](t)$ develops complex *bursts*,*i.e.* periodic excitations with an intricate sub structure. Finally a chaotic time series is observed before the cell turns into an overstimulated staedy state. See Fig. 6.1 for an experimental example of bursting $[Ca^{2+}](t)$ derived from the intensity signal of a bioluminescent $Ca^{2+}$ indicator in incubated hepatocytes of rat. Many metabolic and genetic processes in the cell depend on $[Ca^{2+}](t)$ and will be altered accordingly [198]. A similar model of the calcium dynamics was recently analysed by T. Haberichter *et al.* [199].

Fig. 6.2 represents a schematic drawing of the cell with a few elements important for $[Ca^{2+}](t)$ regulation. For more details see [200, 201]. The intracellular space (cytosol) is heterogeneous containing networks of interior membranes and organelles. Moreover $Ca^{2+}$ is released and taken up at discrete locations, channels and pumps. However, in the first approach the heterogeneities may be neglected because the examined phenomenon occures on a time scale slow enough for $Ca^{2+}$ to diffuse and reach a rather homogeneous distribution. Here the bursting $[Ca^{2+}](t)$ is a temporal rather than spatio-temporal pattern. More sophisticated attempts will also consider heterogeneities [202].

Recently a model was put forward by U. Kummer *et al.* [88] that captures the essential mechanisms that regulate cytosolic calcium concentration $[Ca^{2+}](t)$ and thereby influence signal transduction,*i.e.* the response of a cell to very low concentrations of hormones de-

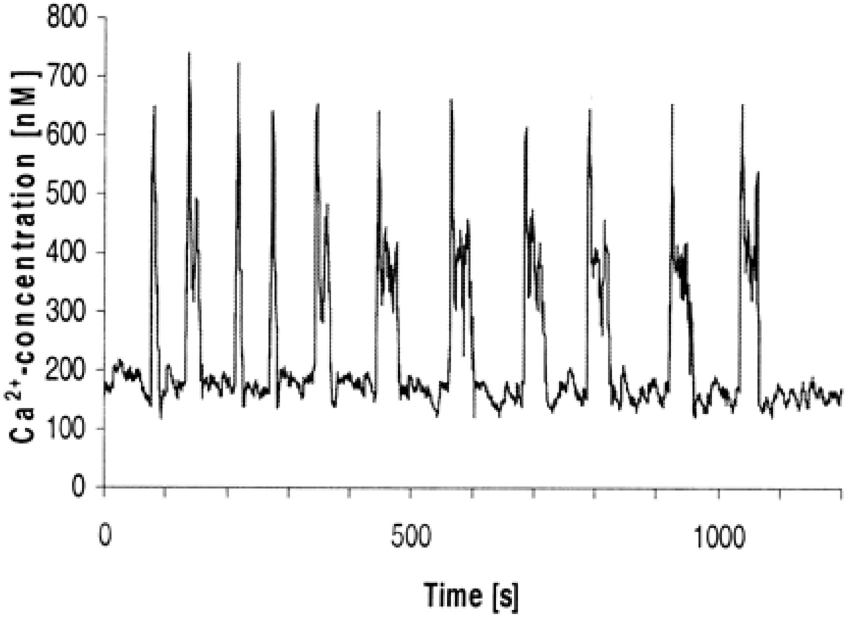

Fig. 6.1: Experimental observation of bursting calcium concentration in hepatocytes of rat. Note the smaller secondary spikes following each large initial spike.

livered by the blood stream. Section 6.2 will introduce the model equations. U. Kummer *et al.* studied this model by numerical integration. We will supplement their results by a bifurcation analysis of the temporally periodic solutions that represent the oscillations of $[\mathrm{Ca}^{2+}](t)$. The results of the bifurcation analysis are presented in Section 6.3. The oscillations emerge sinusoidal from a supercritical Hopf bifurcation of the steady state. Near this onset of oscillations in an extended system with the same local kinetics could again be described by the complex Ginzburg-Landau equation as studied in the previous chapters. Away from the Hopf bifurcation the bursts deviate much from a simple oscillation and this complex behavior is of special interest since it is supposed to encode information. Therefore the dynamics has to be studied in the complete model and this system serves as an example for a situation where the amplitude equations approach is not appropriate. Still the calcium bursts may be considered complex patterns in an uniform oscillatory system. The bursts at higher values of the control parameter correspond to complicated limit cycles that will be analysed in more detail in Section 6.4. During a burst the individual variables change on different time scales and this feature will be used to better understand and classify the complicated dynamics. For an overview of bursting behavior and the classification scheme see J. Keener and J. Sneyd [28].

## 6.2 The model

The model describes the temporal evolution of the concentrations of the four quantities that are most relevant for the calcium dynamics (see Fig 6.2). As in other established models [203, 204], it is supposed that through binding of a hormone to the extracellular side of a

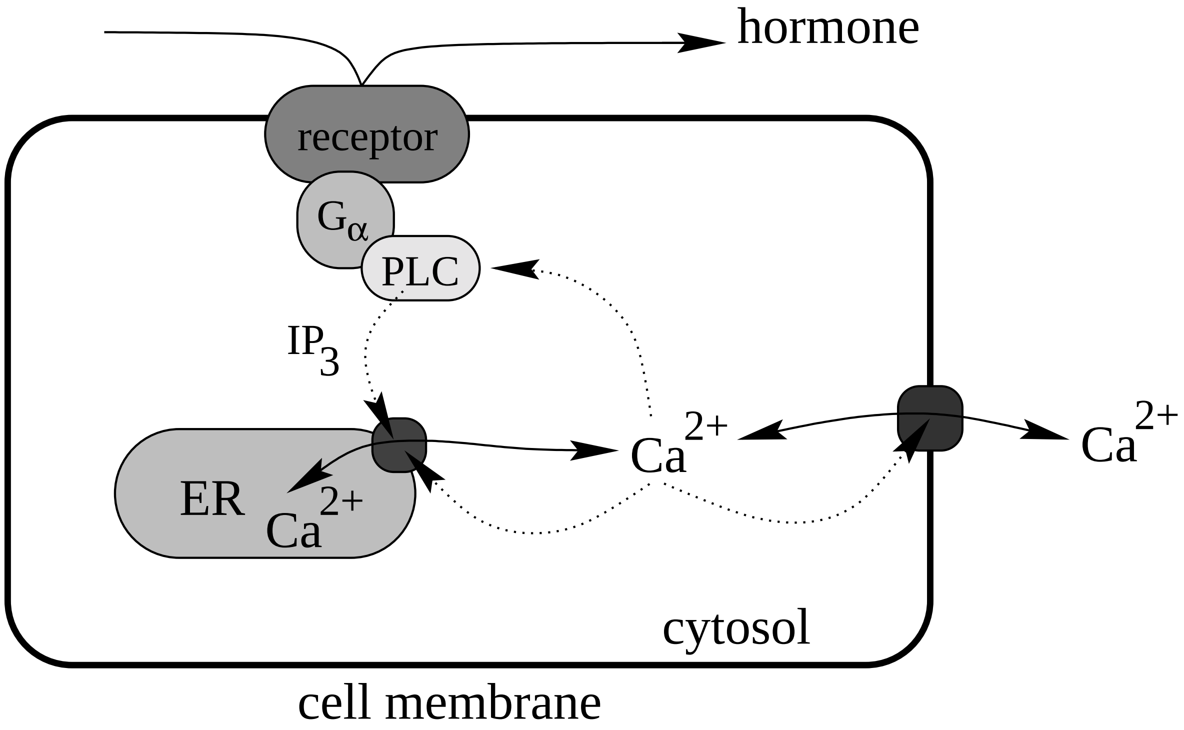

Fig. 6.2: Schematic drawing of the cell with a membrane bound receptor (top) and the endoplasmic reticulum (ER). Dotted arrows denote the main influences on the $Ca^{2+}$ fluxes (solid arrows) that control the dynamics of $[Ca^{2+}](t)$ in the cytosol.

membrane-bound receptor molecule, the $G_\alpha$-subunit of the receptor coupled G-protein is activated. The activated G-protein in turn stimulates a phospholipase C (PLC) which catalyzes formation of inositol-1,4,5-triphosphate ($IP_3$). $IP_3$ binds to receptors of intracellular stores of $Ca^{2+}$ (endoplasmic reticulum) opening their calcium channels. This results in an increased flux of calcium ions into the cytosol. Besides $IP_3$ also $Ca^{2+}$ ions are needed to activate the channels on the ER whereas a high concentration of $Ca^{2+}$ inhibits the channels. This autocatalytic process is called *calcium induced calcium release* (CICR). Further interactions inside the cytosol as well as uptake and release of $Ca^{2+}$ across the membrane have also been incorporated. A feedback loop couples the dynamics of intracellular $Ca^{2+}$ back to the activation of the $G_\alpha$-subunit. Thereby oscillations of $[Ca^{2+}](t)$ also influence the PLC and the concentration of $IP_3$. All individual processes have been observed experimentally. The corresponding terms in the equations represent simple Michaelis-Menten kinetics [24, 28] for enzyme catalysed reactions.

In the full model (6.1)-(6.4) below $a(t)$ denotes the concentration of active $G_\alpha$-subunits, $b(t)$ denotes the concentration of active PLC, $c(t)$ denotes the concentration of free calcium in the cytosol and $d(t)$ denotes the concentration of calcium in the intracellular stores. $IP_3$ is assumed to adiabatically follow the dynamics of active PLC and so it is not considered as a separate variable.

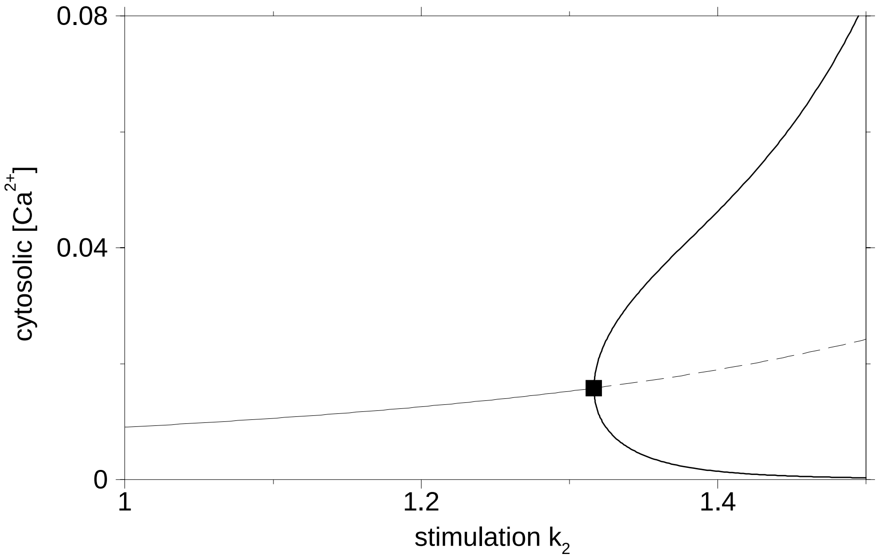

Fig. 6.3: Bifurcation diagram showing maximum and minimum of cytosolic $[\mathrm{Ca}^{2+}](t) = c(t)$ (thick curves). The steady state (thin curve) is stable below the Hopf bifurcation (square) and unstable above. The core model (6.5)-(6.7) was used.

$$\frac{\mathrm{d}a}{\mathrm{d}t} = k_1 + k_2 a - \frac{k_3 ab}{a + k_4} - \frac{k_5 ac}{a + k_6} \tag{6.1}$$

$$\frac{\mathrm{d}b}{\mathrm{d}t} = k_7 a - \frac{k_8 b}{b + k_9} \tag{6.2}$$

$$\frac{\mathrm{d}c}{\mathrm{d}t} = \frac{k_{10} cbd}{d + k_{11}} + k_{12} b + k_{13} a - \frac{k_{14} c}{c + k_{15}} - \frac{k_{16} c}{c + k_{17}} \tag{6.3}$$

$$\frac{\mathrm{d}d}{\mathrm{d}t} = -\frac{k_{10} cbd}{d + k_{11}} + \frac{k_{16} c}{c + k_{17}} \tag{6.4}$$

The model contains 17 parameters estimated from experimental data. In dimensionless units the parameter values $k_1 = 0.09, k_3 = 0.64, k_4 = 0.19, k_5 = 4.88, k_6 = 1.18, k_7 = 2.08, k_8 = 32.24, k_9 = 29.09, k_{10} = 5.0, k_{11} = 2.67, k_{12} = 0.7, k_{13} = 13.58, k_{14} = 153, k_{15} = 0.16, k_{16} = 4.85, k_{17} = 0.05$ are fixed. We will study the behavior of this set of nonlinear ODEs under variation of the parameter $k_2$ which is of order 1. Parameter $k_2$ describes the stimulation from extracellular space, *i.e.* the concentration of the respective hormone. To represent the calculated solutions we choose to display the concentration $c(t)$ of $\mathrm{Ca}^{2+}$ in the cytosol.

## 6.3 Bifurcation analysis

To calculate periodic temporal behavior of the system (6.1)-(6.4) we again use a continuation scheme and the software package AUTO97 [161]. We start from a steady state solution that corresponds to a fixed point in the phase space. In the Eqs. (6.1)-(6.4) this fixed point

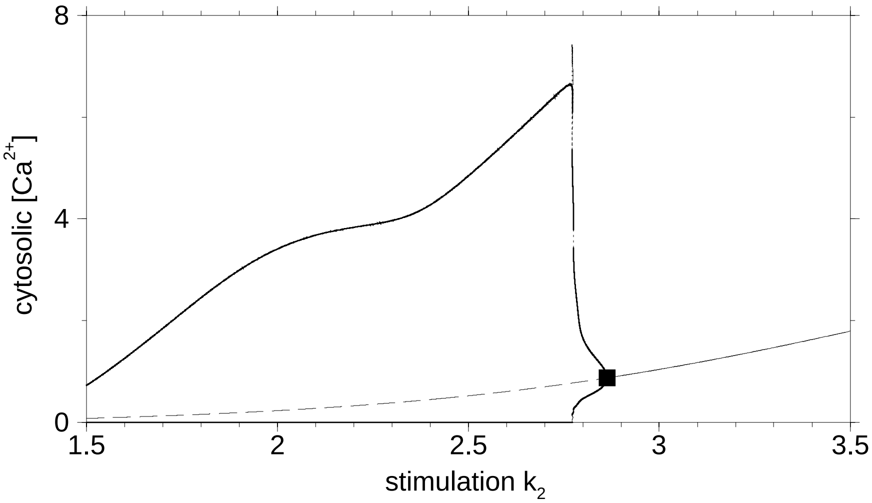

Fig. 6.4: Bifurcation diagram of the full model (6.1)-(6.4). Curves have the same interpretation as in Fig. 6.3.

does not exist for arbitrarily weak stimulations $k_2$. For $k_2 < 1.5$ the model predicts Ca$^{2+}$ to be continuously pumped into the stores (ER). Here the model needs to be modified to saturate the increase of $d(t)$.

U. Kummer *et al.* [88] also put forward a "core model" (6.5)-(6.7) which neglects the influence of $d(t)$ and drops the terms proportional to $k_{12}$ and $k_{16}$. The latter is justified by the observation $k_{14} \gg k_{16}$ but the other simplifications are crude approximations.

$$\frac{\mathrm{d}a}{\mathrm{d}t} = k_1 + k_2 a - \frac{k_3 ab}{a + k_4} - \frac{k_5 ac}{a + k_6} \tag{6.5}$$

$$\frac{\mathrm{d}b}{\mathrm{d}t} = k_7 a - \frac{k_8 b}{b + k_9} \tag{6.6}$$

$$\frac{\mathrm{d}c}{\mathrm{d}t} = k_{13} a - \frac{k_{14} c}{c + k_{15}} \tag{6.7}$$

Using the model (6.5)-(6.7) we varied the control parameter $1 < k_2 < 1.5$ in Eq. (6.5). At $k_2 = 1.32$ the fixed point $a = 1.01, b = 1.18, c = 0.016$ undergoes a Hopf bifurcation. It is stable at smaller $k_2$ and unstable at larger $k_2$. For $k_2 > 1.32$ stable limit cycles coexist with the unstable fixed point. In Fig. 6.3 the maximum and minimum Ca$^{2+}$ concentration of the oscillation are plotted together with the steady state.

For higher levels of the stimulation $k_2$, we continue to use the full model (6.1)-(6.4). In the interval $1.5 < k_2 < 2.86$ the oscillations become increasingly complex and develop secondary maxima in $c(t)$. At $k_2 = 2.86$ the branch of limit cycles returns back to the steady state branch and ends in another Hopf bifurcation. For $2.86 < k_2 < 3.5$ the steady state is stable and corresponds to overstimulation with constant high concentration of Ca$^{2+}$ in the cytosol. Fig. 6.4 shows the bifurcation diagram of the full model (6.1)-(6.4).

As long as the limit cycle shows simple spiking at low stimulation level $k_2$ the information may be encoded in the frequency of the temporal oscillation. Fig. 6.5 shows this dependency

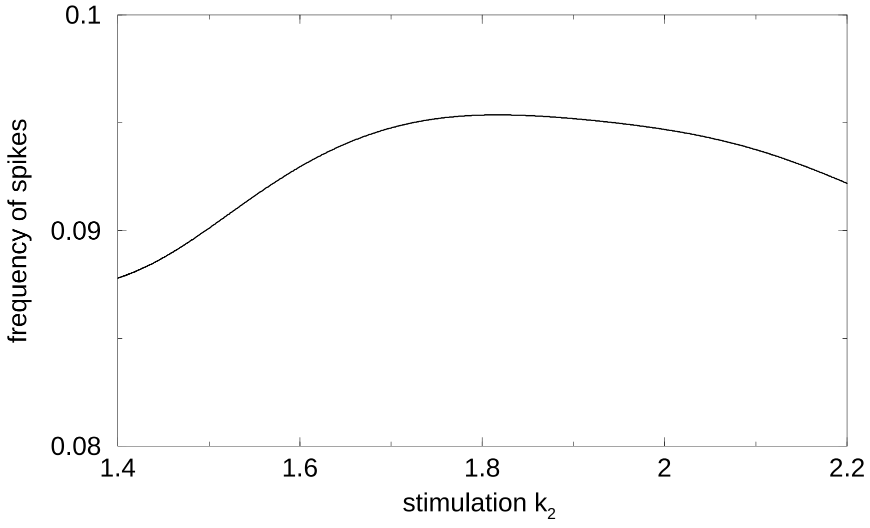

Fig. 6.5: Frequency (1/period) of the temporal oscillation in the full model (6.1)-(6.4).

for the calculated limit cycles. For $k_2 < 1.8$ the frequency increases with $k_2$ whereas it has a plateau and decreases for higher $k_2$. In order to associate two signals with the same frequency to a higher and lower $k_2$, respectively, these signals have to be distinguishable by their shape. This is possible due to the complex substructure that the bursts possess at higher $k_2$. As $k_2$ increases the secondary spikes develop continuously.

The contrast of simple spiking and complex bursting is illustrated in Fig. 6.6. We compare solutions of the full model (6.1)-(6.4) for $k_2 = 1.4$ (a)-(d) and $k_2 = 2.7665$ (e)-(h). The secondary maxima of cytosolic $[\mathrm{Ca}^{2+}](t) = c(t)$ are evident from Fig. 6.6(g). Hence information encoding in the model suggested by U. Kummer *et al.* [88] is achieved in two different ways, frequency encoding at low and additional shape encoding at higher stimulation level. The systematic bifurcation analysis thereby supplements the results obtained by U. Kummer *et al.* in numerical simulations.

## 6.4 Classification of bursting

In this section the complex bursting will be further analysed by separating the fast dynamics from the slow variations. We display the dynamics in the phase space projected onto the $b - c$ plane and compare the exact limit cycle with an approximation that we derive in the limit of a slow evolution in $b(t)$ compared to $c(t)$. From Fig. 6.6(f),(g) it is clear that the smooth oscillations of $b(t)$ evolve on a slower time scale than the secondary spikes of $c(t)$. Also $a(t)$ and $d(t)$ show fast but weak secondary spikes.

To derive an approximation to the burst we treat the variable $b(t)$ as a slowly varying parameter. This separation of time scales neglects feedback of the dynamic variables onto $b(t)$. The models simplify by dropping Eqs. (6.2) and (6.6). The remaining equations are again solved by AUTO97 which yields bifurcation diagrams for the dependence of cytosolic $\mathrm{Ca}^{2+}$ on the concentration of active PLC. Fig. 6.7 shows the results for the two models, the

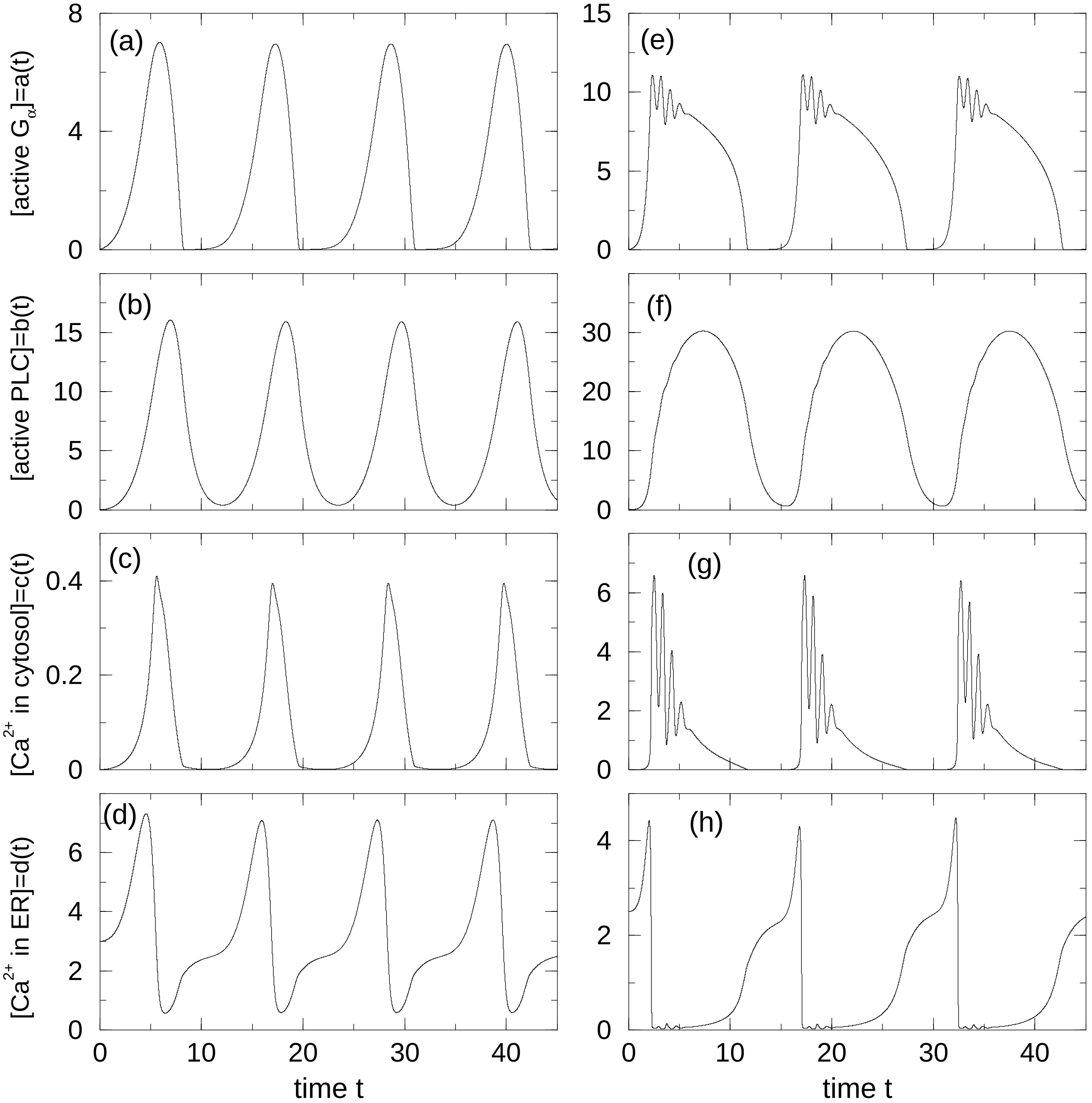

Fig. 6.6: Portraits of simple spiking (a)-(d) at $k_2 = 1.4$ and complex bursting (e)-(h) at $k_2 = 2.7665$ in the full model (6.1)-(6.4). The ordinate labels apply to both panels in each row.

full model (Fig. 6.7(a)) and the core model (Fig. 6.7(b)), respectively. Note, the parameter $k_2 = 2.7665$ is the same as in Fig. 6.6.

Both models (full and core) qualitatively show the same behavior. As $b$ is varied the steady state solution (thin curves) for $c$ shows a hysteresis limited by two saddle-node bifurcations (triangles). The lower branch is stable and the middle branch unstable. On the upper branch a Hopf bifurcation (square) gives raise to fast oscillations at lower values of $b$. The superimposed points denote the exact solution including the evolution of $b(t)$. The points should have followed the curves of the approximation if the time scale separation had developed stronger. In the present model the time scale separation is moderate and the points clearly deviate from the curves in Fig. 6.7.

However, we can gain a qualitative understanding of the complex structure of bursting $c(t)$ if we follow the points in clockwise direction as time progresses. Starting in a state of the burst where $c(t)$ is low (compare Fig. 6.6) the dynamics is close to the lower stable branch of $c(b)$. $c(t)$ follows this branch as $b$ decreases until the lower saddle-node bifurcation is exceeded. Then no stable steady state exists any more and the dynamics approaches the fast oscillation (thick curve) while $b$ increases again. The crossing of the saddle-node bifurcation triggers the burst of $c(t)$ which starts with a large spike followed by secondary spikes of decreasing amplitude. The spikes correspond to the oscillations in $c(b)$ and at larger $b$ these oscillations become smaller and continuously vanish in a Hopf bifurcation (square). After a short plateau (upper stable steady state) the saddle-node bifurcation at large $b$ is exceeded. The lower steady state is approached by $c(t)$ and $b$ starts to decrease. This completes one period of the burst.

The bifuraction diagram of the approximation $c(b)$ can be used to classify the bursting behavior according to a scheme by J. Rinzel [205] and R. Bertram *et al.* [206]. See also J. Keener and J. Sneyd [28]. Three types of bursting are distinguished which are often observed in the electrical activity of membranes,*e.g.* of neurons. In type I the burst starts in a homoclinic bifurcation where the branch of oscillations emerges with finite amplitude. In type II the active phase ends in a homoclinic bifurcation. The model studied here does not exhibit a homoclinic bifurcation in the parameter range of interest. Type III bursting starts at a subcritical Hopf bifurcation. Here the burst starts by exceeding a saddle-node bifurcation of the steady state branch and the first spike has the largest amplitude. The secondary spikes are smaller and via a reverse supercritical Hopf bifurcation the spikes vanish at an elevated level of $Ca^{2+}$. Hence the studied model may be considered as an example of a new type of bursting.

## 6.5 Conclusion

Two models of intracellular $Ca^{2+}$ oscillations by U. Kummer *et al.* were studied by bifuraction analysis and by an analysis of the fast dynamics in phase space. The full model should be slightly modified in order to saturate the $Ca^{2+}$ concentration in the stores at low stimulation level. Apart from this, both the full and the core model qualitatively yield the same results. Frequency and shape encoding of the stimulation level were found which

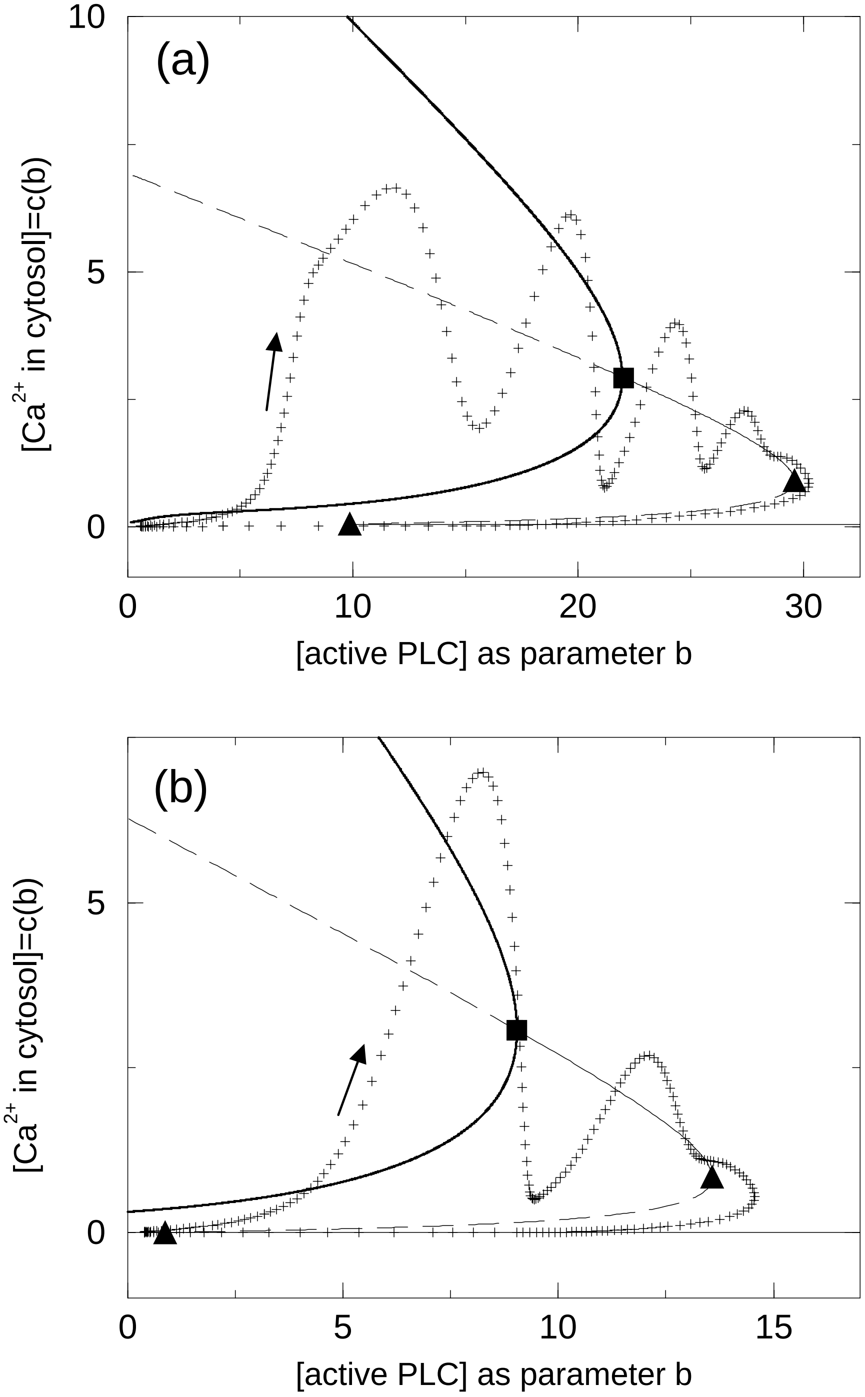

Fig. 6.7: Phase space representation of bursts for (a) $k_2 = 2.7665$ in Eqs. (6.1)-(6.4) and (b) $k_2 = 2.5$ in the core model Eqs. (6.5)-(6.7). The points (crosses) denote the exact solution which is parametrized by time in the clockwise direction following the arrow. The curves represent solutions after parametrization of $b$. Thin (thick) curves stand for steady states (fast oscillations) and dashed (full) curves indicate unstable (stable) solutions. The square denotes a Hopf bifurcation and the triangles denote saddle-node bifurcations.

supports the results by U. Kummer *et al.*.

The particular shape of intracellular $Ca^{2+}$ bursts in both models were found to originate at a saddle-node bifurcation of the unactivated state. This saddle-node bifurcation is exceeded when the concentration of active PLC drops below a critical value in the unactivated phase of the oscillation. As the burst proceeds the concentration of active PLC increases and a reverse Hopf bifurcation stops the secondary spiking. At another saddle-node bifurcation the intracellular $Ca^{2+}$ concentration returns to the unactivated state. To our knowledge this type of bursting is yet unclassified.

Clearly many questions remain to be explored. Further experimental progress in detecting low concentrations of intracellular substances will certainly uncover more dynamical phenomena in biological systems. Complex bursting has for example been observed by M. Hauser *et al.* [207] in the peroxidase-oxidase reaction as well as in the pH value of the hemin - hydrogen peroxide - sulfite reaction. The tools used in this Thesis may help in testing models and developing a deeper understanding of the mechanisms.

# 7 Summary and Outlook

The formation of complex patterns in extended oscillatory systems has been studied by means of bifurcation and stability analysis as well as numerical simulations. The investigations are based on the one-dimensional complex Ginzburg-Landau equation (CGLE) which constitutes a qualitative model system for many universal features of extended oscillatory systems. Near the supercritical onset of oscillations or traveling waves the equation yields quantitatively exact results.

In Chapter 1 an overview on pattern formation and previous results on the CGLE were given. Depending on parameters in the CGLE waves may become unstable. This Eckhaus instability was analysed by linear and weakly nonlinear approximations. In its supercritical case stable modulated amplitude waves (MAWs) coexist with the unstable waves above their instability. On the other hand spatio-temporal chaos has been observed in the CGLE for a wide range of parameter values.

In Chapter 2 the mechanism for transitions from phase to defect chaos in the one-dimensional CGLE was presented. Using the continuation software AUTO97 the MAWs are calculated as coherent structures, *i.e.* their shape does not change when described in a comoving reference frame. They form a continuous two-parameter family of solutions. The average phase gradient $\nu$ and the spatial period $P$ of the modulation parametrize the family. Only MAWs with $\nu = 0$ are relevant near the transition from phase to defect chaos. The existence of these MAWs is limited by a saddle-node bifurcation (SN). For decreasing periods the SN shifts to larger values of the parameters. MAWs of various period $P$ occur naturally in phase chaotic states. For periods beyond the SN, near-MAW structures occur which evolve toward defects. The MAW at the SN may be viewed as a critical nucleus for defect formation. The transition from phase to defect chaos takes place when the periods of MAWs in phase chaos are driven beyond their SN. By a linear stability analysis of MAWs two competing processes are identified. For MAWs of large $P$ the splitting instability tends to reduce the period an thereby delays defect formation. The interaction instability increases some periods of MAWs with small $P$ and promotes the formation of defects. It was shown that even unstable solutions play an important role in simulations. Arbitrary initial conditions quickly converge to the subset in phase space which is close to the unstable solutions. Phase chaos may be viewed as evolution along the unstable manifolds of MAWs. Comparing the linear growth rates of both instabilities yields an upper bound on the transition in parameter space. The curve in parameter space with the SN occuring at infinit period is established as lower bound on the transition. We conjecture that phase chaos persists in the thermodynamic limit for values of the parameters below the lower bound,*i.e.* where no saddle-node bifurcations occur. This result answers many questions of a controversial discussion in the literature. The existence of coherent structures and their SNs have also been analysed in various phase equations. Their the SN was shown to play the same role as a critical nucleus for the blow-up in the phase equation.

In Chapter 3 the results were extended to nonzero average phase gradient. Here MAWs are quasi-periodic structures that correspond to saturated modulations of Eckhaus unstable waves. Defect formation is again possible is the SN is exceeded. The SNs for MAWs with infinite period was established as a lower bound and the onset of the splitting instability at the SN as an upper bound for the limit of wound-up phase chaos. This explains the earlier observations by other authors of a maximum conserved phase gradient. Further investigations should consider the transition from regular to chaotic dynamics near the SN at small $\nu$. Here the statistical tools of Chapter 2 have to be applied.

In Chapter 4 various hydrodynamical experiments were discussed with emphasis on the possibilities to observe MAWs in these systems. Hydrothermal waves seem to be the most promising candidate. There the first MAWs have been obtained and further cooperation with these groups is in progress. The control of the spatial period of perturbations in the experiments will provide a much broader scenario than realized at present. The suggested scenarios of defect formations should be tested by such methods.

In Chapter 5 the obtained results on MAWs were compared to experiments in a chemical system, the oscillatory variant of the Belousov-Zhabotinsky reaction. Recently the observation of super-spiral concentration patterns has been reported in the literature. We presented a new and consistent interpretation of the existence of super-spirals as well as their breakup. In the radial direction the concentration pattern represents a MAW with $\nu$ determined by the wavenumber selection of the source and the period $P$ given by the frequency of the meandering motion of the source. If these parameters are selected below the Hopf bifurcation of the corresponding MAW then the perturbation decays in radial diraction and the rigidly rotating spiral wave is recovered far away from the source. For parameters between Hopf bifurcation and SN the perturbation saturates and a super-spiral structure results. If the SN is exceeded the super-spiral breaks up far away from the source and this distance decreases for parameters further above the SN.

In Chapter 6 a bifurcation analysis has been carried out for a model of a biological system, the complex oscillations of local calcium dynamics in the cell. The results on the existence of bursting calcium concentration verify and support findings that have recently been obtained by other authors via numerical simulations. The specific type of bursting was found to belong to a new yet unclassified group. Although the system is not extended it gives an example of complex oscillations that can not be described by an amplitude equation approach.

We found that the same tools as bifurcation and stability analysis may provide new insight in such diverse fields as hydrodynamics, chemistry and cell biology. Pattern formation and the dynamical systems approach will play a major role in the future exploration of complex dissipative systems.

# Appendix A Continuation software : AUTO97

First the principle of continuation is illustrated and then the application of AUTO97 [161] to the complex Ginzburg-Landau equation is explained including the developed FORTRAN codes.

## A.1 Continuation procedure

Given a nonlinear ordinary differential equation (ODE) with a selected parameter $\mu$

$$\frac{dx}{dt} = f(x, \mu) \tag{A.1}$$

and a known solution $x_0$ at an arbitrarily chosen $\mu = \tilde{\mu}$ with

$$\frac{dx_0}{dt} = 0 \tag{A.2}$$

then the stationary solutions $x_0(\mu)$ for all other values of $\mu$ can be computed by "continuation" in the parameter $\mu$. Eq.(A.2) is the fixed point condition and $x_0$ is called fixed point. The continuation procedure is an iterative algorithm that progresses in small steps $\delta\mu$. Each step involves an approximate prediction of the yet unknown $x_0(\tilde{\mu} + \delta\mu)$ and a subsequent correction to satisfy Eq.(A.2).

The prediction is derived from a Taylor-expansion of $x_0(\tilde{\mu} + \delta\mu)$ for small $\delta\mu$

$$x_0(\tilde{\mu} + \delta\mu) = x_0(\tilde{\mu}) + \left.\frac{\partial x_0(\mu)}{\partial \mu}\right|_{\tilde{\mu}} \delta\mu + \text{h. o. t.} \tag{A.3}$$

where the derivative incorporates the fixed point condition Eq.(A.2) for all solutions $x_0(\mu)$.

$$\begin{aligned} 0 &= f(x_0(\tilde{\mu}), \mu) && \text{(A.4)} \\ &= \frac{df(x_0(\tilde{\mu}), \mu)}{d\mu} && \text{(A.5)} \\ &= \frac{\partial f(x_0, \mu)}{\partial \mu} + \frac{\partial f(x_0, \mu)}{\partial x_0} \frac{\partial x_0(\mu)}{\partial \mu} && \text{(A.6)} \end{aligned}$$

In Eq.(A.6) the dependence of the system on the parameter $b$ (first term) is compensated by $\partial x_0(\mu)/\partial\mu$ in the last term.

$$\frac{\partial x_0(\mu)}{\partial\mu} = -\frac{\partial f(x_0,\mu)}{\partial\mu} \div \frac{\partial f(x_0,\mu)}{\partial x_0} \tag{A.7}$$

$$x_0(\tilde{\mu}+\delta\mu) \approx x_0(\tilde{\mu}) - \frac{\partial f(x_0,\mu)}{\partial\mu} \div \left.\frac{\partial f(x_0,\mu)}{\partial x_0}\right|_{\tilde{\mu}} \delta\mu \tag{A.8}$$

The correction step at fixed $\tilde{\mu}+\delta\mu$ applies the Newton- and/or Chord-method [9] to reveal the higher order terms (h. o. t.) in Eq.(A.3).

The above scheme can be expanded to solve sets of ODEs. AUTO97 can follow stationary solutions to a boundary value problem (BVP) through parameter space. The spatial coordinate is discretized on an adaptive mesh which results in a set of some hundreds of equations and numerical algebra is necessary to treat the large matrices. In each step AUTO97 also computes eigenvalues of the linearization around the obtained solution. These eigenvalues are used to detect bifurcations [9]. At a bifurcation AUTO97 can be forced to switch to an emerging branch of solutions. The numerical parameters of the discretization, bifurcation detection and stepping procedures need to be carefully controlled which requires some experience.

## A.2 Codes for complex Ginzburg-Landau equation

AUTO97 [161] is a software package that needs to include the following FORTRAN codes that are specific to the CGLE. The first three files are used to compute the velocity $v$ at HB as function of the perturbation wave length $P$ at the instability. Alternatively Eq.(1.30) can be used but this requires additional software. In the present form the result is efficiently obtained in AUTO97 compatible format. Further steps are explained below.
1.1 eck.f :

```
C-----------------------------------------------------------------------
C     Numerical analysis of the Eckhaus instability
C     of plane wave solutions to the CGLE.
C     brusch@mpipks-dresden.mpg.de             (2001)
C-----------------------------------------------------------------------
      SUBROUTINE FUNC(NDIM,U,ICP,PAR,IJAC,F,DFDU,DFDP)
      IMPLICIT DOUBLE PRECISION (A-Z)
      DIMENSION U(NDIM), PAR(*), F(NDIM), ICP(*)
C
C  3 ODE of 1st order
       U1=U(1)
       U2=U(2)
       U3=U(3)
C
C  parameters
       C1=PAR(1)
       C3=PAR(3)
       K =PAR(4)
       Z0=PAR(5)
       EPS=PAR(8)
C
C  phase and group velocity
```

```
       W =-C3+(C1+C3)*K*K
       C0=2*K*(C1+C3)*(1-EPS)
C
C  the equations
       F(1)=U2
       F(2)=-1/(1+C1**2)*((1+W*C1+Z0*C0*C1*U3)*U1
     &      +Z0*C0*U2+(C1*C3-1)*U1**3)/Z0**2+U1*(K/Z0+U3)**2
       F(3)=1/(1+C1**2)*(C1-W+Z0*C0*C1*U2/U1-Z0*C0*U3
     &      -(C1+C3)*U1**2)/Z0**2-2*(K/Z0+U3)*U2/U1
C
      RETURN
      END
C----------------------------------------------------------------------
      SUBROUTINE STPNT(NDIM,U,PAR)
      IMPLICIT DOUBLE PRECISION (A-Z)
      DIMENSION U(NDIM), PAR(*)
C
C  Initialize the equation parameters
       PAR(1)=3.5d0
       PAR(3)=0.0d0
       PAR(4)=0.25d0
       PAR(5)=1.0d0
       PAR(8)=0.01d0
C
C  Initialize the plane wave solution
       K=PAR(4)
       U(1)=SQRT(1-K**2)
       U(2)=0.000
       U(3)=0.000
C
      RETURN
      END
C----------------------------------------------------------------------
      SUBROUTINE BCND
      RETURN
      END
C
      SUBROUTINE ICND
      RETURN
      END
C
      SUBROUTINE FOPT
      RETURN
      END
C
      SUBROUTINE PVLS(NDIM,U,PAR)
      IMPLICIT DOUBLE PRECISION (A-Z)
      DIMENSION U(NDIM),PAR(*)
C  record the velocity
       PAR(2)=2*(PAR(1)+PAR(3))*PAR(4)*(1-PAR(8))
      RETURN
      END
C----------------------------------------------------------------------
```

## 1.2 r.eck.1 :

```
3 1 0 0                         NDIM,IPS,IRS,ILP
1   3                           NICP,(ICP(I),I=1,NICP)
5 4 3 2 1 6 0 0                 NTST,NCOL,IAD,ISP,ISW,IPLT,NBC,NINT
100 -1 5 -1 1                   NMX,RL0,RL1,A0,A1
100 2 2 8 7 3 0                 NPR,MXBF,IID,ITMX,ITNW,NWTN,JAC
1e-8 1e-8 1e-7                  EPSL,EPSU,EPSS
0.02 0.0001 0.5 1               DS,DSMIN,DSMAX,IADS
0                               NTHL,((I,THL(I)),I=1,NTHL)
```

```
0                               NTHU,((I,THU(I)),I=1,NTHU)
0                               NUZR,((I,UZR(I)),I=1,NUZR)
```

### 1.3 r.eck.2 :

```
3 1 2 0                         NDIM,IPS,IRS,ILP
4   3 8 11 2                    NICP,(ICP(I),I=1,NICP)
5 4 3 2 2 6 0 0                 NTST,NCOL,IAD,ISP,ISW,IPLT,NBC,NINT
100 -1 5 -1 1                   NMX,RL0,RL1,A0,A1
50 2 2 8 7 3 0                  NPR,MXBF,IID,ITMX,ITNW,NWTN,JAC
1e-8 1e-8 1e-7                  EPSL,EPSU,EPSS
-0.02 0.0001 0.5 1              DS,DSMIN,DSMAX,IADS
0                               NTHL,((I,THL(I)),I=1,NTHL)
0                               NTHU,((I,THU(I)),I=1,NTHU)
1                               NUZR,((I,UZR(I)),I=1,NUZR)
11 58.904862
```

The first run (`> @R eck 1`) detects a Hopf bifurcation (Eckhaus instability) with the corresponding wave length `PAR(11)` of the perturbation to the plane wave with wavenumber `PAR(4)` and chosen velocity $v$ via `PAR(8)`. This result has to be saved (`> @sv eck`) and the second run (`> @R eck 2`) computes a locus of all Hopf bifurcations for the different modes `PAR(11)`. The last command in file `r.eck.2` records the bifurcation for a chosen value of `PAR(11)`. The parameters `PAR(3), PAR(8)` and `PAR(11)` are needed to start (`> @r bif`) a branch of MAWs with the next two files.

### 2.1 bif.f :

```
C----------------------------------------------------------------------
C     Computation of a restart solution for a MAW branch.
C     brusch@mpipks-dresden.mpg.de                  (2001)
C----------------------------------------------------------------------
      SUBROUTINE FUNC(NDIM,U,ICP,PAR,IJAC,F,DFDU,DFDP)
      IMPLICIT DOUBLE PRECISION (A-Z)
      DIMENSION U(NDIM), PAR(*), F(NDIM), ICP(*)
C
C  3 ODE of 1st order
       U1=U(1)
       U2=U(2)
       U3=U(3)
C
C  parameters
       C1=PAR(1)
       C3=PAR(3)
       K =PAR(4)
       Z0=PAR(5)
       EPS=PAR(8)
C
C  phase and group velocity
       W=-C3+(C1+C3)*K*K
       C0=2*(C1+C3)*K*(1-PAR(4))
C
C  the equations
       F(1)=U2
       F(2)=-1/(1+C1**2)*((1+W*C1+Z0*C0*C1*U3)*U1
     &      +Z0*C0*U2+(C1*C3-1)*U1**3)/Z0**2+U1*(K/Z0+U3)**2
       F(3)=1/(1+C1**2)*(C1-W+Z0*C0*C1*U2/U1-Z0*C0*U3
     &      -(C1+C3)*U1**2)/Z0**2-2*(K/Z0+U3)*U2/U1
      RETURN
      END
```

```
C----------------------------------------------------------------------
      SUBROUTINE STPNT(NDIM,U,PAR)
      IMPLICIT DOUBLE PRECISION (A-Z)
      DIMENSION U(NDIM), PAR(*)
C
C  Initialize the equation parameters
       PAR(1)=3.50d0
C  start c3 a bit before the Hopf bifurcation
       PAR(3)=3.034591E-01
       PAR(4)=0.25d0
C  1/PAR(11) for the scaling of space to unit interval
       PAR(5)=1/58.904862
       PAR(8)=1.1321422551E-02
C
C  Initialize the plane wave solution
       K=PAR(4)
       U(1)=SQRT(1-K**2)
       U(2)=0.000
       U(3)=0.000
      RETURN
      END
C----------------------------------------------------------------------
      SUBROUTINE BCND(NDIM,PAR,ICP,NBC,U0,U1,FB,IJAC,DBC)
      IMPLICIT DOUBLE PRECISION (A-Z)
      DIMENSION PAR(*),ICP(*),U0(NDIM),U1(NDIM),FB(NBC)
C
C  periodic boundary conditions and pinning
       FB(1)=U0(1)-U1(1)
       FB(2)=U0(2)-U1(2)
       FB(3)=U0(3)-U1(3)
       FB(4)=U0(2)
C
      RETURN
      END
C----------------------------------------------------------------------
      SUBROUTINE ICND(NDIM,PAR,ICP,NINT,U,UOLD,UDOT,UPOLD,FI,IJAC,DINT)
      IMPLICIT DOUBLE PRECISION (A-Z)
      DIMENSION U(NDIM),UOLD(NDIM),UDOT(NDIM),UPOLD(NDIM)
      DIMENSION FI(NINT),ICP(*),PAR(*)
C
C  constraint on phase gradient
       FI(1)=U(3)
C
      RETURN
      END
C----------------------------------------------------------------------
      SUBROUTINE FOPT
      RETURN
      END
C----------------------------------------------------------------------
      SUBROUTINE PVLS(NDIM,U,PAR)
      IMPLICIT DOUBLE PRECISION (A-Z)
      DIMENSION U(NDIM),PAR(*)
C
C  write the velocities that will change along the MAW branch
       K=PAR(4)
       PAR(2)=2*(PAR(1)+PAR(3))*K*(1-PAR(8))
       PAR(6)=-PAR(3)+(PAR(1)+PAR(3))*K*K
      RETURN
      END
C----------------------------------------------------------------------
```

## 2.2 r.bif :

```
3 4 0 0                         NDIM,IPS,IRS,ILP
```

```
4   3 2 6 7                     NICP,(ICP(I),I=1,NICP)
150 4 3 2 1 6 3 0               NTST,NCOL,IAD,ISP,ISW,IPLT,NBC,NINT
1500 -1 5 -1 2                  NMX,RL0,RL1,A0,A1
100 2 2 8 7 3 0                 NPR,MXBF,IID,ITMX,ITNW,NWTN,JAC
1e-7 1e-7 1e-5                  EPSL,EPSU,EPSS
1e-8 1e-10 1e-8 1               DS,DSMIN,DSMAX,IADS
0                               NTHL,((I,THL(I)),I=1,NTHL)
0                               NTHU,((I,THU(I)),I=1,NTHU)
0                               NUZR,((I,UZR(I)),I=1,NUZR)
```

Using small steps (`1e-8`) the same Hopf bifurcation is detected in the BVP. The result is saved (`> @sv maw`) to be used (`> @r maw`) as restart solution by the next two files.

### 3.1 maw.f :

```
C----------------------------------------------------------------------
C     Continuation of a MAW branch.
C     brusch@mpipks-dresden.mpg.de              (2001)
C----------------------------------------------------------------------
      SUBROUTINE FUNC(NDIM,U,ICP,PAR,IJAC,F,DFDU,DFDP)
      IMPLICIT DOUBLE PRECISION (A-Z)
      DIMENSION U(NDIM), PAR(*), F(NDIM), ICP(*)
C
C  3 ODE of 1st order
       U1=U(1)
       U2=U(2)
       U3=U(3)
C
C  parameters
       C1=PAR(1)
       C0=PAR(2)
       C3=PAR(3)
       K =PAR(4)
       Z0=PAR(5)
       W =PAR(6)
C
C  the equations
       F(1)=U2
       F(2)=-1/(1+C1**2)*((1+W*C1+Z0*C0*C1*U3)*U1
     &      +Z0*C0*U2+(C1*C3-1)*U1**3)/Z0**2+U1*(K/Z0+U3)**2
       F(3)=1/(1+C1**2)*(C1-W+Z0*C0*C1*U2/U1-Z0*C0*U3
     &      -(C1+C3)*U1**2)/Z0**2-2*(K/Z0+U3)*U2/U1
C
      RETURN
      END
C----------------------------------------------------------------------
      SUBROUTINE STPNT
C
C solution and parameters loaded from saved result of previous run: bif
      RETURN
      END
C----------------------------------------------------------------------
      SUBROUTINE BCND(NDIM,PAR,ICP,NBC,U0,U1,FB,IJAC,DBC)
      IMPLICIT DOUBLE PRECISION (A-Z)
      DIMENSION PAR(*),ICP(*),U0(NDIM),U1(NDIM),FB(NBC)
C
C  periodic boundary conditions and pinning
       FB(1)=U0(1)-U1(1)
       FB(2)=U0(2)-U1(2)
       FB(3)=U0(3)-U1(3)
       FB(4)=U0(2)
C
```

```
      RETURN
      END
C----------------------------------------------------------------------
      SUBROUTINE ICND(NDIM,PAR,ICP,NINT,U,UOLD,UDOT,UPOLD,FI,IJAC,DINT)
      IMPLICIT DOUBLE PRECISION (A-Z)
      DIMENSION U(NDIM),UOLD(NDIM),UDOT(NDIM),UPOLD(NDIM)
      DIMENSION FI(NINT),ICP(*),PAR(*)
C
C  constraint on phase gradient
       FI(1)=U(3)
C
      RETURN
      END
C----------------------------------------------------------------------
      SUBROUTINE FOPT
      RETURN
      END
C----------------------------------------------------------------------
      SUBROUTINE PVLS
      RETURN
      END
C----------------------------------------------------------------------
```

## 3.2 r.maw :

```
3 4 2 1                         NDIM,IPS,IRS,ILP
3   3 2 6                       NICP,(ICP(I),I=1,NICP)
50 4 3 2 1 -1 4 1               NTST,NCOL,IAD,ISP,ISW,IPLT,NBC,NINT
1000 -1 5 -1 2                  NMX,RL0,RL1,A0,A1
1000 2 2 8 7 3 0                NPR,MXBF,IID,ITMX,ITNW,NWTN,JAC
1e-7 1e-7 1e-5                  EPSL,EPSU,EPSS
0.01 0.0001 0.1 1               DS,DSMIN,DSMAX,IADS
0                               NTHL,((I,THL(I)),I=1,NTHL)
0                               NTHU,((I,THU(I)),I=1,NTHU)
4                               NUZR,((I,UZR(I)),I=1,NUZR)
3 0.35
3 0.4
3 0.45
3 0.5
```

# Appendix B Scaling of bifurcation thresholds

Using a phase approximation to the CGLE one can analytically study the dependence of bifurcation points on the coefficients $c_1, c_3$. As in the CGLE the drift pitchfork bifurcation is present in all phase equations. A parameter free version of the Kuramoto-Sivashinsky equation (KSE)

$$\frac{\partial \phi}{\partial t} = \Omega_2^{(1)} \frac{\partial^2 \phi}{\partial x^2} + \Omega_2^{(2)} \left( \frac{\partial \phi}{\partial x} \right)^2 + \Omega_4^{(1)} \frac{\partial^4 \phi}{\partial x^4} \tag{B.1}$$

is derived by scaling of $\phi, t, x = x_0 \xi$ hence also $P = P_0 \xi$ . Here $\Omega_2^{(1)} = 1 - c_1 c_3, \Omega_2^{(2)} = -(c_1 + c_3), \Omega_4^{(1)} = -c_1^2(1 + c_3^2)/2, \Omega_4^{(2)} = -2c_1(1 + c_3^2), \Omega_4^{(3)} = -c_1(1 + c_3^2), \Omega_4^{(4)} = -2(1 + c_3^2)$.

$$\xi = \sqrt{\frac{\Omega_4^{(1)}}{\Omega_2^{(1)}}} = \sqrt{\frac{c_1^2(1 + c_3^2)}{2(c_1 c_3 - 1)}} \tag{B.2}$$

The parameter values $c_1, c_3$ of any bifurcation present will also change according to Eq.(B.2) as $P \propto \xi \to \infty$. Since $\xi$ changes inverse to the Benjamin-Feir criterion the Hopf and drift pitchfork bifurcations both will approach the Benjamin-Feir-Newell line in the limit $P \to \infty$. Fig.B.1 confirms this. At the Hopf bifurcation the homogeneous state $\phi = \phi_0$ becomes unstable against Fourier modes with wave number $k = 2\pi/P$ and the branch of coherent structures emerges. Comparison with the results on MAWs in the CGLE shows perfect agreement at big $P$ and small derivations at small $P$ due to the size of $\max(\phi_x)$ at the bifurcations. The linear stability analysis up to order $O(k^4)$ of the homogeneous oscillation in the CGLE also gives

$$P = 2\pi \sqrt{\frac{c_1^2(1 + c_3^2)}{2(c_1 c_3 - 1)}} = 2\pi\xi \tag{B.3}$$

confirming the scaling result for the Hopf bifurcation. At infinite $P$ one can also choose $P_0$ to be infinite and construct the whole branch of coherent structures for $c_1 c_3 > 1$ by rescaling one unique solution. Hence there can be no bifurcations (*i.e.* no saddle-node bifurcation) in the KSE for $c_1 c_3 > 1$ and $P \to \infty$. This is in contrast to the situation in the CGLE and shows the limit of this simplest phase approximation.

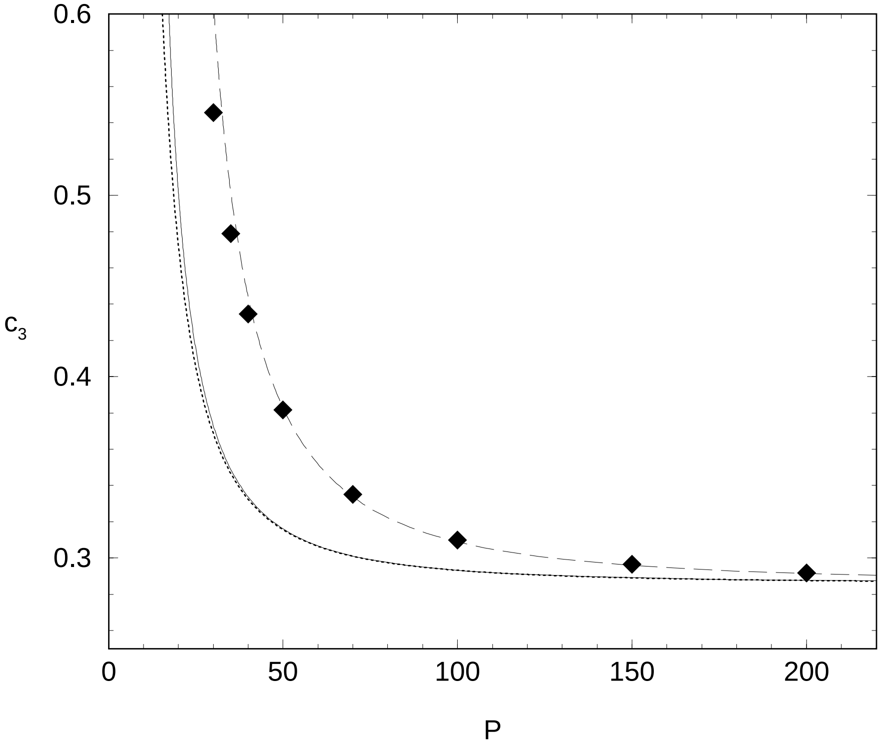

Fig. B.1: Locations of the instability of the homogeneous state in the CGLE (dotted) and in the KSE (full curve) obeying $P = 2\pi * \xi(c_3)$ . Locations of the drift pitchfork bifurcations in the CGLE (symbols) and in the KSE fitted by $P = 11 * \xi(c_3)$ (dashed curve) Parameters are $c_1 = 3.5, \nu = 0$ and $\xi(c_3)$ calculated from Eq. B.2.

# Appendix C  Linear stability analysis

In this Appendix the Bloch method is summarized, the different instabilities of MAWs are studied and their occurence is identified in the parameter space. The case $\nu = 0$ is used for illustrations while similar results are obtained for $\nu \neq 0$.

The stability properties of periodic orbits in the ODEs do not give information on the temporal evolution of perturbations to MAWs in the CGLE. From the stability analysis of fixed points to the ODEs one can only deduce the spatial shape of solutions that approach a homogeneous plateau. The 3 ODEs possess one real and one pair of complex conjugate eigenvalues for the plane wave fixed point. For the "homoclinic holes" that approach the fixed point value at infinity one tail decays exponentially while the other one is oscillating. MAWs of large period $P$ also show an exponential spatial decay on one side of the core region while on the other side the profile alternates around the value of the plateau region.

## C.1 Bloch method

In order to compute the linear stability of MAW solutions in the CGLE we discretize the linearization of the CGLE around the MAW in the comoving reference frame $z = x - vt$. The discretization is done in Fourier space since this already gives the basis of eigenmodes of plane wave solutions. We use 64 modes for each component $\delta a(z)$ and $\delta\phi(z)$ since perturbations of higher wavenumber are damped by the diffusion terms.

To avoid diagonalization of huge matrices for many periods of MAW in big systems we employ the Bloch method [177, 178]. Eigenmodes $r(z)$ of the big system $L = mP$ are

$$r(z) = e^{ikz} w(z) \tag{C.1}$$

where $w(z)$ is periodic with period $P$ and $k = n * 2\pi/(m * P), n \in \mathrm{N}, n \in [1, m]$. The eigenvalue spectrum $\{\lambda_i\}$ in the big system ($L$) is constructed by joining the $m$ sets of eigenvalues of $e^{-ikz}\mathcal{L}(z)e^{ikz}$ where $\mathcal{L}(z)$ is the linearization in the small system ($P$). Thereby the system size parametrizes and one deals with a set of smaller matrices. Fig. C.1a shows the arrangement of eigenvalues for the same MAW at the same parameters in different system sizes. The spectrum of the big system always contains $m - 1$ additional eigenvalues between 2 neighbouring eigenvalues of the short system $L = P$. Thereby the gaps in the spectrum of the finite system close and a set of curves results for the infinite system.

For $L = P$ the spectrum possesses 3 purely real eigenvalues. These we examine first. Next

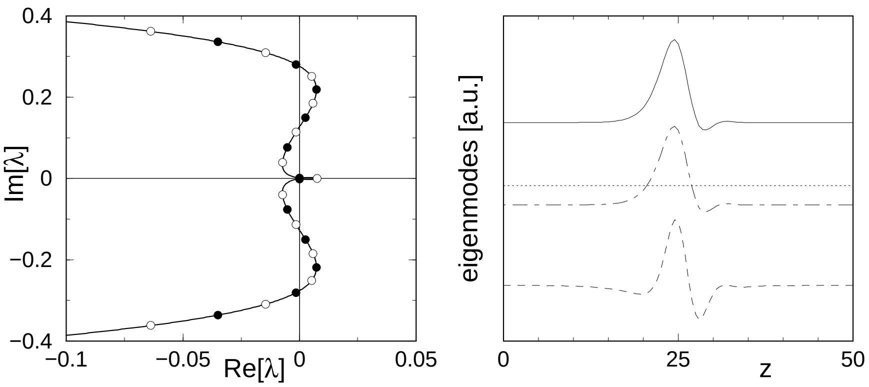

Fig. C.1: (a) Stability spectrum near $L_3$ for $c_1 \approx 0.652, c_3 = 2.0, P = P_{SN} = 50$. The Bloch method is illustrated for a MAW at SN. Filled symbols denote eigenvalues obtained for $L = P$, while open symbols denote additional eigenvalues for $L = 2P$. Full curves show the spectrum for $L \to \infty$. (b) Goldstone modes for translational and phase- symmetry (dot dashed and dotted curves respectively) and derivative of SN eigenmode $\frac{d}{dz}\delta\phi_{SN}(z)$ (dashed) compared with spatial profile $\phi_z(z)$ of the MAW (full curve).

we discuss the main part of the spectrum that arranges in pairs of complex conjugate values followed by the discussion of interactions between subsequent humps of a MAW.

## C.2 Goldstone modes and SN eigenmode

Due to the translational and phase- symmetries of the CGLE the linearization around any solution has 2 neutral modes called Goldstone modes. The corresponding eigenvalues are identically 0 and act as a proof of accuracy for the discretization. The phase symmetry is not affected by the discretization and one eigenvalue is exactly 0. The corresponding Goldstone mode is $(\delta a = 0, \delta\phi = const.)$. Depending on the degree of modulation $(\max(\phi_z))$ we obtain the eigenvalue for the translational Goldstone mode $(\delta a(z) = a_z(z), \delta\phi(z) = \phi_z(z))$ between $10^{-7}$ and $10^{-3}$. As long as the system is translational invariant a Taylor expansion with respect to a small spatial shift reveals

$$A(x + \delta x) = A(x) + \delta x * A_x(x)\ . \tag{C.2}$$

Hence a perturbation of the form $A_x(x)$ (the spatial Goldstone mode) will shift the solution which is a solution again, the corresponding eigenvalue is 0. Fig. C.1b shows the spatial profiles $\delta\phi(z)$ for the 2 Goldstone modes. The numerically obtained translational Goldstone mode indeed equals the spatial derivative of the MAW profile $\frac{d}{dz}\phi(z) = \phi_z(z)$.

Besides these 2 there exists a third purely real eigenvalue which becomes 0 at both the DP and SN bifurcations. We denote this eigenvalue $\lambda_{SN}$. Along the lower branch of MAWs $\lambda_{SN} < 0$ while $\lambda_{SN} > 0$ for the upper branch. In Fig. C.1b the spatial derivative of the SN eigenmode $\frac{d}{dz}\delta\phi_{SN}(z)$ is shown by the dashed curve. The action of this localized eigenmode can be deduced from a comparison with the spatial profile $\frac{d}{dz}\phi(z) = \phi_z(z)$ of the MAW (full curve). Depending on its sign a perturbation proportional to the SN eigenmode will decrease or increase the modulation of the MAW. This manifold has been studied in the case of "homoclinic hole" solutions [145, 172]. Also in the case of MAW initial conditions bejond the upper branch (along this manifold) develop a defect while initial conditions between the lower and upper branch decay towards the lower branch. In Section 2.2.3 this was demonstrated in numerical simulations.

## C.3 Splitting instability

Besides the core region in the spatial profile of a MAW there exists an almost homogeneous plateau (compare Fig. 2.4) that is the longer for bigger $P$. This resembles a part of a plane wave which is Eckhaus unstable in the PT regime. Regardless of deviations in the core region similar eigenmodes also destabilize the MAW. Related to the extent of the homogeneous plateau this instability against delocalized eigenmodes is stronger for bigger $P$. It also increases with the parameters $c_1, c_3$ as does the instability of the plane wave.

The spectrum of eigenvalues for these eigenmodes has a similar shape as for unstable plane waves. The eigenvalues arrange in pairs of complex conjugate values. In the temporal evolution (Fig. 2.16c,d in Section 2.3.4) a small perturbation oscillates between the two corresponding eigenmodes shown by the dashed and dotted curves in Fig. 2.16b. Note that especially the plateau part is disturbed. This initiates the growth of one (or more) new humps on the plateau of the initial MAW. The resulting structure is a sequence of two (or more) short MAWs with smaller $P$. We interpret this process as the splitting of a MAW and we call the eigenmodes "splitting modes".

In the limit $L{\to}\infty$ the splitting eigenvalues form a continuous curve. For small $\mathrm{Im}[\lambda_i]$ this curve either includes the origin with the Goldstone eigenvalues (Fig. 2.16a) or the saddle-node eigenvalue $\lambda_{SN}$ (Fig. 2.17a,C.2a). The former is the case for parameter values near the BFN line while the latter happens for bigger values of $c_1, c_3$.

Minor changes in the Bloch scheme ($k \to k + i\kappa$) allow for the computation of convective or absolute instability properties [164]. We find the splitting instability to be convective in a major part of the unstable regime. This becomes clear since the speed $v$ of the MAW increases towards the SN and the core of the MAW often travels faster then the splitting modes grow. Only from onset (HB) to shortly past the DP bifurcation of the MAW it is absolutely unstable.

## C.4 Interaction instability

The previous instabilities (SN-eigenmode and splitting) already occur in a short system $L{=}P$ with periodic boundary conditions. Now we consider the interaction between several humps in a bigger system. Such interaction modes are a sequence of normal and inverse Goldstone modes. They shift humps in opposite directions depending on the sign of the Goldstone

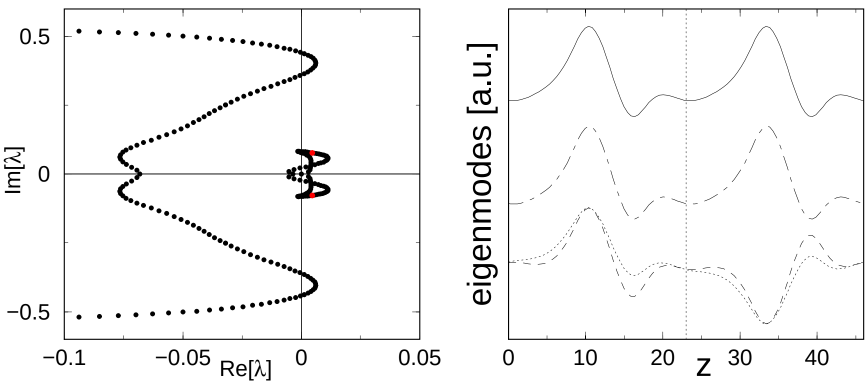

Fig. C.2: (a) Stability spectrum near $L_1$ for $c_1 = 3.0, c_3 = 0.85, P = 23$. (b) Real and imaginary parts of interaction eigenmodes (dashed and dotted) corresponding to $\lambda_{int} = 0.0046 \pm 0.078$ compared with spatial profile of the MAW (full) and Goldstone mode (dot-dashed curve) for $L = 2P$.

mode acting on the individual hump. Since the spatial profile of interaction modes is via the Goldstone mode related to the profile of the solution itself these interaction modes will always be localized around the position of the hump. In contrast the splitting modes are delocalized and mainly disturb the plateau part of the MAW profile.

The 2 interaction eigenvalues present for $L$=$2P$ may both be purely real (Fig. 2.17a) hence distances between humps will exponentially increase or decrease. Or the 2 eigenvalues are complex conjugate (Fig. C.2a) which results in an alternating attraction and repulsion of the humps. Fig. 2.17b,C.2b show the interaction modes for $L$=$2P$. If a MAW of period $P$ is unstable to interaction modes these will dynamically produce (Fig. 2.17c,d in Section 2.3.4) a sequence of different $P$'s. Thereby MAWs with bigger $P$ may occur locally.

In the limit $L \to \infty$ the interaction eigenvalues either form two separate loops if the eigenvalues for $L$=$2P$ are real. Or they form one joined curve near the origin of the spectrum when the eigenvalues for $L$=$2P$ are complex conjugate (Fig. C.2a). The latter only happens if the splitting eigenvalues include $\lambda_{SN}$ and not the origin. This is the case for bigger parameter values $c_1, c_3$. There part of the curve of interaction eigenvalues always has positive real part while for $c_1, c_3$ near the BFN-line this only happens for special values of the parameters and the period $P$. In the next Section we present the parameter dependence of the encountered instabilities in more detail.

## C.5 Parameter dependence of instabilities

We computed the domains of the above instabilities of MAW in several cuts across the parameter plane fixing either $c_1$ or $c_3$. Fig. C.3 presents a representative cut across the $L_1$ transition for $c_1$=3.0 and Fig. C.4 shows a cut across the $L_3$ transition for $c_3$=2.0. MAWs of the *upper* branch always are unstable to the SN-eigenmode in addition to possible splitting or

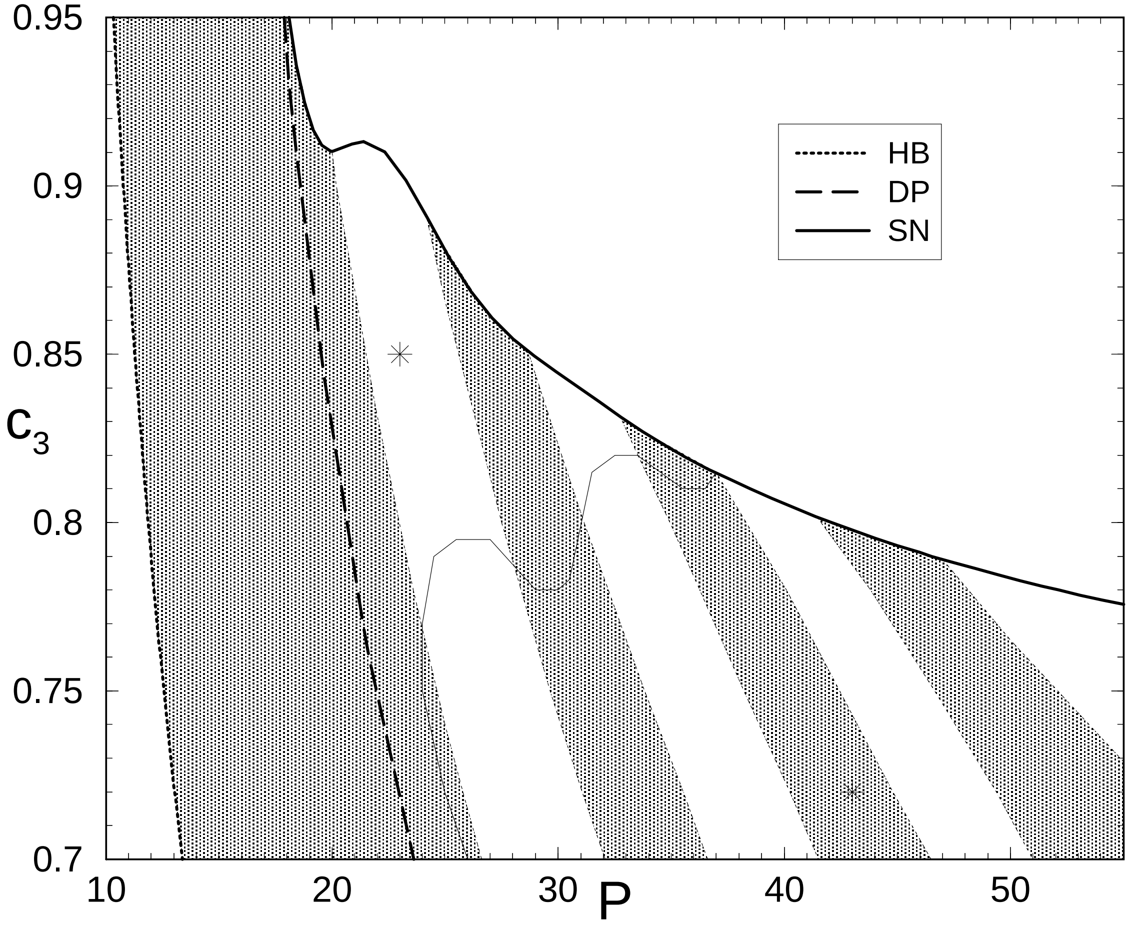

Fig. C.3: Instabilities located in a cut near $L_1$ for $c_1 = 3.0$. Splitting modes are active everywhere to the right of the drift pitchfork bifurcation (DP). Secondary period doubling bifurcations (PD) bound the shaded stripes where periodic MAWs are unstable to interaction modes with purely real eigenvalue. Inside the white stripes at big $c_3$ pairs of Hopf bifurcations (HB) cause instability to alternating interaction (swinging). In the limit $L \rightarrow \infty$ interaction modes are active everywhere. To the right of the thin full line the eigenvalues corresponding to splitting modes have bigger real parts than the eigenvalues corresponding to interaction modes. The SN curve asymptotically approaches $c_3 = 0.704$ for $P \rightarrow \infty$. At small $P$ a hysteresis of the SN locations is present. Stars denote parameter values corresponding to stability spectra shown in Figs. 2.16,C.2.

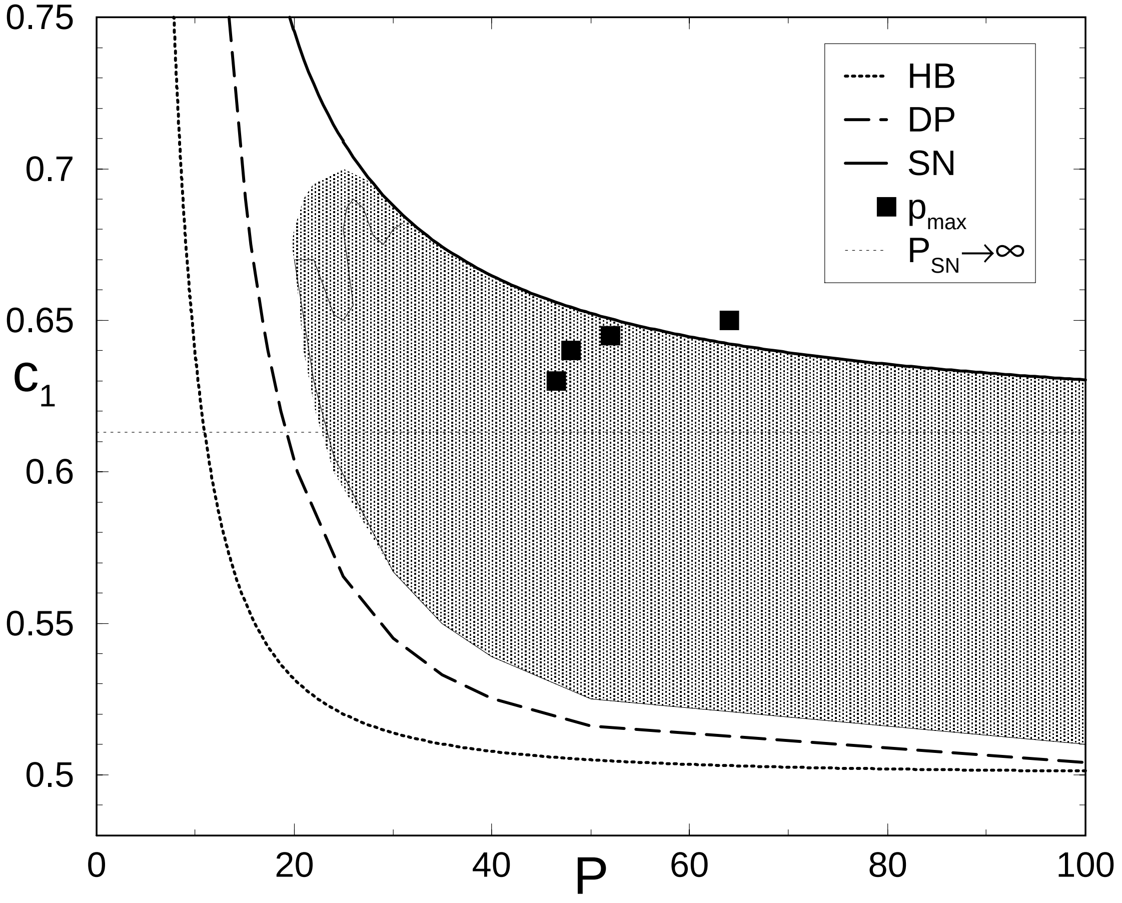

Fig. C.4: Instabilities located in a cut near $L_3$ for $c_3 = 2.0$. Splitting modes are only active inside the shaded area. To the right of the thin full line the eigenvalues corresponding to splitting modes have bigger real parts than the eigenvalues corresponding to interaction modes. Note that Hopf-, drift pitchfork bifurcation and BFN line coincide in the limit $P\to\infty$. Filled squares denote measured peak-to-peak distances in simulations. If the squares lie above the SN curve then defects appear in the corresponding simulation.

interaction instabilities. This explaines features of the spatio-temporal intermittency regime [145, 172]. For phase chaotic dynamics the instabilities of MAWs of the *upper* branch are not important. Therefore in the figures we include instabilities of the *lower* branch for infinite system size $L{\rightarrow}\infty$.

Above their onset (HB) stationary MAWs with period $P < L$ are unstable since they emerge from an unstable homogeneous oscillation. The unstable eigenmodes are interaction modes related to the unstable modes of the homogeneous oscillation which all have a bigger period than $P$. The stationary MAW undergoes a sequence of secondary HBs that restabilize the periodic MAW solution. New branches of time-periodically oscillating solutions emerge. These noncoherent structures include more humps and carry the instabilities of the previous MAW. They are not important and not discussed here.

Above the DP bifurcation the last two interaction eigenvalues are restabilized by 2 PD bifurcations where the purely real eigenvalues separately cross the imaginary axes of the spectrum. Approaching the SN curve the travelling MAW undergoes a sequence of pairs of such PD bifurcations (compare Section 2.2.2) and can be stable against interaction modes only between these pairs. In Fig. C.3 the locations of PDs bound the shaded stripes. Inside the shaded areas one real interaction eigenvalue is positive and neighbouring humps of a periodic MAW attract each other thereby increasing the period of one of the humps.

Between the shaded stripes in Fig. C.3 the interaction eigenvalues may also arrange in complex conjugate pairs (Fig. C.2a). By pairs of HB of these interaction eigenvalues the periodic MAW can also be unstable to oscillatory interaction modes. This is the case for bigger values of $c_1, c_3$ where HBs occur between the shaded stripes but close to their boundaries. For other cuts in the parameter space the interaction instabilities arrange in the same way but in Fig. C.4 the corresponding stripes are omitted.

The interaction between neighbouring humps is the stronger for smaller $P$ and bigger $c_1, c_3$. The interaction eigenvalues dominate the dynamics for such parameter values. In Fig. C.3,C.4 a thin full line denotes parameter values where the real parts of interaction and splitting eigenvalues are of the same order. Below and to the right of this line the splitting instability dominates.

Around the $L_1$ transition all travelling MAW are unstable to splitting modes. Near $L_3$ the splitting instability only occurs for some of the travelling MAW with $P$ big enough. In Fig. C.4 the parameter domain is shaded where MAWs are unstable to splitting in the infinitely large system $L{\rightarrow}\infty$.

Near both $L_1$ and $L_3$ the interaction and splitting instabilities overlap for a wide range of parameters. The resulting increase and decrease of periods of near-MAWs drive the phase chaos. This dynamics breaks down if locally a period increases beyond the corresponding $P_{SN}$ (compare Section 2.2.3). The following transition to defect chaos was investigated in Chapter 2.

# Appendix D MAWs in finite systems

For finite one-dimensional systems both the wavenumber of plane waves (thereby also $\nu$ of MAWs) and the period $P$ of MAWs are restricted to a discrete set by periodic boundary conditions. In this case it is convenient to parametrize MAWs by the average phase gradient $\nu$ and the ratio of wavelength

$$n := \frac{P}{2\pi/\nu} \ . \tag{D.1}$$

The ratio $n$ takes values of integer fractions where the numerator counts the number of underlying wave fronts per system and the denominator the number of humps of the modulation. Hence this quantity is easy accessible in experiments.

Again fixing $c_1 = 3.5$, the existence domains of MAWs with respective $n$ are presented in the $(c_3, \nu)$ parameter plane.

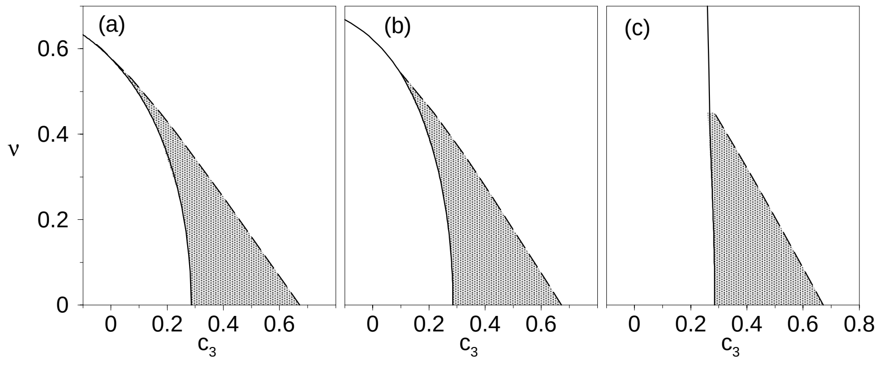

Fig. D.1: Existence domains of lower branch MAWs are denoted by shaded areas and limited by HB (solid curve) from below and by the SN (dashed curve) from above. (a) MAWs with $n = 20$ exist close to the long wavelength instability whereas (b) $n = 4$ and (c) $n = 2$ shift to larger values of $c_3$.

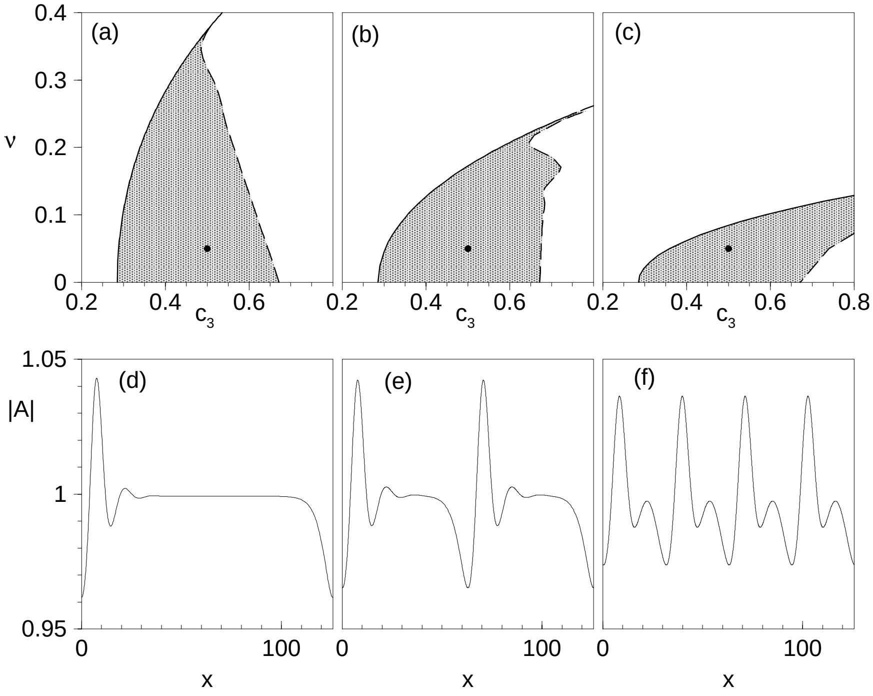

Fig. D.2: Existence domains of lower branch MAWs are denoted by shaded areas in (a) $n = 1$, (b) $n = 1/2$ and (c) $n = 1/4$. They are limited by HB (solid curve) at small $c_3$ and by the SN (dashed curve) at large $c_3$. Spatial profiles of MAWs at $\nu = 0.05, c_3 = 0.5$ are shown for (d) $n = 1$, (e) $n = 1/2$ and (f) $n = 1/4$, corresponding to dots in (a-c).

# Appendix E Meandering Instability

For rigidly rotating spirals $(\xi_1(\alpha_1,\alpha_2),\zeta_1(\alpha_1,\alpha_2))$ are stationary solutions (fixed points of the subsystem $(\xi,\zeta)$ ) and $\dot{\phi}=\gamma_0\sqrt{\zeta_1}$ gives $\phi=\omega_1 t+\phi_1$ with the rotation frequency $\omega_1=\gamma_0\sqrt{\zeta_1}=2\pi/T_C$. Choosing the integration constant $\phi_1=\pi/2$ the tip uniformly rotates $x(t)=\sqrt{\xi_1}/\omega_1\cos\omega_1 t\ +x_S,\ \ y(t)=\sqrt{\xi_1}/\omega_1\sin\omega_1 t\ +y_S$ around the fixed wave source at $(x_S,y_S)$.

Beyond a Hopf bifurcation at $\alpha_2^{HB}(\alpha_1)$ with frequency $\omega_2$ the fixed point $(\xi_1,\zeta_1)$ corresponding to the rigidly rotating spiral is unstable and a stable limit cycle $\xi_2(t)=\xi_1+\sqrt{\epsilon}\sin(\omega_2 t+\phi_2),\quad \zeta_2(t)=\zeta_1+\sqrt{\epsilon}\cos(\omega_2 t+\phi_2)$ emerges from the fixed point. Here $\epsilon=(\alpha_2-\alpha_2^{HB})/\alpha_2^{HB}$ should be small compared with 1 to permit the square root dependence near the Hopf bifurcation and to allow further analytical treatment.

Expanding $\sqrt{\xi_2}=\sqrt{\xi_1}\sqrt{1+\sqrt{\epsilon}/\xi_1\sin(\omega_2 t+\phi_2)}\approx\sqrt{\xi_1}+\sqrt{\epsilon}/2\sin(\omega_2 t+\phi_2)$ and $\sqrt{\zeta_2}$ likewise yields $\phi(t)=\omega_1 t+\phi_1+\sqrt{\epsilon}\gamma_0/(2\omega_2)\sin(\omega_2 t+\phi_2)$ with integration constant $\phi_1$ and

$$\begin{aligned}\dot{x} &= (\sqrt{\xi_1}+\frac{\sqrt{\epsilon}}{2}\sin(\omega_2 t+\phi_2))\cos(\omega_1 t+\phi_1+\frac{\sqrt{\epsilon}\gamma_0}{2\omega_2}\sin(\omega_2 t+\phi_2)) \qquad \text{(E.1)}\\ &= \sqrt{\xi_1}\cos(\omega_1 t+\phi_1)+\frac{\sqrt{\epsilon}}{2}\sin(\omega_2 t+\phi_2)*\left[\cos(\omega_1 t+\phi_1)-\frac{\sqrt{\xi_1}\gamma_0}{\omega_2}\sin(\omega_1 t+\phi_1)\right]\\ &= \sqrt{\xi_1}\cos(\omega_1 t+\phi_1)+\frac{\sqrt{\epsilon}}{2}\sin(\omega_2 t+\phi_2)*\sqrt{1+\frac{\xi_1\gamma_0^2}{\omega_2^2}}\sin(\omega_1 t+\phi_1-\frac{\pi}{2}+\arctan\frac{\sqrt{\xi_1}\gamma_0}{\omega_2})\end{aligned}$$

where trigonometrical functions of arguments proportional to $\sqrt{\epsilon}$ have been expanded to order $\sqrt{\epsilon}$ and the equality $a\cos\beta+b\sin\beta=\sqrt{a^2+b^2}\sin(\beta+\arctan a/b)$ has been used. Assuming $\omega_1\neq\omega_2$ and using $\int d\tau\ \sin a\tau\sin b\tau=\frac{\sin(a-b)\tau}{2(a-b)}-\frac{\sin(a+b)\tau}{2(a+b)}$ the integration yields

$$\begin{aligned} x &= \frac{\sqrt{\xi_1}}{\omega_1}\sin(\omega_1 t+\phi_1)+\frac{\sqrt{\epsilon}}{4}\sqrt{1+\frac{\xi_1\gamma_0^2}{\omega_2^2}} * \qquad \text{(E.2)} \\ &\left[\frac{1}{\omega_1-\omega_2}\sin(\omega_1 t+\phi_1-\frac{\pi}{2}+\arctan\frac{\sqrt{\xi_1}\gamma_0}{\omega_2}-\omega_2 t-\phi_2)-\right. \\ &\left.\frac{1}{\omega_1+\omega_2}\sin(\omega_1 t+\phi_1-\frac{\pi}{2}+\arctan\frac{\sqrt{\xi_1}\gamma_0}{\omega_2}+\omega_2 t+\phi_2)\right] \\ &= \frac{\sqrt{\xi_1}}{\omega_1}\cos\omega_1 t+\frac{\sqrt{\epsilon}}{4}\sqrt{1+\frac{\xi_1\gamma_0^2}{\omega_2^2}} * \qquad \text{(E.3)} \\ &\left[\frac{1}{\omega_1-\omega_2}\cos(\omega_1-\omega_2)t+\frac{1}{\omega_1+\omega_2}\cos((\omega_1+\omega_2)t+2\arctan\frac{\sqrt{\xi_1}\gamma_0}{\omega_2})\right] \end{aligned}$$

where the integration constants $\phi_1 = \pi/2$ and $\phi_2 = 3\pi/2 + \arctan\frac{\sqrt{\xi_1}\gamma_0}{\omega_2}$ were fixed in the second step. A similar expression follows for $y(t)$. For the position $p(t)$ of the tip in the complex plane we get up to order $\sqrt{\epsilon}$

$$\begin{aligned} p(t) &= \frac{\sqrt{\xi_1}}{\omega_1}\mathrm{e}^{i\omega_1 t}+\frac{\sqrt{\epsilon}}{4(\omega_1-\omega_2)}\sqrt{1+\frac{\xi_1\gamma_0^2}{\omega_2^2}}\mathrm{e}^{i(\omega_1-\omega_2)t} \qquad \text{(E.4)} \\ &+\frac{\sqrt{\epsilon}}{4(\omega_1+\omega_2)}\sqrt{1+\frac{\xi_1\gamma_0^2}{\omega_2^2}}\mathrm{e}^{i(\omega_1+\omega_2)t+2\arctan\frac{\sqrt{\xi_1}\gamma_0}{\omega_2}} . \end{aligned}$$

The first term again describes the fast rotation of the tip emitting waves with frequency $\omega_1$. In the amplitude equation for the wave field this reflects the wave number selection by $\omega_1 = \omega(\nu)$. The other two terms describe the motion of the wave source. It has the often discussed epicycloid form. For $\omega_1 - \omega_2 > 0$ (or $< 0$) the tip rotates in the same (opposite) direction as the source and the trajectory possesses inward (outward) petals. The excluded case $\omega_1 = \omega_2$ leads to secular terms due to $\int d\tau\ \sin\omega_1\tau\sin\omega_2\tau$ and describes a travelling spiral. In excitable media the instability to meandering occures with $\omega_2$ close to $\omega_1$ [192, 194]. We expect the same for the oscillatory system ($T_M > 5T_C$ in [70]) and find $|\omega_1 - \omega_2| \ll \omega_1 + \omega_2$ hence the third term in Eq. (E.4) is small compared to the first two terms. Since these small perturbations on a short time scale (due to the fast oscillation with $\omega_1 + \omega_2$) are damped in the wave dynamics (CGLE) we will neglect the last term.

$$\begin{aligned} x_S(t) &= \frac{\sqrt{\epsilon}}{4(\omega_1-\omega_2)}\sqrt{1+\frac{\xi_1\gamma_0^2}{\omega_2^2}} * \cos(\omega_2-\omega_1)t \qquad \text{(E.5)} \\ x_S(t) &= R_S\cos 2\pi t/T_M \qquad \text{(E.6)} \end{aligned}$$

# Bibliography

[1] E. Schrödinger, *Was ist Leben ?* (Francke, Bern, 1951).

[2] P. Glansdorff and I. Prigogine, *Thermodynamics of structure, stability and fluctuations* (Wiley, New York, 1971).

[3] G. Nicolis and I. Prigogine, *Self-organisation in nonequilibrium systems* (Wiley, New York, 1977).

[4] I. Prigogine, *Time, structure and fluctuations (Nobel-presentation)*, Angew. Chemie **90**, 74 (1978).

[5] H. Poincaré, *Les méthodes nouvelles de la méchanique celeste*, (Gauthier-Villars, Paris, 1890,1893,1899).

[6] G. Iooss and D. D. Joseph, *Elementary Stability and Bifurcation Theory* (Springer, Berlin, 1980).

[7] J. Guckenheimer and P. Holmes, *Nonlinear Oscillations, Dynamical Systems, and Bifurcations of Vector Fields* (Springer, New York, 1983).

[8] Y. A. Kuznetsov, *Elements of Applied Bifurcation Theory* (Springer, Berlin, 1985).

[9] R. Seydel, *Practical Bifurcation and Stability Analysis* (Springer, New York, 1994).

[10] D. Walgraef, *Spatio-temporal pattern formation* (Springer, Heidelberg, 1997).

[11] H. Helmholtz, *Über diskontinuierliche Flüssigkeitsbewegungen*, Monats. Königl. Preuss. Akad. Wiss. Berlin **23**, 215 (1868).

[12] Lord Kelvin, *Hydrokinetic solutions and observations*, Phil. Mag. **42**, 362 (1871).

[13] Lord Rayleigh, *On the stability, or instability, of certain fluid motions*, Proc. London Math. Soc. **11**, 57 (1880).

[14] W. Orr, *The stability or instability of the steady motions of a perfect liquid and of a viscous liquid*, Proc. Roy. Irish Acad. A **27**, 9 (1907).

[15] A. Sommerfeld, *Ein Beitrag zur hydrodynamischen Erklärung der turbulenten Flüssigkeitsbewegungen*, Proceedings 4th Int. C. of Math. **III**, Rome, 116 (1908).

[16] A. M. Turing, *The chemical basis of morphogenesis*, Phil. Trans. Roy. Soc. B **237**, 37-72 (1952).

[17] V. Castets, E. Dulos, J. Boissonade and P. De Kepper, *Experimental evidence of a sustained standing Turing-type nonequilibrium chemical pattern*, Phys. Rev. Lett. **64**, 2953 (1990).

[18] J. P. Gollub and J. S. Langer, *Pattern formation in nonequilibrium physics*, Rev. Mod. Phys. **71**, S396 (1999).

[19] M. C. Cross and P. C. Hohenberg, *Spatiotemporal Chaos*, Science **263**, 1569 (1994).

[20] D. A. Egolf, I. V. Melnikov, W. Pesch and R. E. Ecke, *Mechanisms of extensive spatiotemporal chaos in Rayleigh-B'enard convection*, Nature **404**, 733 (2000).

[21] T. Bohr, E. Bosch and W. van de Water, *Spatiotemporal Chaos*, Nature **372**, 48 (1994).

[22] Y. Kuramoto, *Chemical Oscillations, Waves, and Turbulence* (Springer, Berlin, 1984).

[23] A. T. Winfree, *When Time Breaks Down* (Princeton University Press, Princeton, 1987).

[24] J. D. Murray, *Mathematical Biology* (Springer, Berlin, 1989).

[25] P. Manneville, *Dissipative Structures and Weak Turbulence* (Academic Press, San Diego, 1990).

[26] G. Nicolis, *Introduction to Nonlinear Science* (Cambridge University Press, Cambridge, 1995).

[27] *Chemical Waves and Patterns*, edited by R. Kapral and K. Showalter (Kluwer, Doodrecht, 1995).

[28] J. Keener and J. Sneyd, *Mathematical Physiology* (Springer, New York, 1998).

[29] T. Bohr, M. H. Jensen, G. Paladin and A. Vulpiani, *Dynamical systems approach to turbulence* (Cambridge University Press, Cambridge, 1998).

[30] M. C. Cross and P. C. Hohenberg, *Pattern formation outside of equilibrium*, Rev. Mod. Phys. **65**, 851 (1993).

[31] P. C. Hohenberg, *One Hundred Years of Nonequilibrium Patterns*, Phys. Blätter **55**, 53 (1999).

[32] A. DeWit, *Spatial patterns and spatiotemporal dynamics in chemical systems*, Adv. Chem. Phys. **109**, 435 (1999).

[33] H. Bénard, *Les tourbillons cellulaires dans une nappe liquide transportent de la chaleur par convection en regime permanent*, Ann. Chim. Phys. **7** (Ser. 23), 62 (1900).

[34] Lord Rayleigh, *On the dynamics of revolving fluids*, Proc. R. Soc. London Ser. A **93**, 148 (1916).

[35] F. H. Busse, *Non-linear properties of thermal convection*, Rep. Prog. Phys. **41**, 1929 (1978).

[36] E. Bodenschatz, W. Pesch and G. Ahlers, *Recent developments in Rayleigh-B'enard convection*, Annu. Rev. Fluid Mech. **32**, 709 (2000).

[37] E. L. Koschmieder, *Heat transfer through a shallow horizontal convecting fluid layer*, Int. J. Heat Mass Transfer **17**, 991 (1974).

[38] T. Boeck, *Bénard-Marangoni convection at low Prandtl numbers* (Shaker, Aachen, 2000).

[39] R. C. DiPrima and H. L. Swinney, *Instabilities and transition in flow between concentric rotating cylinders*, p. 139 in *Hydrodynamic Instabilities and the Transition to Turbulence*, edited by H. L. Swinney and J. P. Gollub (Springer, New York, 1981).

[40] K. L. Babcock, G. Ahlers and D. S. Cannell, *Noise-sustained structures in Taylor-Couette flow with through flow*, Phys. Rev. Lett. **67**, 3388 (1991).

[41] P. Kolodner and H. Williams, in *Proceedings of the NATO Advanced Research Workshop on Nonlinear Evolution of Spatio-Temporal Structures in Dissipative Continuous Systems*, edited by F. H. Busse and L. Kramer, NATO Advanced Study Ser. B 2, Vol.255 (Plenum, New York, 1990)

[42] F. Daviaud and J. M. Vince, *Traveling waves in a fluid layer subjected to a horizontal temperature gradient*, Phys. Rev. E **48**, 4432 (1993).

[43] N. Mukolobwiez, A. Chiffaudel and F. Daviaud, *Supercritical Eckhaus instability for surface-tension-driven hydrothermal waves*, Phys. Rev. Lett. **80**, 4661 (1998).

[44] J. Burguete, H. Chaté, F. Daviaud and N. Mukolobwiez, *Bekki-Nozaki amplitude holes in hydrothermal nonlinear waves*, Phys. Rev. Lett. **82**, 3252 (1999).

[45] N. Garnier and A. Chiffaudel, *Two dimensional hydrothermal waves in an extended cylindrical vessel*, Eur. Phys. J. B **19**, 87 (2001).

[46] M. K. Smith and S. H. Davis, *Instabilities of dynamic thermocapillary liquid layers*, J. Fluid Mech. **132**, 119 (1983).

[47] J.F. Mercier and C. Normand, *Buoyant-thermocapillary instabilities of differentially heated liquid layers*, Phys. Fluids 8, 1433 (1996).

[48] J. M. Vince and M. Dubois, *Critical properties of convective waves in a one-dimensional system*, Physica D **102**, 93 (1997).

[49] W. van de Water, *Experiments on sources and sinks*, in [181].

[50] M. Rabaud, S. Michalland and Y. Couder, Phys. Rev. Lett. **64**, 184 (1990); D. P. Vallette, G. Jacobs and J. P. Gollub, Phys. Rev. E **55**, 4274 (1997).

[51] S. Akamatsu and G. Faivre, Phys. Rev. E **58**, 3302 (1998).

[52] M. Lücke, W. Barten and M. Kamps, Physica D **61**, 183 (1992).

[53] Y. Liu and R. E. Ecke, *Eckhaus-Benjamin-Feir instability in rotating convection*, Phys. Rev. Lett. **78**, 4391 (1997).

[54] P. Bot and I. Mutabazi, *Dynamics of spatio-temporal defects in the Taylor-Dean system*, Eur. Phys. J. B **13**, 141 (2000).

[55] A. Wierschem, H. Linde and M. G. Velarde, *Internal waves excited by the Marangoni effect*, Phys. Rev. E **62**, 6522 (2000).

[56] B. Janiaud, A. Pumir, D. Bensimon, V. Croquette, H. Richter and L. Kramer, *The Eckhaus instability for traveling waves*, Physica D **55**, 269 (1992).

[57] A. Pumir, B. I. Shraiman, W. van Saarloos, P. C. Hohenberg, H. Chaté and M. Holen, *Phase vs. defect turbulence in the 1D complex Ginzburg-Landau equation*, p. 173 in C. D. Andereck and F. Hayot (Eds.), *Ordered and Turbulent patterns in Taylor-Couette Flow* (Plenum Press, New York, 1992)

[58] A. Torcini, *Order parameter for the transition from phase to amplitude turbulence*, Phys. Rev. Lett. **77**, 1047 (1996).

[59] R. Montagne, E. Hernández-García and M. San Miguel, *Winding number instability in the phase-turbulence regime of the complex Ginzburg-Landau equation*, Phys. Rev. Lett. **77**, 267 (1996);

[60] R. Luther, *Räumliche Fortpflanzung chemischer Reaktionen*, Zeitschr. f. Elektrochemie **32**, 596 (1906).

[61] A. T. Winfree, *The prehistory of the BZ oscillator*, J. Chem. Educ. **61**, 661-663 (1984).

[62] A. M. Zhabotinsky, *A history of chemical oscillations and waves*, Chaos **1**, 379-386 (1991).

[63] *Oscillations and Travelling Waves in Chemical Systems*, R. J. Field and M. Burger, Eds. (Wiley, New York, 1985).

[64] B. P. Belousov, *A periodic reaction and its mechanism*, in *Sbornik Referatov po Radiacioni Medicine*(Medgiz, Moscow, 1959), p.145, English translation in [63], pp. 605-613.

[65] A. N. Zaikin and A. M. Zhabotinsky, *Concentration wave propagation in two-dimensional liquid phase self-oscillating system*, Nature **225**, 535-537 (1970).

[66] A. T. Winfree, Spiral waves of chemical activity, Science **175**, 634-636 (1972)

[67] Q. Ouyang, and J. M. Flesselles, *Transition from spirals to defect turbulence driven by a convective instability*, Nature **379**, 143 (1996).

[68] G. Li, Q. Ouyang, V. Petrov, and H. L. Swinney, *Transition from simple rotating chemical spirals to meandering and traveling spirals*, Phys. Rev. Lett. **77**, 2105 (1996).

[69] Q. Ouyang, H. L. Swinney, and G. Li, *Transition from spirals to defect-mediated turbulence driven by a doppler instability*, Phys. Rev. Lett. **84**, 1047 (2000).

[70] L. Q. Zhou and Q. Ouyang, *Experimental studies on long-wavelength instability and spiral breakup in a reaction-diffusion system*, Phys. Rev. Lett. **85**, 1650 (2000).

[71] L. Q. Zhou and Q. Ouyang, *Spiral instabilities in a reaction-diffusion system*, J. Phys. Chem. A **105**, 112 (2001).

[72] S. Jakubith, H. H. Rotermund, W. Engel, A. von Oertzen and G. Ertl, *Spatiotemporal concentration patterns in a surface reaction : propagating and standing waves, rotating spirals and turbulence*, Phys. Rev. Lett. **65**, 3013 (1990).

[73] M. Bär, *Räumliche Strukturbildung bei einer Oberflächenreaktion*, Ph.D. Thesis, Free University of Berlin, Germany (1993).

[74] M. Falcke and H. Engel, *Pattern formation during the CO oxidation on Pt(110) surfaces under global coupling*, J. Chem. Phys. **101**, 6255 (1994).

[75] S. C. Müller, T. Plesser and B. Hess, Physica D **24**, 71 (1987).

[76] A. Goldbeter, *Biochemical Oscillations and Cellular Rythms* (Cambridge University Press, Cambridge, 1996).

[77] DictyBase in the World Wide Web, URL`http://dictybase.org/`

[78] A. Hodgkin and A. F. Huxley, *A quantitative description of membrane current and its application to conduction and excitation in nerve*, J. Physiol. **117**, 500 (1952).

[79] B. Hille, *Ionic Channels of Excitable Membrans* (Sinauer Associates, Sunderland, 1992).

[80] C.J. Wiggers, *Studies of ventricular fibrillation produced by electric shock*, Am. Heart J. 5, 351-365 (1930).

[81] F. X. Witkowski, L. J. Leon, P. A. Penkoske, W. R. Giles, M. L. Spano, W. L. Ditto, and A. T. Winfree, *Spatiotemporal evolution of ventricular fibrillation*, Nature **392**, 78 (1998).

[82] A. T. Winfree, *Electrical turbulence in three-dimensional heart muscle*, Science **266**, 1003 (1994).

[83] *Focus Issue: Fibrillations in Normal Ventricular Myocardium* [Chaos **8**, No. 1 (1998)].

[84] R.A. Gray et al., *Mechanisms of cardiac fibrillation*, Science **270**, 1222-1225 (1995).

[85] A.V. Holden, The restless heart of a spiral, Nature **387**, 655-657 (1997).

[86] M. J. Berridge, *Inositol triphosphate and calcium signalling*, Nature **361**, 315 (1993).

[87] M. J. Berridge, M. D. Bootman and P. Lipp, *Calcium - a life and death signal*, Nature **395**, 645 (1998).

[88] U. Kummer, L.F. Olsen, C.J. Dixon, A.K. Green, E. Bornberg-Bauer and G. Baier, *Switching from simple to complex oscillations in calcium signaling*, Biophys. J. **79**, 1188 (2000).

[89] R. FitzHugh, *Impulses and physiological states in theoretical models of nerve membrane*, Biophys. J. **1**, 445 (1961).

[90] R. FitzHugh, *Thresholds and plateaus in the Hodgkin-Huxley nerve equations*, J. Gen. Physiol. **43**, 867 (1961).

[91] A. C. Newell and J. A. Whitehead, *Finite bandwidth, finite amplitude convection*, J. Fluid Mech. **38**, 279 (1969).

[92] L. A. Segel, *Distant side-walls cause slow amplitude modulations of cellular convection*, J. Fluid Mech. **38**, 203 (1969).

[93] L. D. Landau, *On the theory of phase transitions* (1937), p.193 in [95].

[94] L. D. Landau, *On the problem of turbulence*, Akad. Nauk. Dok. **44**, 339 (1944). [English translation in [95]]

[95] L. D. Landau, *Collected papers of L. D. Landau*, edited by D. ter Haar (Pergamon, Oxford, 1965).

[96] L. D. Landau and Lifschitz, *Statistical Physics*, Chap.XIV (Addison Wesley, Reading MA, 1958).

[97] H. Haken, *Advanced Synergetics* (Springer, Berlin, 1987).

[98] A. C. Newell, *Envelope equations*, Lect. Appl. Math. **15**, 157 (1974).

[99] M. van Hecke, *The amplitude description of nonequilibrium patterns*, Ph.D. Thesis, Rijks university Leiden, Netherlands (1996).

[100] V. Privman, P. C. Hohenberg and A. Aharony, *Universal critical-point amplitude relations*, in *Phase Transitions and Critical Phenomena*, Vol. 14 edited by C. Domb and J. L. Lebowitz (Academic, London,1991)

[101] M. H. Holmes, *Introduction to Perturbation Methods* (Springer, New York, 1995).

[102] M. Ipsen, F. Hynne, and P. G. Sørensen, *Amplitude equations and chemical reaction-diffusion systems*, Int. J. of Bif. and Chaos **7**, 1539 (1997).

[103] M. Ipsen, L. Kramer and P. G. Sørensen, *Amplitude equations for description of chemical reaction-diffusion systems*, Phys. Reports **337**, 193 (2000).

[104] P. Kano, *Stability of Spatio-Temporal Patterns in a Simple Reaction-Diffusion Model*, Diploma Thesis, Technical University of Dresden, Germany (2000).

[105] P. G. Sørensen and F. Hynne, J. Phys. Chem. **93**, 5467 (1989).

[106] L. Kramer, F. Hynne, P. G. Sørensen, and D. Walgraef, *The Ginzburg-Landau approach to oscillatory media*, Chaos **4**, 443 (1994).

[107] L. D. Landau and V. L. Ginzburg, *On the problem of superconductivity* (1950), p.546 in [95].

[108] A. Schmid, Zeitschrift für Physik A **215**, 210 (1968).

[109] G. M. Eliashberg, Zhurnal Eksperimental'noi i Teoreticheskoi Fisiki **55**, 2443 (1968).

[110] M. Ipsen, P. G. Sørensen, *Finite wavelength instabilities in a slow mode coupled complex Ginzburg-Landau equation*, Phys. Rev. Lett. **84**, 2389 (2000).

[111] E. Nicola, Ph.D. thesis in preparation.

[112] H. Malchow and L. Schimansky-Geier, *Noise and diffusion in bistable nonequilibrium systems* (B. G. Teubner, Leipzig, 1985).

[113] W. Eckhaus, *Studies in Nonlinear Stability Theory* (Springer, Berlin, 1965).

[114] T. B. Benjamin and J. E. Feir, *Disintegration of wave trains on deep water. 1. Theory*, J. Fluid Mech. **27**, 417 (1966).

[115] Y. Pomeau and P. Manneville, *Stability and fluctuations of a spatially periodic convective flow*, J. Phys. Lett. **40**, L-609 (1979).

[116] Y. Kuramoto, *Phase dynamics of weakly unstable periodic structures*, Prog. Theor. Phys. **71**, 1182 (1984).

[117] M. C. Cross and A. C. Newell, *Convection patterns in large aspect ratio systems*, Physica D **10**, 299 (1984).

[118] I. S. Aranson, A. R. Bishop, and L. Kramer, *Dynamics of vortex lines in the three-dimensional complex Ginzburg-Landau equation: Instability, stretching, entanglement, and helices*, Phys. Rev. E **57**, 5276 (1998).

[119] W. van Saarloos and P. C. Hohenberg, *Fronts, pulses, sources and sinks in generalized complex Ginzburg-Landau equations*, Physica D **56**, 303 (1992); **69**, 209 (1993) [Errata].

[120] N. Garnier and A. Chiffaudel, *Nonlinear Transition to a Global Mode for Traveling-Wave Instability in a Finite box*, Phys. Rev. Lett. **86**, 75 (2001).

[121] A. C. Newell and J. V. Moloney, *Nonlinear Optics* (Addison-Wesley, Reading, MA, 1992).

[122] I.S. Aranson and L. Kramer, *The World of the Complex Ginzburg-Landau Equation*, to appear in Rev. Mod. Phys., preprint at cond-mat/0106115.

[123] J. T. Stuart and R. C. DiPrima, *The Eckhaus and Benjamin-Feir resonance mechanisms*, Proc. R. Soc. London A **362**, 27 (1978).

[124] A. Weber, L. Kramer, I. S. Aranson and L. Aranson, *Stability limits of traveling waves and the transition to spatiotemporal chaos in the complex Ginzburg-Landau equation*, Physica D**61**, 279 (1992).

[125] K. Nozaki and N. Bekki, J. Phys. Soc. Jpn. **53**, 1581 (1984).

[126] N. Bekki and K. Nozaki, *Formation of spatial patterns and holes in the generalized Ginzburg-Landau equation*, Phys. Lett. A **110**, 133 (1985).

[127] S. Popp, O. Stiller, I. S. Aranson, A. Weber and L. Kramer, *Localized hole solutions and spatiotemporal chaos in the 1D complex Ginzburg-Landau equation*, Phys. Rev. Lett. **70**, 3880 (1993);

[128] S. Popp, O. Stiller, I. S. Aranson and L. Kramer, *Hole solutions in the 1D complex Ginzburg-Landau equation*, Physica D **84**, 398 (1995).

[129] O. Stiller, S. Popp and L. Kramer, *From dark solitons in the defocusing nonlinear Schrdinger to holes in the complex Ginzburg-Landau equation*, Physica D **84**, 424 (1995).

[130] S. Popp, O. Stiller, I. S. Aranson and L. Kramer, *All we know about hole solutions in the CGLE*, Physica D **87**, 361 (1995).

[131] H. G. Schuster, *Deterministic Chaos* (Physik Verlag, Weinheim, 1984).

[132] J. P. Eckmann and D. Ruelle, *Ergodic-theory of chaos and strange attractors*, Rev. Mod. Phys. **57**, 617 (1985).

[133] J. L. Hansen and T. Bohr, *Fractal tracer distributions in turbulent field theories*, Physica D **118**, 40 (1998).

[134] D. A. Egolf and H.S. Greenside, *Relation between fractal dimension and spatial correlation length for extensive chaos*, Nature **369**, 129 (1994).

[135] D. A. Egolf and H. S. Greenside, *Characterization of the transition from defect to phase turbulence*, Phys. Rev. Lett. **74**, 1751 (1995).

[136] M. V. Bazhenov, M. I. Rabinovich and A. L. Fabrikant, *The amplitude - phase turbulence transition in a Ginzburg-Landau model as a critical phenomenon*, Phys. Lett. A **163**, 87 (1992).

[137] B. I. Shraiman, A. Pumir, W. van Saarloos, P. C. Hohenberg, H. Chaté and M. Holen, *Spatiotemporal chaos in the one-dimensional complex Ginzburg-Landau equation*, Physica D **57**, 241 (1992).

[138] H. Chaté, *Spatiotemporal intermittency regimes of the one-dimensional complex Ginzburg-Landau equation*, Nonlinearity **7**, 185 (1994); p. 33 in P. E. Cladis and Palffy-Muhoray (Eds.), *Spatio-Temporal Pattern Formation in Nonequilibrium Complex Systems* (Addison Wesley, Reading, 1995).

[139] H. Sakaguchi, *Breakdown of the phase dynamics*, Prog. Theor. Phys. **84**, 792 (1990).

[140] G. Giacomelli, R. Hegger, A. Politi and M. Vassalli, *Convective Lyapunov exponents and propagation of correlations*, Phys. Rev. Lett. **85**, 3616 (2000).

[141] A. Torcini, H. Frauenkron and P. Grassberger, *Studies of phase turbulence in the one-dimensional complex Ginzburg-Landau equation*, Phys. Rev. E **55**, 5073 (1997).

[142] R. Montagne, E. Hernández-García, A. Amengual and M. San Miguel, *Wound-up phase turbulence in the complex Ginzburg-Landau equation*, Phys. Rev. E **55**, 151 (1997).

[143] J. A. Yorke and E. D. Yorke, J. Stat. Phys. **21**, 263 (1979).

[144] C. Grebogi, E. Ott and J. A. Yorke, Phys. Rev. Lett. **50**, 935 (1983); Physica D **7**, 181 (1983).

[145] M. van Hecke, *Building blocks of spatiotemporal intermittency*, Phys. Rev. Lett. **80**, 1896 (1998).

[146] H. Chaté and P. Manneville, *Phase diagram on the two-dimensional complex Ginzburg-Landau equation*, Physica A **224**, 348 (1996).

[147] P. Manneville and H. Chaté, *Phase turbulence in the two-dimensional complex Ginzburg-Landau equation*, Physica D **96**, 30 (1996).

[148] Y. Kuramoto and T. Tsuzuki, *On the formation of dissipative structures in reaction-diffusion systems*, Prog. Theor. Phys. **54**, 687 (1975).

[149] G. Sivashinsky, *Nonlinear analysis of hydrodynamic instability in laminar flames, Part I, Deviation of basic equations*, Acta Astronautica **4**, 1177 (1977).

[150] M. Abel, H. Chaté and H. U. Voss, *Effective phase equations from phase turbulent data*, to be published.

[151] G. Grinstein, C. Jayaprakash and R. Pandit, *Conjectures about phase turbulence in the complex Ginzburg-Landau equation*, Physica D **90**, 96 (1996).

[152] M. Kardar, G. Parisi and Y. C. Zhang, *Dynamics of growing interfaces*, Phys. Rev. Lett. **56**, 889 (1986).

[153] L. Brusch, *Zur Theorie der KPZ-Gleichung im Grenzfall starker Kopplung*, Diploma Thesis, Technical University of Dresden, Germany (1997).

[154] J. Krug and H. Spohn, *Kinetic roughening of growing surfaces*, in *Solids far from equilibrium*, C. Goudrèche, ed. (Cambridge University Press, Cambridge, 1991).

[155] T. Halpin-Healy and Y. C. Zhang, *Kinetic roughening phenomena, stochastic growth, directed polymers and all that. Aspects of multidisciplinary statistical mechanics*, Phys. Rep. **254**, 215 (1995).

[156] G. L. Oppo and R. Kapral, *Discrete models for the formation and evolution of spatial structure in dissipative systems*, Phys. Rev. A **33**, 4219 (1986).

[157] F. Schmüser, *Analytische Beiträge zum Raum-Zeit-Chaos: von gekoppelten Abbildungen zum Isingmodell.*, Ph.D. Thesis, Bergische Universität Gesamthochschule Wuppertal, Germany (1999).

[158] S. Wolfram, *Theory and Applications of Cellular Automata*, Ed. (World Scientific, Singapore, 1986).

[159] A. Deutsch, *Cellular automata and biological pattern formation*, Habilitationsschrift, University of Bonn, Germany (1999).

[160] E. Doedel, *Nonlinear numerics*, Int. J. Bifurcation and Chaos **7**, 2127 (1997).

[161] E. Doedel, A. Champneys, T. Fairgrieve, Y. Kusntsov, *et al.*, AUTO97:*Continuation and bifurcation software for ordinary differential equations* (Concordia University, Montreal, 1997).

[162] U. Feudel and W. Jensen, CANDYS/QA - *A software system for qualitative analysis of nonlinear dynamical systems*, J. Bifurcation and Chaos **2**, 773 (1992).

[163] M. Hermann and K. Ullrich, *RWPKV - A software package for continuation and bifurcation problems in 2-point boundary value problems*, Appl. Math. Lett. **5**, 57 (1992).

[164] B. Sandstede and A. Scheel, *Absolute and convective instabilities of waves on unbounded and large bounded domains*, Physica D **145**, 233 (2000).

[165] L. D. Landau and E. M. Lifshitz, *Fluid Mechanics*, p.111 (Pergamon, Oxford, 1959).

[166] I. S. Aranson, L. Aranson, L. Kramer and A. Weber, *Stability limits of spiral and traveling waves in nonequilibrium media*, Rhys. Rev. A**46**, R2992 (1992).

[167] S. M. Tobias, M. R. E. Proctor and E. Knobloch, *Convective and absolute instabilities of fluid flows in finite geometry*, Physica D **113**, 43 (1998).

[168] B. Sandstede and A. Scheel, *Superspiral structures of meandering and drifting spiral waves*, Phys. Rev. Lett. **86**, 171 (2001).

[169] P. Brancher and J. M. Chomaz, *Absolute and Convective Secondary Instabilities in Spatially Periodic Shear Flows*, Phys. Rev. Lett. **78**, 658 (1997).

[170] P. Gondret, P. Ern, L. Meignin and M. Rabaud, *Experimental Evidence of a Nonlinear Transition from Convective to Absolute Instability*, Phys. Rev. Lett. **82**, 1442 (1999).

[171] see URL `http://www.ino.it/ torcini/CGLE/defect.html`

[172] M. van Hecke and M. Howard, *Ordered and self-disordered dynamics of holes and defects in the one-dimensional complex Ginzburg-Landau equation*, Phys. Rev. Lett. **86**, 2018 (2001).

[173] G. Hager, *Quasiperiodische Lösungen der eindimensionalen komplexen Ginzburg-Landau Gleichung*, Diploma Thesis, University of Bayreuth, Germany (1996).

[174] M. Kness, L. Tuckerman and D. Barkley, *Symmetry-breaking bifurcations in one-dimensional excitable media*, Phys. Rev. A **46**, 5054 (1992).

[175] See chapter 3 [6].

[176] H.-C. Chang, E. A. Demekhin and E. Kalaidin, SIAM J. Appl. Math. **58**, 1246 (1998); H.-C. Chang, E. A. Demekhin and D. I. Kopelevich, Physica D **63**, 299 (1993).

[177] N. W. Ashcroft and N. D. Mermin, *Solid State Physics* (Holt, Rinehart and Winston, New York, 1976);

[178] P. Collet and J.-P. Eckmann, *Instabilities and Fronts in Extended Systems* (Princeton University Press, 1990).

[179] M. Or-Guil, I. G. Kevrekidis and M. Bär, *Stable bound states of pulses in an excitable medium*, Physica D **135**, 154 (2000).

[180] A. Torcini, private communication.

[181] Workshop *The complex Ginzburg-Landau equation: theoretical analysis and experimental applications in the dynamics of extended systems*, Firenze, May 21-23 2001.

[182] N. Garnier, *Non-linear traveling waves in a finite geometry*, in [181]; private communication.

[183] J. Burguete, *Models on some convective experiments*, in [181]; private communication.

[184] M. van Hecke, C. Storm C and W. van Saarloos, *Sources, sinks and wavenumber selection in coupled CGL equations and experimental implications for counter-propagating wave systems*, Physica D **134**, 1 (1999).

[185] Y. Liu and R. E. Ecke, *Nonlinear traveling waves in rotating Rayleigh-Bénard convection: Stability boundaries and phase diffusion*, Phys. Rev. E **59**, 4091 (1999).

[186] I. Mutabazi, J. J. Hegesth, C. D. Andereck and J. E. Wesfreid, Phys. Rev. Lett. **64**, 1729 (1990).

[187] P. Bot, O. Cadot and I. Mutabazi, *Secondary instability of a roll pattern and transition to spatiotemporal chaos in the Taylor-Dean system*, Phys. Rev. E **58**, 3089 (1998).

[188] I. Aranson, L. Kramer, and A. Weber, *Core instability and spatiotemporal intermittency of spiral waves in oscillatory media*, Phys. Rev. Lett. **72**, 2316 (1994).

[189] P. S. Hagan, *Spiral waves in reaction-diffusion-equations*, SIAM J. Appl. Math. **42**, 762 (1982).

[190] E. Bodenschatz, A. Weber and L. Kramer, in *Nonlinear Wave Processes in Excitable Media*, edited by A. V. Holden, M. Markus and H. G. Othmer (Plenum Press, New York, 1990).

[191] A. T. Winfree, *Spiral waves of chemical activity*, Science **175**, 634 (1972); *Scroll-shaped waves of chemical activity in 3 dimensions*, Science **181**, 937 (1973).

[192] *Chemical Waves and Patterns*, edited by R. Kapral and K. Showalter (Kluwer, Doodrecht, 1995)

[193] A. S. Mikhailov and V. S. Zykov, *Kinematical theory of spiral waves in excitable media - comparison with numerical simulations*, Physica D**52**, 379 (1991).

[194] D. Barkley, *Linear stability analysis og rotating spiral waves in excitable media*, Phys. Rev. Lett. **68**, 2090 (1992); *Euclidean symmetry and the dynamics of rotating spiral waves*, Phys. Rev. Lett. **72**, 164 (1994).

[195] V. Perez-Munuzuni, M. Gomez-Gesteira, and V. Perez-Villar, *A geometrical-kinematical approach to spiral wave formation: super-spiral waves*, Physica (Amsterdam) **64D**, 420 (1993).

[196] B. Sandstede and A. Scheel, *Superspiral structures of meandering and drifting spiral waves*, Phys. Rev. Lett. **86**, 171 (2001).

[197] A. Weber, *Lokalisierte Strukturen und Übergang zu raum-zeitlichem Chaos in einfachen Ginzburg-Landau-Gleichungen*, Ph.D. Thesis, University of Bayreuth, Germany (1992).

[198] A. Goldbeter, D. Gonze, G. Houart, J.-C. Leloup, J. Halloy and G. Dupont, *From simple to complex oscillatory behavior in metabolic and genetic networks*, CHAOS **11**, 247 (2001).

[199] T. Haberichter, M. Marhl and R. Heinrich, *Birhythmicity, trirhythmicity and chaos in bursting calcium oscillations*, Biophys. Chem. **90**, 17 (2001).

[200] S. Silbernagl and A. Despopoulos, *Taschenatlas der Physiologie* (dtv-Thieme, Stuttgart, 1988).

[201] J. Koolman and K. H. Röhm, *Taschenatlas der Biochemie* (dtv-Thieme, Stuttgart, 1998).

[202] M. Falcke, private communication.

[203] A. Goldbeter, *Calcium oscillations*, p.349 in *Biochemical oscillations and cellular rhythms* (Cambridge University Press, Cambridge, 1996).

[204] J. Sneyd, J. Keizer and M. J. Sanderson, *Mechanisms of calcium oscillations and waves: a quantitative analysis*, FASEB J. **9**, 1463 (1995).

[205] J. Rinzel, *A formal classification of bursting mechanisms in excitable systems*, in *Mathematical topics in population biology, morphogenesis, and neurosciences*, Eds. E. Teramoto and M. Yamaguti (Springer, Berlin, 1987).

[206] R. Bertram, M. J. Butte, T. Kiemel and A. Sherman, *Topological and phenomenological classification of bursting oscillations*, Bull. Math. Bio. **57**, 413 (1995).

[207] M. Hauser, private communication.

# Acknowledgement

To Prof. Dr. P. Fulde, director at the Max-Planck-Institut for the physics of complex systems, I am grateful for his kind support of the junior research groups at that institut. He provided a pleasant working environment and enabled an extensive conference schedule to be enjoyed by the students. I also thank the institut for funding several journeys.

To even larger extent I am indebted to my supervisor Dr. M. Bär, head of the junior research group “Pattern formation in reaction-diffusion-systems”, for introducing me to this fascinating field of research. His ongoing encouragement, ideas and suggestions made this work possible. Also his perfect management of the junior research group created a motivating atmosphere as well as many contacts to external experts in the field.

A number of lectures held by Prof. Dr. U. Bahr, Prof. Dr. G. Diener, Dr. M. Bär, Dr. M. Or-Guil and Dr. H. Hinrichsen at the Technical University of Dresden provided a solid background for my studies. I want to thank all my teachers and collaborators for their commitment, especially Dr. M. van Hecke, Dr. A. Torcini and Dr. M. G. Zimmermann.

Also I want to acknowledge the technical assistence of H. Scherrer-Paulus, H. Deggelmann, T. Goerke, Dr. A. Torcini and Dr. W. Wolf in all computational issues and I thank Dr. M. Bär, Dr. T. Böck and Dr. A. Torcini for criticism on the manuscript of this Thesis. My closest colleagues were Dr. habil. G. Schliecker, Dr. M. Or-Guil, K. Lantsch, U. Gneisse, Dr. M. Bär, PD Dr. A. Deutsch, Dr. M. Falcke, Dr. T. Böck, Dr. C. Utzny, Dr. D. Joseph, Dr. U. Thiele, U. Börner, H. Kühne, E. Nicola, P. Kano and T. Goerke and I wish to thank them for the friendly atmosphere in our team and fruitful discussions especially on our daily walking-tour to the mensa.

I have to beg Katrins and Johannas pardon for not spending enough time with my family in the past month and I want to thank my as well as Katrins parents for their kind help.

# Versicherung

Hiermit versichere ich, dass ich die vorliegende Arbeit ohne unzulässige Hilfe Dritter und ohne Benutzung anderer als der angegebenen Hilfsmittel angefertigt habe; die aus fremden Quellen direkt oder indirekt übernommenen Gedanken sind als solche kenntlich gemacht. Die Arbeit wurde bisher weder im Inland noch im Ausland in gleicher oder ähnlicher Form einer anderen Prüfungsbehörde vorgelegt.

Diese Dissertation wurde in der Nachwuchsgruppe “Musterbildung in Reaktions-Diffusions-Systemen” der Max-Planck-Institutes für Physik komplexer Systeme in Dresden angefertigt und vom Leiter der Nachwuchsgruppe Dr. M. Bär betreut.